




8-2013

Fully Coupled Fluid and Electrodynamic Modeling of Plasmas: A Two-fluid Isomorphism and a Strong Conservative Flux-coupled Finite Volume Framework

Richard Joel Thompson
rthompso@utsi.edu

Follow this and additional works at: https://trace.tennessee.edu/utk_graddiss

 Part of the [Aerodynamics and Fluid Mechanics Commons](#), [Engineering Physics Commons](#), [Fluid Dynamics Commons](#), [Mechanical Engineering Commons](#), [Partial Differential Equations Commons](#), [Plasma and Beam Physics Commons](#), and the [Propulsion and Power Commons](#)

Recommended Citation

Thompson, Richard Joel, "Fully Coupled Fluid and Electrodynamic Modeling of Plasmas: A Two-fluid Isomorphism and a Strong Conservative Flux-coupled Finite Volume Framework. " PhD diss., University of Tennessee, 2013.
https://trace.tennessee.edu/utk_graddiss/2491

This Dissertation is brought to you for free and open access by the Graduate School at TRACE: Tennessee Research and Creative Exchange. It has been accepted for inclusion in Doctoral Dissertations by an authorized administrator of TRACE: Tennessee Research and Creative Exchange. For more information, please contact trace@utk.edu.

To the Graduate Council:

I am submitting herewith a dissertation written by Richard Joel Thompson entitled "Fully Coupled Fluid and Electrodynamic Modeling of Plasmas: A Two-fluid Isomorphism and a Strong Conservative Flux-coupled Finite Volume Framework." I have examined the final electronic copy of this dissertation for form and content and recommend that it be accepted in partial fulfillment of the requirements for the degree of Doctor of Philosophy, with a major in Mechanical Engineering.

Trevor Moeller, Major Professor

We have read this dissertation and recommend its acceptance:

Gary A. Flandro, Roy Schulz, Christian G. Parigger

Accepted for the Council:

Carolyn R. Hodges

Vice Provost and Dean of the Graduate School

(Original signatures are on file with official student records.)

FULLY COUPLED FLUID AND ELECTRODYNAMIC MODELING OF
PLASMAS: A TWO-FLUID ISOMORPHISM AND A STRONG CONSERVATIVE
FLUX-COUPLED FINITE VOLUME FRAMEWORK

A Dissertation
Presented for the
Doctor of Philosophy
Degree
The University of Tennessee, Knoxville

Richard Joel Thompson

August 2013

*To the women in my life — Sarah, Verity and Mary Evangeline;
and to our God, who has brought us together*

וְאַתָּנָה לְבִי לְדַעַת חֻכְמָה וְדַעַת הַלְלוֹת וְשִׁבְלוֹת

“Live with what you cannot change.”

—Moiraine Damodred, *The Wheel of Time*

“You are in a maze of twisty little passages, all alike.”

—ZORK: The Great Underground Empire

Acknowledgments

It started with a nine-year-old, who walked into a building. Until that nine-year-old walked in, the worlds he had seen, the planets he had visited and set foot on in stories and books, had been confined to the fastastical and mythical. But walking into that building, it dawned upon him with true force that those stories were not merely fiction — they could be lived out; they could be given form and flesh, and they could be clothed in substance. The building was the Smithsonian’s National Air and Space Museum, and these were my beginnings on a journey to become an engineer.

The dissertation you are reading is a culmination of that journey so far; it is the close of one chapter, but the opening of another. The journey of the Philosophiae Doctor is meant to be one of demonstrating independence and self-sufficiency, but it has also been an endearing revelation of how much I depend on others, and how grateful I am for their support. I would like to express my gratitude to some of these extraordinary individuals.

My advisor, Dr. Trevor Moeller, deserves the highest praise for his role as an outstanding advisor. He has tirelessly guided my development as a researcher, from the most diminutive question to the global management of this project. He has challenged me to live out my potential as a scientist, and I am grateful for his guidance and friendship. I also have the unique honor of being the first (of what I trust will be many) graduated doctoral students under his instruction.

I am indebted to my doctoral committee, comprised of Dr. Gary Flandro, Dr. Roy Schulz and Dr. Christian Parigger, who have performed an inestimable service to me. The courses I have taken under their instruction, the guidance they have provided and their meritorious faith in my work will not be forgotten.

During my tenure here, I have also been offered opportunities to work further and beyond the doctoral requirements. I sincerely appreciate the wisdom and suggestions of Dr. Charles Merkle (from Purdue University) regarding much of the work being presented in this dissertation, and his willingness to collaborate with UTSI in these efforts. I thank Dr. Christian Parigger for the invaluable opportunity to work on an experimental spectroscopic project, from which I learned a great deal. I thank Dr. Reza Abedi for inviting me to work with him on his fascinating computational research, which we will hopefully see more of in the near future. In addition to my chair and committee members, I would also like to thank Dr. K. C. Reddy for offering some particularly rare and valuable mathematics courses. I am grateful to the University of Tennessee Space Institute and the NASA Tennessee Space Grant Consortium for their financial support,

which has permitted me to pursue this endeavor.

I wish to express my gratitude to my friends and colleagues. To those here at the Space Institute: Nehemiah Williams, Andrew and Jade Wilson, Jason and Amanda King, James Rogers, Matthew and Olivia Parrish, Sabrina Hurlock, Dimitri Kavelakis, Mike Akiki and several others here, it has been rewarding to work with you. To my family at Cedar Lane Church of Christ: Greg and Andrea Muse, Wes and April Winton, Rylan and Sheree Cox, Steven and Kelly Hovater, Joel and Andrea Abrahams, and Dr. Steve and Margaret Bills. To my family at Christ Community Church: Pastor Jim and Lori Zidan, Joe and Tammy O'Connor, Dave and Nancy Waldo, Gregg and Kathy Leisman, Jean Potter and Chrissy Davis-Camp (my wife and I courted at her contradancing sessions). To others I know in the community: Eric and Linda Sutherland (Linda birthed both of my daughters), Dr. Alan and Julie Hale, Ryan Bates, Jeff and Patricia Stewart, Ashley Lapenta, Kathleen Anderson. To my inlaws: Peter and Sally Sherrouse, Paul Sherrouse, Daniel Sherrouse, Samuel Sherrouse and Judah Sherrouse. Paul has also played a role as fellow student, friend and landlord during our time here. I also deeply appreciate all of the wisdom and valuable information on communities such as Stack Overflow, Stack Exchange, Superuser and Phinished.org. To all of these people, I thank you for your continued support — academically, professionally and personally — which I cannot imagine having succeeded without.

The Celtic Cup Coffeehouse of Tullahoma and its owners, Denise and Chris Smith, have played a unique role in my time here. I sincerely thank them for accomodating my wife through and after her pregnancy to continue working there. Their esteemed coffee and pleasant atmosphere have fueled the work contained here.

My family in Nashville has stood by me through all of this. To my father and mother, John Richardson and Lauren Michelle Thompson, my sisters Jennifer Michelle Heath and Jill Marie Hartline, to my brother-in-law Logan Hartline, and to my aunt Nina Katherine Haile, the love you've shown me is beyond words.

I started this degree alone, but was blessed to meet my wife during my time here. Sarah Lynn Thompson, I stand amazed at the unwavering support you have lent me throughout this project. I am incapable of describing how much your love has meant during this season. To my two beautiful daughters, Verity Elizabeth Thompson and Mary Evangeline Thompson, I am blessed to be called your father, and I thank you for filling me with joy when I need it most.

I would like to recognize two individuals who have passed on from this life during my time here. Amy Sutherland was a vibrant young woman that Sarah and I had the pleasure of knowing briefly. Lt. Col. Gregg Bettis played a role as a mentor to me at the beginning of my doctoral work. They are sorely missed.

Finally, I thank our God for the opportunity of joining in His mission and creation, fulfilling his will on earth. Much of this dissertation has been learning of my reliance on you; your love has sustained me through everything.

Abstract

Ideal and resistive magnetohydrodynamics (MHD) have long served as the incumbent framework for modeling plasmas of engineering interest. However, new applications, such as hypersonic flight and propulsion, plasma propulsion, plasma instability in engineering devices, charge separation effects and electromagnetic wave interaction effects may demand a higher-fidelity physical model. For these cases, the two-fluid plasma model or its limiting case of a single bulk fluid, which results in a single-fluid coupled system of the Navier-Stokes and Maxwell equations, is necessary and permits a deeper physical study than the MHD framework. At present, major challenges are imposed on solving these physical models both analytically and numerically.

This dissertation alleviates these challenges by investigating new frameworks that facilitate efficient modeling of plasmas beyond the MHD description. Two investigations are performed: first, an isomorphism is constructed between the two-fluid plasma model and the Maxwell equations. This permits a set of unified Maxwell equations for both the electrodynamic and hydrodynamic behavior, but introduces an analogous notion of charge and current density for a fluid, which must be modeled to solve the new equations. We examine the homogeneous case (where these sources vanish), and then discuss iterative approaches and empirical modeling of the sources. We calculate some simple source models for fluid problems, including Blasius boundary layer flow. We demonstrate solution approaches using Green's functions methods and the method of images, for which a closed-form solution to Blasius boundary layer flow is achieved.

The second investigation recasts the single-fluid model into a strong conservative form. This permits the coupled Navier-Stokes and full Maxwell equations to be written exactly, but with no source terms present, which tend to cause numerical instability during simulation. The removal of the source terms is shown to improve the stability and robustness of the equations, but at the cost of introducing a significantly more complicated eigenstructure; we present the new eigenstructure for this system of equations and demonstrate an effective Riemann solver and flux splitting approach. Validation tests including magnetohydrodynamic problems, radio wave propagation tests and plasma instabilities and turbulence are presented.

Table of Contents

1	Introduction and Motivation	1
1.1	Prologue	1
1.2	An Overview of Plasma Physics	5
1.2.1	Plasma Parameters	5
1.2.1.1	Debye Length, λ_D	6
1.2.1.2	Plasma Parameter, Λ	7
1.2.1.3	Larmor Radius, r_L	7
1.2.1.4	Cyclotron Frequency, ω_c	8
1.2.1.5	Plasma (Langmuir) Frequency, ω_p	8
1.2.1.6	Skin Depth, l_c	9
1.2.1.7	Collision Frequency, $\nu_{\alpha\beta}$	9
1.2.1.8	Mean Free Path, λ_{mfp}	10
1.2.1.9	Hall Parameter, β_H	11
1.2.1.10	Plasma Electrical Conductivity, σ	11
1.2.2	Typical Values for the Plasma Parameters	12
1.2.3	Definition of a Plasma	13
1.3	Limitations to the Magnetohydrodynamic Framework	15
1.4	A Picture of the Problem	17
1.5	Going Beyond the MHD Framework	19
1.6	Contributions to the State of the Art	20
1.7	Outline of the Dissertation	22
2	Mathematical Models for Single-fluid and Two-fluid Plasmas	25
2.1	Maxwell's Equations	26
2.1.1	Maxwell's Equations	26
2.1.2	Charge Continuity	28
2.1.3	Electromagnetic Waves	28
2.1.4	Vector and Scalar Potentials	29
2.1.4.1	Lorentz Gauge	29

2.1.4.2	Coulomb Gauge	30
2.1.5	Divergence Constraints	30
2.2	Kinetic Description of the Fluid	31
2.3	Two-fluid Description	33
2.4	Single-fluid Description	37
2.5	Constitutive Relation for Current Density: Ohm's Law	38
2.6	Magnetohydrodynamic Description	40
2.7	Summary of Models	46
3	An Isomorphism Between Two-fluid Plasmas and Classical Electrodynamics	51
3.1	Motivation and State of the Art	51
3.2	Objective	54
3.3	An Isomorphism Between Multifluid Plasmas and Maxwell's Equations	55
3.4	Convolutions of the Field Equations	60
3.5	Immediate Consequences and Ramifications of the Isomorphism	63
3.5.1	Reduction to Fluid Dynamics	63
3.5.2	Potentials, Gauge Transformations and Gauge Analogies	64
3.5.3	Boundary Conditions	66
3.5.4	Lagrangian Formalism for Two-fluid Plasmas	67
3.5.5	Inverse Transformation: An Analogous Drift Relation	70
3.6	Summary of the Isomorphic Framework	71
4	Source Modeling and Solution Approaches Using the Isomorphic Framework	72
4.1	Introduction	72
4.2	Homogeneous Solutions	74
4.2.1	Homogeneous Wave Equations	75
4.2.2	Recovering Magnetohydrodynamic Waves	75
4.3	Inhomogeneous Solutions	77
4.3.1	Inhomogeneous Wave Equations	78
4.3.2	Iterative Source Modeling	80
4.4	Empirical Source Modeling, Reconstructive and Green's Function Approaches for Fluids	84
4.4.1	Couette Flow Solution	84
4.4.2	Duct Flow Solution	87
4.4.3	Blasius Boundary Layer Flow Solution	93
4.4.4	Closed-form Blasius Solution Using a Bounded-Domain Green's Function Approach	102
4.4.5	Gasdynamic and Magnetohydrodynamic Charge from Numerical Simulations	104
4.5	Summary of Solution Approaches	109

5	A Strong Conservative Finite Volume Framework for Plasma Simulations	114
5.1	Motivation and State of the Art	114
5.2	Objective	117
5.3	Single-fluid Source-coupled Form	118
5.4	Conservation Form of Maxwell's Equations	119
5.5	Single-fluid Strong Conservative Form	121
5.6	Overview of the Numerical Formulation	121
5.7	Systems of Hyperbolic Conservation Laws	122
5.7.1	Quasilinear Form, Jacobian, Eigenstructure	123
5.7.2	The Scalar Linear Advective Wave Equation	125
5.7.3	Characteristics and the General Solution of the Linear Cauchy Problem	126
5.7.4	The Riemann Problem	127
5.8	The Finite Volume Method	130
5.9	Dual-time Implicit Scheme	132
5.10	Divergence Cleaning	135
5.10.1	Brackbill-Barnes Divergence Cleaning	135
5.10.2	Lagrange Multiplier Approach (Perfectly Hyperbolic Maxwell Equations) Divergence Cleaning Approach	136
5.11	Roe Approximate Riemann Solver Flux Scheme	137
5.11.1	Jacobian Matrix	140
5.11.2	Eigenvalues	140
5.11.3	Eigenvectors	141
5.11.4	Solutions to the Riemann Problem	141
5.12	Advected Upstream Splitting Method (AUSM) Flux Scheme	142
5.13	Boundary Conditions	145
5.13.1	Periodic Boundary Conditions	145
5.13.2	Transmissive Outflow and Inviscid Wall Boundary Conditions	145
5.14	Putting It All Together: Meshing, Interpolation, Gradient Reconstruction and Solver Algorithm	146
6	Validation Tests for the Strong Conservative Formulation	151
6.1	Brio and Wu Plasma Shock Riemann Problem	151
6.2	Jiang and Wu Plasma Shock Riemann Problem	153
6.3	Mixed Wave/Diffusion Test: Radio Wave Propagation in Plasma	159
6.4	Kelvin-Helmholtz Instability with Applied Magnetic Field	164
6.5	Orszag-Tang Plasma Turbulence Problem	164
6.6	Magnetohydrodynamic Rotor Problem	166

6.7	Comparisons Between Source-coupled and Strong Conservative Schemes	174
6.8	Comparisons Between Roe and AUSM Flux Schemes	176
6.9	A Strong Conservative Form for the Two-fluid Plasma Model	176
7	Discussion, Conclusions, Future Directions	179
7.1	Review of the Objective	179
7.2	Summary of Findings	180
7.2.1	Findings for the Two-fluid Isomorphism	180
7.2.2	Findings for Comparison of Strong Conservative and Source-coupled Forms	181
7.3	Contributions to the State-of-the-Art	182
7.4	Future Directions	183
7.5	Concluding Remarks	184
	Bibliography	185
	Appendix	203
A.1	Derivation of the Two-fluid Maxwell Equations	204
A.1.1	Gauss Laws	204
A.1.2	Faraday Law	204
A.1.3	First Ampere-Maxwell Law	205
A.1.4	Second Ampere-Maxwell Law	206
A.2	Jacobians and Eigenstructure of the Navier-Stokes Equations	208
A.2.1	Jacobian Matrix	209
A.2.2	Eigenvalues	210
A.2.3	Eigenvectors	210
A.2.4	Solution to the Linearized Riemann Problem	211
A.3	Jacobians and Eigenstructure of the Maxwell Equations	213
A.3.1	Jacobian Matrix	214
A.3.2	Eigenvalues	215
A.3.3	Eigenvectors	216
A.3.4	Solution to the Riemann Problem	217
A.4	Jacobians and Eigenstructure of the Source-coupled Navier-Stokes and Maxwell Equations . .	218
A.4.1	Jacobian Matrix	219
A.4.2	Eigenvalues	219
A.4.3	Eigenvectors	219
A.4.4	Jacobian Matrices for Implicit Scheme	219

A.5	Jacobians, Eigenvalues, and Eigenvectors of the Strong Conservative Navier-Stokes and Maxwell	
	Equations	222
A.5.1	Jacobian Matrix	222
A.5.2	Eigenvalues	224
A.5.3	Eigenvectors	224
A.5.4	Jacobian Matrices for Implicit Scheme	229
Vita		232

List of Tables

1.1	Typical plasma parameters for various plasmas. [10, 15]	12
2.1	Physical units of electromagnetic quantities, using base dimensions of length $[l]$, time $[t]$, mass $[m]$, and charge $[q]$, and derived units of voltage $[V] = [ml^2t^{-2}q^{-1}]$, current $[I] = [qt^{-1}]$, magnetic flux $[\Phi] = [Vt]$, capacitance $[C] = [qV^{-1}]$, inductance $[L] = [\Phi I^{-1}]$, and conductance $[G] = [IV^{-1}]$	27
2.2	Two-fluid plasmadynamic equations.	47
2.3	Single-fluid plasmadynamic equations, including full Maxwell equations.	48
2.4	Resistive magnetohydrodynamic (MHD) equations. [16]	49
2.5	Ideal magnetohydrodynamic (MHD) equations. [16]	50
3.1	The relationships between the species-specific quantities in a multifluid plasma and their analogues in classical electrodynamics.	63
4.1	Coefficients for a tenth-order polynomial fit for the Blasius charge distribution.	98
5.1	Nomenclature of mesh data structures.	149
6.1	A comparison of the performance of the source-coupled and strong conservative formulations for the Brio and Wu problem.	153
6.2	A comparison of the performance of the source-coupled and strong conservative formulations for the Jiang and Wu problem.	159

List of Figures

1.1	A diagram of plasma in the known universe, plotted by electron number density versus temperature. [10, 15]	13
2.1	A diagram of Feynman's example of displacement current [106]. Spherically symmetric radial distribution of current and electric field. What is the magnetic field around an Amperian loop?	43
3.1	A two-dimensional axisymmetric contour plot of the percent gradient in a plasma thruster plume [118, 135, 136]. The variation was typically less than 1% for an averaging length of $R = 10\mu m = 0.10\lambda_{D,max}$. This suggests that the relative difference between $\langle u^2 \nabla \times \mathbf{\Omega} \rangle$ and $\langle u^2 \rangle \nabla \times \langle \mathbf{\Omega} \rangle$ can be expected to be small in such a plasma.	62
3.2	A diagram of the Gaussian pillbox and rectangular contour used for deriving the boundary conditions across an interface surface of charge density ρ_{surf} and current density \mathbf{j}_{surf} .	67
4.1	A diagram of the particle in cell algorithm. Each timestep requires four substeps: (1) Starting with position, \mathbf{x}_i , and velocity, \mathbf{v}_i , data for each particle i , we sum each particle's contribution to the total charge and current density, $\rho(x, t)$ and $\mathbf{j}(x, t)$, respectively. (2) With the charge and current density, solve the Maxwell equations for the electromagnetic fields. (3) With the electromagnetic fields in hand, use the Lorentz force and Newton's law to determine the acceleration acting on each particle, \mathbf{a}_i . (4) Integrate the acceleration to calculate the new velocity, \mathbf{v}_i , and integrate again to determine the new position, \mathbf{x}_i , for the next timestep.	81
4.2	A diagram of the usual configuration for Couette flow. Coordinate system is shown in green. The velocity vanishes at the lower plate, $u(-b) = 0$, and matches the velocity U of the upper plate at $y = b$, $u(b) = U$. [7]	85
4.3	A diagram of the usual configuration for fully developed duct flow. The coordinate system is shown in green. The diameter of the duct is $2b$. At both solid surfaces, the no slip boundary condition is applied, $u(b) = u(-b) = 0$. A parabolic velocity profile results. [6, 7]	87
4.4	A plot of the Lamb vector, ζ_y , and vorticity, ω_z , for duct flow.	89
4.5	A plot of the nondimensional fluid charge and current density for the duct flow problem. The analytical form of the velocity, as given in equation 4.43, is shown for comparison. Only half of the domain is shown; here the solid wall is at $y = -1$ and the centerline is at $y = 0$.	90

4.6	Plot of the different solution methods described in the text compared to the analytical duct velocity profile. Only half of the domain is shown for clarity, with the solid wall at $y = -1$ and the centerline at $y = 0$; the solution is symmetric across $y = 0$. Solution Methods A and B are reconstructive, using equation 4.41 to calculate the velocity, whereas Solution Methods C and D use Green's function approaches to solve for the potential. Solution Methods A and B achieve errors of 0.2% and 0.9% in the vortical region ($y < -0.1$), but reach errors of 2% and 100% in the center, since the vorticity vanishes and equation 4.41 becomes indeterminant. l'Hôpital's rule may be applied here to calculate the correct values of the velocity at the centerline. Solution Methods C and D achieve very low error (less than hundreds of a percent) across the entire domain.	94
4.7	Diagram of the Blasius boundary layer flow problem. In the physical plane, the flow is two-dimensional, but the problem admits a similarity solution in the similarity plane. The quantity $\delta(x)$ denotes the boundary layer thickness. [6]	95
4.8	The classic numerical solution to the Blasius equation, equation 4.61. This solution was computed using the shooting method in a Python code.	96
4.9	The calculated Lamb vector, ζ_y , and vorticity, ω_z , for the Blasius solution. Differencing the solution directly and using the expressions given in equations 4.65 and 4.62 give identical results.	98
4.10	The calculated source terms, ϱ_F and $j_{F,x}$, for Blasius layer flow. These results qualitatively agree with Marmanis' results for turbulent, incompressible flow [108,109], although the source terms are closer to the wall in turbulent flows since the velocity profile is flatter. In the freestream, the flow becomes homogeneous, and no source terms appear.	99
4.11	Blasius solution calculated using the isomorphic equations with a given charge distribution. Four different solution methods were attempted: (A) a check on the drift relation, (B) an iterative scheme that reconstructs the velocity by solving for Lamb vector and vorticity and using the drift relation, (C) a bounded-domain Green's function approach for calculating the kinetic energy, and (D) a method of images approach. The reconstructive schemes failed in the irrotational region, since the drift relation becomes indeterminant as $\omega \rightarrow 0$. Methods (C) and (D) matched remarkably well, with error much less than 1%.	103
4.12	Comparison of the accepted Blasius velocity profile (computed numerically using the shooting method), and the numerical and closed-form (equation 4.91) solutions obtained using the bounded-domain Green's function approach. This approach requires some estimated upper limit that bounds the boundary layer, L . It is not necessary that L be the boundary layer thickness, $\delta(x)$, simply that $\delta(x) < L$. Here, $L = 7$	105
4.13	Unstructured mesh used for calculating the oblique shock. The mesh is composed of 36,389 elements.	106

4.14	Mach number of the oblique shock solution after a steady-state condition was reached. The Mach number left of the shock is 2.5, while the Mach number behind the shock reaches a minimum of 1.848 along the lower boundary (a slight dip in the solution occurs here), while the oblique shock relations yield a downstream Mach number of 1.874; this is within 1.4% of the theoretical value. The angle of the oblique shock was measured visually to be 36.5° , while the predicted shock angle is 36.9° ; this is within 1.2%.	107
4.15	The microscopic gasdynamic charge for the oblique shock problem.	108
4.16	A convolved macroscopic gasdynamic charge distribution for the oblique shock problem. The averaging length here was $R = 5\Delta x \sim 0.158m$. The region of charge near the shock is thinner and more uniform than the microscopic charge presented in Figure 4.15. This investigation implies that the charge at a shock could potentially be treated as a surface of charge, similar to an interface with a discontinuous jump in classical electrodynamics.	109
4.17	The microscopic form of the generalized charge for the Orzsag-Tang MHD vortex problem. The charge is intrinsically time-dependent, and so is changing each timestep.	110
4.18	The macroscopic, convolved charge distribution for the Orzsag-Tang MHD vortex problem. The averaging length here was $R = 3\Delta x \sim 0.194m$. Notice that the small-scale noise and ripples have been averaged out; only the surface charge due to shocks remain, similar to that seen in the oblique shock source data.	111
4.19	The microscopic charge distribution from a Kelvin-Helmholtz hydrodynamic instability. . . .	112
4.20	The convolved charge distribution for a Kelvin-Helmholtz hydrodynamic instability. The convolved form is not much different in structure from the microscopic form. The charge appears along the boundary between the high- and low-density fluids. The averaging length used here was $R = 0.077m$	113
5.1	Schematic of the classic Riemann problem. (a) The initial condition for a scalar system; there is a discontinuity at $x = 0$. The initial data is U_L for $x < 0$ and U_R for $x > 0$. (b) The propagation of the waves for a system of m conservation laws; m different waves result. In this figure, $m = 5$; the black lines trace the m characteristic lines, $x = \lambda^{(p)}t$	128
5.2	An example of constructing the solution to the Riemann problem for $m = 3$. Tracing back along the characteristics, we determine $W^{(p)}$ from the initial conditions. The solution \mathbf{U} is constant in each sector. The general solution is $\mathbf{U}(x, t) = \sum_{p=H+1}^m W_L^{(p)} \mathbf{K}^{(p)} + \sum_{p=1}^H W_R^{(p)} \mathbf{K}^{(p)}$, where $\lambda_H < x/t < \lambda_{H+1}$. The left-most and right-most sectors are known (given in the initial conditions); they are $\mathbf{U}_L = \sum_{p=1}^m W_L^{(p)} \mathbf{K}^{(p)}$ and $\mathbf{U}_R = \sum_{p=1}^m W_R^{(p)} \mathbf{K}^{(p)}$, respectively. In the sector \mathbf{U}_L^* , the $p = 1$ characteristic has been crossed, but not the second two, so $H = 1$, and the solution is $\mathbf{U}_L^* = W_R^{(1)} \mathbf{K}^{(1)} + W_L^{(2)} \mathbf{K}^{(2)} + W_L^{(3)} \mathbf{K}^{(3)}$. In Sector \mathbf{U}_R^* , the first two characteristics have been crossed, but not the third; here, $H = 2$, and the solution in this region is $\mathbf{U}_R^* = W_R^{(1)} \mathbf{K}^{(1)} + W_R^{(2)} \mathbf{K}^{(2)} + W_L^{(3)} \mathbf{K}^{(3)}$. [151]	129

5.3	A sample two-dimensional control volume bounded by four sides. If faces were indexed by an integer j , then all four faces could be specified as $j \in \{1, \dots, 4\}$; the corresponding faces bounding the volume would be $\mathcal{F} = \{1, 2, 3, 4\}$. The \mathbf{n}_j represents the normal unit vectors for $j \in \{1, 2, 3, 4\}$.	131
5.4	Godunov methods treat the discretized mesh of solution vectors \mathbf{U}_k as a series of Riemann problems. (a) In a one-dimensional mesh, considering the solution vector \mathbf{U}_k to be piecewise constant across the mesh (constant in each separate volume k), we see that the face adjoining two volumes (face j in the figure) may be regarded as a Riemann problem, where the solution data in the two volumes represents the left and right data, \mathbf{U}_L and \mathbf{U}_R , respectively. (b) The extrapolation of this scheme to multiple dimensions holds as well. In this two-dimensional example, the quadrilateral mesh of piecewise constant data \mathbf{U}_k forms a Riemann problem in the direction normal to a given face j .	138
5.5	A diagrammatic sketch of connectivity within the mesh. An example two-dimensional mesh is shown on the left, composed of triangles (shown in solid lines). Elements are indicated for nodes as red indices in circles, for faces as blue indices in squares, and for volumes as green indices in triangles. Connectivity between the different elements are shown via dashed lines. Elements are not restricted to triangular in shape; each element can carry as many constituent edges and nodes as memory permits.	148
6.1	Solution to the one-dimensional Brio and Wu problem [145] using the source-coupled and strong conservative flux-coupled solutions at $t = 0.10$. The system was uncoupled here ($\sigma = 0$). The solutions lie on top of each other. No magnetic field is visible because it has already propagated out of the domain (see Figure 6.2 for visualizations of the early wave motion.)	154
6.2	Wave propagation of the tangential fields at $200\Delta t$, $400\Delta t$, $600\Delta t$ and $800\Delta t$ for the Brio and Wu problem [145]. The electric field has been scaled down by $1/c_0$ to fit.	155
6.3	Solution to the one-dimensional Brio and Wu problem [145] using the source-coupled and strong conservative flux-coupled solutions. The accepted magnetohydrodynamic solution is also shown. The waves are denoted in the density plot: two fast rarefaction waves (FR), a slow compound wave (SC), a contact discontinuity (CD), and a slow shock wave (SS). The MHD solution (gray solid line) is almost exactly underneath the strong conservative solution (blue points).	156
6.4	Early wave/diffusion behavior for different conductivities in the Brio and Wu problem [145]. Redder curves indicate a higher conductivity.	157
6.5	The tangential magnetic field at the final simulation time $t = 0.10$ for different conductivities in the Brio and Wu problem [145]. Redder curves indicate a higher conductivity. In the $\sigma = 0$ case, the waves have already propagated out of the domain by this late in the simulation.	158

6.6	Solutions to the Jiang and Wu hypersonic MHD problem [142,145], using the source-coupled formulation and the strong conservative formulation, and a comparison to the analytical MHD solution. Both source-coupled and strong conservative solutions are on top of the analytical solution.	160
6.7	One-dimensional simulation where $B_z = 1.0$ is imposed on the left boundary ($x = 0\text{m}$) for all time. (a) The vacuum ($\sigma = 0\text{mho/m}$) test. The wave impinges on the right of the domain ($x = 1\text{m}$) at $t = 3.33\text{ns}$, indicating pure wave propagation. (b) The $\sigma = 10^{-2}\text{mho/m}$ test. Mixed wave and diffusion behavior of the magnetic field results. For comparison, the one-dimensional analytical solution for the pure diffusion (MHD) magnetic field is shown for identical times. Here, the MHD solution is suspect, because the displacement current is significant. (c) The $\sigma = 10^{-1}\text{mho/m}$ test. The magnetic field exhibits more diffusion than wave behavior. At $t = 0.66\text{ns}$, some wave contribution is present, but is severely damped by the diffusion. The remaining four times agree very closely with the expected MHD solution.	162
6.8	Radio wave propagation through vacuum region ($x < 0.5\text{m}$) impinging on a plasma slab of finite conductivity ($x > 0.5\text{m}$, depicted in gray). The conductivity is (a) vacuum ($\sigma = 0\text{mho/m}$), (b) $\sigma = 10^{-1}\text{mho/m}$, (c) $\sigma = 1\text{mho/m}$. Times (starting with top and ending with bottom plot) are 1.67ns, 2.00ns, 2.33ns, 2.67ns, and 3.00ns, respectively.	163
6.9	A visual depiction of the evolution of the Kelvin-Helmholtz instability without (left column) and with (right column) a weak applied magnetic field (initially uniform $B_x = 0.3$). Times (from top to bottom) are approximately $t = 1.5, 3.0, 5.8$. The presence of the magnetic field suppresses the small-wavelength instabilities and tends to stabilize the flow.	165
6.10	Two-dimensional spatial contour plots of (a) density, and (b) pressure, and two-dimensional vector plots of (c) velocity field, and (d) magnetic field for the Orszag-Tang problem [142] calculated at the final time $t = 3.0$. The vector plots present only every ninth vector, to make the plot more visible. This solution was calculated on the 256×256 grid, and agrees well with the accepted magnetohydrodynamic solution [142].	167
6.11	A visual comparison of the strong conservative Roe solution on 256×256 grid (left column) to the MHD solution on comparable grid size (right column). The top comparison shows density contour plots; the middle comparison shows vector plots of the velocity field; the bottom comparison shows vector plots of the magnetic field. Contour levels and vector densities were not matched to the MHD solution, although the minimum and maximum contour levels were the same as those used in MHD solutions. The MHD density plot is reprinted from [176] with permission from Elsevier; the MHD vector plots are reprinted from [142] with permission from Elsevier.	168

6.12	This simulation was run using the AUSM strong conservative scheme on the 256×256 grid, but was run for much longer to see the long-term development of turbulence. Times are $t =$ (a) 0.5, (b) 1.0, (c) 2.0, (d) 3.0, (e) 4.0, (f) 5.0, (g) 6.0, (h) 7.0.	169
6.13	Two-dimensional contour plot of the density for the Orszag-Tang vortex solution [142] calculated at time $t = 3.0$ for different grid meshes. (a) 64×64 . (b) 128×128 . (c) 192×192 . (d) 256×256	170
6.14	Two-dimensional contour plot of the density for the Orszag-Tang vortex solution [142] calculated at time $t = 3.0$ for different grid meshes. (a) 64×64 . (b) 128×128 . (c) 192×192 . (d) 256×256	171
6.15	Spatial contour plots of the (a) density and (b) pressure, and vector plots of the (c) velocity field and (d) magnetic field at the final solution time of $t = 0.15$ using the 256×256 grid. The solution matches very well to the accepted MHD solutions [176, 202]. Torsional Alfvén waves transmit the angular momentum of the dense rotor to the ambient fluid. Only every eighteenth vector is shown to improve visibility.	173
6.16	A visual comparison of (left) the pressure calculated using the MHD theory [176] and (right) the pressure calculated by the new fully coupled strong conservative Roe solver. Left image is reprinted from [176], with permission from Elsevier.	174
6.17	A comparison of the pressure calculated for the MHD rotor solution using grid size (a) 64×64 , (b) 128×128 , (c) 192×192 , and (d) 256×256 . The lower-resolution solutions show several regions where the solution depends on the grid size. The higher-resolution meshes show consistent agreement of the solution.	175
6.18	Image differences of the Roe and AUSM schemes for the Orszag-Tang magnetohydrodynamic vortex problem, as discussed in Section 6.5. The images were produced as 1024×1024 -pixel contour plots at identical levels, color map, time, and figure placement. The images were subtracted in grayscale color space. Subfigures here show different grid resolutions: (a) 64×64 , (b) 128×128 , (c) 192×192 , and (d) 256×256 . It is clear from subfigure (a) that, at low grid resolutions, the Roe and AUSM approaches differ. In these low-res cases, the Roe method proved much more accurate to the expected grid-independent solution. As the grid resolution is increased, the Roe and AUSM methods agree more and more closely, although the execution time for the Roe method becomes excessive compared to the AUSM scheme. In the highest grid resolution tested in subfigure (d), we see that there is a slight discrepancy in the locations of the shocks. This is suspected to be a diffusion issue with the AUSM scheme, since the AUSM method adds more diffusion across shocks than the Roe method.	177

Nomenclature

Roman Symbols

$\hat{\mathbf{A}}$	Jacobian matrix
\mathbf{A}	Vector potential, Tm
A	Coefficient for duct flow (Chapter 4); area of a face (Chapter 5)
a	Speed of sound, m/s
\mathbf{B}	Magnetic induction field, H/m
\mathcal{B}	Set of associated neighbors
B	Magnetic induction field strength, T
\mathbf{c}	Geometric vector (defined in equation 5.98)
C	Collision operator
c_0	Speed of light, 2.9979×10^8 m/s
$\hat{\mathbf{curl}}(\mathbf{a})$	Matrix operator (see equation 5.5)
\mathbf{D}	Electric displacement field, C/m ²
\mathbf{E}	Electric field, V/m
\mathcal{E}	Gasdynamic total energy density
\mathcal{E}^T	Total energy (defined in equation 3.14)
\mathcal{E}^{EM}	Electromagnetic energy density (defined in equation 5.11)
e	Fundamental charge, 1.602×10^{-19} C
\mathcal{F}	Set of bounding faces for a control volume, Ω (Chapter 5)

\mathbf{F}	Force, N (Chapter 4); flux vector (Chapter 5)
F	A generic function
f	Distribution function (Chapter 2); generalized streamfunction for boundary layer flow (Chapter 4); an auxiliar initial condition function (Section 6.6)
$\mathbf{F}^{(A)}$	Advective flux for AUSM (Chapter 5)
$\hat{\mathbf{F}}^{(A)}$	Upwinded AUSM numerical convective flux (defined in equation 5.85)
$\mathbf{F}^{(P)}$	Pressure flux for AUSM (Chapter 5)
$\hat{\mathbf{F}}^{(P)}$	Upwinded AUSM numerical pressure flux (defined in equation 5.86)
$\hat{\mathbf{G}}$	Precomputed geometric matrix (defined in equation 5.97)
G	Green's function (Chapter 4)
\mathbf{H}	Magnetic field intensity, A/m ² (Chapter 2); Source vector (Chapter 5)
H	Total (stagnation) enthalpy, J/K
h	Enthalpy, J/kg
$\hat{\mathbf{I}}$	Identity matrix
\mathbf{j}_e	Electrical current density, A/m ²
\mathbf{j}_α	Generalized current density
$\hat{\mathbf{K}}$	Matrix of right eigenvectors
\mathbf{K}	Right eigenvector
k_B	Boltzmann's constant, 1.381×10^{-23} J/K
Kn	Knudsen number, dimensionless (see equation 1.28)
$\hat{\mathbf{L}}$	Matrix of left eigenvectors (also denoted $\hat{\mathbf{K}}^{-1}$)
\mathbf{L}	Left eigenvector
L	Length scale, m
l_c	Skin depth, m (see equation 1.14)
Re_m	Magnetic Reynolds number, dimensionless (see equation 2.79)
M	Mach number (Chapter 5)

m	Mass, kg
M^\pm	AUSM Mach number higher-order polynomial (defined in equation 5.89)
M_1^\pm	AUSM lower-order polynomial (defined in equation 5.91)
M_2^\pm	AUSM lower-order polynomial (defined in equation 5.92)
\widehat{M}	Upwinded Mach number for AUSM (Chapter 5; defined in equation 5.87)
\mathcal{N}	Set of associated nodes
\mathbf{n}	Normal vector
n	Number density, m^{-3}
N_F	Number of faces in mesh
N_N	Number of nodes in mesh
N_Ω	Number of control volumes in mesh
\mathbf{P}	Specific canonical momentum (defined in equation 3.11)
P	Pressure tensor
p	Gasdynamic pressure
p^\pm	AUSM pressure higher-order polynomial (defined in equation 5.90)
\widehat{p}	Upwinded pressure for AUSM (Chapter 5; defined in equation 5.88)
\mathbf{Q}	State vector (Chapter 5)
q	Charge of a particle (denoted by its subscript)
\mathbf{R}	Residual vector (Chapter 5)
R	Species drag (Chapter 2); averaging distance, m (Chapter 3)
r_L	Larmor radius, m (see equation 1.9)
\mathbf{r}_{ik}	Position vector from node i to face j (defined in equation 5.96)
\mathbf{r}_{Lj}	Position vector from adjoining volume L to face j
\mathbf{S}^{EM}	Poynting propagation vector (defined in equation 5.10)
s	Entropy, J/kg·K

T	Temperature, K or eV
t	Time, s
\mathbf{U}	Solution vector
\mathbf{u}	Velocity vector, m/s
U	Reference velocity (Chapter 4)
u	Fluid velocity (Chapter 4)
\mathbf{v}_A	Alfvénic velocity, m/s
\mathcal{V}	Set of associated control volumes
v_α	An appropriate velocity, m/s
\mathbf{W}	Characteristic
w	Scalar characteristic (without subscripts); interpolate weight for node-weighting scheme (with subscripts)
$\hat{\mathbf{X}}$	Generic matrix
x	Position, m
y	Coordinate variable
$\Delta \mathbf{U}$	Difference in jump conditions for Riemann problem
$\nabla \mathbf{Q}$	Gradient of state vector

Greek Symbols

α	Coefficients of polynomial interpolation (Chapter 4); decomposition coefficients for Riemann problem (Chapter 5 and Appendix ??)
β_H	Hall parameter, dimensionless (see equation 1.23)
δ	Kronecker delta (with subscripts) or Dirac delta distribution (with dependency)
$\epsilon_0 = 8.854 \times 10^{-12} \text{F/m}$	Permittivity of free space (in SI units)
η	Coordinate variable in the transformed similar plane (Chapter 4)
Γ	Preconditioning matrix (Chapter 5)
γ	Specific heat ratio, dimensionless

λ_D	Debye length, m (see equation 1.6)
Λ	Plasma Parameter, dimensionless
λ	Eigenvalue
λ_{mfp}	Mean free path, m (see equation 1.21)
$\hat{\mathbf{\Lambda}}$	Diagonal matrix of eigenvalues
$\mu_0 = 4\pi \times 10^{-7} \text{H/m}$	Permeability of free space (in SI units)
ν	Collision frequency, Hz (subscripts denote the species; see Section 1.2.1.7); kinematic coefficient of viscous (Chapter 4)
Ψ	Potential for divergence cleaning (Chapter 5)
ϕ	Electric potential, V
π	Mathematical constant, $\pi = 3.14159\dots$
ψ	Fluid potential (Chapter 4)
ϱ_e	Electrical charge density, C/m ³
ϱ_α	Generalized charge density
$\hat{\mathbf{\Sigma}}^{EM}$	Maxwell stress tensor (defined in equation 5.12)
σ	Plasma electrical conductivity, mho/m (see equation 1.24)
τ	Time scale (Chapters 1 and 2), dual-time (Chapter 5)
ω_c	Cyclotron (gyration) frequency, Hz (see equation 1.10)
$\hat{\mathbf{\Omega}}$	Generalized vorticity unit vector
Ω	Control volume (Chapter 5)
ω_p	Plasma frequency, Hz (see equation 1.13)
$\mathbf{\Omega}$	Generalized vorticity, s ⁻¹ (defined in equation 3.12)
$\mathbf{\omega}$	Vorticity, s ⁻¹
Δt	Physical timestep
$\Delta \tau$	Dual timestep
ζ_α	Generalized Lamb vector, ms ⁻² (defined in equation 3.13)

Subscripts and Superscripts

0	Zero-order (mean flow) quantity in perturbation (Chapter 4)
1	First-order perturbed quantity (Chapter 4)
α	Species index
B	Magnetic field divergence cleaning
c	Denotes the coupling between the fluid and Maxwell systems (Chapter 5)
E	Electric field divergence cleaning
E	Electron species
F	Fluid quantity (Chapter 4); strong conservative form (Chapter 5)
f	Denotes the fluid system (Chapter 5)
I	Ion species
i	Node index (Chapter 5)
j	Face index (Chapter 5)
k	Control volume index (Chapter 5)
L	Left volume adjoined to face (Chapter 5)
m	Denotes the Maxwell system (Chapter 5)
N	Neutral species
R	Right volume adjoined to face (Chapter 5)
x	x -direction quantity
y	y -direction quantity
∞	Freestream quantity
z	z -direction quantity
\mathbf{a}	Denotes the Roe-averaged form of \mathbf{a}

Chapter 1

Introduction and Motivation

“They say great science is built on the shoulders of giants. Not here. At Aperture, we do all our science from scratch. No hand holding.”

Cave Johnson [1]

1.1 Prologue

Key technologies, including hypersonic flight, advanced propulsion and fusion energy, rely on the construction of a sound physical model to characterize the plasma physics these technologies possess. Major strides have been taken in both the development of new engineering devices based on these technologies, and our capability to understand, model and predict them. However, lack of a complete understanding of the underlying physics, and major challenges that beset our capability to accurately and efficiently model them with only modest computational effort, requires new advances to our knowledge.

If a plasma is subjected to forces consistent with a fluid treatment, then a minimal physical model may be fashioned by the union of the electromagnetic equations (Maxwell’s equations¹) and the fluid dynamic equations (Navier-Stokes equations²). Coupling between these two models must additionally be prescribed, which will be discussed in detail later. More complex models must be supplemented for other significant phenomena (such as radiation transport, surface wall chemistry, nonequilibrium processes, laser/plasma interactions, ablation, etc.) Our capability to model these is challenged by three major factors: the appearance

¹Maxwell’s equations, as popularized in vector form by Heaviside [2,3], include the Gauss laws for the electric and magnetic field, Faraday’s law, and the Ampere-Maxwell law. Maxwell assembled these equations with his displacement current correction to Ampere’s law in 1865 [4,5]. When we use the term *Maxwell’s equations*, we will always imply the inclusion of the displacement current.

²The Navier-Stokes equations are comprised of the mass, momentum and energy conservation laws for viscous compressible flows. [6] The Navier-Stokes equations were independently derived five different times: by Navier in 1821, by Cauchy in 1823, by Poisson in 1829, by Saint-Venant in 1837, and by Stokes in 1845. [7]

of multiple and highly disparate frequencies in the system, numerical stability and stiffness issues incurred in the solution procedure by the presence of large and rapidly varying source terms, and the appearance of both wave and diffusion transport behavior in the same domain of interest.

The inclusion of all of the relevant frequencies belabors any computational approach to solving the system. If, for simplicity, only the electromagnetic and inviscid gasdynamic equations are considered, then the speeds involved in characterizing the system behavior are velocity, sonic velocity, and the speed of light. If we consider a Mach 20 flow in the upper atmosphere, then our fluid and sonic velocities will be on the order of $\sim 7,000\text{m/s}$, which is still five orders of magnitude smaller than the speed of light, $c_0 = 2.9979 \times 10^8\text{m/s}$. Since explicit numerical schemes are typically limited to time scales based on the fastest speed in the system, we will be forced to spend an excessive amount of computational effort to resolve even modest problems, in order to see responses that occur on the fluid time scale while resolving transients in the electrodynamic behavior [8].

In a plasma, the electromagnetic and fluid behaviors are coupled. When writing the equations, the most frequent way of expressing this coupling is by adding explicit source terms to the equations. The Lorentz body force and Ohmic dissipation terms are added to the fluid momentum and energy equations, and the current density, which now depends on the fluid velocity, is added to the Maxwell equations. Physically, this is a perfectly valid formulation of the coupling. Numerically, however, these source terms can grow very large and very stiff, which can drive the maximum stable timestep even lower than the time scale of the speed of light. This presents a significant difficulty to our capability to resolve a numerical solution to these equations.

Finally, the electromagnetic and fluid dynamic equations are, in their full time dependent form, *hyperbolic* partial differential equations, characterized by wave transport of information. But when the electrical conductivity becomes very high (high-conductivity plasmas are ubiquitous to many plasmas of engineering interest) the equations often reach a *parabolic* limit, characterized by diffusive transport of information. If we are to solve these equations and resolve their full behavior, then we are compelled to use hyperbolic methods. But if the conductivity becomes large, and the parabolic limit is reached, the equations become stiff and sometimes even numerically ill-posed for hyperbolic techniques.

One approach to dealing with the difficulties described above is to make an appropriate approximation to the coupled system. For example, since high conductivities appear very frequently in plasmas of engineering interest, and since in the high-conductivity limit the magnetic field behaves parabolically (i.e., diffusively), we could simply take the parabolic limit of the magnetic field. This conveniently assumes that the propagation speed of the electromagnetics (the speed of light) is infinite, so we lose the vast disparity in speeds. Since we've taken the parabolic limit, we expect no hyperbolic behavior to result. This approximation is called the *magnetohydrodynamic* (MHD) approximation, and the resulting simplified system is called the *magnetohydrodynamic* (MHD) model. Credit for the development of this model is usually given to Swedish physicist Hannes Olof Gösta Alfvén, who in 1970 was awarded the Nobel prize in physics “for

fundamental work and discoveries in magnetohydrodynamics with fruitful applications in different parts of plasma physics.” [9] Indeed, the MHD model has successfully predicted the existence of a series of waves (called magnetohydrodynamic waves) that have found application throughout plasma physics, even including general relativistic astrophysical phenomena.

The MHD model has become the incumbent approach for modeling and predicting the behavior of macroscopic plasmas. However, there are some significant drawbacks that limit the validity of this model. When the conductivity is not high, the MHD approximation cannot be valid, and a wave description of the magnetic field must be included. Instabilities that are driven by waves and modes not permitted in the MHD model due to its limiting assumptions cannot be predicted or studied using this framework. The missing physics, often collectively referred to as *two-fluid effects*, manifest themselves as singular perturbations in the MHD system, since they have been neglected in this model. Furthermore, any study of the electromagnetic wave interaction with the plasma is simply not permitted, since we have restricted ourselves by assumption only to parabolic phenomena, and excluded any hyperbolic electromagnetic behavior.

In the cases where the MHD model is of questionable validity, particle and kinetic approaches can be used instead. Particle techniques, such as particle-in-cell (PIC) schemes and related methods, retain the full ensemble of particles composing the plasma (or, more frequently, some representative *superparticles* approximating smaller ensembles). Kinetic methods seek to construct a solution to Boltzmann’s equation [10], which will determine the equilibrium distribution function of the particles in the plasma. In either case, a knowledge of the collective particles allows for a prediction of the behavior of the plasma. However, PIC and kinetic methods are usually cumbersome when the plasma is sufficiently high-density enough that an excessive number of particles are needed. When large numbers of particles are required, PIC and kinetic methods become intractable to solve on modern hardware, and even in the cases where they can be calculated, the computational time required is excessive. Fluid models are more economical for higher-density problems, but again, we are restricted either by the approximations to the physical system (as in the case of the MHD model) or by the challenges imposed on solving the complete system, as aforementioned.

This dissertation improves upon our capabilities to model plasmas by constructing a method by which we can more efficiently model dense plasmas including the underlying physics missing in the MHD theory. Two particular models are of interest: the *two-fluid plasma model*, sometimes called the *multi-fluid* plasma model, which consists of a set of moment equations per species (usually two suffices), coupled to the full Maxwell equations. The second model is less general, but still retains much of the missing effects discarded in the MHD model; since the electron mass is typically several orders of magnitude smaller than the ion mass, we discard the electron fluid and introduce a bulk single-fluid model coupling a single set of moment equations to the full Maxwell equations. This model permits charge separation effects, electromagnetic wave propagation, and low-conductivity resolution where the MHD framework fails. The two-fluid model additionally adds multiple species effects and intrinsically captures Hall effects. We present two approaches explored to improve our capabilities for modeling plasmas described by these more general frameworks.

The first approach is a more creative exploration that constructs an isomorphism between the two-fluid plasma model and the Maxwell equations of classical electrodynamics. Doing so reveals a set of Maxwell equations for the plasma in new, generalized fields that unite the electrodynamic and hydrodynamic character of the plasma. This extends previous efforts for formulating the Maxwell equations for fluids to the case of a plasma. The challenge in utilizing the new framework is the presence of new generalized charge and current densities, which are superpositions of the normal electric charge and current densities, and new *fluid* charge and current densities. Either iterative approaches or empirical modeling must be used for solving the isomorphic field equations for the fields and the sources (charge and current densities). This investigation revealed that, at present, iterative approaches are not advantageous, and so instead empirical modeling of the source terms was attempted. Since the electric charge and current densities are already understood, most of the challenge lies in determining the properties and behavior of the fluid charge and current densities. Furthermore, it is of benefit to construct simple models, since these simple models may be used as fundamental building blocks for constructing sources for more complicated phenomena. In order to examine some of these simple models, we first take an analytical approach to examining steady, incompressible charge and current densities for some simple flows. To examine more difficult flows, we resort to numerical simulation to reveal qualitatively the nature of the fluid charge and current. We show that typical methods from electromagnetism are sufficient for solving these problems, given a form for the fluid sources. The ultimate challenge with this framework is a deficit of available data to harvest source terms; this led to the second approach, which proved much more successful in directly meeting our stated objective.

The second approach examines a finite volume numerical solution approach, wherein the equations of motion are cast into a *strong conservative* form. The coupling between the fluid dynamic and electrodynamic systems in this framework is typically accomplished by adding source terms to these equations which depend on the other respective system. In this investigation, we examine a new way of recasting the equations into a strong conservative form that does not have explicit source terms, even though the system is exactly coupled to the full Maxwell equations. This is accomplished by introducing the conservation equations of electrodynamics and posing the coupling in terms of the Poynting propagation vector, Maxwell stress tensor and electromagnetic energy density. By rewriting the coupling in this manner, the Lorentz body force and Ohmic dissipation terms appear as derivatives of the new electromagnetic quantities, and may be united directly in the solution and flux vectors. This removes the appearance of explicit source terms in the system, which is shown to significantly stabilize the equations numerically. The new strong conservative form is implemented in an implicit finite volume solver, and validations for several problems are presented using both the Roe [11] and Advected Upstream Splitting Method (AUSM³) [12] flux schemes. The strong conservative form is benchmarked against the traditional source-coupled approach, and improvements in both accuracy and computational speed are seen in the new method for finite conductivities. It is further shown that the two-fluid plasma system cannot directly enjoy this approach without either some approximation,

³Pronounced ‘awesome’

fortuitous mass ratio between the different species, or reformulation of the equations.

1.2 An Overview of Plasma Physics

At low temperatures, gases and fluids are typically electrically inert, and the microscopic processes governing their bulk behavior is best given by elastic collisions (for gases) and Van der Waals forces (for liquids). Applied electromagnetic fields typically cause little effect here. As heat is added and the temperature of the gas or fluid is raised, the molecules dissociate, and at even higher temperatures, the addition of heat will eventually ionize neutral constituents by providing sufficient ionization energies to the bound electrons. The freed electrons and resulting ions provide a net microscopic charge within a Debye length of the fluid (defined below); it is well known that charges respond very well to applied fields. Therefore, at higher temperatures, gases and fluids possess new dominant behaviors introduced when electromagnetic fields are applied, due to the presence of free microscopic charge. We refer to any such fluid that responds well to applied electromagnetic fields as a *plasma*.⁴

Plasmas possess a very diverse and complicated underlying structure, due to the interaction between the fluid and electrodynamic fields. The presence of microscopic charge, multiple species and multiple frequencies constitute an abundance of phenomena that may result. The dominant physical mechanisms that govern the bulk behavior of a plasma depend strongly on the state of the plasma. The conventional approach to describe this mixture of behavior is to identify a small number of *plasma parameters* that govern the overall plasma. These plasma parameters form a phase space within which different competing physical mechanisms dominate in different parts of the phase space. This leads to a diverse landscape of possible phenomena, which is most directly amenable to a zoological approach of classification [13].

It is sensible to define and quantify some of these parameters before continuing our discussion regarding them.

1.2.1 Plasma Parameters

All plasmas are endowed with some characteristic length scale, L , usually associated with the scale of the apparatus or the phenomenon of interest, a collection of temperatures, T_α , for each species α in the plasma, an electron number density, n_e , and a characteristic magnetic induction field strength, B . Below, we briefly introduce some of the other significant parameters of interest. A more complete presentation can be found in [10, 14–16]. These parameters characterize the different length and time scales present in a plasma.

⁴Dispensing with the single process of ionization identified (i.e., heat transfer), we will extend this term to include fluids that respond to electromagnetic fields due to *any* process of ionization, such as photoionization or chemiionization.

1.2.1.1 Debye Length, λ_D

The *Debye shielding length* is a length scale over which charge non-neutralities are detectable and significant. A charged test particle may detect and influence other charged particles that are present within the a Debye length; particles beyond the Debye length essentially cannot be felt or influenced by the test particle.

Suppose we have a collection of N species. The charges and number concentrations of each species, k , are given by q_k and n_k , $k \in (1, \dots, N)$. A static arrangement of these particles will form a net charge, and hence, a net electrostatic field, $\phi(\mathbf{x})$, given by Poisson's equation,

$$\nabla^2 \phi(\mathbf{x}) = -\frac{1}{\epsilon_0} \sum_{k=1}^N q_k n_k(\mathbf{x}) \quad (1.1)$$

We can usually additionally assume that the collection of particles is in thermodynamic equilibrium, which implies that the number density of species k is given by the Maxwell-Boltzmann equilibrium solution,

$$n_k(\mathbf{x}) = n_{0k} \exp\left(\frac{-q_k \phi(\mathbf{x})}{k_B T}\right) \quad (1.2)$$

where k_B is the Boltzmann constant, n_{0k} is the mean number density of species k , and T is the temperature. Substitution of this for the instantaneous field leads to a Poisson-Boltzmann equation describing the net electrostatic field generated,

$$\nabla^2 \phi(\mathbf{x}) = -\frac{1}{\epsilon_0} \sum_{k=1}^N q_k n_{0k} \exp\left(-\frac{q_k \phi(\mathbf{x})}{k_B T}\right) \quad (1.3)$$

This is a nonlinear equation, for which solutions may be determined for some simple cases; however, if we consider the system weakly coupled and the thermal energy, $k_B T$, to be much larger than the electric energy, $q_k \phi$, then we can expand the exponential to first order, and we additionally assume the system was initially electrically neutral, $\sum_{k=1}^N q_k n_{0k} = 0$; our equation becomes the *Debye-Hückel* equation for high-temperature systems,

$$\nabla^2 \phi(\mathbf{x}) - \left(\frac{\sum_{k=1}^N q_k^2 n_{0k}}{\epsilon_0 k_B T}\right) \phi(\mathbf{x}) \equiv \nabla^2 \phi(\mathbf{x}) - \frac{1}{\lambda_D^2} \phi(\mathbf{x}) = 0 \quad (1.4)$$

which is a Helmholtz equation for the electrostatic potential, $\phi(\mathbf{x})$. The solution takes the form of a Yukawa potential,

$$\phi(\mathbf{x}) = \frac{qT}{4\pi\epsilon_0 r} \exp(-r/\lambda_D) \quad (1.5)$$

The characteristic length scale, λ_D , determines the distance over which the charge is effectively screened by surrounding charges. Therefore, in a qualitative sense, charges may only detect or 'sense' other charges within their Debye sphere; outside of the Debye sphere, the potential generated by a charge falls off and

effectively cannot be sensed. This phenomenon is collectively referred to as *Debye screening* or *shielding*. Typically, the ion contribution to the term λ_D can safely be neglected, and we arrive at the accepted form for the Debye length in a plasma,

$$\lambda_D \equiv \sqrt{\frac{\epsilon_0 k_B T}{e^2 n_e}} \quad (1.6)$$

where n_e is the electron number density and e is the fundamental charge of the electron.

1.2.1.2 Plasma Parameter, Λ

Moving charged particles will experience Coulombic collisions as they pass. These long-range collisions compete with gasdynamic elastic collisions. Weakly and strongly ionized gases can be quantitatively characterized by comparing the relaxation times of the electron-neutral and electron-ion collisions. In order to establish the ratio of these relaxation times, some quantity representative of the character of the Coulombic collisions must be developed. Most developments [10, 14–17] solve the Rutherford scattering problem to determine an effective cross-section for cumulative ‘grazing’ (long-range) collisions and close-range impacts. Developing a ratio for the grazing-to-long-range collisions will introduce this parameter directly.

Alternately, we could simply define the plasma parameter directly as

$$\Lambda = \frac{4}{3} \pi n_e \lambda_D^3 \quad (1.7)$$

This value represents the number of electrons within a sphere of Debye radius. The logarithm of this parameter can be shown to be proportional to the ratio of long-range and close-range Coulombic interactions,

$$\frac{\tau_{90}}{\tau_D} \simeq \frac{\sigma_D}{\sigma_{90}} \simeq \ln(\Lambda) \quad (1.8)$$

Here τ indicates a relaxation time, σ indicates a cross-section, and subscripts 90 and D indicate close-range and cumulative grazing effects, respectively. The close-range effects exhibit a complete loss of the initial momentum associated with their initial velocity (i.e., a 90-degree collision).

The plasma parameter, Λ is particularly effective in determining whether the plasma is weakly or strongly ionized. The electron-ion relaxation time is inversely proportional to $\ln(\Lambda)$, which means that as $\ln(\Lambda)$ increases, the Coulombic collisions play a more and more important role (generally meaning the plasma is more strongly ionized). The plasma parameter tends to increase with increasing temperature and decrease with increasing electron number density. The typical range of $\ln \Lambda$ is between 1 and 10.

1.2.1.3 Larmor Radius, r_L

Charged particles immersed in a magnetic field tend to gyrate. The radius of gyration (called the Larmor or cyclotronic radius) can be computed directly by equating the Lorentz force law with the centripetal

acceleration of the particle. This yields the Larmor length for a particle,

$$r_L = \frac{mv_{\perp}}{qB} \quad (1.9)$$

where \mathbf{v} is the velocity vector, \mathbf{B} is the magnetic field, v_{\perp} is the component of velocity perpendicular to \mathbf{B} , and m and q are the mass and charge of the particle, respectively.

1.2.1.4 Cyclotron Frequency, ω_c

The frequency of orbits gyrated by a particle is given by the cyclotron frequency, ω_c , given by

$$\omega_c = \frac{qB}{m} \quad (1.10)$$

The cyclotron frequency and radius are hence related as

$$r_L = \frac{v_{\perp}}{\omega_c} \quad (1.11)$$

where v_{\perp} is the component of velocity perpendicular to the magnetic field.

1.2.1.5 Plasma (Langmuir) Frequency, ω_p

Consider a plasma in which the electrons are uniformly displaced some distance from the ions. Associated with the subsequent motion, there is a natural harmonic oscillation established between the ions and electrons. Since the ions are much more massive than the electrons, assume that they are fixed. The electronic motion in one dimension may be given succinctly by a force equation,

$$\frac{d^2x}{dt^2} = -\frac{n_e e^2}{m_e \epsilon_0} x \equiv -\omega_p^2 x \quad (1.12)$$

which implies that

$$\omega_p^2 = \frac{n_e e^2}{m_e \epsilon_0} \quad (1.13)$$

where n_e is the electron number density, m_e is the electron mass, and e is the fundamental electron charge. A distribution of electrons undergoing an oscillation with this frequency is called a *Langmuir wave*. In solid state plasmas, an effective semiclassical mass, m_e^* , may be determined to replace the m_e in the above expression, representing the plasma frequency associated with solid state devices; typically, the plasma frequency in a solid state plasma is much higher than a gaseous plasma, due to a much higher number density, n_e [18].

In practice, the plasma frequency, ω_p , establishes several other very important characteristics of the plasma. A particularly striking example is the propagation of a radio wave into a plasma. If the plasma frequency is higher than the frequency of the electromagnetic wave, then the charges within the plasma are

capable of rearranging fast enough to counter the wave and cancel it out. In this case, electromagnetic waves cannot penetrate a plasma with a higher plasma frequency. An obvious point of experimental demonstration of this fact is the reflection of short-wave radio off of the ionosphere. This behavior poses a problem for radio communications to vehicles re-entering the earth's atmosphere, as a plasma sheath with a high plasma frequency will tend to envelope such craft.

1.2.1.6 Skin Depth, l_c

When electromagnetic radiation impinges on a material, there will be a reflected and transmitted component. The transmitted component may propagate into the material, or die off very quickly. The depth to which the radiation travels before falling to $1/e$ of its surface (or 'skin') value is a meaningful length scale to associate with a plasma. This can be a particularly important quantity in dealing with plasma waves. This distance is called the *penetration depth* or *skin depth*⁵. In a plasma, the Langmuir frequency, ω_p , usually determines the frequency of behavior, and so a meaningful plasma length scale (also termed the *skin depth*) is

$$l_c = \frac{c}{\omega_p} \quad (1.14)$$

where ω_p is the Langmuir frequency of the plasma.

1.2.1.7 Collision Frequency, $\nu_{\alpha\beta}$

The frequency of collisions between two species, α and β , is usually denoted $\nu_{\alpha\beta}$ and is typically strongly tied to the *cross section* of the collision of the two species. In weakly ionized plasmas, generally the electrons will collide most frequently with neutral atoms and molecules; hence, the electron-neutral collision frequency, ν_{EN} , will dominate over the electron-ion collision frequency, ν_{EI} . Since the plasma parameter, $\ln \Lambda$, depends as the inverse of the relaxation times between these two different classes of collision, generally a weakly ionized plasma requires only a moderate value of Λ (usually about 10). Larger Λ will tend to indicate that the Coulombic collision frequency, ν_{IE} , is not insignificant relative to the neutral collision frequency.

For elastic collisions, we may take the cross section of the particles to be $Q_n = \pi d_0^2$, where d_0 is the effective radius of the neutral particle. Typically this cross section is of the order $\sim 10^{-19} \text{m}^2$. From this, the collision frequency will be $\nu_{EN} = Q_n n_n \langle v_e \rangle$, where n_n is the number density of the neutral collision partners and $\langle v_e \rangle$ is the average speed of the colliding electrons.

If the plasma is highly ionized and the Coulombic collisions dominate, then most of the collisions are small-angle scattering collisions between all particles in a Debye sphere. In this case, the electron-ion collision frequency governs most of the character of the collisionality in the plasma, $\nu_{EI} = n_e Q_c \langle v_e \rangle$, where Q_c is the Coulombic cross section. Calculating this cross section can be very involved, but typically an effective

⁵In the literature, different definitions prevail. Sometimes there is a factor of 2 difference between these two quantities. Sometimes there is not.

impact parameter is taken as

$$d_c \sim \frac{e^2}{4\pi\epsilon_0 m_e \langle v_e \rangle^2} \quad (1.15)$$

and thus the Coulombic cross section is given by

$$Q_c = \pi d_c^2 \sim \frac{e^4}{16\pi\epsilon_0^2 m_e^2 \langle v_e \rangle^4} \quad (1.16)$$

and thus the Coulombic collision frequency is rough proportional to

$$\nu_{EI} = n_e Q_c \langle v_e \rangle \sim \frac{n_e e^4}{16\pi\epsilon_0^2 m_e^2 \langle v_e \rangle^3} \quad (1.17)$$

If we assume that the plasma is in thermal equilibrium, then the following ratio scaling applies:

$$\nu_{EE} \sim \nu_{EI} \quad (1.18)$$

$$\nu_{II} \sim \sqrt{m_e/m_i} \nu_{EE} \quad (1.19)$$

$$\nu_{IE} \sim (m_e/m_i) \nu_{EE} \quad (1.20)$$

1.2.1.8 Mean Free Path, λ_{mfp}

The *mean free path* is a length scale representing the distance that a particle is most likely to travel before a collision is expected. In terms of the collision frequency, the mean free path is most directly defined as

$$\lambda_{\text{mfp}} = \frac{\langle v \rangle}{\nu} = \frac{1}{Qn} \quad (1.21)$$

where $\langle v \rangle$ is the average speed of the species of interest, and ν is the collision frequency of interest. Q is the cross section corresponding to the collision frequency, and n is the number density of the corresponding colliding species. There exists a mean free path for each permutation of collision possible, although generally the dominant mean free path is that determined by the most dominant collision to be expected (in weakly ionized plasmas, the electron-neutral collision frequency).

For a fully-ionized plasma, the dominant collision is the Coulombic long-range scattering, which is characterized by ν_{EI} . We can show that

$$\lambda_{\text{mfp}} \sim \frac{\langle v_e \rangle}{\nu_{EI}} \sim 64\pi\lambda_D \frac{\Lambda}{\ln(\Lambda)} \quad (1.22)$$

and since $\ln \Lambda \geq \sim 10$, the mean free path is enormous compared to the Debye length.

1.2.1.9 Hall Parameter, β_H

As aforementioned, a particle immersed in a magnetic field tends to gyrate about the field lines. The current in a plasma of particles subjected to a background magnetic field tends to be proportional to the effective electric field. However, we can imagine that, if the magnetic field is strong enough to cause sufficient gyration, there will be a transverse component of current introduced due to the curved motion of the particles between collision impacts.

This transverse current is realized in a plasma with a sufficiently strong magnetic field that causes strong gyration relative to the longitudinal current. The new transverse component is the *Hall current*, analogous to a similar effect seen in conductive solids and liquids. To quantify the influence of the Hall current, we introduce the *Hall parameter*, which measures the ratio of the gyration frequency, ω_c , relative to the collision frequency,

$$\beta_H = \frac{\omega_c}{\nu_{E\alpha}} = \frac{eB}{m_e \nu_{E\alpha}} = \frac{\lambda_{\text{mfp}}}{r_L} \quad (1.23)$$

where α here denotes the heavy particles. If the Hall parameter is sufficiently large, then the transverse component of current is significant and must be included. When the Hall parameter is much lower than unity, the Hall current behaves in a linear sense (with no significant trajectory introduced by gyration in the magnetic field), and Hall effects are negligible. The Hall parameter is proportional to the magnetic field strength. The form of the Hall current will be discussed in Section 2.5.

1.2.1.10 Plasma Electrical Conductivity, σ

The electrical conductivity, σ , of a plasma is a macroscopic measure of how easily current may flow across it. In many plasmas, the conductivity is usually very high, such that one may frequently neglect terms proportional to the inverse of conductivity (this leads to the ideal MHD model). The *classical scalar conductivity* of a plasma is usually given as

$$\sigma = \frac{n_e e^2}{m_e \nu_{E\alpha}} \quad (1.24)$$

where α can denote either the ions or neutrals, whichever dominates. For macroscopic models, Ohm's law is a constitutive relation that fashions a quantitative form of the current density. The form of the current density based on Ohm's law will be discussed in detail in Section 2.5; if we neglect Hall and other transverse currents, we can simplify Ohm's law to a very simple vector form,

$$\mathbf{j}_e = \sigma \mathbf{E} + \sigma \mathbf{u} \times \mathbf{B} \quad (1.25)$$

Table 1.1: Typical plasma parameters for various plasmas. [10, 15]

	n (m^{-3})	T (eV)	L (m)	λ_D (m)	r_L (m)	$\ln(\Lambda)$	ω_p (Hz)	ω_c (Hz)
Gas Discharge	10^{16}	1	1	10^{-4}	—	10	10^{10}	—
Magnetic Fusion (Tokamak)	10^{20}	10^4	10	10^{-4}	10^{-5}	20	10^{12}	10^{12}
Inertial Fusion	10^{31}	10^4	10^{-5}	10^{-10}	—	8	10^{18}	—
Ionosphere	10^{11}	0.1	10^5	10^{-2}	10^{-1}	14	10^8	10^6
Solar Wind	10^7	10	10^{11}	10	10^4	25	10^5	10^2
Magnetosphere	10^4	10	10^8	10^2	10^4	28	10^5	10^3

Here $\mathbf{E} + \mathbf{u} \times \mathbf{B}$ is an effective electric field due to the motion of the plasma. The magnitude of the conductivity, σ , is given in its simplest form by equation 1.24; however, the conductivity is more generally tensorial and cannot be expressed by a scalar value. In this case, transverse currents (often due to the Hall effect) must be accounted for as well. In the case of a solid state plasma, the conductivity is typically larger, due to a higher electron mobility.

1.2.2 Typical Values for the Plasma Parameters

The scales spanned by these parameters are immense. We can refer to the same governing behavior of the magnetic field in a bead of liquid metal, or the molten interior of the earth’s core. We can examine similar shock structures formed from a laboratory plasma in a shock tube spanning microns, or an astrophysical dusty plasma covering astronomical units. Of course, not all of the behavior of the plasma will be preserved with all scale changes; a plasma could be as dense as a near vacuum, or as dense as the interior of a star. It could possess energies we experience on an everyday basis to energies that demand a relativistic treatment. It is therefore unlikely that we should expect a single physical model to adequately address all possible phenomena with equal validity across all ranges of these parameters. In many cases, certain behaviors of the plasma are essentially completely suppressed, and in other cases they are so important that they cannot be discarded. We are posed with the challenge of constructing physical models that accurately include all of the necessary phenomena, but ignore the unnecessary, for the range of parameters of interest.

Figure 1.1 shows a typical schematic that maps some of the various regimes of plasma physics, as a log plot of number density and temperature. The disparate scales over which these parameters vary are clear; furthermore, examination of the graph shows several important plasmas of engineering interest scattered across these regimes. The development of a single model that describes all of these different cases is clearly beyond us. To supplement the overall picture of the vastness of these scales, some common parameters describing plasma behavior is given in Table 1.1.

Plasma Phenomena Plotted Against Electron Density and Temperature

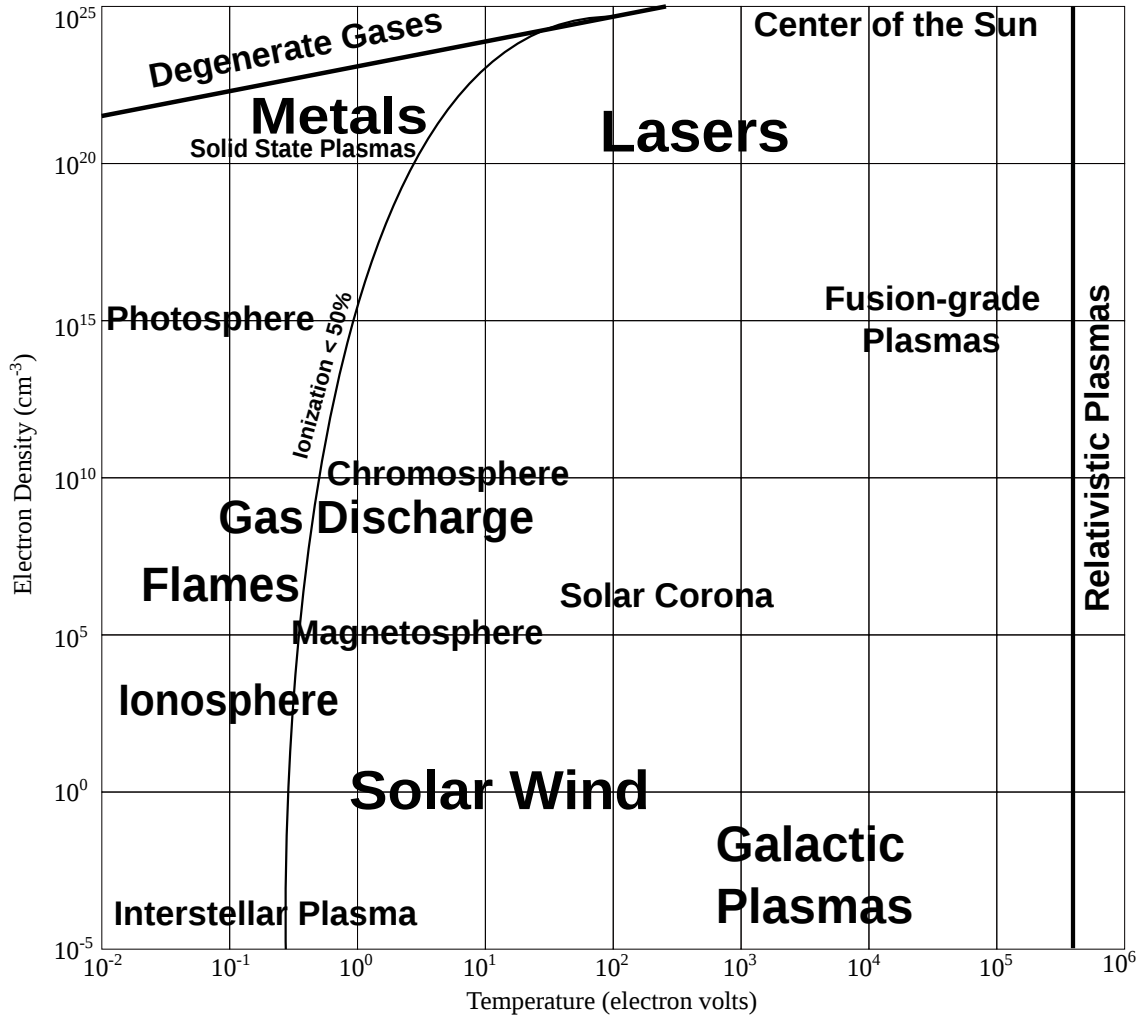


Figure 1.1: A diagram of plasma in the known universe, plotted by electron number density versus temperature. [10, 15]

1.2.3 Definition of a Plasma

It is impossible to give a comprehensive definition of a plasma, even in terms of the plasma parameters listed above. However, it is fruitful to consider the distinction between the different models via the parameters. A typical definition for a plasma often offers the following two conditions [10, 15, 16, 19]:

- The number of charge carriers must be sufficiently large that particles interact with several other particles within their Debye sphere. This provides the collective behavior observed in most plasmas. Since $\Lambda = (4/3)\pi n\lambda_D^2$ represents the number of particles within a Debye sphere, this may most readily

be written as

$$\Lambda \gg 1 \tag{1.26}$$

Most common plasmas can be approximated well by assuming $\ln(\Lambda) \simeq 10$.

- The Debye length is assumed to be much smaller than the apparatus length,

$$\lambda_D \ll L \tag{1.27}$$

This means that, while on the microscopic scale we acknowledge that charges are present, on the macroscopic scale there is no significant charge separation, which implies that the plasma is *quasineutral* (does not possess a macroscopic electric charge on the overall length scale, L). Plasmas not satisfying this condition are somewhat awkwardly referred to as *non-neutral plasmas*.

Plasmas that do not satisfy these conditions are often relegated to a peripheral role in engineering, but occur frequently in many very important applications. For example, plasma sheaths are intrinsically non-neutral, and occur along any boundary surface in contact with the plasma. Therefore, many plasmas of engineering interest will experience non-neutral sheaths at boundaries, and their role in engineering cannot be understated. Some plasma devices, such as the single barrier dielectric discharge plasma actuator, involve the application of an electric body force to accelerate the plasma flow; in this case, the plasma must possess a net electric charge, since the electric body force is proportional to the net charge. We will discuss other applications that violate these conditions in more detail shortly.

Further distinctions between plasmas can be made. Another characteristic quantity in determining the nature of the plasma is the *Knudsen number*, denoted Kn , defined as

$$\text{Kn} = \frac{\lambda_{\text{mfp}}}{L} \tag{1.28}$$

The Knudsen number is typically used to distinguish between low-density and high-density plasmas. When the Knudsen number is large, this implies that the mean free path is large compared to the overall length scale of interest. This means collisionality does not play a significant role in the plasma, and sometimes a collisionless model is even appropriate (free-molecular flow). Conversely, when the Knudsen number is very small, this implies that collisionality is strongly present in the plasma, and cannot generally be ignored. When the Knudsen number is of order unity, this region is referred to as the transitional region, and often is not well characterized by either low- or high-density assumptions. When the Knudsen number is small, continuum models are appropriate and more economical than kinetic or microscopic modeling approaches; when the Knudsen number is high, tensorial behavior may sustain anisotropies that cannot be handled using continuum models, and usually a kinetic or particle approach taking advantage of a microscopic description of the plasma is necessary. In this dissertation, we will focus on dense plasmas, such that the Knudsen

number will always be considered low enough that a continuum approximation is valid.

The characteristic frequency of interest and its comparisons to the other dominant frequencies in the system permit different assumptions of the behavior of the plasma. For example, if the characteristic frequency is much lower than the plasma frequency, ω_p , then we may neglect the charge rearrangement timescale; since charges rearrange on the timescale of $1/\omega_p$, the charges may be approximated well by an electrostatic assumption. Similar arguments can be made for the cyclotron and collision frequencies as well. An example that will be presented later is the Hall effect thruster, in which the electron cyclotron and electron collision frequencies are very comparable, whereas the ion cyclotron and ion collision frequencies are very different. This means the electrons experience a strong Hall effect, whereas the ions perceive the plasma essentially in an electrostatic way.

It is apparent that an abundance of different possibilities, as roughly sketched in Figure 1.1 and Table 1.1, are possible. As such, no definition comprehensively captures all effects in the diverse landscape formed by the plasma parameters. We will focus on cases where some of the above conditions that are often taken for granted may not be assumed, such as cases where quasineutrality may be violated and characteristic frequencies exceed the plasma frequency.

1.3 Limitations to the Magnetohydrodynamic Framework

We discussed that a minimal coupled model for a dense plasma with a sufficiently small Knudsen number would involve a coupled system of the Navier-Stokes and Maxwell equations. Coupling is provided in the form of a Lorentz body force and Ohmic dissipation acting on the fluid, and a current density that depends on the fluid properties. As pointed out, the time scales of the systems involved are highly disparate, and this poses a unique challenge for solving the coupled systems of equations.

The incumbent approach for simplifying this minimal model is to reduce the system of equations to a single species with only a single characteristic time scale. The resulting model is the *magnetohydrodynamic* (MHD) model. The MHD model imposes two primary assumptions on the plasma: (i) the plasma is *quasineutral*, (ii) the displacement current in the Ampere-Maxwell equation, describing the time variation of the electric field, is sufficiently small as to be negligible.

Let us examine these two conditions more carefully. The former requires that no clumps of electric charge are visible on the scale of the apparatus. The collective of charged particles arranges itself such that a charge at some point cannot be detected some distance, λ_D , away. This happens on a timescale much faster than the fluid scale; thus, the net potential a certain sufficient distance away will not look substantial. This effect is known as *Debye shielding*, and the *Debye length*, λ_D , represents the distance over which the potential, ϕ , introduced by the test charge is sufficiently small. Within the Debye length, the microscopic test charge may be ‘felt’, whereas outside the Debye length the charge’s influence is effectively screened by the surrounding attracted and repelled charges. Hence, this first condition amounts to insisting that the Debye length be

much smaller than the scale of the apparatus, $\lambda_D \ll L$.

The latter condition imposed in the MHD theory requires that the displacement current, $1/c_0^2 \partial \mathbf{E} / \partial t$, be discarded from the Ampere-Maxwell equation. This reduces the hyperbolic system to a *diffusive* system, frequently called the *magnetic diffusion approximation*. The telegrapher equation reveals the full nature of the magnetic field,

$$\frac{1}{c_0^2} \frac{\partial^2 \mathbf{B}}{\partial t^2} + \mu_0 \sigma \frac{\partial \mathbf{B}}{\partial t} - \nabla^2 \mathbf{B} = 0 \quad (1.29)$$

where \mathbf{B} is the magnetic induction field, c_0 is the speed of light in vacuum, μ_0 is the permeability of free space, and σ is the electrical conductivity. It is evident from equation 1.29 that two limits in the time-varying nature of the magnetic field may be realized. In the first case, we may have the first term dominate the second; if the second term is sufficiently small, we may neglect it, and a pure wave equation in \mathbf{B} results,

$$\frac{1}{c_0^2} \frac{\partial^2 \mathbf{B}}{\partial t^2} - \nabla^2 \mathbf{B} = 0 \quad (1.30)$$

However, in the opposite limit, the second term may dominate over the first. In this case, the first term may be small enough to discard, in which case

$$\frac{\partial \mathbf{B}}{\partial t} - \frac{1}{\mu_0 \sigma} \nabla^2 \mathbf{B} = 0 \quad (1.31)$$

Clearly, this is a diffusion equation for the magnetic field. The first term in equation 1.29 is contributed by the displacement current, so neglecting the displacement current renders equation 1.29 into the form of equation 1.31. Applying a scale analysis between the first and second terms in equation 1.29 reveals that these limits depend strongly on the electrical conductivity. For high-conductivity plasma, the magnetic diffusion approximation becomes very appropriate for describing the plasma behavior; however, in the low-conductivity limit (for example, vacuum) the wave nature of the magnetic field cannot be ignored. Since the MHD framework assumes that the displacement current is negligible, this description tends to be valid for high-conductivity plasma.

Three significant results of the MHD theory are worth observing. First, the assumption of no net macroscopic charge means that the electric body force plays an insignificant role on the fluid, since the electric force varies linearly with the net charge. Second, the discarding of the displacement current renders the Maxwell equations diffusive as an approximation to their true hyperbolic nature. This means that electromagnetic waves are no longer permitted to propagate in an MHD plasma. Finally, the magnetic diffusion approximation possesses a very different character for its current distribution. The charge continuity equation, which expresses the conservation of electric charge, may be derived from the Maxwell equations;

its form is

$$\frac{\partial \varrho_e}{\partial t} + \nabla \cdot \mathbf{j}_e = 0 \quad (1.32)$$

where ϱ_e is the net charge density and \mathbf{j}_e is the current density. But since, by quasineutrality, $\varrho_e = 0$, the current density becomes *solenoidal*. An ad hoc constitutive relationship must be fashioned for \mathbf{j}_e , which can be given by a form of Ohm's law.

1.4 A Picture of the Problem

The study of plasmas has far-reaching effects for the development of modern technologies, particularly in aerospace and energy applications. A major impetus for further understanding and modeling the interaction between fluids and electrodynamics has involved an ongoing drive to control and improve fluid flow applications with the presence of electromagnetic fields. However, in many of these applications, the underlying physics of the plasma is not fully understood, and for several of these applications, these underlying processes are often neglected in modeling. It can be shown that these processes can potentially dictate the long-term behavior of the device, and lifetime, degradation and performance issues can result. Furthermore, they usually indicate the onset of instabilities in the plasma, and are therefore critical for examining long-term behaviors of plasmas. Below, we examine more closely some specific examples of applications in aerospace and energy where the underlying effects not captured by the MHD model become significant and non-negligible.

- *Electromagnetic flow control.* The use of electromagnetic fields in aerospace applications to control and improve flow situations is a very popular topic of current interest [20]. Plasma actuators based on the asymmetric configuration of the single dielectric barrier discharge (SDBD) have received significant attention in the last decade, due to their very simple construction and operation and wide design space that allows flow separation control [21–26], viscous drag reduction [27–29] and possibly shock control and mitigation applications [26, 30–34]. Despite numerous experimental and computational investigations, the detailed physics of the actuator operation are still not fully understood [35–41]. The modeling of plasma actuators is particularly different from typical applications of EM fields for aerospace applications because the flow is *electrohydrodynamic* [21, 22], and draws on an *electric* field to shape the flow, rather than a magnetic field. The application of an electric body force to the flow requires some charge separation to be present, since the electric body force is proportional to the net charge density. The interactions of multiple species and the highly transient nature of the device make accurate prediction of the plasma actuator a very difficult task; presently, most fluid simulations utilize phenomenological models for the electric body force [21, 23, 24, 42–44].
- *Hypersonic flight and propulsion.* The application of magnetic and electric fields have been suggested for several applications of hypersonic flight. The presence of a strong imposed magnetic field from a

vehicle nosetip is known to push the blunt-body shock away from the vehicle front [45–48], which can potentially reduce the temperature on the nose. It has been shown that self-induced fields created behind the shock due to the interaction of high-conductivity flow and applied fields, Hall effect and ion slip can be significant [46–48]. The prediction of a strong shock in hypersonic flow has been shown to possess charge separation effects that cannot be predicted using the MHD theory. [49, 50] The application of an energy bypass arrangement for improving scramjet performance by using magnetic fields is currently being explored [51–55]

- *Radio communications and blackout.* The communications blackout effect is a direct result of the formation of a plasma sheath around a vehicle in the upper atmosphere; the sheath is non-neutral and possesses a plasma frequency. Radio waves impinging on the plasma must have a frequency higher than the plasma frequency in order to penetrate the plasma, or they are reflected. Waves that are transmitted into the plasma attenuate rapidly due to the strong conductivity. Although the mitigation of electron number density has been investigated using the magnetohydrodynamic model and kinetic approaches [56, 57], the actual propagation of the wave into the sheath cannot be properly investigated using the magnetohydrodynamic framework.
- *Space plasma propulsion.* The exhaust of a plasma thruster involves a transition from a high-conductivity plasma into a low-conductivity domain. In the low-conductivity (vacuum) region, the wave nature of the magnetic field dominates, and must be correctly capturing propagating at the speed of light. In cases involving plasmas generated by capacitive discharges, such as the pulsed plasma thruster [58], transient modeling should include a displacement current across the rails as the thruster is initiated [59–64]. Previous work that has sought to model plasma thrusters using the existing magnetohydrodynamic framework have injected a massless, conductive ‘ether’ field in the vacuum region to circumvent this problem [62, 63]. More recent simulation work has begun investigating the inclusion of this displacement current and vacuum behavior while still resolving the high-conductivity plasma during operation [59–61].
- *Plasma stability.* The onset of instabilities in high-energy-density plasmas are often caused by plasma oscillations that are not permitted in the MHD theory. These oscillations appear as singular perturbations in the MHD equations. In Hall effect thrusters, for example, it has been shown that the appearance of evanescent waves can degrade performance and stability; this causes a significant drop in the specific impulse of the thruster [65–69]. The operation of Hall thrusters due to anomalous electron mobility is also not well understood [70, 71]. Devices such as the Z-pinch and field-reversed configuration [72], which offer major potential advantages for energy and propulsion, necessarily require stability models that supercede the magnetohydrodynamic model.

The above applications motivate the migration to a more physically correct plasma model, if we wish to model these phenomena. Several different models are available, but of particular interest in this dissertation is the multifluid plasma model. This dense plasma model uses a set of moment equations to describe the

fluid behavior of each species (usually only two species, hydrogenic ions and electrons, are considered, hence the frequent name *two-fluid plasma model*), coupled to the full Maxwell equations. We will also examine this model's limit to a single species, in which the electron inertia is neglected. This *single-fluid model* will involve a coupled system of the Navier-Stokes and full Maxwell equations, including the displacement and convective currents. While the single-fluid model is more limited than the two-fluid model in that inter-species effects and electron inertia have been neglected, this model still retains strong generality over the MHD model, and permits explorations of electromagnetic wave propagation, charge separation effects and low-conductivity limits that are not permitted in the MHD model.

1.5 Going Beyond the MHD Framework

Although the MHD theory has been applied to a great deal of plasmas, there can be cases in which the assumptions made are invalid. Particularly, in cases where charge separation effects, multiple species effects, electromagnetic wave propagation, and long-term equilibrium behavior for instabilities are important, the full physics must be included.

With the limitations detailed in the last section, a migration to more accurate physical models to study these problems is expected. Investigations in plasma stability and equilibria for plasma and fusion devices have focused on utilizing the two-fluid plasma model [72–82] while recent work centered on the applications of electromagnetic fields for hypersonic flight have explored the application of the single-fluid model [8, 46–50, 59, 61, 62, 64, 83–98]. The former have emphasized the need to include multiple species effects, electron inertia effects and higher-frequency plasma oscillations to study the behavior of relaxation in fusion devices and stability behavior in devices such as the Z-pinch; the latter have investigated the inclusion of charge separation effects and induced magnetic field behavior for hypersonic sheath development and propulsion operation. The behavior of electromagnetic wave propagation through hypersonic sheaths has also been the focus of much investigation to mitigate the communications blackout effect [56, 57]. Since the blackout effect is predominantly determined by the plasma frequency and involves studying the propagation of radio waves, the MHD model is incapable of resolving the detailed behavior of this problem.

Several of the investigations mentioned above have explored the construction of analytical and numerical solutions to the two-fluid and single-fluid models presented; however, the equations admit analytical solutions only in very limited cases, and the capability to numerically solve these coupled systems is complicated by the presence of multiple and highly disparate frequencies that characterize both systems [49, 59, 73, 74, 99]. In the simplest case of the single-species bulk model, a disparity between the characteristic fluid speeds and the speed of light must be resolved; recall the Mach 20 flow in the upper atmosphere where the fluid characteristic speed is about 7,000m/s, which is still five orders of magnitude smaller than the characteristic electromagnetic speed, the speed of light. This problem requires considerable attention for modeling efficiently with only modest effort. This problem is exacerbated by the presence of numerical

stability issues due to the form of the coupling expressed in the above systems; the presence of the Lorentz body force and Ohmic dissipation terms are conventionally incorporated as explicit source terms to the Navier-Stokes equations, which introduce significant numerical stability constraints on the solution of these equations that cannot typically be circumvented in a straightforward manner. Thus, while the two-fluid and single-fluid systems permit the full physical treatment of plasmas that may otherwise not be investigated properly with the MHD framework, our capabilities to analytically and numerically model these two systems are limited.

It is our broad objective, then, to discover new tools for mathematically modeling these two systems with only modest effort. Achieving new ways to model these systems will permit predictions of the above problems. Our major challenges lie in the coupling between different species, the nonlinear nature of the equations, the presence of highly disparate frequencies and numerical stability issues introduced by the presence of the source terms.

1.6 Contributions to the State of the Art

While a detailed discussion of the state-of-the-art is relegated to sections 3.1 and 5.1, a summary of the state-of-the-art and the contributions of this dissertation is presented here.

In this dissertation, we address the problem of modeling the fully-coupled single-fluid and two-fluid models in two ways. Our initial approach involved the construction of an isomorphism between the two-fluid plasma equations and the Maxwell equations of electrodynamics, but this framework was limited by the availability of data. Our original goal was to take advantage of this new set of isomorphic Maxwell equations for the plasma, and to solve the system and reconstruct the primitive data from the generalized fields. However, the new Maxwell equations have added source terms, analogous to the electric charge and current density, and some representative model for these sources must be known before solving for the generalized fields. The issue of finding source term models imposed a significant limitation on our capabilities to utilize this model for plasmas. We describe source term data that could be acquired, primarily by examining simple analytical solutions and postprocessing numerical solutions to determine the form and behavior of the source terms for this model.

During the process of investigating the source terms, an efficient numerical scheme was required to catalyze the data collection process. This led to a separate investigation in which a new numerical formulation suggested in [59] was explored in an effort to improve the simulation of single-fluid and two-fluid plasmas. The new method poses the governing fluid equations in a *strong conservative* form, in which no explicit source terms are present, although the equations are still exactly coupled to the full Maxwell equations. This is possible by using the Poynting propagation vector, Maxwell stress tensor and electromagnetic energy density; the conservation form of Maxwell's equations permits the Lorentz body force and Ohmic heating terms to be recast into derivatives of these quantities, uniting them with the solution and flux vectors.

Unfortunately, it is shown that this approach cannot work for the two-fluid plasma model, since, in their general form, the equations cannot take advantage of the conservation form of Maxwell's equations; however, in the case that the electron inertia is neglected, the single-fluid model coupled to the full Maxwell equations can be solved much more efficiently using this approach. A comparison of the traditional source-coupled formulation and this new strong conservative form are explored, and validation simulations are performed that demonstrate the feasibility of applying this approach for efficient simulation of plasmas including charge separation effects, electromagnetic wave propagation and higher-frequency effects.

For the isomorphism, we specifically perform the following:

- Starting in Chapter 3, we present the Maxwell equations for a two-fluid plasma, which poses a set of Gauss laws, Faraday law and an Ampere-Maxwell law for the generalized vorticity and generalized Lamb vector in a two-fluid plasma. The convolved form of these equations are discussed as well.
- The ramifications of constructing this isomorphism is explored as well. Specifically, we show the reduction to the previous fluid dynamic work, and the new framework introduced in this dissertation unites the efforts of three different veins of literature that have explored isomorphic field equations for fluids and plasmas.
- The new feature in this exploration is the presence of source terms for the plasma, analogous charge and current densities in classical electrodynamics. The analytical forms are derived, which present the generation mechanisms that give rise to the generalized fields.
- In Chapter 4, we discuss different methodologies for solving the two-fluid Maxwell equations. It is shown that the most significant aspect of these methodologies is the means by which the new source terms are treated. Three approaches are explored: the homogeneous case (in which the source terms naturally vanish), iterative approaches (which ultimately did not produce accurate results), and empirical modeling (which, at present, is the most promising approach).
- For empirical modeling, it is desirable to build up a collection of foundational source terms that can be used as building blocks for constructing flow patterns in larger problems later. To this end, we investigate three simple cases of steady, incompressible fluid flow, and demonstrate the feasibility of applying numerical reconstructive schemes and Green's function approaches to these problems.

For the strong conservative numerical formulation, we specifically perform the following:

- Beginning in Chapter 5, we present the traditional (source-coupled) formulation, and introduce the new strong conservative form. This new form has been noted in the literature previously, but has not been investigated or validated. The new formulation is demonstrated to significantly improve the stability and robustness of the numerical scheme.
- We present the details for constructing accurate finite volume numerical schemes for the new equations using the Roe approximate Riemann solver approach and the Advected Upstream Splitting Method (AUSM) approach. A preconditioned implicit scheme was used to improve convergence and speed. The solver works on structured and fully unstructured meshes.

- In Chapter 6, we present validation test cases for the strong conservative form in one and two dimensions. We investigate Riemann problems that involve shocks, steep gradients and discontinuities, and show that the solver is very capable of resolving these solutions accurately. Turbulence and instability problems are also explored to demonstrate agreement between the new solver and accepted solutions. To demonstrate capabilities that cannot be captured in the MHD framework, we explore the propagation of electromagnetic waves into plasmas and low-conductivity limits of the plasma.
- Comparisons are made between the strong conservative and source-coupled form to verify the improvement in efficiency over the source term formulation. Significant improvements in both the accuracy and speed were realized.
- Comparisons between the Roe and AUSM flux schemes are presented; using these two independent approaches, we validate the new mathematical formulation introduced for the Riemann solver approach, including the new jacobian matrices and eigenvectors, which are required for the construction of a Roe solver.

1.7 Outline of the Dissertation

To disclose more fully the models of interest, we devote Chapter 2 to describing the overall models of interest. Our discussion begins with a brief description of Maxwell’s equations in Section 2.1; this is necessary both because the models of interest are fully coupled to Maxwell’s equations, and because the isomorphic approach will rely on a knowledge of these equations. We briefly discuss kinetic approach in Section 2.2, and from the kinetic description we outline the derivation of the two-fluid model in Section 2.3. In Section 2.4, we take the limiting case of negligible electron inertia to reduce the two-fluid model to the single-fluid model. We describe the development of Ohm’s law for this model in Section 2.5. In Section 2.6, we further reduce the single-fluid model to the typical magnetohydrodynamic model, and finally in Section 2.7, we summarize these different models of interest.

Our discussion of the isomorphic approach begins in Chapter 3; in Sections 3.1 and 3.2 we discuss the state of the art and the objective of this investigation, respectively. In Section 3.3, we introduce the isomorphic field equations, although the finer details of the derivation have been relegated to Appendix A.1. Following our presentation of the new isomorphic field equations, which mathematically are identical to Maxwell’s equations of classical electrodynamics, we spend Section 3.5 exploring some of the ramifications and consequences of this isomorphism. We do not provide an exhaustive account, since this is neither necessary nor useful, but we elaborate on five important points of interest: (a) the reduction of the equations to a Maxwell system for fluid dynamics in Section 3.5.1, which agrees with previous work, (b) potential theory and gauge transformations in Section 3.5.2, (c) appropriate boundary conditions in Section 3.5.3, (d) a Lagrangian formalism in Section 3.5.4, and (e) an analogous drift relation constructed by vector identity that permits an inverse transformation from the dynamical fields to the velocity, shown in Section 3.5.5. Finally, in

Section 3.6, we summarize the theory we have presented by means of introducing the isomorphism.

Chapter 4 presents our attempts in this investigation to solve the isomorphic field equations in lieu of the traditional formulation. We outline in Section 4.1 the major difficulty encountered here, which is a scarcity of source term data. If more source term data were available, this approach would be much more likely to succeed. However, the deficit in available source term data makes solving the equations difficult. Three approaches were explored to circumvent this issue: in Section 4.2, we explore the mathematically convenient case that the plasma is *homogeneous*, such that no source terms are present; we show that the typical MHD waves can be recovered using this approach. In Section 4.3, we discuss the possibility of constructing iterative approaches, wherein the source terms are calculated from the primitive variables, the field equations are then solved using the source data, and the primitive variables are then reconstructed, leading to an iterative scheme not unlike the particle-in-cell (PIC) method, except including the fluid character as well as the electrodynamic behavior. However, in this investigation, we never found a feasible means of constructing an efficient iterative scheme. Finally, in Section 4.4, we resort to empirically modeling the source terms, which proved the most successful, although still limited, approach. The easiest method to determine empirical models for the source term data was to start with a known analytical solution for a simple problem (steady, incompressible fluid flow is examined); this led to general source term models that could be used to construct more complicated flow patterns, permitting a solution of the field equations for more difficult flows. The fluid problems were used as a test bed for constructing numerical and closed-form solutions using the isomorphic approach; when the flow is non-vortical (or when the plasma has no generalized vorticity), the equations break down since the drift relation cannot be used. However, we show that using a potential approach can circumvent this issue, leading us to successful numerical simulations of fluid flow, including a closed-form solution to Blasius boundary layer flow. To further explicate the source term data for non-simple cases of compressible flow and plasmas, we postprocess numerical simulations for compressible flows and plasmas to reveal the nature of the source terms.

Our investigation of the source terms by postprocessing numerical simulations led to a separate investigation to improve the efficiency of solving the plasma equations, which itself succeeded in improving the efficiency of plasma modeling and surpassed our capabilities using the isomorphic approach. This second approach is discussed in Chapter 5, where we present the strong conservative formulation used to improve the stability of the equations. In Sections 5.1 and 5.2, we present the state of the art and our specific objective for utilizing this new numerical approach. In Section 5.3, we present the traditional (source-coupled) formulation; we construct some identities in Section 5.4 for the conservation form of Maxwell's equations, and apply them in Section 5.5 to derive the new strong conservative form of the equations. Sections 5.6 through 5.14 are devoted to providing a detailed exposition of the numerical scheme implemented for this investigation.

Having introduced the approach in Chapter 5, we present validation results of the new approach in Chapter 6. In Sections 6.1 and 6.2, we consider classic Riemann problems from plasma physics, and provide

a comparison between the strong conservative and traditional source-coupled formulations. We present in Section 6.3 a radio wave propagation test that demonstrates the capabilities of capturing both the low- and high-conductivity limits of the electromagnetics. Section 6.4 investigates our capabilities of capturing the onset of instability of plasmas by examining the Kelvin-Helmholtz magnetohydrodynamic instability. In Section 6.5, we further confirm this capability by presenting validation tests of a magnetohydrodynamic vortex problem that demonstrates plasma turbulence modeling capabilities. The approach demonstrates the capabilities to capture the charge separation effects at the electrodes.

Finally, in Chapter 7, we present our conclusions from this work; in Section 7.1 we review our stated objective, and Section 7.2 outlines the findings for the isomorphic approach and the strong conservative approach, respectively. In Section 7.3, we specifically point out the contributions presented in this dissertation that push the state of the art. Section 7.4 points out the potential future applications and directions to follow from this work, and in Section 7.5, we provide some concluding remarks about these investigations.

Chapter 2

Mathematical Models for Single-fluid and Two-fluid Plasmas

“Your test assignment will vary, depending on the manner in which you have bent the world to your will.”

Cave Johnson [1]

Plasma modeling may essentially be divided into *microscopic* and *macroscopic* approaches. Microscopic models are concerned with describing the constituent particles that comprise the plasma; macroscopic models apply continuum principles and formulate equations for the statistical averages of the constituents, in order to simplify the number of variables needed. Microscopic approaches are physically more accurate, and can capture anisotropies and tensorial behaviors much more straightforwardly, but, in some cases, can be more demanding of computational resources than continuum approaches.

Two primary forms of microscopic modeling are individual particle tracking and kinetic modeling. The former leads to particle-in-cell (PIC) simulations, where forces and collisions are applied iteratively in conjunction with updating the particle’s position, momentum, and contribution to the electromagnetic sources; the latter insists on solving a Boltzmann equation for a distribution function (or one for each species) which encapsulates all information about that species. Microscopic approaches require some form of collisional modeling to be incorporated; in the case of PIC approaches, collisions are often modeled using direct-simulation Monte Carlo (DSMC) techniques [100], while kinetic modeling [10, 14] usually requires the calculation of a collision integral that accurately describes the collisional behavior of the plasma. In both cases, the appropriate modeling of the collisionality of the plasma is an open question with no trivial answer. Furthermore, the nature of the outcome of collisional terms depends strongly on the plasma under study.

The number of particles required to resolve the plasma behavior using microscopic approaches generally increases with decreasing Knudsen number. When the necessary number of particles becomes very large, or when the collisional nature is either unknown or extremely complicated, solutions using microscopic

approaches become intractable even on modern hardware due to speed and memory limitations. It then becomes more economical to apply a continuum approach and consider only the bulk motion of the plasma. This can be done by statistically averaging over the microscopic equations describing the evolution of the constituent particles. The averaging permits a much simpler treatment of the collision terms, but at the cost of removing the individual nature of the particle motion; by averaging over the microscopic equations, we lose the spread of different possible behaviors of separate particles and retain only the bulk behavior of each species. Thus, anisotropies can be very challenging to correctly capture in continuum approaches.

Our effort is aimed at improving modeling of dense plasmas using continuum assumptions. Within the realm of continuum models, there is a diverse resumé of different choices available for modeling the fluid and electromagnetic behavior. As we have discussed in Chapter 1, the magnetohydrodynamic approximation represents the incumbent approach for modeling dense plasmas, but, as already mentioned, this approach leaves out some significant details that we are motivated to capture. Therefore, some intermediate fluid model must be derived and applied for the problems of interest. We will investigate the two-fluid and single-fluid plasma models, each of which arrests a more physically complete picture for the applications outlined in Chapter 1. In this chapter, we discuss the derivation of these models from the kinetic theory of plasmas, and also detail the comparison between these models and the magnetohydrodynamic framework. We finally provide a set of tables that clearly delineate the equations of interest for later chapters.

2.1 Maxwell's Equations

Maxwell's equations play a pivotal role in this dissertation not only because they are coupled to both plasma models of interest, but also because, in Chapter 3, we draw an analogy between the two-fluid generalized fields and the electromagnetic fields, which reveals an isomorphism between the two systems. To facilitate understanding the isomorphism, this section will also serve as a reference guide for our discussion in Chapter 3. References [5, 101] provide much more detail.

2.1.1 Maxwell's Equations

The electromagnetic fields in a plasma are solutions to Maxwell's celebrated equations. In the vector form popularized by Oliver Heaviside [2, 3], these equations are comprised of the *Gauss law divergence constraints for magnetic and electric fields*, *Faraday's law*, and the *Ampere-Maxwell law*, given in order as

$$\nabla \cdot \mathbf{B} = 0 \tag{2.1}$$

$$\nabla \cdot \mathbf{D} = \varrho_{\text{efree}} \tag{2.2}$$

$$\frac{\partial \mathbf{B}}{\partial t} + \nabla \times \mathbf{E} = 0 \tag{2.3}$$

$$\frac{\partial \mathbf{D}}{\partial t} + \mathbf{j}_{\text{efree}} = \nabla \times \mathbf{H} \tag{2.4}$$

Table 2.1: Physical units of electromagnetic quantities, using base dimensions of length $[l]$, time $[t]$, mass $[m]$, and charge $[q]$, and derived units of voltage $[V] = [ml^2t^{-2}q^{-1}]$, current $[I] = [qt^{-1}]$, magnetic flux $[\Phi] = [Vt]$, capacitance $[C] = [qV^{-1}]$, inductance $[L] = [\Phi I^{-1}]$, and conductance $[G] = [IV^{-1}]$.

Notation	Units	Name
\mathbf{E}	$[Vl^{-1}]$	Electric field
\mathbf{H}	$[Il^{-1}]$	Magnetic field
\mathbf{D}	$[ql^{-2}]$	Electric displacement field
\mathbf{B}	$[\Phi l^{-2}]$	Magnetic induction field
ϱ_e	$[ql^{-3}]$	Electric charge density
\mathbf{j}_e	$[Il^{-2}]$	Electric current density
$\bar{\bar{\epsilon}}$	$[Cl^{-1}]$	Permittivity tensor
$\bar{\bar{\mu}}$	$[Ll^{-1}]$	Permeability tensor
$\bar{\bar{\sigma}}$	$[Gl^{-1}]$	Conductivity tensor
$\bar{\bar{\eta}}$	$[G^{-1}l]$	Resistivity tensor

Here $\varrho_{e\text{free}}$ and $\mathbf{j}_{e\text{free}}$ are the free¹ charge and current densities, the fields \mathbf{E} and \mathbf{H} are the electric and magnetic field intensities proper, and \mathbf{D} and \mathbf{B} are the electric displacement and magnetic induction fields. The fields \mathbf{D} and \mathbf{H} are sometimes called the *auxiliary fields*. These equations constitute a system of eight scalar (two scalar plus two vector) representing a first-order system of partial differential equations. The physical units associated with each field are shown in Table 2.1. The auxiliary fields are generally very complicated functions of all of the other fields as well as the medium. However, often a simple dependence may be constructed by the following approximations,

$$\mathbf{D} = \bar{\bar{\epsilon}} \cdot \mathbf{E} + \mathbf{P} \quad (2.5)$$

$$\mathbf{H} = \bar{\bar{\mu}}^{-1} \cdot \mathbf{B} + \mathbf{M} \quad (2.6)$$

where \mathbf{P} and \mathbf{M} are polarization and magnetization vectors, respectively, representing bound charges and currents. We will assume that these fields are zero. We will further assume that the medium is sufficiently isotropic, such that the permittivity tensor, $\bar{\bar{\epsilon}}$, and permeability tensor, $\bar{\bar{\mu}}$, reduce to scalars, ϵ and μ . These values frequently can be taken as their vacuum values, $\epsilon_0 = 8.854 \times 10^{-12} \text{F/m}$ and $\mu_0 = 1.257 \times 10^{-6} \text{H/m}$. They are connected through the Weber relation,

$$\epsilon_0 \mu_0 = \frac{1}{c_0^2} \quad (2.7)$$

¹this excludes *bound* charges, which may be contributed by the medium.

where c_0^2 is the square of the speed of light. In vacuum, $c_0 = 2.9979 \times 10^8 \text{m/s}$. Thus, Maxwell's equations in linear, isotropic media are written as

$$\nabla \cdot \mathbf{B} = 0 \quad (2.8)$$

$$\nabla \cdot \mathbf{E} = \varrho_e / \epsilon_0 \quad (2.9)$$

$$\frac{\partial \mathbf{B}}{\partial t} + \nabla \times \mathbf{E} = 0 \quad (2.10)$$

$$\frac{1}{c_0^2} \frac{\partial \mathbf{E}}{\partial t} + \mu_0 \mathbf{j}_e = \nabla \times \mathbf{B} \quad (2.11)$$

Equations 2.8 through 2.11 are what we will refer to as *Maxwell's equations*.

2.1.2 Charge Continuity

A significant result from Maxwell's equations is the *charge continuity equation*. We can arrive at this equation by taking the divergence of Ampere's law, equation 2.11, and using equation 2.9, to get

$$\frac{\partial \varrho_e}{\partial t} + \nabla \cdot \mathbf{j}_e = 0 \quad (2.12)$$

This equation states that the amount of current leaving through an arbitrary surface is equal to the decreasing rate of charge per time, which equates the idea of charges moving with current.

2.1.3 Electromagnetic Waves

The first-order form of equations 2.10 and 2.11 may be rewritten in second-order form. We take the curl of equation 2.10 and the time derivative of equation 2.11 and eliminate the common term to arrive at a wave equation for the electric field, \mathbf{E} . Similarly, we may exchange the operations on the same equations and once again eliminate the common term to derive a wave equation for the magnetic induction field, \mathbf{B} (henceforth simply referred to as the magnetic field). Assuming that the medium is vacuum and has no charge or current density present, then we have

$$\frac{\partial^2 \mathbf{B}}{\partial t^2} - c_0^2 \nabla^2 \mathbf{B} = -\square^2 \mathbf{B} = 0 \quad (2.13)$$

$$\frac{\partial^2 \mathbf{E}}{\partial t^2} - c_0^2 \nabla^2 \mathbf{E} = -\square^2 \mathbf{E} = 0 \quad (2.14)$$

where we have introduced the D'Alembertian (or wave) operator, $-\square^2 = (\partial^2 / \partial t^2 - \nabla^2)$. Thus, in the absence of charge and current, the fields propagate as waves moving at speed c_0 .

2.1.4 Vector and Scalar Potentials

Examining the form of equation 2.8, and noting the vector identity $\nabla \cdot \nabla \times \mathbf{A} = 0$, we may posit that a vector potential, \mathbf{A} , could be defined that allows the magnetic field to be defined as

$$\mathbf{B} = \nabla \times \mathbf{A} \quad (2.15)$$

This definition automatically satisfies equation 2.8 by identity. If we substitute this into Faraday's law, then we have

$$\nabla \times \left\{ \frac{\partial \mathbf{A}}{\partial t} + \mathbf{E} \right\} = 0 \quad (2.16)$$

Noting the vector identity $\nabla \times \nabla \phi = 0$ for any scalar ϕ , this implies that

$$\frac{\partial \mathbf{A}}{\partial t} + \mathbf{E} = -\nabla \phi \quad (2.17)$$

and, rearranging, we have

$$\mathbf{E} = -\nabla \phi - \frac{\partial \mathbf{A}}{\partial t} \quad (2.18)$$

Thus, if we use \mathbf{A} and ϕ (the *vector potential* and *scalar potential*, respectively) as our primary unknowns, we have reduced the eight first-order equations 2.8 through 2.11 to four second-order equations,

$$\frac{1}{c_0^2} \frac{\partial^2 \phi}{\partial t^2} - \nabla^2 \phi = -\square^2 \phi = \frac{\rho_e}{\epsilon_0} + \frac{\partial}{\partial t} \left\{ \nabla \cdot \mathbf{A} + \frac{1}{c_0^2} \frac{\partial \phi}{\partial t} \right\} \quad (2.19)$$

$$\frac{1}{c_0^2} \frac{\partial^2 \mathbf{A}}{\partial t^2} - \nabla^2 \mathbf{A} = -\square^2 \mathbf{A} = \mu_0 \mathbf{j}_e - \nabla \left\{ \nabla \cdot \mathbf{A} + \frac{1}{c_0^2} \frac{\partial \phi}{\partial t} \right\} \quad (2.20)$$

One of the appealing aspects of this approach is the notion of *gauge transformation*. Since the quantity $\nabla \cdot \mathbf{A}$ is physically meaningless (only the curl of the vector potential represents a physical quantity), we are at liberty to take this value to be anything that is mathematically convenient. In our case, two particular choices are of significant interest.

2.1.4.1 Lorentz Gauge

The easiest approach to simplify equations 2.19 and 2.20 would be to completely eliminate the last term in brackets entirely. To do so, we could choose

$$\nabla \cdot \mathbf{A} = -\frac{1}{c_0^2} \frac{\partial \phi}{\partial t} \quad (2.21)$$

which is the *Lorentz gauge*.² Choosing this gauge will simplify equations 2.19 and 2.20 to inhomogeneous wave equations,

$$-\square^2 \phi = \frac{\rho_e}{\epsilon_0} \quad (2.22)$$

$$-\square^2 \mathbf{A} = \mu_0 \mathbf{j}_e \quad (2.23)$$

2.1.4.2 Coulomb Gauge

An alternate gauge that is sometimes also very convenient would be to simply take $\nabla \cdot \mathbf{A} = 0$. In this case, equation 2.19 reduces to a Poisson equation in ϕ and equation 2.20 reduces to a wave equation that depends on the potential as a source term,

$$-\nabla^2 \phi = \frac{\rho_e}{\epsilon_0} \quad (2.24)$$

$$-\square^2 \mathbf{A} = \mu_0 \mathbf{j}_e - \frac{1}{c_0^2} \nabla \frac{\partial \phi}{\partial t} \quad (2.25)$$

2.1.5 Divergence Constraints

A simple count of unknowns and equations will reveal that Maxwell's equations are overconstrained (eight equations for six unknowns, \mathbf{E} and \mathbf{B}). The Gauss laws, equations 2.8 and 2.9, are considered *divergence constraints* in this respect; that is, physical solutions of the Faraday and Ampere-Maxwell equations must further satisfy the divergence constraints. Candidate solutions that satisfy the Faraday and Ampere-Maxwell equations and do not satisfy the divergence conditions are considered unphysical and are not permitted.

Analytically, if we pose a Cauchy problem with some initial conditions, then if the initial conditions satisfy these divergence constraints, the solution will *always* satisfy these constraints. However, numerically, this is not generally true. The discretization of the equations 2.10 and 2.11 permits numerical error to accumulate unchecked in the divergences of the fields. These numerical monopoles sabotage the simulation, since the resulting solution to the Faraday and Ampere-Maxwell laws are no longer eligible to be physical solutions. Boundary conditions can exacerbate this problem as well. Therefore, care must be taken when constructing a numerical solution to the Maxwell equations. In one spatial dimension, the divergence constraints can be met exactly by a clever choice of initial conditions and coordinate system. However, in two or more spatial dimensions, we must generally perform some kind of process (usually referred to as *divergence cleaning*) in order to force the divergence constraints to be met. Neglecting this, divergence cleaning can lead to significant numerical catastrophies (see, for example, the discussions in References [5, 101, 103], and the example of results without divergence cleaning in References [47, 103]). Note that, if one is solving the potential formulation (equations 2.19 and 2.20) instead, then the divergence constraints are automatically met; however, we will prefer to solve the equations in their first-order form since this will lend directly to

²This is also commonly known as the Lorenz-Lorentz gauge or sometimes the Lorenz gauge [102].

the finite volume method later. In Chapter 5, when we address the numerical schemes implemented, we will discuss the approaches taken to enforce these divergence constraints.

2.2 Kinetic Description of the Fluid

This section details the kinetic description of a plasma and is taken largely from [10, 14]. The kinetic description assumes that all information or data describing the state of each species α in the plasma are encapsulated in a function called the *distribution function*, f_α , which is defined to be the number of particles at a specific point x with a specific velocity v at a specific time t for a species α . The distribution function spans a phase space that is a union of the configuration (spatial) and velocity (or alternately momentum) space. If we can construct an equation that determines the evolution of f_α , then we can solve it to advance this function in time, which permits a knowledge of how the plasma behaves. All significant information about the plasma's behavior can be derived from the distribution function, f_α .

Just such an equation is provided by the *Boltzmann equation*. This equation is constructed by considering the conservation of number of particles between two times in a Taylor expansion of the distribution function. The Boltzmann equation's form is

$$\frac{\partial f_\alpha}{\partial t} + \frac{\partial}{\partial x_k} (v_k f_\alpha) + \frac{\partial}{\partial v_k} (a_k f_\alpha) = \sum_\lambda C_{\alpha\lambda}(f_\alpha) \quad (2.26)$$

Here, v_k is the velocity and a_k the acceleration, and $C_{\alpha\lambda}$ is a collision operator between two species α and λ . Determining the form of the collision operator is usually an extremely complicated problem with no easy answer, and depends significantly on the frequency and nature of the different collisions occurring in the plasma. For classical gases, Boltzmann's Stosszahl ansatz [14] approach is valid, which assumes only elastic binary collisions occur, and that the colliding particles are uncorrelated prior to the collision. This approach can also work for weakly ionized plasmas, if the Coulombic collisions can be neglected. When Coulombic collisions are significant, the Fokker-Planck approach [14] can be taken, which assumes that the collision integral can be approximated by a series of weak binary collisions; this approach leads to the Fokker-Planck equation [14], which is valid for strongly ionized plasmas.

Due to the presence of the collision operator, the distribution function may not be well behaved. It can have perceived discontinuities where particles 'jump' across the phase space due to interactions. However, this equation can be solved directly to reveal the evolution of the plasma. There are some advantages to doing this. The kinetic description maintains a higher level of information regarding the separate particles than macroscopic models; therefore, high-frequency effects and anisotropies can be captured well using this approach. However, this model (as well as the particle-in-cell method) becomes excessively expensive and infeasible with modern computer hardware when the Knudsen number, Kn , is sufficiently small (usually around order unity), which reduces the statistical bases for the function f_α , at which point Monte Carlo

methods are more fruitful [104]

In the case that the Knudsen number becomes small, macroscopic models become superior. The kinetic description serves as a starting point on the microscopic level to construct macroscopic models. These can be constructed by *taking moments* of the Boltzmann equation for each species. This process involves multiplying equation 2.26 through by some species-specific property (called the *moment*), ϕ_α , and integrating over the velocity space,

$$\int \phi_\alpha \left\{ \frac{\partial f_\alpha}{\partial t} + \frac{\partial}{\partial x_k} (v_k f_\alpha) + \frac{\partial}{\partial v_k} (a_k f_\alpha) \right\} dv_k = \sum_\lambda \int \phi_\alpha C_{\alpha\lambda}(f_\alpha) dv_k \quad (2.27)$$

This removes the velocity dependence by integrating it out. Also, because some key identities can be developed about the nature of collisions with respect to the bulk plasma, the collision operator also disappears by doing this. The remaining integrations are taken as definitions of an average of some bulk property of the flow, which is taken as the new unknown in the macroscopic model. Thus, after integration over the velocity space (and often, some clever applications of vector identities and teasing out the physical meaning of large tensorial quantities), we can arrive at a series of statements about the bulk averages for each equation. Note that taking a moment will always introduce a higher-order moment, so this leads to an indefinite process that requires some form of closure to cut off the moment-taking. This can be accomplished with additional assumptions regarding the nature of heat transfer (adiabatic or isothermal assumptions), or, if higher moments are desired, assumptions placed on the third- or fourth-order moment terms.

The following identities will assist in the integration of the collision integral term:

- Collisions are not permitted to change the total number of particles at a location in the phase space,

$$\int C_{\alpha\lambda}(f_\alpha) dv_k = 0 \quad (2.28)$$

- Collisions between members of the same species is not allowed to change the overall momentum of the species,

$$\int m_\alpha v_k C_{\alpha\alpha}(f_\alpha) dv_k = 0 \quad (2.29)$$

Additionally, collisions between different species must conserve the total momentum of both species,

$$\int m_\alpha v_k C_{\alpha\lambda}(f_\alpha) dv_k + \int m_\lambda v_k C_{\lambda\alpha}(f_\lambda) dv_k = 0 \quad (2.30)$$

- Collisions between different members of the same species are not permitted to change the total energy of that species,

$$\int m_\alpha v_k v_k C_{\alpha\alpha}(f_\alpha) dv_k = 0 \quad (2.31)$$

Furthermore, collisions between different species must conserve the total energy of both species together,

$$\int m_\alpha v_k v_k C_{\alpha\lambda}(f_\alpha) dv_k + \int m_\alpha v_k v_k C_{\lambda\alpha}(f_\lambda) dv_k = 0 \quad (2.32)$$

where $v_k v_k$ is assumed as an index form of $\mathbf{v} \cdot \mathbf{v} = v^2$.

We will spare the reader most of the details of the development of this process. Details can be found readily in several texts [10, 14].

2.3 Two-fluid Description

The multi-fluid plasma model is a continuum approach that assumes the constituent species of the plasma may be described as separate fluids. Often, this is reduced to the case of only hydrogenic ions and electrons, hence the term *two-fluid*. In the case of weakly ionized plasmas, we may add the neutrals as an additional separate fluid, or as separate fluids per neutral species.

In order to derive these equations, we take the moments ϕ_α to be m_α , $m_\alpha v_k$, and $(1/2)m_\alpha v_k v_k$. For the first case, we have $\phi_\alpha = m_\alpha$, which becomes

$$\int m_\alpha \left\{ \frac{\partial f_\alpha}{\partial t} + \frac{\partial}{\partial x_k} (v_k f_\alpha) + \frac{\partial}{\partial v_k} (a_k f_\alpha) \right\} dv_k = \sum_\lambda \int m_\alpha C_{\alpha\lambda}(f_\alpha) dv_k \quad (2.33)$$

We can drop the summation on the right-hand term if we imply that λ must be the opposite of α for the two possible species. Recalling equation 2.28, the right-hand side vanishes. We can readily exchange differentiation and integration, since x_k , v_k and t are all independent in the phase space. Thus, we have

$$m_\alpha \frac{\partial}{\partial t} \int f_\alpha dv_k + m_\alpha \frac{\partial}{\partial x_k} \int v_k f_\alpha dv_k + m_\alpha \frac{\partial}{\partial v_k} \int a_k f_\alpha dv_k = 0 \quad (2.34)$$

The third term equates to a surface integral in velocity space by Gauss's divergence theorem. However, since the integration is over all velocity space, and we assume that the distribution function $f_\alpha \rightarrow 0$ as $v_k \rightarrow \infty$ (that is, no particle has an infinite velocity), this term vanishes. Thus, we are left with

$$m_\alpha \frac{\partial}{\partial t} \int f_\alpha dv_k + m_\alpha \frac{\partial}{\partial x_k} \int v_k f_\alpha dv_k = 0 \quad (2.35)$$

If we introduce the *number density* as

$$\langle n_\alpha \rangle = \int f_\alpha dv_k \quad (2.36)$$

where $\langle \rangle$ denotes the average over velocity space, and the *mean species velocity*, \mathbf{u}_α , as

$$\langle u_{\alpha,k} \rangle = \frac{\int v_k f_\alpha dv_k}{n_\alpha} \quad (2.37)$$

and defining the mass density to be

$$\varrho_\alpha = \langle m_\alpha n_\alpha \rangle = m_\alpha \langle n_\alpha \rangle \quad (2.38)$$

then our equation becomes

$$\frac{\partial \varrho_\alpha}{\partial t} + \frac{\partial}{\partial x_k} (\varrho_\alpha u_{\alpha,k}) = 0 \quad (2.39)$$

which is simply a statement of species mass continuity.

Deriving the momentum and energy equations is far more involved and will not be shown in detail (see [10, 14] for the details). Before presenting their form, a major point of caution must be addressed regarding the pressure tensor, which is defined as

$$P_{\alpha,ik} = m_\alpha \int (v_i - u_{\alpha,i}) (v_k - u_{\alpha,k}) f_\alpha dv_k \quad (2.40)$$

We will assume that the pressure is *isotropic*, so that it can be reduced to

$$\begin{aligned} p_\alpha = P_{\alpha,kk} &= m_\alpha \int (v_k - u_{\alpha,k}) (v_k - u_{\alpha,k}) f_\alpha d(\mathbf{v} - \mathbf{u}_\alpha) \\ &= m_\alpha \int (\mathbf{v} - \mathbf{u}_\alpha) \cdot (\mathbf{v} - \mathbf{u}_\alpha) f_\alpha d(\mathbf{v} - \mathbf{u}_\alpha) \end{aligned} \quad (2.41)$$

It is important to realize that plasmas can frequently possess distribution functions that are anisotropic, and hence this assumption of isotropy may not always be valid. The nature of the isotropy of the distribution function is determined by competing effects in the microscopic level; collisions, which are essentially randomized, drive the distribution function towards an isotropic nature, while organized effects, such as a strong background magnetic field, drive it towards directional preference and anisotropy. It is possible to include the full pressure tensor in this derivation, which leads to the *ten-moment* and *twenty-moment two-fluid models*. This approach will not be pursued in this dissertation; more information on this approach can be found in References [105].

Applying the moment $\phi_\alpha = m_\alpha v_k$ and integrating over the velocity space reveals the species momentum equations,

$$\frac{\partial}{\partial t} (\varrho_\alpha u_{\alpha,k}) + \frac{\partial}{\partial x_k} (\varrho_\alpha u_{\alpha,k} u_{\alpha,r} - p_\alpha \delta_{kr}) = \frac{e_\alpha}{m_\alpha} \varrho_\alpha [E_k + \epsilon_{klm} u_{\alpha,l} B_m] - R_{\alpha\lambda,k} \quad (2.42)$$

where ϱ_α is once again the mean species mass density, \mathbf{u}_α is the mean species velocity, p_α is the mean species

static pressure, e_α/m_α is the charge-to-mass ratio of the species α , E_k is the electric field, B_m is the magnetic field, ϵ_{klm} is the Levi-Civita tensor, and $R_{\alpha\lambda,k}$ is the species friction (or drag). The species friction is given as

$$R_{\alpha\lambda,k} = \nu_{\alpha\lambda} m_\alpha m_\lambda (u_{\alpha,k} - u_{\lambda,k}) \quad (2.43)$$

where $\nu_{\alpha\lambda}$ is the collision frequency between the two species. Note that $R_{\alpha\alpha,k} = 0$, since a species cannot dissipate its own momentum, and $\sum_\alpha \sum_\lambda R_{\alpha\lambda} = 0$, since the plasma cannot decrease its own momentum internally.

Finally, an energy equation may be obtained by taking the momentum $\phi_\alpha = (1/2)m_\alpha v_k v_k$. We will assume for closure that the system is internally adiabatic, in which case the next-higher moment, the heat tensor, vanishes, and we can cease taking moments. This leads to the following energy equation:

$$\frac{\partial \mathcal{E}_\alpha}{\partial t} + \frac{\partial}{\partial x_k} ([p_\alpha + \mathcal{E}_\alpha] u_{\alpha,k}) = \frac{e_\alpha}{m_\alpha} \varrho_\alpha u_{\alpha,k} E_k + R_{\alpha\lambda,k} u_{\alpha,k} - \dot{W}_{\alpha\lambda}^E + \frac{\partial Q_{ik}}{\partial x_k} \quad (2.44)$$

Here \mathcal{E}_α is the species total energy density, $\dot{W}_{\alpha\lambda}^E$ is an additional heat source and Q_{ik} is the higher-moment heat flux tensor, which we will assume is negligible.

In summary, our equations for the two-fluid plasma model may be collected as

$$\frac{\partial \varrho_\alpha}{\partial t} + \frac{\partial}{\partial x_k} (\varrho_\alpha u_{\alpha,k}) = 0 \quad (2.45)$$

$$\frac{\partial}{\partial t} (\varrho_\alpha u_{\alpha,k}) + \frac{\partial}{\partial x_k} (\varrho_\alpha u_{\alpha,k} u_{\alpha,r} - p_\alpha \delta_{kr}) = \frac{e_\alpha}{m_\alpha} \varrho_\alpha [E_k + \epsilon_{klm} u_{\alpha,l} B_m] - R_{\alpha\lambda,k} \quad (2.46)$$

$$\frac{\partial \mathcal{E}_\alpha}{\partial t} + \frac{\partial}{\partial x_k} ([p_\alpha + \mathcal{E}_\alpha] u_{\alpha,k}) = \frac{\partial Q_{ik}}{\partial x_k} + \frac{e_\alpha}{m_\alpha} \varrho_\alpha u_{\alpha,k} E_k \quad (2.47)$$

where

$$\varrho_\alpha = \langle m_\alpha n_\alpha \rangle = m_\alpha \int f_\alpha dv_k \quad (2.48)$$

$$u_{\alpha,k} = \frac{\int v_k f_\alpha dv_k}{\langle n_\alpha \rangle} \quad (2.49)$$

$$p_\alpha = \frac{m_\alpha}{3} \int (v_k - u_{\alpha,k})(v_l - u_{\alpha,l}) f_\alpha d(v_m - u_{\alpha,m}) \quad (2.50)$$

$$\mathcal{E}_\alpha = \frac{m_\alpha}{2} \int v_k v_k f_\alpha dv_l \quad (2.51)$$

$$R_{\alpha\lambda,k} = \nu_{\alpha\lambda} \varrho_\alpha (u_{\alpha,k} - u_{\lambda,k}) \quad (2.52)$$

We call ϱ_α the mass density, $u_{\alpha,k}$ the species velocity, p_α the scalar species pressure, \mathcal{E}_α the total energy of the species, and $R_{\alpha\lambda,k}$ the friction.

If the gas of species α is calorically and thermally perfect, then it is customary to assume that the species

total gasdynamic energy, \mathcal{E}_α , can be written as the sum of the total internal energy and kinetic energy,

$$\mathcal{E}_\alpha = \varrho_\alpha e_\alpha + \frac{1}{2} \varrho_\alpha (\mathbf{u}_\alpha \cdot \mathbf{u}_\alpha) \quad (2.53)$$

where the internal energy for a calorically and thermally perfect gas is

$$e = \frac{p_\alpha}{\varrho_\alpha (\gamma_\alpha - 1)} \quad (2.54)$$

For higher temperatures, the assumption of a calorically and thermally perfect gas may not be accurate; in these cases, we must include the dependence of the fluid properties with temperature and pressure. We can always use more complicated models to capture the correct behavior for higher-temperature systems by resorting to interpolations from chemical calculations or by using tabular data.

Using equations 2.50 and 2.51, we can show that the total energy and pressure in the plasma are related as

$$\mathcal{E}_\alpha = \frac{3}{2} p_\alpha + \frac{1}{2} \varrho_\alpha u_{\alpha,k} u_{\alpha,k} \quad (2.55)$$

Examining the form of equation 2.53 and 2.55, we can take the species gas to be calorically and thermally perfect if we take the ratio of specific heats to be $\gamma_\alpha = 5/3$ for each species.

Our equations for a two-fluid plasma can thus be taken as

$$\frac{\partial \varrho_\alpha}{\partial t} + \nabla \cdot (\varrho_\alpha \mathbf{u}_\alpha) = 0 \quad (2.56)$$

$$\frac{\partial}{\partial t} (\varrho_\alpha \mathbf{u}_\alpha) + \nabla \cdot (\varrho_\alpha \mathbf{u}_\alpha \mathbf{u}_\alpha + \hat{\mathbf{l}} p_\alpha) = \varrho_{e,\alpha} \mathbf{E} + \mathbf{j}_\alpha \times \mathbf{B} - \mathbf{R}_{\alpha\lambda} \quad (2.57)$$

$$\frac{\partial \mathcal{E}_\alpha}{\partial t} + \nabla \cdot ([\mathcal{E}_\alpha + p_\alpha] \mathbf{u}_\alpha) = \mathbf{j}_\alpha \cdot \mathbf{E} \quad (2.58)$$

where

$$\varrho_{e,\alpha} = \frac{e_\alpha}{m_\alpha} \varrho_\alpha \quad (2.59)$$

$$\mathbf{j}_\alpha = \varrho_{e,\alpha} \mathbf{u}_\alpha = \frac{e_\alpha}{m_\alpha} \varrho_\alpha \mathbf{u}_\alpha \quad (2.60)$$

The total charge and current densities are taken as

$$\varrho_e = \sum_\alpha \varrho_{e,\alpha} = \sum_\alpha \frac{e_\alpha}{m_\alpha} \varrho_\alpha \quad (2.61)$$

$$\mathbf{j}_e = \sum_\alpha \mathbf{j}_\alpha = \sum_\alpha \varrho_{e,\alpha} \mathbf{u}_\alpha \quad (2.62)$$

The system of equations 2.56 through 2.58 represents a set of moment equations for a single species, α , in the plasma. Every species possesses its own set of moment equations. Since there are five moment

equations, and N_s species, there will be $5N_s$ equations for the fluid system, plus the Faraday and Ampere laws from Maxwell's equations. This means the total two-fluid system that we are dealing with constitutes $5N_s + 6$ equations. For the typical two-species assumption, this amounts to 16 separate equations that must be solved simultaneously.

2.4 Single-fluid Description

The two-fluid model retains separate fluid models for each species in the plasma. However, if we compare the ratio of the ion mass to the electron mass (1830 : 1), it is easy to imagine that the electron inertia may be insignificant. Conversely, due to the high mobility the electrons possess, it is also reasonable to assume that the electrical transport in the plasma (electrical conductivity) is largely due to the electrons, and the ions play a negligible role. Identifying these key behaviors and further applying them as assumptions to the two-fluid model, the system of equations may be reduced to only a single set of moment equations for the bulk fluid (this will usually coincide with the ion fluid equations). The conductivity is then given by Ohm's law, which is derived from the electron momentum equation. Doing so removes the need for solving electron equations, while still retaining several key features that are absent from the MHD theory.

We take moments in a very similar fashion to constructing the two-fluid model, using zeroth, first and second order moments of $\phi_\alpha = m_\alpha$, $\phi_\alpha = m_\alpha v_k$, and $(1/2)m_\alpha v_k v_k$ respectively, except that we also sum over all species α ,

$$\sum_\alpha \int \phi_\alpha \left\{ \frac{\partial f_\alpha}{\partial t} + \frac{\partial}{\partial x_k} (v_k f_\alpha) + \frac{\partial}{\partial v_k} (a_k f_\alpha) \right\} dv_k = \sum_\alpha \sum_\lambda \int \phi_\alpha C_{\alpha\lambda}(f_\alpha) dv_k \quad (2.63)$$

The collision integral term can now enjoy the identities provided in equations 2.29 through 2.32, which will effectively remove them from appearing in the single-fluid description. We also take $m_e \rightarrow 0$, which eliminates the electron equations, although we will see in the next section that it is useful to consider manipulating the electron momentum equation differently in order to establish a constitutive relation for the net current density.

Performing the moment procedure is essentially the same as in the two-fluid case, except that identities 2.29 through 2.32 play an important role here to eliminate the collision integral, and, because of summation, the drag terms drop out because $\sum_\alpha R_{\alpha\lambda} = 0$ and will reward us with the following bulk-flow equations,

$$\frac{\partial \varrho}{\partial t} + \nabla \cdot (\varrho \mathbf{u}) = 0 \quad (2.64)$$

$$\frac{\partial}{\partial t} (\varrho \mathbf{u}) + \nabla \cdot (\varrho \mathbf{u} \mathbf{u} + \hat{\mathbf{p}}) = \varrho_e \mathbf{E} + \mathbf{j}_e \times \mathbf{B} \quad (2.65)$$

$$\frac{\partial \mathcal{E}}{\partial t} + \nabla \cdot ([\mathcal{E} + p] \mathbf{u}) = \mathbf{j}_e \cdot \mathbf{E} \quad (2.66)$$

We have dropped the subscript α to denote that the quantity is now a bulk-flow quantity. Since the ions and neutrals tend to be much heavier than the electrons, the bulk-flow quantities will essentially be the combined heavy-species flow fields. Here ϱ is the bulk mass density, \mathbf{u} is the barycentric velocity field, \mathbf{E} and \mathbf{B} are the electric and magnetic field, ϱ_e and \mathbf{j}_e are the electric charge and current densities, and \mathcal{E} is the total gasdynamic energy. For an ideal and calorically perfect gas, the total gasdynamic energy is related to the pressure as

$$\mathcal{E} = \varrho e + \frac{1}{2} \varrho \mathbf{u} \cdot \mathbf{u} = \frac{p}{\gamma - 1} + \frac{1}{2} \varrho \mathbf{u} \cdot \mathbf{u} \quad (2.67)$$

where γ is the ratio of specific heats.

The same guarded comments about the assumption of an isotropic pressure are still in order for collision-dominated plasmas. This assumption can be very limiting for a certain class of plasmas in which strong anisotropies may exist.

2.5 Constitutive Relation for Current Density: Ohm's Law

In the two-fluid model, we primarily rely on the velocities of the electrons and ions, \mathbf{u}_e and \mathbf{u}_i , as our unknowns for the momentum. The current density is a simple linear function of these. However, in the single-fluid model, we have eliminated the moment equations for the electrons, and we cannot use the convective form of the current anymore. Therefore, we must construct a model for the current density for the single-fluid model. To construct such a model, we take the two momentum equations for the ions and electrons (from the two-fluid model, equation 2.57), divide each equation by the mass of each species and multiply by the charge, and then add the two equations together. This gives us

$$\begin{aligned} & \frac{\partial}{\partial t} e (n_i \mathbf{u}_i - n_e \mathbf{u}_e) + \nabla \cdot e (n_i \mathbf{u}_i \mathbf{u}_i - n_e \mathbf{u}_e \mathbf{u}_e) = \\ & e^2 \left[\left(\frac{n_i}{m_i} + \frac{n_e}{m_e} \right) \mathbf{E} + \left(\frac{n_i \mathbf{u}_i}{m_i} + \frac{n_e \mathbf{u}_e}{m_e} \right) \times \mathbf{B} \right] - \frac{e}{m_i} \nabla p_i + \frac{e}{m_e} \nabla p_e \\ & - e (\nu_{IE} n_i \mathbf{u}_i - \nu_{EI} n_e \mathbf{u}_e) \end{aligned} \quad (2.68)$$

Since $m_i \gg m_e$, we dismiss the terms of order m_i^{-1} . We take the net current density in the plasma to be the difference in convected currents, $\mathbf{j}_e = e (n_i \mathbf{u}_i - n_e \mathbf{u}_e)$ in this equation, and we assume the ion velocity is approximately the bulk velocity, $\mathbf{u} \approx \mathbf{u}_i$. Recall from our discussion in Chapter 1 (specifically, equation 1.20) that the ion-electron collision frequency, ν_{IE} , scales with ν_{EI} as m_e/m_i ; therefore, to be consistent with our assumption of the ion mass, we assume that $\nu_{IE} \rightarrow 0$ as well. We have

$$\frac{\partial \mathbf{j}_e}{\partial t} + \nabla \cdot (\mathbf{j}_e \mathbf{u} + \mathbf{u} \mathbf{j}_e) = \frac{n_e e^2}{m_e} (\mathbf{E} + \mathbf{u} \times \mathbf{B}) + \frac{e}{m_e} \mathbf{j}_e \times \mathbf{B} + \frac{e}{m_e} \nabla p_e - \nu_{EI} \mathbf{j}_e \quad (2.69)$$

The left-hand terms are referred to as the *inertial* terms. Generally, the time variation of the current is larger than the spatial variation, so we approximate the inertia terms by dropping the divergence term. The $\mathbf{j}_e \times \mathbf{B}$ term on the right-hand side is called the *Hall term*. Usually the pressure gradient term will not contribute much, so we further approximate this system by dropping it. The final term on the right-hand side is the *resistive term*.

It is customary to rearrange this equation and multiply through by $m_e/n_e e^2$,

$$\mathbf{E} + \mathbf{u} \times \mathbf{B} = \frac{1}{n_e e} \mathbf{j}_e \times \mathbf{B} + \frac{m_e}{n_e e^2} \frac{\partial \mathbf{j}_e}{\partial t} + \frac{m_e \nu_{EI}}{n_e e^2} \mathbf{j}_e \quad (2.70)$$

This is the generalized form of Ohm's law. Note that $m_e \nu / n_e e^2 = 1/\sigma$. We are now in a position to perform a scale analysis on the final terms of equation 2.70. We will assume that the left-hand side scales as

$$|\mathbf{E} + \mathbf{u} \times \mathbf{B}| \sim \frac{LB}{\tau} \quad (2.71)$$

where B is the characteristic field strength and L and τ are characteristic length and time scales. Notice that this scale corresponds to a scaling of the Lorentz force law, and since in a plasma the Lorentz force is generally significant, these scales must be of interest. The scales of the right-hand side terms can be derived by substituting in the Ampere law for the current density,

$$\frac{LB}{\tau} \sim \frac{1}{n_e e} \frac{1}{\mu_0} \frac{B^2}{L} + \frac{m_e}{n_e e^2} \frac{B}{\mu_0 \tau L} + \frac{m_e \nu_{EI}}{n_e e^2} \frac{1}{\mu_0} \frac{B}{L} \quad (2.72)$$

Substituting out μ_0 in favor of ϵ_0 via the Weber relation (equation 2.7) in all but the last term, and introducing the plasma and cyclotron frequencies ($\omega_p^2 = n_e e^2 / m_e \epsilon_0$ and $\omega_c = eB / m_e$), we have

$$\frac{LB}{\tau} \sim \frac{m_e \epsilon_0 c^2}{n_e e^2} \frac{e B^2}{m_e} + \frac{m_e \epsilon_0 c^2}{n_e e^2} \frac{B}{\tau L} + \frac{m_e \nu_{EI}}{n_e e^2 \mu_0} \frac{B}{L} \quad (2.73)$$

$$L^2 \sim \frac{c^2}{\omega_p^2} \omega_c \tau + \frac{c^2}{\omega_p^2} + \frac{1}{\mu_0 \sigma} \quad (2.74)$$

where we have introduced the substitution $\sigma = n_e e^2 / m_e \nu_{EI}$. Recall that the term c/ω_p is referred to as the *skin depth* of the plasma, and has units of length. The scaling requirements are now exposed in order to neglect different terms in the generalized Ohm's law. Comparing the left-hand side of equation 2.70 to each term on the right, we can make the following conclusions:

- Comparison of the characteristic length scale and product of the skin depth and cyclotron frequency,

$$\frac{L^2}{\tau} \sim \frac{c^2}{\omega_p^2} \omega_c \quad (2.75)$$

determines if the Hall term is negligible. This corresponds to a physical situation where the length scale of variation is greater than the skin depth, and the time scale of variation is greater than the

cyclotron frequency. Note that this implies that the Hall term is constrained by both length *and* time scales.

- A comparison of the length scale and skin depth for the inertia term,

$$L^2 \sim \frac{c^2}{\omega_p^2} \quad (2.76)$$

indicates that if the length scale of variation is much larger than the skin depth, then the inertial term is insignificant. Conversely, the inertia term must be considered when a large gradient occurs on the order of the skin depth in the plasma.

- The resistive term scales as the characteristic speed,

$$\frac{L}{\tau} \sim U \sim \frac{1}{\mu_0 \sigma L} \quad (2.77)$$

where $\sigma = n_e e^2 / m_e \nu_{EI}$ is defined to be the *scalar electrical conductivity* in the single-fluid model. A fascinating analogy follows from equation 2.77. Suppose that, for a moment, we introduce a substitution, $\nu = 1/\mu_0 \sigma$. Then the scale of interest governing the last term in equation 2.70 is

$$\frac{UL}{\nu} \quad (2.78)$$

which looks identical in form to the Reynolds number in classical fluid dynamics. Thus, this ‘viscous ratio’ represents a scaling of the inertia terms to the *magnetic diffusivity*, ν . This quantity is in fact named the *magnetic Reynolds number*, denoted Re_m ,

$$Re_m = \mu_0 \sigma UL \quad (2.79)$$

and, just as the Reynolds number does for classical fluid theory, the magnetic Reynolds number represents a ratio of the advective and diffusive limits of the equation. In the case that the electrical conductivity is high, the advective behavior dominates and the diffusion can be neglected. In the opposite case, the magnetic diffusion dominates over the advective nature.

2.6 Magnetohydrodynamic Description

At length, we have derived equations for the two-fluid description, and we simplified the system to a single-fluid system by assuming the electron mass was negligible. This led to a second, simpler system that consists of the coupled Navier-Stokes and full Maxwell equations after neglecting the electron inertia. The current must now be fashioned by Ohm’s law, and a convective component can be added if a net charge density is present in the plasma. This system can still support charge separation effects, electromagnetic wave propagation and higher-frequency behavior, even if it does not capture as many frequencies as the two-

fluid model. Furthermore, the Hall effect can be added to Ohm's law if the cyclotron frequencies become significant. We can further simplify the single-fluid system to the typical magnetohydrodynamic model by making additional assumptions in the Maxwell equations.

The MHD theory is founded on two principle assumptions:

- The plasma is *quasineutral*, so that there is no net charge density anywhere
- The displacement current term is negligible

The first assumption here requires that $\varrho_e = 0$ everywhere in the plasma. The definition of a plasma is usually posed with this assumption in mind, when the assertion that the characteristic length scale is much larger than a Debye length, $L \gg \lambda_D$, is made. Quasineutrality leads to some significant results. First, recall that the electric body force term acting on the fluid is $\varrho_e \mathbf{E}$; if the plasma is quasineutral, then we expect the electric body force term to be very small. This does not restrict us from including an applied electric field, but an applied field may only affect the current in this model, and cannot directly induce a body force on the plasma anymore.

A second result of quasineutrality is that it changes the nature of the continuity equation of charge, equation 2.12. If $\varrho_e = 0$, then

$$\frac{\partial \varrho_e}{\partial t} + \nabla \cdot \mathbf{j}_e = 0 \quad \rightarrow \quad \nabla \cdot \mathbf{j}_e = 0 \quad (2.80)$$

So a quasineutral plasma can only possess a solenoidal current density. Physically, we may interpret this statement as an indication that the rearrangement of charge in the plasma occurs on a time scale much faster than the smallest time scale of significance. Since the motion of the electrons is characterized by the plasma frequency, ω_p , then this assumption can be valid for cases where the plasma frequency is significantly larger than the largest frequency of interest.

The second assumption typically invokes a scale analysis to neglect the displacement current term in the Ampere-Maxwell equation. Let us assume the current is given by Ohm's law, with negligible Hall effect and inertia terms. Then $\mathbf{j}_e = \sigma \mathbf{E} + \sigma \mathbf{u} \times \mathbf{B} \sim E + UB$, and let the electric field scale according to the moving-frame transformation, $E \sim UB$, which means that the scale of the current is just $\mathbf{j}_e \sim UB$ (we omit the factor of two). The Ampere-Maxwell equation, equation 2.11, can be shown to scale as [15]

$$\mu_0 \sigma UB \sim \frac{1}{c^2} \frac{E}{\tau} + \frac{B}{L} \quad (2.81)$$

$$\mu_0 \sigma ULB \sim \frac{U}{c^2} \frac{L}{\tau} B + B \quad (2.82)$$

$$Re_m \sim \mu_0 \sigma UL \sim \frac{U^2}{c^2} + 1 \quad (2.83)$$

Thus, the curl of the magnetic field will contribute a factor approximately on the order of the magnetic Reynolds number, while the displacement current term will contribute a factor of U^2/c^2 to correct this. To construct a numerical example, let's suppose we are examining a plasma propulsion system capable of

producing an extremely large specific impulse of 10,000s. That roughly corresponds to an exhaust velocity of $\sim 100,000\text{m/s}$. The scales for the terms of the Ampere law reveal that the displacement current term will offer a contribution on the order of 0.00001% of the curl term. Thus, we could simply discard the displacement current, which would give us the Ampere law in its pre-Maxwell form,

$$\mu_0 \mathbf{j}_e = \nabla \times \mathbf{B} \quad (2.84)$$

This scale analysis is almost always the justification made for neglecting the displacement current. However, cases can arise where the displacement current is not negligible. Of particular importance are cases where the mathematical nature of the electromagnetics is sacrificed by this approximation. As a counterexample, let us recite Feynman's example [106] of a case where the displacement current is critical to resolving the behavior of the magnetic field.

Consider a spherically symmetric radial distribution of current, as shown in Figure 2.1. Some source of current is at the center of this distribution. We want to calculate the magnetic field, \mathbf{B} , produced by the currents in this situation. The current can be calculated via the charge continuity equation,

$$\frac{\partial Q(R)}{\partial t} = -4\pi r^2 j(R) \quad (2.85)$$

where $Q(R)$ is the charge enclosed in a sphere of radius R . Now, we turn our attention to the magnetic field. We start by drawing an Amperian loop, denoted Γ , on some surface of radius R in Figure 2.1, and use the right-hand rule to determine the direction of the magnetic field.

However, we are already at an impasse. A different choice of the Amperian loop Γ would give us a different magnetic field. This is confusing, since the current distribution is spherically symmetric, but yet it seems that the magnetic field depends on the direction. However, it quickly becomes absurd – we can choose yet a different Amperian loop that tells us that the magnetic field should be in exactly the *opposite* direction as the first loop gave. So how can there be *any* circulation of the magnetic field around the currents at all?

This problem is completely solved by the displacement current term. We are reminded that the circulation of \mathbf{B} depends not only on the total current through the Amperian loop Γ , but also on the time rate of change of the electric flux through it (the displacement current). The electric field is radial, and at radius R is

$$E_R = \frac{1}{4\pi\epsilon_0} \frac{Q(R)}{r^2} \quad (2.86)$$

The time rate of change of this field is

$$\frac{\partial E}{\partial t} = \frac{1}{4\pi\epsilon_0 r^2} \frac{\partial Q(R)}{\partial t} \quad (2.87)$$

By substitution of equation 2.85 for the current and equation 2.87 for the displacement current, Ampere's

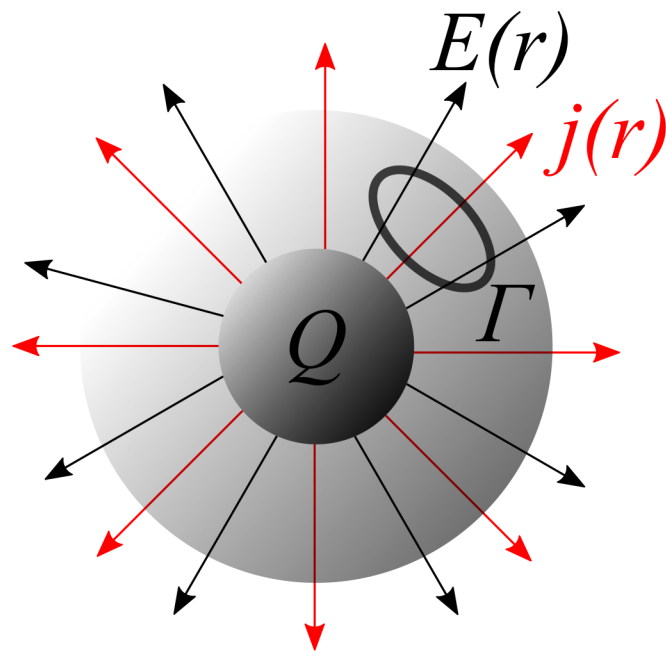


Figure 2.1: A diagram of Feynman's example of displacement current [106]. Spherically symmetric radial distribution of current and electric field. What is the magnetic field around an Amperian loop?

law is

$$c^2 \nabla \times \mathbf{B} = \frac{\mathbf{j}}{\epsilon_0} + \frac{\partial \mathbf{E}}{\partial t} = -\frac{1}{4\pi\epsilon_0 r^2} \frac{\partial Q(R)}{\partial t} + \frac{1}{4\pi\epsilon_0 r^2} \frac{\partial Q(R)}{\partial t} = 0 \quad (2.88)$$

i.e., the contributions from the real and displacement currents *exactly cancel*. With an additional boundary condition, we can easily show that this proves that the magnetic field is in fact zero everywhere on the surface of the sphere, which solves the directional problem associated with the construction of our Amperian loop.

Feynman's example makes it clear that we cannot always dispense with displacement current, even when the magnitude is small; there are cases where the nature of the equations change form with its disappearance. Furthermore, the charge continuity equation is only exactly satisfied when the displacement current is taken into account. The applications outlined in the introduction represent several problems where we cannot neglect this term, even for engineering problems. Particularly poignant are examples such as that given in [59], during the initial transient startup of a pulsed plasma thruster. Because the thruster operates principally using a capacitive discharge across a forming arc plasma, there is a strong appearance of charge in the plasma, and a displacement current occurs in the surrounding vacuum regions to complete the circuit.

Another approach that reveals the full behavior of the magnetic field and shows clearly how the MHD theory treats the displacement current is to consider again the derivation of the wave equation for the magnetic field, equation 2.13. When we showed this result, we mentioned that it was valid when no charge or current was present (the medium is vacuum). If we instead retain a net current density, we arrive at a more general equation,

$$\frac{\partial^2 \mathbf{B}}{\partial t^2} - c_0^2 \nabla^2 \mathbf{B} = -\frac{1}{\epsilon_0} \nabla \times \mathbf{j}_e \quad (2.89)$$

Here, the presence of current density acts to dampen the wave behavior of the magnetic field. For simplicity, assume Ohm's law here may be written as $\mathbf{j}_e \sim \sigma \mathbf{E}$, where σ is the plasma electrical conductivity. Substitution into the right-hand side and application of Faraday's law to exchange $\nabla \times \mathbf{E}$ for $-\partial \mathbf{B} / \partial t$ gives us

$$\frac{1}{c_0^2} \frac{\partial^2 \mathbf{B}}{\partial t^2} + \mu_0 \sigma \frac{\partial \mathbf{B}}{\partial t} - \nabla^2 \mathbf{B} = 0 \quad (2.90)$$

Equation 2.90 is the celebrated telegrapher's equation for the magnetic field [5]. As presented in Section 1.3, if we ignore the spatial behavior temporarily, two limits of the temporal evolution of the magnetic field become clear. In the first case, the conductivity could be very large, and in the limit that $\sigma \rightarrow \infty$, the second term dominates the first term,

$$\mu_0 \sigma \frac{\partial \mathbf{B}}{\partial t} \gg \frac{1}{c_0^2} \frac{\partial^2 \mathbf{B}}{\partial t^2} \quad (2.91)$$

This is identical to the case of the magnetic Reynolds number being very large. In this case, we may neglect

the displacement current, and we are left with a *diffusion equation* for the magnetic field,

$$\frac{\partial \mathbf{B}}{\partial t} - \frac{1}{\mu_0 \sigma} \nabla^2 \mathbf{B} = 0 \quad (2.92)$$

This is the essential result enforced by the assumption that the displacement current is negligible. It is only applicable when equation 2.91 is true. In the converse limit, if the conductivity is very small, we could have

$$\mu_0 \sigma \frac{\partial \mathbf{B}}{\partial t} \ll \frac{1}{c_0^2} \frac{\partial^2 \mathbf{B}}{\partial t^2} \quad (2.93)$$

In which case the damping term is negligible, and we are rewarded with a pure wave in the magnetic field,

$$\frac{1}{c_0^2} \frac{\partial^2 \mathbf{B}}{\partial t^2} - \nabla^2 \mathbf{B} = -\square^2 \mathbf{B} = 0 \quad (2.94)$$

This is a well-known result for vacuum, where the conductivity is classically zero. We could further have an intermediate case, where the two terms are on order to one another,

$$\mu_0 \sigma \frac{\partial \mathbf{B}}{\partial t} \sim \frac{1}{c_0^2} \frac{\partial^2 \mathbf{B}}{\partial t^2} \quad (2.95)$$

In this case, the equation is still hyperbolic, but the damping term cannot be neglected. This corresponds to the physical case of mixed wave and diffusion behavior occuring the magnetic field.

The MHD theory is again only applicable in the limit when equation 2.91 is realized. If this is true, the magnetic field approaches its diffusive limit, and the wave nature of the field is small enough to be ignored. However, in general, the behavior of the magnetic field is truly hyperbolic, and it is only in the case of a large conductivity that we may apply the MHD model.

If we neglect the displacement current and proceed with the pre-Maxwell form of the Ampere law ($\nabla \times \mathbf{B} = \mu_0 \mathbf{j}_e$), we have effectively removed the speed of light from Maxwell's equations, and the Ampere-Maxwell equation is no longer hyperbolic, but parabolic. This assumption is called the *magnetic diffusion approximation*, and is one of the fundamental tenets of the MHD theory. Equation 2.84 fashions an equation for the current density that may be substituted into the Lorentz force expression in equation 2.65,

$$\frac{\partial}{\partial t} (\varrho \mathbf{u}) + \nabla \cdot (\varrho \mathbf{u} \mathbf{u} + \hat{\mathbf{l}} p) = (\nabla \times \mathbf{B}) \times \mathbf{B} \quad (2.96)$$

An equation for the evolution of the the magnetic field itself can be found by substituting the generalized Ohm's law into Faraday's law, equation 2.10, to eliminate the electric field. Continuing to use our simplified

form of the Ohm's law, $\mathbf{j}_e = \sigma \mathbf{E} + \sigma \mathbf{u} \times \mathbf{B}$, this yields

$$\frac{\partial \mathbf{B}}{\partial t} + \nabla \times \left\{ \frac{\mathbf{j}_e - \sigma \mathbf{u} \times \mathbf{B}}{\sigma} \right\} = 0 \quad (2.97)$$

$$\frac{\partial \mathbf{B}}{\partial t} - \nabla \times (\mathbf{u} \times \mathbf{B}) + \frac{1}{\sigma} \nabla \times \mathbf{j}_e = 0 \quad (2.98)$$

and substituting equation 2.84 in for the current in equation 2.98,

$$\frac{\partial \mathbf{B}}{\partial t} - \nabla \times (\mathbf{u} \times \mathbf{B}) + \frac{1}{\sigma \mu_0} \nabla \times (\nabla \times \mathbf{B}) = 0 \quad (2.99)$$

Applying the vector identity $\nabla \times \nabla \times \mathbf{B} = \nabla (\nabla \cdot \mathbf{B}) - \nabla^2 \mathbf{B} = -\nabla^2 \mathbf{B}$, this can be simplified to

$$\frac{\partial \mathbf{B}}{\partial t} - \nabla \times (\mathbf{u} \times \mathbf{B}) + \frac{1}{\sigma \mu_0} \nabla^2 \mathbf{B} = 0 \quad (2.100)$$

If this equation were nondimensionalized, the magnetic diffusivity appearing in front of the diffusion term $\nabla^2 \mathbf{B}$ would become the magnetic Reynolds number, Re_m . Here we finally see the meaning of the magnetic Reynolds number in terms of the limiting cases for the magnetic field; if $Re_m \rightarrow \infty$ is assumed (leading to *ideal* magnetohydrodynamics), then the advective term $\nabla \times (\mathbf{u} \times \mathbf{B})$ is dominant, and the diffusion of the magnetic field is negligible. However, if the magnetic Reynolds number is finite (a more difficult model called the *resistive* magnetohydrodynamic model), the magnetic field behaves in a diffusive fashion, with competing processes of advection and diffusion evolving the field. Finally, if the magnetic Reynolds number tends to zero, then the advective processes dominate over the diffusion, and the equation once again becomes first-order.

2.7 Summary of Models

Collecting our results in this chapter, we present the basic plasma models of interest. The full two-fluid plasmadynamic equations are shown in Table 2.2. Here, we again stress that α represents the species; in the case of the usual two-fluid model, this often consists of hydrogenic ions and electrons, $\alpha \in \{e, i\}$. If N_s represents the number of species, then we have $5N_s + 8$ equations, plus additional constitutive relations employed to close the system. These equations represent the statistical average of the bulk motion in the plasma from the kinetic model. In Table 2.3, we show the full system of the single-fluid model; this model assumes that the electron inertia is negligible in the two-fluid model, and formulates a different constitutive relation (Ohm's law) for the current density. Finally, the reduction of the Maxwell equations to a diffusive approximation by discarding the displacement current and insisting on electrical quasineutrality yields the usual magnetohydrodynamic approximation. The MHD equations may either be resistive or ideal, depending on if the conductivity is taken to be finite or infinite, respectively. The resistive and ideal MHD equations are presented for comparison purposes in Tables 2.4 and 2.5, respectively. Our investigations for the remainder

Table 2.2: Two-fluid plasmadynamic equations.

Fluid equations ($\alpha \in \{e, i, \dots\}$):	
$\frac{\partial \varrho_\alpha}{\partial t} + \nabla \cdot (\varrho_\alpha \mathbf{u}_\alpha) = 0$	(2.101)
$\frac{\partial}{\partial t} (\varrho_\alpha \mathbf{u}_\alpha) + \nabla \cdot (\varrho_\alpha \mathbf{u}_\alpha \mathbf{u}_\alpha + \hat{\mathbf{l}} p_\alpha) = \varrho_{e,\alpha} \mathbf{E} + \mathbf{j}_\alpha \times \mathbf{B}$	(2.102)
$\frac{\partial \mathcal{E}_\alpha}{\partial t} + \nabla \cdot ([\mathcal{E}_\alpha + p_\alpha] \mathbf{u}_\alpha) = \mathbf{j}_\alpha \cdot \mathbf{E}$	(2.103)
Maxwell equations:	
$\frac{\partial \mathbf{B}}{\partial t} + \nabla \times \mathbf{E} = 0$	(2.104)
$\frac{1}{c_0^2} \frac{\partial \mathbf{E}}{\partial t} + \mu_0 \mathbf{j}_e = \nabla \times \mathbf{B}$	(2.105)
Constraints:	
$\nabla \cdot \mathbf{E} = \varrho_e / \epsilon_0$	(2.106)
$\nabla \cdot \mathbf{B} = 0$	(2.107)
Total charge and current:	
$\varrho_e = \sum_\alpha \varrho_\alpha = \sum_\alpha \frac{e_\alpha}{m_\alpha} \varrho_\alpha$	(2.108)
$\mathbf{j}_e = \sum_\alpha \mathbf{j}_\alpha = \sum_\alpha \frac{e_\alpha}{m_\alpha} \varrho_\alpha \mathbf{u}_\alpha$	(2.109)
Equation of state:	
Perfect gas,	$p_\alpha = \varrho_\alpha R_\alpha T_\alpha$
Calorically perfect gas,	$\mathcal{E}_\alpha = \frac{p_\alpha}{\gamma - 1} + \frac{1}{2} \varrho_\alpha \mathbf{u}_\alpha \cdot \mathbf{u}_\alpha$
Approximations used:	
Strongly collisional,	$\lambda_{\text{mfp}} \ll L$
Nonrelativistic,	$u \ll c_0$

of this dissertation will pursue the solution of the single-fluid and two-fluid plasma models retaining the full Maxwell equations, as presented in Tables 2.3 and 2.2, respectively.

Table 2.3: Single-fluid plasmadynamic equations, including full Maxwell equations.

Fluid equations:	
$\frac{\partial \varrho}{\partial t} + \nabla \cdot (\varrho \mathbf{u}) = 0$	(2.110)
$\frac{\partial}{\partial t} (\varrho \mathbf{u}) + \nabla \cdot (\varrho \mathbf{u} \mathbf{u} + \hat{\mathbf{l}} p) = \varrho_e \mathbf{E} + \mathbf{j} \times \mathbf{B}$	(2.111)
$\frac{\partial \mathcal{E}}{\partial t} + \nabla \cdot ([\mathcal{E} + p] \mathbf{u}) = \mathbf{j} \cdot \mathbf{E}$	(2.112)
Maxwell's equations:	
$\frac{\partial \mathbf{B}}{\partial t} + \nabla \times \mathbf{E} = 0$	(2.113)
$\frac{1}{c_0^2} \frac{\partial \mathbf{E}}{\partial t} + \mu_0 \mathbf{j}_e = \nabla \times \mathbf{B}$	(2.114)
Constraints:	
$\nabla \cdot \mathbf{E} = \varrho_e / \epsilon_0$	(2.115)
$\nabla \cdot \mathbf{B} = 0$	(2.116)
Total charge and current density:	
$\frac{\partial \varrho_e}{\partial t} + \nabla \cdot \mathbf{j}_e = 0$	(2.117)
$\mathbf{j}_e = \sigma \cdot \mathbf{E} + \sigma \mathbf{u} \times \mathbf{B} + \varrho_e \mathbf{u}$	(2.118)
Equation of state:	
Perfect gas,	$p = \varrho R_{gas} T$
Calorically perfect gas,	$\mathcal{E} = \frac{p}{\gamma - 1} + \frac{1}{2} \varrho \mathbf{u} \cdot \mathbf{u}$
Approximations used:	
Strongly collisional,	$\lambda_{mfp} \ll L$
Nonrelativistic,	$u \ll c_0$
Small Larmor radius,	$r_L \ll L$
Scalar plasma conductivity,	$ \omega_c \ll \nu$

Table 2.4: Resistive magnetohydrodynamic (MHD) equations. [16]

Fluid equations:	
$\frac{\partial \varrho}{\partial t} + \nabla \cdot (\varrho \mathbf{u}) = 0$	(2.119)
$\frac{\partial}{\partial t} (\varrho \mathbf{u}) + \nabla \cdot (\varrho \mathbf{u} \mathbf{u} + \hat{\mathbf{p}} p) = (\nabla \times \mathbf{B}) \times \mathbf{B}$	(2.120)
$\frac{\partial \mathcal{E}}{\partial t} + ([\mathcal{E} + p] \mathbf{u}) = \frac{(\nabla \times \mathbf{B})^2}{\mu_0^2 \sigma}$	(2.121)
Magnetic diffusion:	
$\frac{\partial \mathbf{B}}{\partial t} = \nabla \times (\mathbf{u} \times \mathbf{B}) - \frac{1}{\sigma \mu_0} \nabla^2 \mathbf{B}$	(2.122)
Current density:	
$\mathbf{j}_e = \sigma \mathbf{E} + \sigma \mathbf{u} \times \mathbf{B}$	(2.123)
Constraints:	
$\nabla \cdot \mathbf{B} = 0$	(2.124)
Equation of state:	
Perfect gas,	$p = \varrho R_{gas} T$
Calorically perfect gas,	$\mathcal{E} = \frac{p}{\gamma - 1} + \frac{1}{2} \varrho \mathbf{u} \cdot \mathbf{u}$
Approximations used:	
Strongly collisional,	$\lambda_{mfp} \ll L$
Nonrelativistic,	$u \ll c_0$
Quasineutrality,	$\lambda_D \ll L$
Small Larmor radius,	$r_L \ll L$
Scalar plasma conductivity,	$ \omega_c \ll \nu$

Table 2.5: Ideal magnetohydrodynamic (MHD) equations. [16]

Fluid equations:	
$\frac{\partial \varrho}{\partial t} + \nabla \cdot (\varrho \mathbf{u}) = 0$	(2.125)
$\frac{\partial}{\partial t} (\varrho \mathbf{u}) + \nabla \cdot (\varrho \mathbf{u} \mathbf{u} + \hat{\mathbf{l}} p) = (\nabla \times \mathbf{B}) \times \mathbf{B}$	(2.126)
$\frac{\partial \mathcal{E}}{\partial t} + ([\mathcal{E} + p] \mathbf{u}) = \frac{(\nabla \times \mathbf{B})^2}{\mu_0^2 \sigma}$	(2.127)
Magnetic field advection:	
$\frac{\partial \mathbf{B}}{\partial t} - \nabla \times (\mathbf{u} \times \mathbf{B}) = 0$	(2.128)
Current density:	
$\mathbf{j}_e = \sigma \mathbf{E} + \sigma \mathbf{u} \times \mathbf{B}$	(2.129)
Constraints:	
$\nabla \cdot \mathbf{B} = 0$	(2.130)
Equation of state:	
Perfect gas,	$p = \varrho R_{gas} T$
Calorically perfect gas,	$\mathcal{E} = \frac{p}{\gamma - 1} + \frac{1}{2} \varrho \mathbf{u} \cdot \mathbf{u}$
Approximations used:	
Strongly collisional,	$\lambda_{mfp} \ll L$
Nonrelativistic,	$u \ll c_0$
Quasineutrality,	$\lambda_D \ll L$
Small Larmor radius,	$r_L \ll L$
Scalar plasma conductivity,	$ \omega_c \ll \nu$
Large magnetic Reynolds number,	$Re_m \rightarrow \infty$

Chapter 3

An Isomorphism Between Two-fluid Plasmas and Classical Electrodynamics

“Just a heads up. We’re gonna have a superconductor turned up full blast and pointed at you for the duration of this next test. I’ll be honest, we’re throwing science at the walls here to see what sticks. No idea what it’ll do.”

Cave Johnson [1]

3.1 Motivation and State of the Art

Our initial investigation examines an analytical approach to modeling two-fluid plasmas. The approach taken here is to construct an isomorphism between the equations for each species and another, well-understood system of equations (in our case, the Maxwell equations). Then the theorems and techniques of classical electrodynamics can be shown to hold with equal mathematical validity for the two-fluid equations.

Although the remarkable mathematical similarity that often exists between two completely separate physical theories has undergone many names, we have borrowed the language of Towne [107] to call such a relationship an *isomorphism*. The essential utility in constructing such a relationship is that the theorems and techniques of one well-developed physical theory may be enjoyed by another. Careful attention must be paid to the construction of these analogies, since certain conditions can often damage the nature of this relationship.

A student of physics commonly confronts examples of the utility in drawing these connections between different fields of study. A straightforward example is the mathematical analogy that is evident in a discussion

of linear and angular kinematics. After one understands linear kinematics, it becomes obvious that angular kinematics proceeds in the same fashion, only with angular quantities transplanting the linear quantities. Although this is born out of a genuine physical connection between the two fields, this need not be the case. The study of electrical circuits and signals is often introduced through analogy, appealing to the idea that a voltage difference is analogous to a pressure difference or temperature difference. In the study of ideal flow, a Poisson equation for a velocity potential is presented, which forms an identical mathematical framework as electrostatics. As Towne points out [107], the formulation of these analogies is not unique between different fields. For example, one may take the form of the continuity equation for an incompressible flow, $\nabla \cdot \mathbf{u} = 0$, and the Gauss law for the magnetic field, $\nabla \cdot \mathbf{B} = 0$, as the basis for forming an analogy between fluid dynamics and electrodynamics. However, as has been observed previously [108–110] and is used as a basis for our development, we could equally take the Coulomb gauge, $\nabla \cdot \mathbf{A} = 0$, to be analogous to the form of the continuity equation for incompressible flow. It is only necessary that the construction of the isomorphism identify fields that behave in an analogous mathematical fashion; with sufficient manipulation, this should reveal an identical set of equations for both systems.

The similarity between fluid dynamics and classical electrodynamics has long been recognized. Whittaker [111], Spiegel [112], Wise [113] and Nersessian [114] all provide fascinating accounts of its important role in the infancy of classical electrodynamics. Faraday’s suggestion of a connection between the magnetic induction vector with the velocity of an incompressible fluid impressed Maxwell during his earlier endeavors to establish a theory of electromagnetism. Maxwell himself realized the value of this connection, as he wrote in 1855 [4] that “of the laws of elastic solids, and of the motions of viscous fluids, I hope to discover a method of forming a mechanical conception of this electrotonic state adapted to general reasoning.” Helmholtz’s work [115] on vortex motion strengthened this analogy between magnetism and the incompressible fluid, whereby many theorems of hydrodynamics were correlated to electromagnetism. With such an intimate place in the early development of classical electrodynamics, it is somewhat remarkable that the equations describing the behavior of electric and magnetic fields were not written directly as fluid equations.

More recently, the converse recognition of this analogy has been exploited to rewrite the equations of motion for a fluid into the form of Maxwell’s equations. During the 1960’s, work produced a set of Maxwell equations for specific fluid problems in which a set of analogous field equations were solved in lieu of the fluid equations [116, 117]. More recently, Marmanis [108, 109] provided a novel reformulation of the Navier-Stokes equations into a set of Maxwell equations that were exploited to study turbulent flow. The work identified the notion of fluid charge and current, for which some empirical model must be known in order for the incompressible Maxwell equations to be solved. This concept of a fluid set of Maxwell equations was generalized by Kambe [110] to compressible flow.

Presently, only one approach in the literature seems to have attempted to extend this idea to the two-fluid plasma framework, in addition to the author’s work [118–120]; this is work of Mahajan [121], followed by later work by Mahajan, et al. [122–124], who have shown that the two-fluid equations may be rewritten

in a compact form as a set of unified Maxwell equations. However, the work seems to only identify the homogeneous Maxwell equations (the inhomogeneous equations are not mentioned [121]), and a different resulting system of equations is arrived at and solved for specific cases. This differs from the present work since we consider a full isomorphism in which both homogeneous and inhomogeneous equations are constructed. The difference in these approaches can be seen in the Chapter 4, where some different solution approaches are considered in light of the presence of the new source terms.

It will be seen that the inclusion of the inhomogeneous equations substantially reposes the problem. The notion of generalized charge and current density will need to be addressed, and the process whereby this issue is dealt with changes the nature of how the isomorphism may be exploited. A further advantage of extending the isomorphism for the two-fluid plasma system is that it unites the efforts of Marmanis [108, 109], Kambe [110] and Mahajan [121] into a common framework wherein the subtle differences of definitions are revealed. Others have sought to explicate a physical meaning from the relationship between the fluid equations and electrodynamics [125]; this is also connected to the ramifications that we will shortly see in Section 3.5.

It is known that the generalized vorticity of a plasma is an important quantity. The generalized vorticity and canonical momentum can be used to formulate the *self-helicity* of the plasma, a generalization of the magnetic helicity from magnetohydrodynamics, which is a rugged invariant of the plasma [80, 81]. The generalized vorticity and self-helicity offer a different description of the plasma in which the evolution to equilibrium states can be determined by a set of evolution equations [78–81, 126]. The isomorphism presented here thus directly connects to the active work in formulating an analytical framework that describes the generalized behavior of the plasma without resorting to just describing the primitive variables. This could also provide an alternate variational description of the plasma in its generalized quantities, since these approaches could be used to construct means of calculation of the plasma evolution [127].

Another vein of literature that should be mentioned in connection with this work is the Lighthill analogy [128, 129]. This work was introduced in 1952 by Lighthill [128], addressing the problem of noise generation in fluid dynamics; the resulting approach proposed by Lighthill birthed the field of aeroacoustics. In this approach, the fluid dynamic equations are rearranged into the form of an inhomogeneous wave equation with a quadrupole source term. If the velocity field can be solved, or is already known, then the source term is explicitly given. The inhomogeneous wave equation may then be solved for the acoustic field induced by the source. This has led to numerical simulation approaches [130–133] wherein the fluid dynamic behavior is calculated first for the velocity field, the source term is then considered to be fully known, and the far-field acoustic radiation is calculated given the source term. This approach has shown great success in quantitatively predicting acoustic noise generated by aerodynamic flows. Although the application is entirely different and the approach is slightly different, the core notion that the rearrangement of a set of equations can reveal a different approach to solving the problem is common to the approach taken here.

3.2 Objective

Our objective in this chapter is to formulate a set of Maxwell equations for new generalized fields that determine the combined electrodynamic and hydrodynamic behavior of the plasma. The formulation of the equations is described; the details of the derivation are lengthy, and are deferred to Appendix A.1. After the identification of the new isomorphic Maxwell equations and the new *generalized* fields for a two-fluid plasma, we explore some of the immediate consequences. Particularly, the recognition of a vector and scalar potential form may be realized, with analogies between gauge transformations and the continuity equation. We also briefly examine the concept of a Lagrangian function being constructed using the isomorphism.

One of the more interesting elements of the new equations is the concept of the source terms, which are analogues to the charge and current densities of classical electrodynamics. The analytical form of the source terms as functions of the primitive variables is easy to determine, which reveals the generation mechanisms of the generalized fields. Due to the nature of Maxwell's equations, we must possess some knowledge of these source terms to solve the system for the fields. A large part of our investigation addresses the treatment of the source term. The simplest approach is to consider the homogeneous case in which the source terms vanish, which may be solved in a straightforward manner.

In the case of an inhomogeneous plasma where sources are nonzero, however, some other approach must be used and the problem is nontrivial. Two approaches were considered in this investigation; first, the idea of *iteratively* calculating the source terms and fields was scrutinized. This would give rise to an algorithm similar to that used in particle-in-cell simulations to calculate the sources first, solve for the fields, and update the sources. However, some major limitations were encountered that makes this approach unrealistic. Second, the idea of *empirically* modeling the source terms was considered. This approach leads to solution techniques that are successful, given some empirical form of the source terms for the problem at hand. It is proposed that the source terms for simple problems be collected and formed into a library, similar to previous approaches exploring isomorphic systems in fluid dynamics. More difficult problems could then be posed using an understanding of the simpler source models as building blocks.

As an illustration of the empirical modeling approach, three classic fluid problems are reconsidered: the case of Couette flow, duct flow, and Blasius boundary layer flow. Although these problems are simple, they permit analytical models for the source terms to be constructed, and the solution approaches of using reconstructive techniques and classic electrostatic methods such as Green's functions or method of images can be applied and demonstrated to work correctly. Furthermore, they appear ubiquitously in fluids and plasmas, and hence are prime candidates for simple empirical models that may be applied to predict more difficult problems. Unfortunately, more complicated problems require an excessive analysis to discover an analytical model for the source terms, so we also illustrate the approach of using numerical simulation and

postprocessing to qualitatively demonstrate some key features of the source terms for compressible fluids and plasmas.

3.3 An Isomorphism Between Multifluid Plasmas and Maxwell's Equations

To construct our analogy, we begin by considering the equations for an isentropic plasma¹,

$$\frac{D_\alpha \varrho_\alpha}{Dt} + \varrho_\alpha \nabla \cdot \mathbf{u}_\alpha = 0 \quad (3.1)$$

$$\varrho_\alpha \frac{D_\alpha \mathbf{u}_\alpha}{Dt} = -\nabla p_\alpha + \frac{e_\alpha}{m_\alpha} \varrho_\alpha \{ \mathbf{E} + \mathbf{u}_\alpha \times \mathbf{B} \} \quad (3.2)$$

Equation 3.1 and 3.2 are just the species continuity and species momentum equations for each species α , respectively. By our isentropic assumption, the following thermodynamic relations hold,

$$T_\alpha ds_\alpha = 0 = dh_\alpha - dp_\alpha / \varrho_\alpha \quad (3.3)$$

$$dh_\alpha = \frac{dp_\alpha}{\varrho_\alpha} = \frac{1}{\varrho_\alpha} \frac{dp_\alpha}{d\varrho_\alpha} d\varrho_\alpha = \frac{a_\alpha^2}{\varrho_\alpha} d\varrho_\alpha \quad (3.4)$$

where T_α is the species temperature, s_α is the species entropy, h_α is the species enthalpy, p_α is the species pressure, ϱ_α is the species mass density, and $a_\alpha = dp_\alpha/d\varrho_\alpha|_{s=\text{const}}$ is the species sonic speed. This allows us to rewrite equation 3.1 and 3.2 in favor of the species enthalpy h_α ,

$$\frac{\partial h_\alpha}{\partial t} + \mathbf{u}_\alpha \cdot \nabla h_\alpha + a_\alpha^2 \nabla \cdot \mathbf{u}_\alpha = \frac{D_\alpha h_\alpha}{Dt} + a_\alpha^2 \nabla \cdot \mathbf{u}_\alpha = 0 \quad (3.5)$$

$$\frac{\partial \mathbf{u}_\alpha}{\partial t} + \mathbf{u}_\alpha \cdot \nabla \mathbf{u}_\alpha = -\nabla h_\alpha + \frac{e_\alpha}{m_\alpha} \{ \mathbf{E} + \mathbf{u}_\alpha \times \mathbf{B} \} \quad (3.6)$$

We can introduce the vector and scalar potential fields into equation 3.6 if we apply equations 2.15 and 2.18,

$$\frac{\partial \mathbf{u}_\alpha}{\partial t} + \mathbf{u}_\alpha \cdot \nabla \mathbf{u}_\alpha = -\nabla h_\alpha + \frac{e_\alpha}{m_\alpha} \left\{ -\nabla \phi - \frac{\partial \mathbf{A}}{\partial t} + \mathbf{u}_\alpha \times (\nabla \times \mathbf{A}) \right\} \quad (3.7)$$

After some rearrangement, this becomes

$$\frac{\partial}{\partial t} \left\{ \mathbf{u}_\alpha + \frac{e_\alpha}{m_\alpha} \mathbf{A} \right\} + \mathbf{u}_\alpha \cdot \nabla \mathbf{u}_\alpha = -\nabla \left\{ h_\alpha + \frac{e_\alpha}{m_\alpha} \phi \right\} + \mathbf{u}_\alpha \times (\nabla \times \mathbf{A}) \quad (3.8)$$

¹viscous and entropic terms are gracefully handled in this formulation, as we have presented in [118, 119], but will not be discussed here. These additional terms will essentially add new contributions to the source terms of the equations. A starting point for seeing this is by taking the divergence of Crocco's equation, which provides a more general form of equation 3.29 below.

The advective term, $\mathbf{u}_\alpha \cdot \nabla \mathbf{u}_\alpha$, is known to be equivalently stated as a vector identity,

$$\mathbf{u}_\alpha \cdot \nabla \mathbf{u}_\alpha = \boldsymbol{\omega}_\alpha \times \mathbf{u}_\alpha + \nabla \left(\frac{1}{2} \mathbf{u}_\alpha \cdot \mathbf{u}_\alpha \right) \quad (3.9)$$

where $\boldsymbol{\omega}_\alpha = \nabla \times \mathbf{u}_\alpha$ is the fluid vorticity. The quantity $\boldsymbol{\omega}_\alpha \times \mathbf{u}_\alpha$ is the *Lamb vector*, a quantity that seems to receive relatively little attention despite its importance in understanding complicated flows. Substitution of this identity for the advective term and some manipulation allows equation 3.8 to be rewritten as

$$\frac{\partial}{\partial t} \left\{ \mathbf{u}_\alpha + \frac{e_\alpha}{m_\alpha} \mathbf{A} \right\} + \left\{ \boldsymbol{\omega}_\alpha + \frac{e_\alpha}{m_\alpha} \mathbf{B} \right\} \times \mathbf{u}_\alpha = -\nabla \left\{ h_\alpha + \frac{1}{2} \mathbf{u}_\alpha \cdot \mathbf{u}_\alpha + \frac{e_\alpha}{m_\alpha} \phi \right\} \quad (3.10)$$

We now introduce the following mass-specific definitions:

- The *species specific canonical momentum* is defined as

$$\mathbf{P}_\alpha = \mathbf{u}_\alpha + \frac{e_\alpha}{m_\alpha} \mathbf{A} \quad (3.11)$$

- The *generalized vorticity*, which is the curl of the canonical momentum, is defined as

$$\boldsymbol{\Omega}_\alpha = \nabla \times \mathbf{P}_\alpha = \nabla \times \left\{ \mathbf{u}_\alpha + \frac{e_\alpha}{m_\alpha} \mathbf{A} \right\} = \boldsymbol{\omega}_\alpha + \frac{e_\alpha}{m_\alpha} \mathbf{B} \quad (3.12)$$

- The *generalized Lamb vector* is defined as

$$\boldsymbol{\zeta}_\alpha = \boldsymbol{\Omega}_\alpha \times \mathbf{u}_\alpha = \left\{ \boldsymbol{\omega}_\alpha + \frac{e_\alpha}{m_\alpha} \mathbf{B} \right\} \times \mathbf{u}_\alpha \quad (3.13)$$

- The *specific total energy* is defined as

$$\mathcal{E}_\alpha^T = h_\alpha + \frac{1}{2} \mathbf{u}_\alpha \cdot \mathbf{u}_\alpha + \frac{e_\alpha}{m_\alpha} \phi = H_\alpha + \frac{e_\alpha}{m_\alpha} \phi \quad (3.14)$$

where $H_\alpha = h_\alpha + (1/2) \mathbf{u}_\alpha \cdot \mathbf{u}_\alpha$ is the *species stagnation enthalpy*.

Rewriting equation 3.10 in terms of these definitions, we are finally rewarded with a very compact result,

$$\frac{\partial \mathbf{P}_\alpha}{\partial t} + \boldsymbol{\zeta}_\alpha = -\nabla \mathcal{E}_\alpha^T \quad (3.15)$$

Equation 3.15 is identical to equation 8 in [80], except that a vector identity has been applied to break up the advective term. This relates the present work to considerations of evolution equations for the generalized invariants describing the plasma [80, 81].

In order to see an analogy emerge, we can first rewrite equation 3.15 by solving algebraically for the generalized Lamb vector, ζ_α ,

$$\zeta_\alpha = -\frac{\partial \mathbf{P}_\alpha}{\partial t} - \nabla \mathcal{E}_\alpha^T \quad (3.16)$$

This form is mathematically identical to equation 2.18, which defines a relationship between the electric field and the vector and scalar potentials of electrodynamics. Here, ζ_α can be perceived as an electric field, and \mathbf{P}_α and \mathcal{E}_α^T play the role of the vector and scalar potential. This analogy is further encouraged by the relationship between the generalized vorticity and the canonical momentum,

$$\Omega_\alpha = \nabla \times \mathbf{P}_\alpha \quad (3.17)$$

which is reflective of equation 2.15, the definition of the magnetic field in terms of the vector potential. Hence, we expect there to be a correspondence in the following form:

$$\zeta_\alpha \rightarrow \mathbf{E}, \quad \Omega_\alpha \rightarrow \mathbf{B}, \quad \mathbf{P} \rightarrow \mathbf{A}, \quad \mathcal{E}_\alpha^T \rightarrow \phi \quad (3.18)$$

In the analogy just realized, the quantities ζ_α and Ω_α play roles as electric and magnetic fields for the two-fluid plasma. We would therefore expect that a set of Maxwell equations could be derived to govern the behavior of these fields, which we will shortly show. However, there are some other interesting features about the idea of solving for these new dynamical quantities. Notice that since ζ_α was born from a vector identity concerning the nonlinear advective term, we are in part taking the nonlinear term now to be our unknown (there is still another contribution of the nonlinear term buried in the energy term \mathcal{E}_α^T , but we won't be solving for this quantity). In a sense, this means that the new Maxwell equations are (at least, explicitly) *linear*. Also, since the coupling between species is buried inside Ω_α (as the magnetic field, \mathbf{B}) and \mathbf{P}_α (as the vector potential, \mathbf{A}) and in the energy term, \mathcal{E}_α^T (as the scalar potential, ϕ), our system of equations will be *explicitly decoupled* between different species.

To derive the Maxwell equations, we consider the derivatives (divergence, curl and time derivative) of equation 3.15. The actual calculations are deferred to Appendix A.1, since they are tedious and involve repeated applications of vector identities and manipulation. The divergence and curl of equation 3.15 are straightforward, while the time derivative of equation 3.15 is much more complicated. However, these three calculations yield Gauss, Faraday and Ampere-Maxwell laws, respectively, for the generalized Lamb vector and generalized vorticity. To complete this set, we take the divergence of the vorticity (which must, by vector identity, be zero), $\nabla \cdot \Omega_\alpha = \nabla \cdot \nabla \times \mathbf{P}_\alpha$, as our final Gauss law. Collecting our results we have the

following equations,

$$\nabla \cdot \Omega_\alpha = 0 \quad (3.19)$$

$$\nabla \cdot \zeta_\alpha = \varrho_\alpha \quad (3.20)$$

$$\frac{\partial \Omega_\alpha}{\partial t} + \nabla \times \zeta_\alpha = 0 \quad (3.21)$$

$$\frac{\partial \zeta_\alpha}{\partial t} + \mathbf{j}_\alpha = a_\alpha^2 \nabla \times \boldsymbol{\omega}_\alpha + c_0^2 \nabla \times \left(\frac{e_\alpha}{m_\alpha} \mathbf{B} \right) \quad (3.22)$$

where we have introduced the substitutions

$$\varrho_\alpha = -\frac{\partial}{\partial t} (\nabla \cdot \mathbf{u}_\alpha) - \nabla^2 H_\alpha + \frac{e_\alpha}{m_\alpha} \frac{\varrho_e}{\epsilon_0} \quad (3.23)$$

$$\mathbf{j}_\alpha = \nabla \frac{\partial k_\alpha}{\partial t} + \left(\frac{\partial^2 \mathbf{u}_\alpha}{\partial t^2} - a_\alpha^2 \nabla^2 \mathbf{u}_\alpha \right) - \nabla (\mathbf{u}_\alpha \cdot \nabla h_\alpha) + \frac{e_\alpha}{m_\alpha} \frac{\mathbf{j}_e}{\epsilon_0} \quad (3.24)$$

where we have introduced the specific kinetic energy $k_\alpha = (1/2) \mathbf{u}_\alpha \cdot \mathbf{u}_\alpha$ and the stagnation enthalpy, $H_\alpha = h_\alpha + k_\alpha$. The quantities ϱ_α and \mathbf{j}_α are source terms to the equations 3.19 through 3.22. This system of equations is remarkably similar to the Maxwell equations, except for right-hand side of equation 3.22, where we have two components of the generalized vorticity, Ω_α , but they are weighted according to their separate wave speeds. In one sense, this is encouraging, since it verifies that the two distinct wave speeds remain intact through the derivation; however, it hinders our original goal of formulating an exact analogy to the Maxwell system. To proceed, we move the terms on the right-hand side of equation 3.22 to the left-hand side, and add the quantity $v_\alpha^2 \nabla \times \Omega_\alpha$ to both sides. On the left, we then include the $a_\alpha^2 \nabla \times \boldsymbol{\omega}_\alpha$ and $c_0^2 \nabla \times (e_\alpha/\alpha \mathbf{B})$ terms and the $v_\alpha \nabla \times \Omega_\alpha$ on the left-hand side in the definition of \mathbf{j}_α , which will later be assumed given. This gives us a *complete* form of the Maxwell equations

$$\nabla \cdot \Omega_\alpha = 0 \quad (3.25)$$

$$\nabla \cdot \zeta_\alpha = \varrho_\alpha \quad (3.26)$$

$$\frac{\partial \Omega_\alpha}{\partial t} + \nabla \times \zeta_\alpha = 0 \quad (3.27)$$

$$\frac{\partial \zeta_\alpha}{\partial t} + \mathbf{j}_\alpha = v_\alpha^2 \nabla \times \Omega_\alpha \quad (3.28)$$

where we have introduced the substitutions

$$\varrho_\alpha = -\frac{\partial}{\partial t} (\nabla \cdot \mathbf{u}_\alpha) - \nabla^2 H_\alpha + \frac{e_\alpha}{m_\alpha} \frac{\varrho_e}{\epsilon_0} \quad (3.29)$$

$$\begin{aligned} \mathbf{j}_\alpha = & \nabla \frac{\partial k_\alpha}{\partial t} + \left(\frac{\partial^2 \mathbf{u}_\alpha}{\partial t^2} - a_\alpha^2 \nabla^2 \mathbf{u}_\alpha \right) - \nabla (\mathbf{u}_\alpha \cdot \nabla h_\alpha) + \frac{e_\alpha}{m_\alpha} \frac{\mathbf{j}_e}{\epsilon_0} + \\ & [v_\alpha^2 - a_\alpha^2] \nabla \times \boldsymbol{\omega}_\alpha + \frac{e_\alpha}{m_\alpha} [v_\alpha^2 - c_0^2] \nabla \times \mathbf{B} \end{aligned} \quad (3.30)$$

where now ϱ_α and \mathbf{j}_α are the new source terms (we have included the terms that did not match the Maxwell set within these quantities), and the new speed v_α is an arbitrary speed, as long as this speed is chosen identically for equations 3.28 and 3.30.

It is clear that equations 3.25 through 3.28 are mathematically identical to the Maxwell equations of classical electrodynamics. In this isomorphism, the generalized fields $\mathbf{\Omega}_\alpha$ and $\mathbf{\zeta}_\alpha$ play the role of the magnetic and electric fields, respectively. The terms ϱ_α and \mathbf{j}_α are analogous to the charge and current densities of electrodynamics. The generalized quantities $\mathbf{\Omega}_\alpha$, $\mathbf{\zeta}_\alpha$, ϱ_α and \mathbf{j}_α unify the hydrodynamic and electrodynamic character of the plasma into a single isomorphic framework. Since the Maxwell equations have well-known solution techniques and approaches, we may apply these approaches to the two-fluid system by considering them in the form of the equations given. Note that there exists a separate Maxwell system for each species α in the plasma.

Since v_α is arbitrary, we are free to choose the speed v_α in equations 3.28 and 3.30 as long as the choice is consistent. Three candidate choices should be immediately obvious: the local sonic speed, a_α , the speed of light, c_0 , and the local fluid velocity, $|\mathbf{u}_\alpha|$. The first two have the benefit of alleviating the form of equation 3.30 by cancelling terms. However, the fluid velocity is the most consistent choice, since in the most limiting case of an incompressible fluid neither of the first two choices are sensible. Hence, the choice of $v_\alpha = |\mathbf{u}_\alpha|$ will always be available, whereas the other choices will depend on the nature of the problem. In addition, since we will seek to model the form of \mathbf{j}_α empirically, it behooves us to choose the speed $v_\alpha = |\mathbf{u}_\alpha|$, since choosing one of the other choices will require different empirical models for different classes of problems. Note that, in the limit that we take the electromagnetics to vanish, we have a fluid problem with possible speed choices of a_α and \mathbf{u}_α . In the case that the flow is incompressible and we take $v_\alpha = |\mathbf{u}_\alpha|$, our Maxwell equations reduce to those discovered previously for incompressible flow [108, 109]; if we instead have a compressible flow and take $v_\alpha = |\mathbf{u}_\alpha|$, our system reduces to the compressible fluid Maxwell equations presented in previous work [110].

If we take the local fluid velocity as the speed in equations 3.28 and 3.30, $v_\alpha = |\mathbf{u}_\alpha|$, then we may derive equation 3.30 using vector identities. This is presented in Appendix A.1. We can show that the form of \mathbf{j}_α for $v_\alpha = \mathbf{u}_\alpha$ is alternately given as

$$\begin{aligned} \mathbf{j}_\alpha = & \varrho_\alpha \mathbf{u}_\alpha - \mathbf{\zeta}_\alpha \nabla \cdot \mathbf{u}_\alpha + 2\mathbf{\zeta}_\alpha \cdot \nabla \mathbf{u}_\alpha + \mathbf{\zeta}_\alpha \times \mathbf{\Omega}_\alpha - \mathbf{\Omega}_\alpha \times \frac{\partial \mathbf{u}_\alpha}{\partial t} + \\ & \nabla \times [(\mathbf{u}_\alpha \cdot \mathbf{\Omega}_\alpha) \mathbf{u}_\alpha] - \nabla (\mathbf{u}_\alpha^2) \times \mathbf{\Omega}_\alpha \end{aligned} \quad (3.31)$$

This is an extension of the previous incompressible model [108, 109] to the case of compressible flows with electromagnetic body forces. Furthermore, this relates the previous incompressible [108, 109] and compressible work [110] to each other in form.

3.4 Convolutions of the Field Equations

Equations 3.25 through 3.28 correspond to the *microscopic* Maxwell equations, in the sense that small perturbations to the primitive variables will inevitably induce rapidly fluctuating sources and fields. In most respects, it is neither necessary nor desirable to capture these small-scale fluctuations. It would instead be preferable to determine the macroscopic, overall behavior of the fields and sources.

A similar perspective is faced in classical electrodynamics. In a microscopic world composed of electrons and nuclei, the charges and currents are in incessant motion, and introduce extremely rapidly fluctuating microscopic fields on the order of 10^{-10}m and between 10^{-13}s to 10^{-17}s . Since macroscopic measuring devices average over much larger intervals in space and time, these microscopic fluctuations are averaged out, and only the relatively smooth, macroscopic quantities are of interest.

In order to average out the small-scale fluctuations in the sources and fields, we follow a similar line of thought as that presented by Jackson [5], Russakoff [134], and Marmanis [108, 109]. We introduce a spatial average of some function $F(\mathbf{x}, t)$ as

$$\langle F(\mathbf{x}, t) \rangle = \int f(\mathbf{x}') F(\mathbf{x} - \mathbf{x}', t) d\mathbf{x}' \quad (3.32)$$

where we take $f(\mathbf{x})$ to be some real, nonzero, isotropic function. We further insist that the function $f(\mathbf{x})$ and its derivative be smooth, since discontinuities in either $f(\mathbf{x})$ or its derivative can introduce jitter to the sources and fields. A typical function that meets these requirements is

$$f(\mathbf{x}) = (\pi R^2)^{-3/2} \exp(-r^2/R^2) \quad (3.33)$$

where $r^2 = \mathbf{x} \cdot \mathbf{x}$ and some averaging distance, R , must be selected; R must be large compared to the small-scale behavior. The major goal in introducing $f(\mathbf{x})$ is to permit a rapidly converging Taylor series expansion of $f(\mathbf{x})$ over small-scale dimensions. It is straightforward to show that $\partial/\partial x_i \langle F(\mathbf{x}, t) \rangle = \langle \partial F(\mathbf{x}, t)/\partial x_i \rangle$ and $\partial/\partial t \langle F(\mathbf{x}, t) \rangle = \langle \partial F(\mathbf{x}, t)/\partial t \rangle$. We can take the average of equations 3.25 through 3.28 to arrive at

$$\nabla \cdot \langle \mathbf{\Omega}_\alpha \rangle = 0 \quad (3.34)$$

$$\nabla \cdot \langle \mathbf{\zeta}_\alpha \rangle = \langle \varrho_\alpha \rangle \quad (3.35)$$

$$\frac{\partial \langle \mathbf{\Omega}_\alpha \rangle}{\partial t} + \nabla \times \langle \mathbf{\zeta}_\alpha \rangle = 0 \quad (3.36)$$

$$\frac{\partial \langle \mathbf{\zeta}_\alpha \rangle}{\partial t} + \langle \mathbf{j}_\alpha \rangle = \langle v_\alpha^2 \nabla \times \mathbf{\Omega}_\alpha \rangle \quad (3.37)$$

A mathematical difficulty presents itself here. The equations are not closed, since in the last term in equation 3.37 there is a convolution of the square of the speed and the curl of the generalized vorticity.

Previously, in the fluid dynamic work, this problem was avoided by assuming the following,

$$\langle v_\alpha^2 \nabla \times \Omega_\alpha \rangle \approx \langle v_\alpha^2 \rangle \nabla \times \langle \Omega_\alpha \rangle \quad (3.38)$$

This assumption may be true if the square of the speed v_α^2 is sufficiently constant within R such that we can pull it out of the integration in equation 3.32; we then choose this speed as $v_\alpha^2 = \langle u_\alpha^2 \rangle$. We cannot provide a proof that this will be the case, and it may not always be, but we can resort to numerical simulations of plasmas in order to explore the justification for this assumption.

As a simple demonstration that justifies our approximation in a representative problem, we examine a simulation of a pulsed plasma thruster operating in an ablative mode, one of the several applications we are interested in. The results of this simulation were presented in [135, 136], and the details of the plasma thruster operation are contained there as well. In the plasma plume expansion that emerged from the thruster, a region was chosen and postprocessed to calculate the gradient of the average velocity, $\nabla \langle v^2 \rangle$, using equation 3.32 to average the velocity; this calculation is presented in Figure 3.1 [118]. Since this value is very small, the value of $\langle u_\alpha^2 \rangle$ is relatively smooth, and our approximation in equation 3.38 is reasonable for this case.

Correspondingly, convolutions of the source terms are necessary as well. Convolving equations 3.29 and 3.31, we have

$$\langle \varrho_\alpha \rangle = -\frac{\partial}{\partial t} (\nabla \cdot \langle \mathbf{u}_\alpha \rangle) - \nabla^2 \langle H_\alpha \rangle + \frac{e_\alpha}{m_\alpha} \frac{\langle \varrho_e \rangle}{\epsilon_0} \quad (3.39)$$

$$\begin{aligned} \langle \mathbf{j}_\alpha \rangle &= \langle \varrho_\alpha \mathbf{u}_\alpha \rangle - \langle \zeta_\alpha \nabla \cdot \mathbf{u}_\alpha \rangle + \langle 2\zeta_\alpha \cdot \nabla \mathbf{u}_\alpha \rangle + \langle \zeta_\alpha \times \boldsymbol{\omega}_\alpha \rangle - \langle \Omega_\alpha \times \frac{\partial \mathbf{u}_\alpha}{\partial t} \rangle + \\ &\quad \langle \nabla \times [(\mathbf{u}_\alpha \cdot \Omega_\alpha) \mathbf{u}_\alpha] \rangle - \langle \nabla (\mathbf{u}_\alpha^2) \times \Omega_\alpha \rangle \end{aligned} \quad (3.40)$$

Furthermore, we can show that a continuity equation exists for the source terms. This can be done by taking the divergence of equation 3.37, the time derivative of equation 3.35, and eliminating the common term. Our result is

$$\frac{\partial \langle \varrho_\alpha \rangle}{\partial t} + \nabla \cdot \langle \mathbf{j}_\alpha \rangle = 0 \quad (3.41)$$

For the remainder of our investigation, we will drop the brackets and use the quantities Ω_α , ζ_α , ϱ_α , and \mathbf{j}_α to denote the convolved averages. We will consider equations 3.34 through 3.37 to be the isomorphic Maxwell equations for a macroscopic description of two-fluid plasmas. We have summarized the isomorphism in Table 3.1.

One of the most welcome properties of equations 3.34 through 3.37 is that, strictly speaking, they are mathematically *linear*. This reduction to a linear system was also seen in the Maxwell equations for incompressible [108, 109] and compressible [110] flow. We should initially be skeptical of such a simplification. However, recall that we split the nonlinear advective term, $\mathbf{u}_\alpha \cdot \nabla \mathbf{u}_\alpha$, into two components. We have now

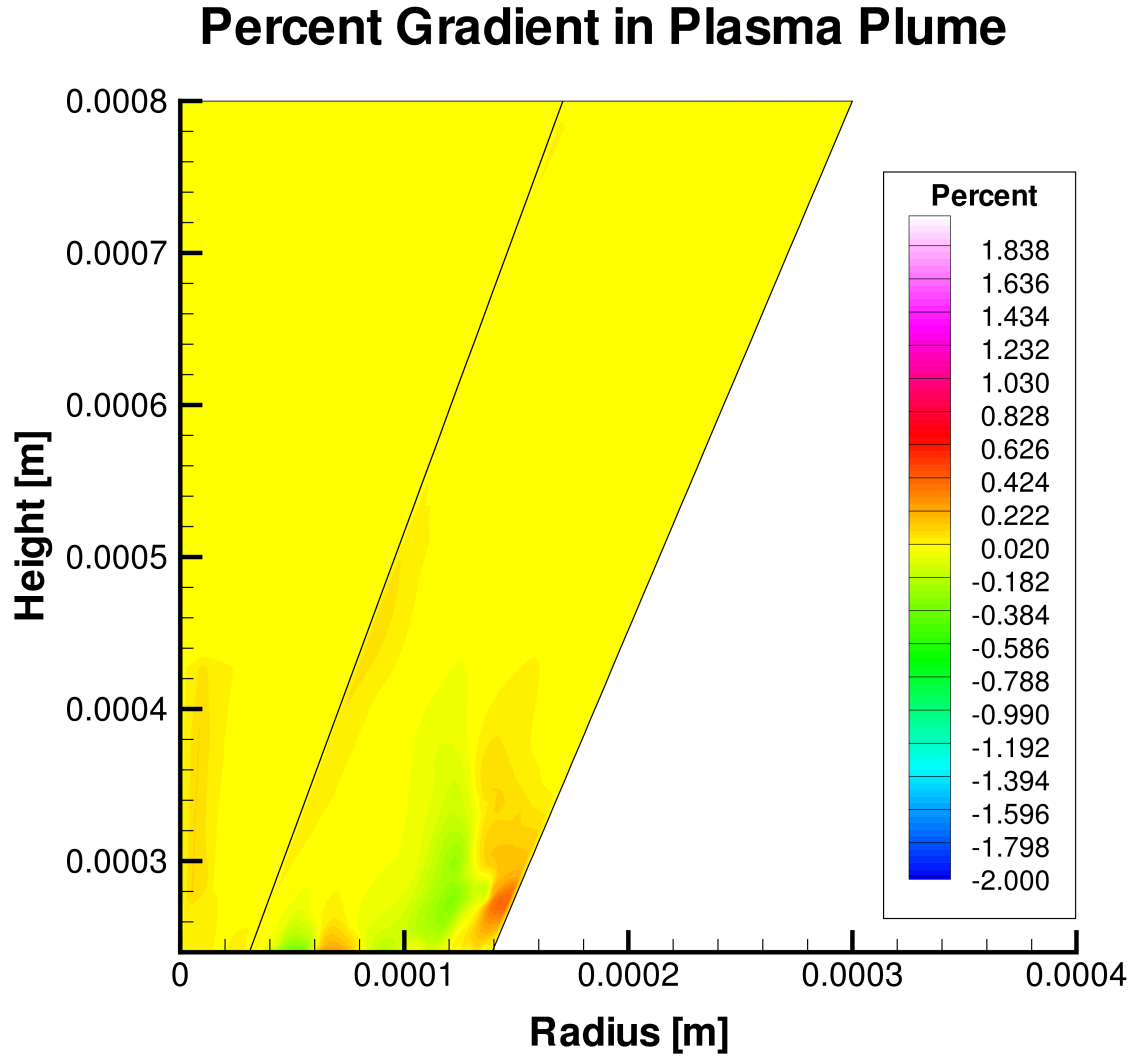


Figure 3.1: A two-dimensional axisymmetric contour plot of the percent gradient in a plasma thruster plume [118, 135, 136]. The variation was typically less than 1% for an averaging length of $R = 10\mu m = 0.10\lambda_{D,max}$. This suggests that the relative difference between $\langle u^2 \nabla \times \Omega \rangle$ and $\langle u^2 \rangle \nabla \times \langle \Omega \rangle$ can be expected to be small in such a plasma.

Table 3.1: The relationships between the species-specific quantities in a multifluid plasma and their analogues in classical electrodynamics.

Plasma Quantity	Electrodynamic Quantity
Species canonical momenta, \mathbf{P}_α	Vector potential, \mathbf{A}
Species total energy, \mathcal{E}_α	Scalar potential, ϕ
Species generalized vorticity, $\boldsymbol{\Omega}_\alpha$	Magnetic field, \mathbf{B}
Species generalized Lamb vector, $\boldsymbol{\zeta}_\alpha = \boldsymbol{\Omega}_\alpha \times \mathbf{u}_\alpha = \left(\boldsymbol{\omega}_\alpha + \frac{e_\alpha}{m_\alpha} \mathbf{B}\right) \times \mathbf{u}_\alpha$	Electric field, \mathbf{E}
Species generalized plasma charge, ϱ_α	Electric charge, ϱ_e
Species generalized plasma current, \mathbf{j}_α	Electric current, \mathbf{j}_e
Equation 3.34	No magnetic charge
Equation 3.35	Gauss law for \mathbf{E}
Equation 3.36	Faraday law
Equation 3.37	Ampere-Maxwell law

cleverly chosen one part as our unknown quantity (the Lamb vector, $\boldsymbol{\zeta}_\alpha$), while the other part has been buried within the source term. If source models can be constructed that depend on known parameters of the system (such as nondimensional fluid parameters), then the source term is considered given at the outset of solving equations 3.34 through 3.37 for the fields, and the equations themselves are linear.

3.5 Immediate Consequences and Ramifications of the Isomorphism

Now that we have introduced the two-fluid ($\alpha = \{i, e\}$) Maxwell equations, some observations are immediately available by implication of the isomorphism. Of course, we could attempt to exhaust the analogy and find every possible implication based on the relationship we have established, but we will be content to only briefly outline some of the more significant results before moving on to determine solutions.

3.5.1 Reduction to Fluid Dynamics

We may directly show that, taking the electromagnetic contributions to vanish, equations 3.34 through 3.37 reduce to the compressible and incompressible Maxwell systems derived previously [108–110]. It will be useful later to know this form of the equations, and it supports the validity of the plasma system if we can show this reduction.

If we choose $v_\alpha \rightarrow a$, and assume only a single species in the compressible gas, we have

$$\nabla \cdot \boldsymbol{\omega} = 0 \quad (3.42)$$

$$\nabla \cdot \boldsymbol{\zeta} = \varrho_F \quad (3.43)$$

$$\frac{\partial \boldsymbol{\omega}}{\partial t} + \nabla \times \boldsymbol{\zeta} = 0 \quad (3.44)$$

$$\frac{\partial \boldsymbol{\zeta}}{\partial t} + \mathbf{j}_F = a^2 \nabla \times \boldsymbol{\omega} \quad (3.45)$$

where

$$\varrho_F = -\frac{\partial}{\partial t} (\nabla \cdot \mathbf{u}) - \nabla^2 h - \nabla^2 k \quad (3.46)$$

$$\mathbf{j}_F = \nabla \frac{\partial k}{\partial t} + \left(\frac{\partial^2 \mathbf{u}}{\partial t^2} - a^2 \nabla^2 \mathbf{u} \right) - \nabla (\mathbf{u} \cdot \nabla h) \quad (3.47)$$

Here $\boldsymbol{\omega}$ and $\boldsymbol{\zeta}$ are the fluid vorticity and Lamb vector, respectively, and ϱ_F and \mathbf{j}_F are the fluid source terms. We could also instead elect to choose $\boldsymbol{\zeta} = \mathbf{u} \cdot \nabla \mathbf{u}$ directly, in which case we delegate the entire advective nonlinear term to become an unknown quantity; this would remove the kinetic energy contribution, k , in equations 3.46 and 3.47.

If the fluid is incompressible, then choosing $v_\alpha \rightarrow |\mathbf{u}|$ and once again taking only a single species in the fluid, we arrive at the incompressible equations derived by Marmanis [108, 109],

$$\nabla \cdot \boldsymbol{\omega} = 0 \quad (3.48)$$

$$\nabla \cdot \boldsymbol{\zeta} = \varrho_F \quad (3.49)$$

$$\frac{\partial \boldsymbol{\omega}}{\partial t} + \nabla \times \boldsymbol{\zeta} = 0 \quad (3.50)$$

$$\frac{\partial \boldsymbol{\zeta}}{\partial t} + \mathbf{j}_F = u^2 \nabla \times \boldsymbol{\omega} \quad (3.51)$$

where

$$\varrho_F = -\nabla^2 \left\{ \frac{p}{\varrho} + \frac{1}{2} \mathbf{u} \cdot \mathbf{u} \right\} \quad (3.52)$$

$$\mathbf{j}_F = \varrho_\alpha \mathbf{u} + 2\boldsymbol{\zeta} \cdot \nabla \mathbf{u} + \boldsymbol{\zeta} \times \boldsymbol{\omega} - \boldsymbol{\omega} \times \frac{\partial \mathbf{u}_\alpha}{\partial t} + \nabla \times [(\mathbf{u} \cdot \boldsymbol{\omega}) \mathbf{u}] - \nabla (\mathbf{u}^2) \times \boldsymbol{\omega} \quad (3.53)$$

Here we have assumed that $\nabla \cdot \mathbf{u} = 0$, and u^2 should be taken to be the average of $\mathbf{u} \cdot \mathbf{u}$.

3.5.2 Potentials, Gauge Transformations and Gauge Analogies

The derivation of the isomorphism is based principally on the similarity between ϕ and \mathcal{E}_α and \mathbf{A} and \mathbf{P}_α . The plasma quantities \mathcal{E}_α and \mathbf{P}_α hence behave as scalar and vector potentials, respectively, for the two-fluid Maxwell equations. We may leverage the isomorphism to produce direct equations for these potentials in

terms of the sources ϱ_α and \mathbf{j}_α ,

$$\frac{1}{v_\alpha^2} \frac{\partial^2 \mathcal{E}_\alpha}{\partial t^2} - \nabla^2 \mathcal{E}_\alpha = \varrho_\alpha + \frac{\partial}{\partial t} \left\{ \frac{1}{v_\alpha^2} \frac{\partial \mathcal{E}_\alpha}{\partial t} + \nabla \cdot \mathbf{P}_\alpha \right\} \quad (3.54)$$

$$\frac{\partial \mathbf{P}_\alpha}{\partial t} - v_\alpha^2 \nabla^2 \mathcal{E}_\alpha = \mathbf{j}_\alpha - \nabla \left\{ \frac{\partial \mathcal{E}_\alpha}{\partial t} + v_\alpha^2 \nabla \cdot \mathbf{P}_\alpha \right\} \quad (3.55)$$

These equations reflect the well known potential equations of classical electrodynamics, which would typically be written as

$$\frac{1}{c_0^2} \frac{\partial^2 \phi}{\partial t^2} - \nabla^2 \phi = \frac{\varrho_e}{\epsilon_0} + \frac{\partial}{\partial t} \left\{ \frac{1}{c_0^2} \frac{\partial \phi}{\partial t} + \nabla \cdot \mathbf{A} \right\} \quad (3.56)$$

$$\frac{1}{c_0^2} \frac{\partial^2 \mathbf{A}}{\partial t^2} - \nabla^2 \mathbf{A} = \mu_0 \mathbf{j}_e - \nabla \left\{ \nabla \cdot \mathbf{A} + \frac{1}{c_0^2} \frac{\partial \phi}{\partial t} \right\} \quad (3.57)$$

Since $\nabla \cdot \mathbf{A}$ is not significant (only $\nabla \times \mathbf{A}$ represents a physical quantity), we are free to choose it arbitrarily; it is called a gauge in the electrodynamic system. Choosing a form for $\nabla \cdot \mathbf{A}$ that simplifies the above electrodynamic potential equations is known as applying a gauge transformation. In the above equations, two classic gauges are immediately obvious. First, we may choose the *Lorentz gauge*²,

$$\nabla \cdot \mathbf{A} = -\frac{1}{c_0^2} \frac{\partial \phi}{\partial t} \quad (3.58)$$

in which case the terms in brackets on the right-hand side of equations 3.56 and 3.57 vanish, and we are awarded with two decoupled inhomogeneous wave equations for ϕ and \mathbf{A} . A second choice would be the *Coulomb gauge*, where

$$\nabla \cdot \mathbf{A} = 0 \quad (3.59)$$

The second time derivative of ϕ then drops out of equation 3.56, and it reduces to a Poisson equation for the scalar potential, identical to the electrostatic case. Equation 3.57 is still coupled to ϕ , and depends on the solution of equation 3.56.

In our analogy, the same form of the electrodynamic potential equations is present in equations 3.54 and 3.55. However, unlike the case in electrodynamics, the term $\nabla \cdot \mathbf{P}_\alpha$ does not truly represent a gauge, since we do not have the freedom to choose its form to be whatever we wish. To understand this more clearly, consider the case where no electromagnetics are present. Then equations 3.54 and 3.55 reduce to a compressible flow; take a single species and $v_\alpha \rightarrow a$ to get

$$\frac{1}{a^2} \frac{\partial^2 H_\alpha}{\partial t^2} - \nabla^2 H_\alpha = \varrho_F + \frac{\partial}{\partial t} \left\{ \frac{1}{a^2} \frac{\partial H}{\partial t} + \nabla \cdot \mathbf{u} \right\} \quad (3.60)$$

$$\frac{\partial^2 \mathbf{u}}{\partial t^2} - a^2 \nabla^2 \mathbf{u} = \mathbf{j}_F - \nabla \left\{ \frac{\partial H}{\partial t} + a^2 \nabla \cdot \mathbf{u} \right\} \quad (3.61)$$

²This is also referred to as the *Lorenz gauge* or sometimes as the *Lorentz-Lorenz gauge*. [102]

Here, the quantity $\nabla \cdot \mathbf{u}$ behaves as the gauge. But we are not permitted to simply choose the form of $\nabla \cdot \mathbf{u}$; it is a reflection of the form of the continuity equation.

If the fluid is compressible, the term $\nabla \cdot \mathbf{u}$ can be solved for algebraically in the continuity equation. Using the form of equation 3.5, where the continuity equation has been cast in terms of the enthalpy, h ,

$$\nabla \cdot \mathbf{u} = -\frac{1}{a^2} \frac{Dh}{Dt} \quad (3.62)$$

This form of the continuity equation is analogous to the Lorentz gauge of electrodynamics, equation 3.58. Similarly, if the fluid were *incompressible*, then the continuity equation reduces to its typical form

$$\nabla \cdot \mathbf{u} = 0 \quad (3.63)$$

which is reflective of the Coulomb gauge in electrodynamics, equation 3.59.

Since the divergence of the velocity appears in $\nabla \cdot \mathbf{P}$, the physical significance of the continuity of mass is inherited in this term. Therefore, $\nabla \cdot \mathbf{P}$ is not truly a gauge, since it is not permitted the same freedom of choice. Notice further that, even with an analogous Lorentz gauge form of the divergence of velocity (the compressible case given in equation 3.62), equations 3.60 and 3.61 still do not fully uncouple since there is a remaining term of $\mathbf{u} \cdot \nabla h$.

3.5.3 Boundary Conditions

In electromagnetic theory, across a material interface the fields can jump discontinuously. Knowledge of the boundary conditions for the fields is important in most applications. We can construct an analogous set of boundary conditions for the new field equations.

A schematic of our approach is shown in Figure 3.2. Typically, we are interested in boundaries across which the dynamical quantities ζ_α and Ω_α vanish (such as solid boundaries). To calculate the boundary conditions, we consider a Gaussian pillbox staggered across an interface that divides two regions of different field strengths for ζ_α and Ω_α , and an Amperian loop across the surface. Allowing for the surface to have some specified charge and current density, denoted ϱ_{surf} and \mathbf{j}_{surf} , respectively, and taking the limit as $\delta \rightarrow 0$, then our boundary conditions may be posed as

$$\left(\zeta_\alpha^{(1)} - \zeta_\alpha^{(2)} \right) \cdot \mathbf{n} = \varrho_{\text{surf}} \quad (3.64)$$

$$\mathbf{n} \times \left(\zeta_\alpha^{(1)} - \zeta_\alpha^{(2)} \right) = 0 \quad (3.65)$$

$$\left(\Omega_\alpha^{(1)} - \Omega_\alpha^{(2)} \right) \cdot \mathbf{n} = 0 \quad (3.66)$$

$$\mathbf{n} \times \left(\Omega_\alpha^{(1)} - \Omega_\alpha^{(2)} \right) = \mathbf{j}_{\text{surf}} \quad (3.67)$$

where superscripts (1) and (2) denote the different sides of the interface, as depicted in Figure 3.2. These

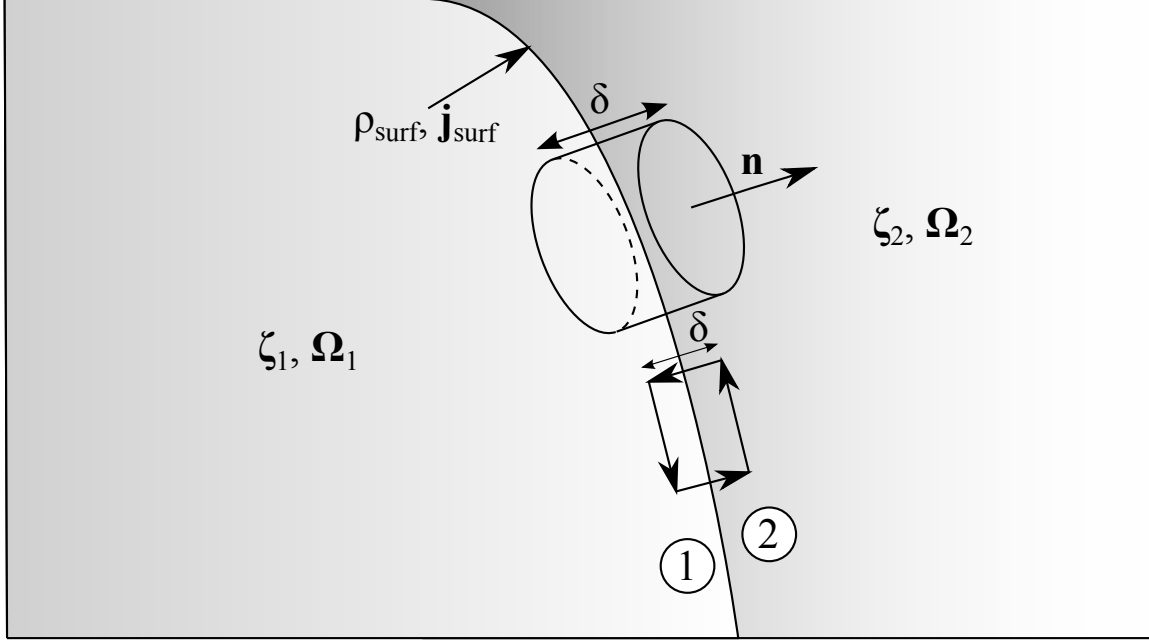


Figure 3.2: A diagram of the Gaussian pillbox and rectangular contour used for deriving the boundary conditions across an interface surface of charge density ρ_{surf} and current density \mathbf{j}_{surf} .

conditions imply that there is a discontinuous jump in the normal component of ζ_α and in the tangential component of Ω_α proportional to the charge and current on the surface, but the tangential component of ζ_α and the normal component of Ω_α are preserved across the interface.

3.5.4 Lagrangian Formalism for Two-fluid Plasmas

We can further profit from the connection realized between the two-fluid equations the electromagnetic theory by following the usual construction of a Lagrangian for the fields. This has the particularly interesting effect of unifying the Lagrangian for the fluid and electrodynamic fields into a single, compact framework. The resulting unified Lagrangian formalism for the plasma has significant potential applications for variational schemes describing the evolution of the generalized fields. Exploring this Lagrangian framework also makes clear the connection between the work introduced in this dissertation and previous efforts examining analogies in two-fluid plasmas [121]. We can facilitate the discussion by introducing plasma four-vectors and four-tensors analogous to those in classical electrodynamics. Following the usual convention [5, 101], we express the vectors and tensor in index form, and choose greek indices for spanning the spacetime range, $\mu, \nu \in \{0, 1, 2, 3\}$ (to avoid confusion, we drop the species index α , and the equations are simply understood to be on a per-

species basis) and latin indices for spanning the spatial range, $k \in \{1, 2, 3\}$, where the zeroth index represents time. The plasma four-current, j^μ , is analogous to the electrodynamic four-current [5],

$$j^\mu = (v\rho, \mathbf{j}) \quad (3.68)$$

The analogous Faraday tensor for the two-fluid plasma becomes

$$F^{\mu\nu} = \begin{pmatrix} 0 & -\zeta_x & -\zeta_y & -\zeta_z \\ \zeta_x & 0 & -\Omega_z & \Omega_y \\ \zeta_y & \Omega_z & 0 & -\Omega_x \\ \zeta_z & -\Omega_y & \Omega_x & 0 \end{pmatrix} \quad (3.69)$$

and the corresponding covariant tensor can be built by lowering the indices using the metric tensor,

$$F_{\mu\nu} = g_{\mu\alpha} F^{\alpha\beta} g_{\beta\nu} = \begin{pmatrix} 0 & \zeta_x & \zeta_y & \zeta_z \\ -\zeta_x & 0 & -\Omega_z & \Omega_y \\ -\zeta_y & \Omega_z & 0 & -\Omega_x \\ -\zeta_z & -\Omega_y & \Omega_x & 0 \end{pmatrix} \quad (3.70)$$

i.e., we effectively have let $\zeta_\alpha \rightarrow -\zeta_\alpha$.

The dual tensor can also be defined analogous to that of electrodynamics,

$$\mathfrak{F}^{\mu\nu} = \frac{1}{2} \epsilon^{\alpha\beta\gamma\delta} F_{\gamma\delta} = \begin{pmatrix} 0 & -\Omega_x & -\Omega_y & -\Omega_z \\ \Omega_x & 0 & \zeta_z & -\zeta_y \\ \Omega_y & -\zeta_z & 0 & \zeta_x \\ \Omega_z & \zeta_y & -\zeta_x & 0 \end{pmatrix} \quad (3.71)$$

which can be effectively constructed from the Faraday tensor, $F^{\mu\nu}$, by taking $\zeta \rightarrow \Omega$ and $\Omega \rightarrow \zeta$.

Per the discussions of Lagrangian dynamics for continuum mechanics [137], we introduce the Lagrangian, L , as an integration of a *Lagrangian density*, \mathcal{L} ,

$$L = \int \mathcal{L}(\phi_k, \partial^\alpha \phi_k) d\mathbf{x} \quad (3.72)$$

where ϕ_k represents the continuum fields (analogous to the generalized coordinates in discrete mechanics). The appropriate choice of the Lagrangian density is analogous to that of classical electrodynamics, which involves a free Lagrangian and an interaction Lagrangian due to the presence of a continuous source term, j^μ ,

$$\mathcal{L} = -\frac{1}{4} F_{\mu\nu} F^{\mu\nu} - j_\mu A^\mu \quad (3.73)$$

Given this form of the Lagrangian, the continuum form of the Euler-Lagrange equations are

$$\partial^\mu \frac{\partial \mathcal{L}}{\partial (\partial^\mu \phi_k)} = \frac{\partial \mathcal{L}}{\partial \phi_k} \quad (3.74)$$

Taking $\phi_k = A^\mu$, we can construct the inhomogeneous Maxwell equations (Gauss and Ampere-Maxwell laws) by noting that

$$\frac{\partial \mathcal{L}}{\partial (\partial^\mu A^\nu)} = -F_{\mu\nu} \quad (3.75)$$

$$\frac{\partial \mathcal{L}}{\partial A^\mu} = -\frac{1}{v} j_\mu \quad (3.76)$$

and thus the inhomogeneous Maxwell equation is

$$\partial^\mu F_{\mu\nu} = j_\nu \quad (3.77)$$

The homogeneous Maxwell equations are already satisfied by the definition of A^μ ; however, we may write it explicitly as

$$\partial_\mu \mathfrak{F}^{\mu\nu} = 0 \quad (3.78)$$

An appropriate question of transformation surfaces here. Recall from our initial assumptions that the fluid equations were written in a *Galilean-invariant* form, whereas the Maxwell equations are *Lorentz-invariant*. Thus, the framework presented here is not truly complete in a physical sense, and the fluid and electrodynamic behavior is not fully unified yet, because transformation of the equations still requires breaking up the fluid and electrodynamic parts and transforming each separately. The above framework succeeds only in a mathematical sense; a true unification requires that the equations transform identically, and thus may be evaluated without separation between the fluid and electrodynamic parts. If the fluid dynamic equations were cast into their relativistic form, then we would expect that the transformation would be complete. The previous work by Mahajan [121] has shown that this unification is possible, although the framework introduced there differs from the present formalism. Specifically, the Lagrangian given in equation 3.73 includes an interaction Lagrangian that did not appear in the previous work, due to differences of definition and exploitation of the isomorphism. It does not make either framework less valuable, just different in their approaches, and the present discussion can be seen as an effort to unify the pre-existing literature and the present investigation. In our framework, the introduction of source terms potentially allows for a solution approach identical to that in electrodynamics, but at the cost of requiring that the source terms be somehow provided, if the fields are to be solved. We will see in Chapter 4 that the issue of constructing models for the source terms is not a trivial issue.

3.5.5 Inverse Transformation: An Analogous Drift Relation

A final ramification of the isomorphism is a vector identity for the fluid velocity that is analogous to the drift velocity of a charged particle in electromagnetic fields; we will use this identity later as an inverse transformation to calculate the velocity field given the generalized fields. Any successful calculation of the plasma using the generalized fields will require a means of reconstructing the primitive data from the fields; this drift relation permits such a connection. We can introduce this drift relation simply by the application of the vector identity $\mathbf{a} \times (\mathbf{b} \times \mathbf{c}) = (\mathbf{a} \cdot \mathbf{c})\mathbf{b} - (\mathbf{a} \cdot \mathbf{b})\mathbf{c}$. This yields

$$\boldsymbol{\zeta}_\alpha \times \boldsymbol{\Omega}_\alpha = (\boldsymbol{\Omega}_\alpha \times \mathbf{u}_\alpha) \times \boldsymbol{\Omega}_\alpha = -\boldsymbol{\Omega}_\alpha \times (\boldsymbol{\Omega}_\alpha \times \mathbf{u}_\alpha) = -(\boldsymbol{\Omega}_\alpha \cdot \mathbf{u}_\alpha) \boldsymbol{\Omega}_\alpha + (\boldsymbol{\Omega}_\alpha \cdot \boldsymbol{\Omega}_\alpha) \mathbf{u}_\alpha \quad (3.79)$$

Rearranging this, we have

$$\frac{\boldsymbol{\zeta}_\alpha \times \boldsymbol{\Omega}_\alpha}{|\boldsymbol{\Omega}_\alpha|^2} = \mathbf{u}_\alpha - (\hat{\boldsymbol{\Omega}}_\alpha \cdot \mathbf{u}_\alpha) \hat{\boldsymbol{\Omega}}_\alpha \quad (3.80)$$

where $\hat{\boldsymbol{\Omega}}_\alpha = \boldsymbol{\Omega}_\alpha / |\boldsymbol{\Omega}_\alpha|$ is a unit vector. In Chapter 4, we will refer to equation 3.80 as the *drift relation*. In many cases, the second term on the right-hand side can vanish, which reduces to an exact analogy of the drift velocity in a crossed electromagnetic field,

$$\frac{\boldsymbol{\zeta}_\alpha \times \boldsymbol{\Omega}_\alpha}{|\boldsymbol{\Omega}_\alpha|^2} = \mathbf{u}_\alpha \quad (3.81)$$

An important limitation of the isomorphism can be seen clearly here, and will be seen even more clearly later. In the case that there is no generalized vorticity, $\boldsymbol{\Omega}_\alpha \rightarrow 0$, we end up with an indeterminate form for the velocity vector. This is because *the isomorphism breaks down in regions where $\boldsymbol{\Omega}_\alpha \rightarrow 0$* . For the case of fluids, Remember that the analogy we have posed relates the Lamb vector, which acts as an electric field, as $\boldsymbol{\zeta}_\alpha = \boldsymbol{\Omega}_\alpha \times \mathbf{u}_\alpha$. In the case where $\boldsymbol{\Omega}_\alpha \rightarrow 0$, the Lamb vector and generalized vorticity both vanish. This problem echoes the discussion given by Nobel laureate Julian Schwinger in his lecture notes on the inference of Faraday's law, [138]

This shows that the desired differential equation will hold if

$$\mathbf{E} = -\frac{\mathbf{v}}{c} \times \mathbf{B}$$

But this cannot be a completely correct statement, since then $\mathbf{v} \rightarrow 0$ would require $\mathbf{E} \rightarrow 0$. No electrostatics! However, all that is really necessary is that the curl of this tentative identification be valid:

$$\nabla \times \mathbf{E} = -\nabla \times \left(\frac{\mathbf{v}}{c} \times \mathbf{B} \right)$$

or, if we use $[\partial \mathbf{B} / \partial t = \nabla \times (\mathbf{v} \times \mathbf{B})]$,

$$\nabla \times \mathbf{E} = -\frac{1}{c} \frac{\partial \mathbf{B}}{\partial t}$$

Although this comment arises from a very different context, a similar degeneracy is observed; if the generalized vorticity vanishes, we must resort to some other method to determine the velocity. In Chapter 4, when considering the reconstruction of the velocity field using this approach, l'Hôpital's rule can be used for simple problems; during numerical simulations, either controlling the division-by-zero by use of a $\max()$ function or special case consideration must be applied to circumvent this issue. It will be particularly disastrous for some solution approaches considered in Section 4.4.3, where the solution fails in the freestream region of a boundary layer; other methods utilizing Green's functions will prove more successful.

3.6 Summary of the Isomorphic Framework

This chapter has focused on introducing the isomorphic field equations, given in their microscopic form in equations 3.25 through 3.28; the associated form of the generalized charge density is presented in equation 3.29, and the generalized current density is presented in equation 3.30 and in an alternative form for the speed $v_\alpha = |\mathbf{u}_\alpha|$ in equation 3.31. The convolved form of the equations are given in equations 3.34 through 3.37, which relies on the assumption provided in equation 3.38, and the associated convolved source terms are shown in equations 3.39 and 3.40. A conservation equation for the source terms may also be formulated, as shown in equation 3.41. It is particularly interesting that the convolved equations are strictly *linear* for the generalized fields, since we have relegated the nonlinearities in part to the unknown Lamb vector, $\boldsymbol{\zeta}_\alpha$, and to the source terms, ϱ_F and \mathbf{j}_α .

The new framework discards the familiar primitive variables in the plasma in favor of the new dynamical quantities $\boldsymbol{\Omega}_\alpha$ and $\boldsymbol{\zeta}_\alpha$, which represent the generalized vorticity and generalized Lamb vector for a species α in the plasma. If we exchange the primitive variables for these generalized quantities, the Maxwell set of equations derived above governs the evolution of these fields. These generalized quantities unite the hydrodynamic and electrodynamic behavior of the plasma. Although we have already expanded on previous work in fluid dynamics [108–110] and plasmas [121] that take advantage of analogous formulations, our intent in this dissertation was to go beyond this and exploit these new field equations for numerical simulations to improve the efficiency for solving the two-fluid equations. The next chapter is devoted entirely to this subject. The issue of determining the source terms still overshadows this approach; however, and we will see that the framework is challenged by the lack of available source term data. We succeed in demonstrating some solution approaches, however, given adequate models of the source term data.

Chapter 4

Source Modeling and Solution Approaches Using the Isomorphic Framework

“Well done. Here are the test results: You are a horrible person. I’m serious.
That’s what it says. A horrible person. We weren’t even testing for that. Don’t
let that horrible-person thing discourage you. It’s just a data point.”

GLaDOS [1]

4.1 Introduction

Having discussed the new framework of solving the system via the new dynamical quantities ζ_α and Ω_α , and having posed some of the ramifications of the isomorphism in Chapter 3, we now turn our attention to the issue of solving the equations for specific problems. At this point, it is inevitable to avoid a philosophical discussion regarding the nature of solutions to Maxwell’s equations. The basic problem is eloquently outlined by Jackson [5],

“... the problems of electrodynamics have been divided into two classes: one in which the sources of charge and current are specified and the resulting electromagnetic fields are calculated, and the other in which the external electromagnetic fields are specified and the motions of charged particles or currents are calculated. Waveguides, cavities, and radiation from prescribed multipole sources are examples of the first type of problem, while motion of charges in electric and magnetic fields and energy-loss phenomena are examples of the second type. Occasionally, as in the discussion of *bremssstrahlung*, the two problems are combined. But the

treatment is a stepwise one – first the motion of the charged particle in an external field is determined, neglecting the emission of radiation; then the radiation is calculated from the trajectory as a given source distribution. It is evident that this manner of handling problems in electrodynamics can be of only approximate validity.”

In the above generalized Maxwell equations that we have derived, we inherit the same behavior. Generally, we would prefer that the fields were the unknowns, since the velocity and thermodynamic data could be calculated from these fields, but, as Jackson points out, this requires that we know source term data. During the early history of classical electrodynamics, the accumulation of experimental data had been ongoing well before Maxwell’s involvement (see, for example, Faraday’s published experimental research [139], which Maxwell drew from [112]), and this access to a wealth of information propelled the development of Maxwell’s theory. In contrast to Maxwell’s setting in the 1860’s, there was very little data available to the author regarding two-fluid plasmas during the development of this dissertation. Therefore, the most significant present challenge that belabors the utility of solving the isomorphic framework discussed in Chapter 3 is *a lack of available source term data*.

This challenge is common to all approaches using Maxwell’s equations for solving problems, including electrodynamics itself. There is a major impetus in the study of plasma actuators to characterize the spatial and temporal behavior of charges around the electrodes, since the charge largely determines the body force exerted on the surrounding fluid; a similar effort is being made in the characterization of plasma sheaths for the same reason that the electric charge determines the overall behavior. Having a phenomenological knowledge of the source terms allows for a direct attempt at solving Maxwell’s equations, whereas not knowing it usually necessitates the approximate effort discussed by Jackson, to iteratively resolve both the fields and sources. In the previous fluid dynamic work, Marmanis [108, 109], Kambe [110] and Logan [116, 117] all derive elegant theories based on the solution of Maxwell’s equations, but the resounding silence that follows these publications in terms of their application testifies to the difficulty in determining adequate source term information for fluid problems. Likewise, we anticipate that compressible flow and plasmadynamics will encounter a similar problem.

Faced with this deficit of source term information, we must actually first *reverse* our interest, and examine problems in which the *fields* are known, and the *sources* are unknown. Given simple problems where perhaps only a single salient feature is present, we may determine the form of the source term for each of these cases, which in turn supplies us with a library of very fundamental source term models for each salient feature. Recalling that the source terms superpose, this collection permits us to construct superposed models for more complicated flows in which we desire the fields. To build up our collection of source models, problems in which analytical solutions exist are of interest, since the full flow field data is fully available to harvest source terms for these problems, and with relatively modest effort; for more complicated problems, we resort to numerical simulation to explicate the nature of the source terms. If more resources had been available during this investigation, experimental approaches could have been utilized as well; in fact, experimental

determinations of fluid dynamic charge for Marmanis' model have actually been performed [140].

In addition to collecting some simple source term data, we also aim to illustrate the utility of the isomorphism by borrowing techniques from classical electrodynamics and applying them to problems for which we can derive the source terms to show that numerical and closed-form solutions using these techniques are feasible. We openly admit that this becomes a chicken and egg problem: first, we must assume the fields are known in order to derive the source terms (requirement of the fields essentially insists on knowing the solution beforehand), and then, we reverse these conditions, assuming the source terms were somehow given, and solve for the fields. Again, we reiterate that this is a necessary step to start collecting these simple models. More complicated phenomena would involve superposing these simple sources to gain an overall source for the new problem, but collected from known previous source data, thus permitting the fields for the more complicated problems to be solved directly without needing their own source data to be determined first.

An obvious question arises: why not just follow Jackson's suggestion, and iteratively converge both the sources and fields? Such an approach would yield something akin to a particle-in-cell numerical scheme, but for both the electrodynamic and fluid dynamic fields. At the outset of this dissertation, this was surmised to be the ultimate goal of this investigation. Due to a number of complicating factors that will be discussed in detail in Section 4.3, this was not feasible, and, at present, is not considered to be a promising avenue of research. The major complicating factors can be summarized by pointing out that, generally, source term data is noisy for finite volume simulations (as more completely discussed in Chapter 5), the approximations necessary for the full system of two-fluid equations to be solved in Maxwell form require an excessively small timestep, and the approach explored in this investigation revealed that solving the equations did not capture the contact discontinuity wave present in most simple shock tube simulations.

4.2 Homogeneous Solutions

The most straightforward case we can envision is the situation where the source terms vanish, $\varrho_\alpha = 0$ and $\mathbf{j}_\alpha = 0$. In such cases, the primitive variables must be consistent with the sources reducing to zero. Despite their intimidating forms, there may be physical cases in which this happens. For example, if we consider a quasineutral, incompressible plasma away from any bounding solid walls, then a homogeneous solution is sensible. Furthermore, in the previous work examining the Maxwell equations for incompressible turbulent flow, the turbulent nature of the flow sufficiently averaged out the source contributions to a small result away from the walls, despite the form of equation 3.53. Viscous conditions near the walls, energy sources and shocks all tend to introduce sources that require some inhomogeneous treatment. However, since plasmas may become fully turbulent even in inviscid cases [141, 142], problems can be expected where the homogeneous form of the solution can be of value.

When $\varrho_\alpha = 0$ and $\mathbf{j}_\alpha = 0$, we can write the isomorphic field equations as

$$\nabla \cdot \boldsymbol{\Omega}_\alpha = 0 \quad (4.1)$$

$$\nabla \cdot \boldsymbol{\zeta}_\alpha = 0 \quad (4.2)$$

$$\frac{\partial \boldsymbol{\Omega}_\alpha}{\partial t} = -\nabla \times \boldsymbol{\zeta}_\alpha \quad (4.3)$$

$$\frac{\partial \boldsymbol{\zeta}_\alpha}{\partial t} = v_\alpha^2 \nabla \times \boldsymbol{\Omega}_\alpha \quad (4.4)$$

We will consider the Cauchy problem for $\boldsymbol{\Omega}_\alpha$ and $\boldsymbol{\zeta}_\alpha$ in an infinite spatial domain, since boundaries tend to induce source contributions, and show the development of homogeneous wave equations. Then, we will show that the resulting wave equations still retain the usual variety of MHD waves, as expected.

4.2.1 Homogeneous Wave Equations

If we take the spatial domain to be infinite, we may consider the unsteady evolution of equations 4.3 and 4.4 for some initial conditions $\boldsymbol{\Omega}_\alpha(\mathbf{x}, t=0) = \boldsymbol{\Omega}_\alpha^0$ and $\boldsymbol{\zeta}_\alpha(\mathbf{x}, t=0) = \boldsymbol{\zeta}_\alpha^0$ that are assumed to satisfy equations 4.1 and 4.2. For the sake of completeness, let us assume that equations 4.1 through 4.4 are in their *microscopic* form, such that they are not convolved. This is permissible since no source terms are included, so no averaging is immediately necessary to filter small-scale phenomena. In fact, by using the microscopic form in this section, we may examine the effects of perturbing the system only slightly; this could be of great advantage in the study of plasma turbulence. We may take the time derivative of equation 4.3 and the curl of equation 4.4 and eliminate the common term to achieve a wave equation in $\boldsymbol{\Omega}_\alpha$; similarly, reversing the operations on the same equations, and again eliminating the common term, we can arrive at a wave equation in $\boldsymbol{\zeta}_\alpha$. These equations are

$$\frac{\partial^2 \boldsymbol{\Omega}_\alpha}{\partial t^2} - v_\alpha^2 \nabla^2 \boldsymbol{\Omega}_\alpha = -\square^2 \boldsymbol{\Omega}_\alpha = -\nabla (v_\alpha^2) \times (\nabla \times \boldsymbol{\Omega}_\alpha) \quad (4.5)$$

$$\frac{\partial^2 \boldsymbol{\zeta}_\alpha}{\partial t^2} - v_\alpha^2 \nabla^2 \boldsymbol{\zeta}_\alpha = -\square^2 \boldsymbol{\zeta}_\alpha = \frac{\partial}{\partial t} (v_\alpha^2) \nabla \times \boldsymbol{\Omega}_\alpha \quad (4.6)$$

Here, v_α is one of the candidate speeds discussed earlier in Section 3.3. These wave equations govern the evolution of the generalized fields for problems in which no source terms influence the evolution.

4.2.2 Recovering Magnetohydrodynamic Waves

As an example of examining the homogeneous case, we can show that the typical variety of MHD waves exists as a subset of the waves in the generalized vorticity and Lamb vector. To do so, we consider a magnetohydrodynamic plasma; it has only a single species, it is quasineutral (which implies that the electric body force has insignificant effect on it, so the Lorentz force is dominated by the $\mathbf{j}_e \times \mathbf{B}$ term) and we neglect the displacement current. We also assume that the current is given by Ohm's law, so that $\mathbf{j}_e = \sigma \mathbf{E} + \sigma \mathbf{u} \times \mathbf{B}$.

The evolution of the magnetic field can now be given by Faraday's law with Ohm's law substituted in,

$$\frac{\partial \mathbf{B}}{\partial t} = -\nabla \times \mathbf{E} = \nabla \times \left(\frac{\mathbf{j}_e - \sigma \mathbf{u} \times \mathbf{B}}{\sigma} \right) = \nabla \times (\mathbf{u} \times \mathbf{B}) - \frac{1}{\sigma} \nabla \times \mathbf{j}_e \quad (4.7)$$

Substituting in the Ampere-Maxwell equation for \mathbf{j}_e (and again remembering that we dropped the displacement current), this becomes

$$\frac{\partial \mathbf{B}}{\partial t} = \nabla \times (\mathbf{u} \times \mathbf{B}) - \frac{1}{\sigma \mu_0} \nabla \times \nabla \times \mathbf{B} \quad (4.8)$$

This is the traditional magnetic induction equation of the MHD theory. We will now further assume that the plasma is an *ideal MHD* plasma, in the sense that the conductivity is large enough to be considered infinite. If this is true, the second term on the right-hand side becomes negligible (if we retained it, it would not change our results), and we retain only the advective limit of the magnetic field,

$$\frac{\partial \mathbf{B}}{\partial t} = \nabla \times (\mathbf{u} \times \mathbf{B}) \quad (4.9)$$

The Lorentz body force acting on the plasma is now composed entirely of the $\mathbf{j}_e \times \mathbf{B}$ term,

$$\mathbf{F}_B = -\frac{1}{\varrho \mu_0} \mathbf{B} \times (\nabla \times \mathbf{B}) \quad (4.10)$$

Now, we introduce a perturbation expansion. The flow is assumed to be initially unperturbed, such that the mean flow is zero. We have

$$\mathbf{B} = \mathbf{B}_0 + \mathbf{B}_1 \quad (4.11)$$

$$\varrho = \varrho_0 + \varrho_1 \quad (4.12)$$

$$\mathbf{u} = \mathbf{u}_0 + \mathbf{u}_1 = \mathbf{u}_1 \quad (4.13)$$

Quantities with subscript zero are assumed to be constant with respect to time and space. Substituting these expansions to first order into our wave equations, equations 4.5 and 4.6, then we have

$$\frac{\partial^2 \mathbf{u}}{\partial t^2} - a^2 \nabla^2 \mathbf{u} = -\nabla \left(a^2 \nabla \cdot \mathbf{u} + \frac{\partial^2 h}{\partial t^2} \right) - \frac{1}{\varrho \mu_0} \frac{\partial}{\partial t} (\mathbf{B} \times (\nabla \times \mathbf{B})) \quad (4.14)$$

$$\frac{\partial^2 \mathbf{u}_1}{\partial t^2} + a^2 \nabla (\nabla \cdot \mathbf{u}_1) - \frac{1}{\varrho \mu_0} \frac{\partial}{\partial t} (\mathbf{B}_0 \times (\nabla \times \mathbf{B}_1)) = 0 \quad (4.15)$$

Since the derivative of \mathbf{B}_0 is zero, the body force term can be rewritten as

$$\frac{\partial}{\partial t} [\mathbf{B}_0 \times (\nabla \times \mathbf{B}_1)] = \mathbf{B}_0 \times \left(\nabla \times \frac{\partial \mathbf{B}_1}{\partial t} \right) \quad (4.16)$$

We can now substitute equation 4.9 under the assumed perturbation expansion, $\partial \mathbf{B}_1 / \partial t = \nabla \times (\mathbf{u}_1 \times \mathbf{B}_0)$, here,

$$\frac{\partial}{\partial t} [\mathbf{B}_0 \times (\nabla \times \mathbf{B}_1)] = \mathbf{B}_0 \times (\nabla \times \nabla \times (\mathbf{u}_1 \times \mathbf{B}_0)) \quad (4.17)$$

and finally substituting this into equation 4.15, we have

$$\frac{\partial^2 \mathbf{u}_1}{\partial t^2} - a^2 \nabla (\nabla \cdot \mathbf{u}_1) + \frac{1}{\rho \mu_0} [\mathbf{B}_0 \times \nabla \times \nabla \times (\mathbf{u}_1 \times \mathbf{B}_0)] = 0 \quad (4.18)$$

where we have used thermodynamic manipulations to recast the $a^2 \nabla (\nabla \cdot \mathbf{u})$ term. This exact equation appears in Jackson's discussion [5] of MHD waves. We can distribute a factor of $1/\sqrt{\rho \mu_0}$ to each of the \mathbf{B}_0 terms, which introduces the Alfvén velocity, $\mathbf{v}_A = \mathbf{B}_0 / \sqrt{\rho \mu_0}$, in the equation. If we assumed that the velocity was a plane-wave form, $\mathbf{u}_1 = \mathbf{A} \exp(i\mathbf{k} \cdot \mathbf{x} - i\omega t)$, then three classes of waves result: longitudinal magnetosonic waves with a phase velocity $\sqrt{a^2 + v_A^2}$, another longitudinal mode with a phase velocity equal to the sonic speed a , and a third transverse wave with a phase velocity equal to the Alfvén velocity, v_A . Thus, the usual variety of MHD waves are apparent within the waves of the generalized vorticity.

4.3 Inhomogeneous Solutions

While the homogeneous form involves solving only a ‘vacuum’ set of Maxwell equations with no sources, many interesting phenomena we wish to study are relegated to the source terms. Furthermore, it becomes apparent that the sources often are associated with boundary effects, which represent important considerations in the modeling of plasmas for engineering applications.

The concept of electric charge is rather familiar. The notion of *fluid* charge, however, is more foreign. Prerequisite to solving the Maxwell equations for the fields, we must have some mathematical form for these sources in the full equations, if we wish to include source term effects.

There are two essential approaches that could be taken. The first is to model the source term using *iterative modeling*. In this approach, the source terms are calculated given primitive data (\mathbf{u} , ρ , \mathbf{E} , \mathbf{B} , etc.), the Maxwell equations are solved for the source terms, and finally the primitive data is reconstructed from the generalized fields. This allows an iterative approach that may be used to construct approximate solutions to the Maxwell equations. This echoes Jackson's comment about an approximate, iterative approach for electrodynamics, wherein the sources are calculated, the fields are solved given the new sources, and the sources are updated.

The second approach is to model the source term using *empirical modeling*. In this approach, we begin by separately investigating the form of the source terms given the fields (remember that this is a valid case wherein the Maxwell equations may be solved, where now the source terms are considered the unknowns). This could be done using experimental, numerical or analytical approaches, as long as the fields, ζ_α and Ω_α ,

were known. Once a knowledge of the source terms were built up, they could be superimposed for different problems. It is clear that considering very simple problems is profitable here, since they may be readily extended to more complicated problems by utilizing the superposition of charge and current density.

In the remainder of this chapter, we investigate approaches to solving inhomogeneous problems. Since calculating the forms of the source terms for different cases resembles a zoological approach of identification, it can continue indefinitely. Therefore, it was deemed beyond the scope of a single dissertation to explore the form of the source terms for every possible condition. Instead, only a few specific cases of interest are explored.

We begin by discussing the iterative modeling approach. While this seems an intuitive and appealing approach for numerically constructing solutions to the equations, it seems at present to offer no advantages of improving efficiency of numerical simulation of two-fluid plasmas. A more difficult aspect of the problem is the reconstructive nature of recalculating the primitive data from the generalized fields; it will turn out that this is only valid in regions where generalized vorticity is present. Instead, the empirical modeling approach seems much more promising, and so our attention will primarily be centered on developing some empirical models in order to show the basic process, reveal the nature of the source terms, and illustrate different solution approaches using these models.

Our investigation of empirical modeling is divided into two approaches. The first examines simple fluid problems for analytical forms of the sources, and illustrates some basic solution approaches that may be applied to solve the isomorphic equations. There are two motivations for focusing here on simple fluid problems. First, since the form of the source terms is cumbersome, some simplifying assumptions are necessary to construct any kind of analytical expression. Second, by studying and formulating analytical models of the source terms for simple problems, more complicated problems may be constructed by using these models as building blocks. Since the source terms superpose, fluid source terms will be directly applicable for plasmas. Furthermore, since the three problems studied are ubiquitous to fluid and plasma problems, it is fruitful to focus on such problems. The second approach will resort to numerical simulation and postprocessing to reveal the forms of the source terms for a few more complicated cases, including shocks in compressible flow and plasmas of engineering interest.

4.3.1 Inhomogeneous Wave Equations

A first approach at determining solutions for inhomogeneous plasmas may consider the development and solution of wave equations. Similar to the homogeneous section (equations 4.5 and 4.6), we start by considering the *microscopic* field equations; we will introduce a linearization to the equations that will reduce them to a more amenable form instead.

The inhomogeneous wave equations for the microscopic system may be written by considering the same

derivation as in the homogeneous case, except including the source terms. We have

$$\frac{\partial^2 \mathbf{\Omega}_\alpha}{\partial t^2} - v_\alpha^2 \nabla^2 \mathbf{\Omega}_\alpha = -\square^2 \mathbf{\Omega}_\alpha = \nabla \times \mathbf{j}_\alpha - \nabla (v_\alpha^2) \times (\nabla \times \mathbf{\Omega}_\alpha) \quad (4.19)$$

$$\frac{\partial^2 \boldsymbol{\zeta}_\alpha}{\partial t^2} - v_\alpha^2 \nabla^2 \boldsymbol{\zeta}_\alpha = -\square^2 \boldsymbol{\zeta}_\alpha = -\frac{\partial \mathbf{j}_\alpha}{\partial t} - u_\alpha^2 \nabla \varrho_\alpha + \frac{\partial}{\partial t} (v_\alpha^2) \nabla \times \mathbf{\Omega}_\alpha \quad (4.20)$$

We may linearize these equations in the following fashion. Consider an expansion of the fields for each species in the form

$$\mathbf{u}(\mathbf{x}, t) = \mathbf{u}_0 + \mathbf{u}_1(\mathbf{x}, t) + \dots, \quad (4.21)$$

$$\boldsymbol{\omega}(\mathbf{x}, t) = \boldsymbol{\omega}_0 + \boldsymbol{\omega}_1(\mathbf{x}, t) + \dots, \quad (4.22)$$

$$\varrho(\mathbf{x}, t) = \varrho_0 + \varrho_1(\mathbf{x}, t) = \frac{e_\alpha}{m_\alpha} \frac{\varrho_e}{\epsilon_0} + \varrho_1(\mathbf{x}, t) + \dots, \quad (4.23)$$

$$\mathbf{\Omega}(\mathbf{x}, t) = \mathbf{\Omega}_0 + \mathbf{\Omega}_1(\mathbf{x}, t) + \dots = \mathbf{\Omega}_1(\mathbf{x}, t) + \dots, \quad (4.24)$$

$$\boldsymbol{\zeta}(\mathbf{x}, t) = \boldsymbol{\zeta}_0 + \boldsymbol{\zeta}_1(\mathbf{x}, t) + \dots = \boldsymbol{\zeta}_1(\mathbf{x}, t) = \mathbf{\Omega}_0 \times \mathbf{u}_1 + \mathbf{\Omega}_1 \times \mathbf{u}_0 = \mathbf{\Omega}_1 \times \mathbf{u}_0 \quad (4.25)$$

We have dropped the species index α , although these equations and expansions should be understood to apply to each species. Any quantity with a 0 index is a constant with respect to \mathbf{x} and t ; first-order terms are denoted with subscript 1. For simplicity, we retain only first-order terms, so any products that yield higher-order terms are neglected. Here \mathbf{u}_0 is taken to indicate a non-zero mean flow. Since the the derivative of a zero-order term is zero, the terms $\boldsymbol{\omega}$, $\mathbf{\Omega}$ and $\boldsymbol{\zeta}$ reduce to first-order terms only. Notice also that ϱ_0 reduces only to the net electric charge density, since the derivatives of the zero-order terms vanish.

Retaining only first-order terms, we can effectively eliminate most of the contributions in the sources. The only contributions that survive in the current density are the convective term $\varrho_0 \mathbf{u}_1 + \varrho_1 \mathbf{u}_0$ and a curl term $\nabla \times [(\mathbf{u}_0 \cdot \mathbf{\Omega}_1) \mathbf{u}_0]$. This latter term vanishes for all derivatives in equations 4.19 and 4.20 except for the time derivative of \mathbf{j}_α appearing in the wave equation for $\boldsymbol{\zeta}_\alpha$. For mathematical simplicity, we consider the case where this term also vanishes. By substituting the expanded fields (equations 4.21 through 4.25) into the source terms given in equations 3.29 and 3.30, we may arrive at the following approximate form for the wave equations,

$$\frac{\partial^2 \mathbf{\Omega}_1}{\partial t^2} - u_0^2 \nabla^2 \mathbf{\Omega}_1 = \nabla \times (\varrho_0 \mathbf{u}_1 + \varrho_1 \mathbf{u}_0) \quad (4.26)$$

$$\frac{\partial^2 \boldsymbol{\zeta}_1}{\partial t^2} - u_0^2 \nabla^2 \boldsymbol{\zeta}_1 = -\frac{\partial}{\partial t} (\varrho_0 \mathbf{u}_1 + \varrho_1 \mathbf{u}_0) - u_0^2 \nabla \varrho_1 \quad (4.27)$$

Typical solution techniques could be applied at this point to solve these equations for specific problems. Another very interesting approach is to consider that, since $\boldsymbol{\zeta}_1 = \mathbf{\Omega}_1 \times \mathbf{u}_0$, we could rewrite the left-hand side of equation 4.27 as

$$\frac{\partial^2}{\partial t^2} (\mathbf{\Omega}_1 \times \mathbf{u}_0) - u_0^2 \nabla^2 (\mathbf{\Omega}_1 \times \mathbf{u}_0) = \left\{ \frac{\partial^2 \mathbf{\Omega}_1}{\partial t^2} - u_0^2 \nabla^2 \mathbf{\Omega}_1 \right\} \times \mathbf{u}_0 \quad (4.28)$$

But equation A.32 may be substituted into the brackets, and thus we have the following identity,

$$\frac{\partial}{\partial t} (\varrho_0 \mathbf{u}_1 + \varrho_1 \mathbf{u}_0) + [\nabla \times (\varrho_0 \mathbf{u}_1 + \varrho_1 \mathbf{u}_0)] \times \mathbf{u}_0 = -u_0^2 \nabla \varrho_1 \quad (4.29)$$

This equation resembles a momentum equation of the form $\partial \mathbf{u} / \partial t + \boldsymbol{\omega} \times \mathbf{u} = -a^2 \nabla \varrho$. Furthermore, in the expanded variables, the charge conservation equation 3.41 holds, so

$$\frac{\partial \varrho_1}{\partial t} + \nabla \cdot (\varrho_0 \mathbf{u}_1 + \varrho_1 \mathbf{u}_0) = 0 \quad (4.30)$$

Thus, equations 4.30 and 4.29 constitute a similar form to the continuity and momentum equations, respectively. These equations can be considered evolution equations that describe the change in the generalized convective current $\varrho_0 \mathbf{u}_1 + \varrho_1 \mathbf{u}_0$. Here the plasma charge density ϱ_0 and ϱ_1 still includes both electrodynamic and hydrodynamic contributions, so the evolution of the two equations above will determine the generalized behavior in the plasma.

4.3.2 Iterative Source Modeling

Inspired by Jackson's comment regarding iteratively converging both the fields and sources, a very simple numerical approach was identified at the outset of this investigation, much akin to the particle-in-cell (PIC) solution procedure for low-density plasmas. If such an approach could be implemented for solving the isomorphic Maxwell equations, we could envision a PIC scheme that resolves both the fluid and electrodynamic character of the plasma simultaneously.

The simplified PIC approach can be briefly sketched as four primary steps (depicted graphically in Figure 4.1)

1. Given a distribution of charged particles, each of which possesses a position, \mathbf{x}_i , and a velocity, \mathbf{v}_i , we can calculate the overall net charge and current density, $\sum_i q_i$ and $\sum_i q_i \mathbf{v}_i$, respectively.
2. Given the charge and current density, we may compute the solution to Maxwell's equations for the electric and magnetic fields, \mathbf{E} and \mathbf{B} .
3. Equipped with a knowledge of the fields, we may compute the Lorentz force acting on each particle everywhere in the domain, $\mathbf{F} = q\mathbf{E} + q\mathbf{v} \times \mathbf{B}$.
4. Once the Lorentz force is known, the effective acceleration of the particle is known within a small amount of time. By integrating the equations of motion, we may determine the subsequent changes in velocity and position of each particle, and return to step (1).

This procedure can be progressed using a small timestep to study the evolution of the constituents in the plasma over time.

Guided by the simplicity and success of this computational model, we can construct a similar approach for the isomorphic field equations. Such an analogous algorithm may be posed as follows:

1. Given the primitive data in the plasma (velocity, thermodynamic data and electromagnetic fields), we may calculate the form of the source terms at the current timestep by utilizing direct substitution of the primitive data into equations of the form 3.29 and 3.31.
2. With the source terms in hand, we may calculate the change in the generalized fields via the isomorphic Maxwell equations (equations 3.34 through 3.37). This could take advantage of any of a number of numerical schemes for calculating the new fields a small timestep later. Akin to the discussion offered in Section 2.1.5, divergence cleaning would be necessary to guarantee that the divergence constraints were met.
3. Given the new generalized fields, Ω_α and ζ_α , we would need to apply an inverse transformation to reconstruct the primitive variable data from these fields. This could theoretically be done via the drift

Algorithm for Particle-in-Cell (PIC)

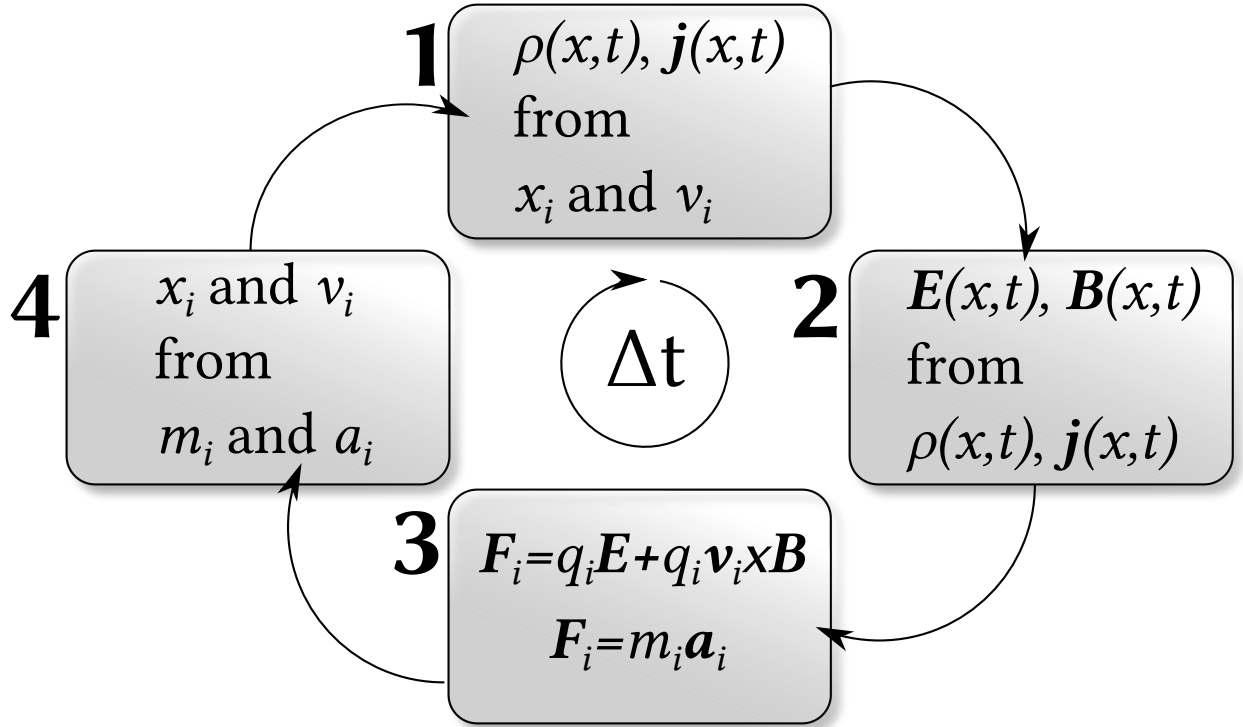


Figure 4.1: A diagram of the particle in cell algorithm. Each timestep requires four substeps: (1) Starting with position, \mathbf{x}_i , and velocity, \mathbf{v}_i , data for each particle i , we sum each particle's contribution to the total charge and current density, $\rho(x,t)$ and $\mathbf{j}(x,t)$, respectively. (2) With the charge and current density, solve the Maxwell equations for the electromagnetic fields. (3) With the electromagnetic fields in hand, use the Lorentz force and Newton's law to determine the acceleration acting on each particle, \mathbf{a}_i . (4) Integrate the acceleration to calculate the new velocity, \mathbf{v}_i , and integrate again to determine the new position, \mathbf{x}_i , for the next timestep.

relation, equation 3.80, to determine the velocity vector; the selection of an appropriate analogous gauge transformation would allow for using the new velocity vector to update the thermodynamic data.

This imaginative approach would allow for a straightforward resolution of both the fields and sources, without recourse to modeling the source terms at all. This algorithm was developed for the compressible fluid dynamic Maxwell equations discussed in Section 3.5.1 and the full plasma equations; the solution of the Maxwell equations was implemented via an upwinded Roe method [11, 143] and a first-order upwind differenced method [103]. Other approaches could have been applied as well. These approaches were tested for Maxwell’s equations of electrodynamics (using a fixed speed of light) and the typical solutions for electromagnetic wave propagation were confirmed to be resolved correctly. Then, the solver was adapted using the algorithm discussed above. The source terms were calculated from the primitive variable data via equations 3.29 and 3.31, and the drift relation given in equation 3.80 was used to solve the velocity field after the generalized fields were obtained from the Maxwell solver. The thermodynamic data was calculated by differencing the analogous Lorentz gauge in time, and updating the thermodynamic variables using the divergence of the updated velocity field. The solver was applied to the Sod shock tube problem [144] for compressible flow, and the Brio and Wu [75, 145] problem for two-fluid plasmas. Ultimately, all of the solution approaches described here failed, and no solution was constructed successfully.

While we provided an extensive discussion in Chapter 1 that motivated the use of implicit schemes for plasmas, the intimidating forms of equations 3.29 and 3.31 make the calculation of jacobian matrices for implicit schemes very difficult. Therefore, a second-order Runge-Kutta explicit scheme was used instead. Although this approach is clearly more expensive for plasmas, the author [118] has shown that the Brio and Wu problem can be successfully resolved using an explicit approach. For compressible flows, this is not a problem, since there is only a single timescale of interest. Other methods, such as the Adams-Moulten or Adams-Bashforth methods [146], could also be used to improve this scheme.

In the case of the Sod shock tube simulation using the compressible solver, the assumption of a one-dimensional domain is questionable within the framework of the isomorphism, since no vorticity is permitted in just one dimension. This problem was circumvented by rewriting the compressible flow Maxwell equations to match the definitions given in [110], where we instead define the analogous electric field to be the *entire* advective term, $\zeta = \mathbf{u} \cdot \nabla \mathbf{u}$; this is different from the equations presented in Chapter 3 by retaining the kinetic energy term, k on the left-hand side as part of the unknown; this allows one-dimensional simulation of the compressible flow equations, although a different reconstructive equation must be used (the drift relation, equation 3.80, is no longer valid and a differenced form of the definition of ζ was used). The two-fluid plasma Maxwell equations have no such problem in one dimension, since, due to the presence of a tangential magnetic field, the flow will always have a three-dimensional generalized vorticity.

The simplest summary that can be given for these approaches is, despite our efforts, all approaches to utilize the iterative algorithm given above failed. Both solvers were plagued by numerical instabilities, despite

providing accurate solutions for electrodynamic test problems; however, some important observations were permitted which may be credited with the difficulties encountered:

- The implementation of highly nonlinear, complicated, discontinuous source terms given in equations 3.29 and 3.31 caused significant instability in the equations. This could have potentially been relaxed by migrating to a fully implicit scheme, but, as discussed, the cumbersome forms of the sources made the calculations of jacobian matrices for implicit methods difficult. The enormous source terms encountered in the test problems required excessively small timesteps to be needed for numerical stability, which made long-duration simulations impractical. The application of the convolving approaches discussed in Section 3.4 helped mitigate the source term issue (essentially by smearing the sources slightly, in a very similar manner to the application of numerical dissipation across shocks), but this ultimately did not improve the quality or longevity of the simulation.
- One major cause for concern is found by examining the velocity reconstruction approach more closely. Note that, in the limit when no generalized vorticity is encountered, equation 3.80 becomes indeterminate. When this happens, the velocity vector cannot straightforwardly be reconstructed from the generalized fields by using the drift relation. This indicates a breakdown of the isomorphism in irrotational regions; for example, when $\mathbf{\Omega} = 0$, the Lamb vector also vanishes by definition, $\boldsymbol{\zeta} = \mathbf{\Omega} \times \mathbf{u} = 0$. Thus, in regions where the generalized vorticity vanishes, we cannot actually reconstruct the velocity vector very efficiently. This is a major limitation of the simple algorithm introduced above. We will later see that a similar problem is seen when empirically modeling the source terms as well.
- Although not responsible for the failure of the simulation, another significant observation was that both solvers were incapable of capturing the contact discontinuity wave. This is a problem that has arisen before for several time-marching numerical schemes [147], and this is perceived as a major deficiency of the proposed algorithm.
- Another point of interest was that the CPU time required to calculate a single cycle of the algorithm described above was *significantly larger* than traditional approaches, implying that this algorithm is actually *less* efficient than traditional approaches. This is due to the complicated nature of the source terms that must be updated every iteration (several different derivatives must be calculated). The solution of an additional equation for the thermodynamic data further hinders the efficiency of such an algorithm. Even with a number of simplifying assumptions, the calculation of the primitive data from the generalized fields cannot be performed in a reasonably efficient way. Cases where these assumptions cannot be applied further exacerbate this problem and make the algorithm even more inefficient.

Given all of the above difficulties, it was concluded that, at present, iterative schemes are simply beyond the scope of our investigation. We hope that future work may realize methods or algorithms that were not envisioned during this investigation that could take advantage of not needing source data for the calculation of the fields. We will instead turn our attention to approaches that empirically model the source term; although this requires some source data, we will see that the solution approaches utilizing this form of

modeling permit excellent results.

4.4 Empirical Source Modeling, Reconstructive and Green's Function Approaches for Fluids

The most promising approach for dealing with the source terms is to construct empirical models representing simple problems. Once a basic understanding of the plasma charge and current is known and the rudimentary models have been collected, they may be used as building blocks for understanding more complicated plasmas. The real challenge here is focused on understanding the notion of the *fluid* charge and current, ϱ_F and \mathbf{j}_F . Since the electric sources are understood, we really seek a knowledge of how the more complicated fluid sources behave for specific cases. Once this understanding has been laid down, we may apply models for simpler cases to more complicated problems.

Since the fluid source terms represent what we do not understand in the generalized sources, and since it is of more benefit to examine simple problems to construct basic building block charges and currents, we will first focus on three cases of steady, incompressible fluid flow. Although these problems are simple, they represent very basic phenomena we expect to encounter in plasma flows, and they are thus fruitful to consider. Furthermore, since the electromagnetic source terms superpose, we may always add electromagnetic contributions to the sources. The process for solving a complicated problem then becomes a process of adding a new source term for each phenomenon of interest.

In the following, we will re-examine Couette flow, duct flow, and Blasius boundary layer flow over a flat plate. The form of the fields and sources are discussed, and we illustrate different approaches to solving these basic problems using the isomorphic equations. Particularly, we explore the application of a reconstructive scheme that iteratively corrects the source terms until some convergence is reached, and then we explore the use of Green's functions and the method of images to calculate the solution directly using an interpolated model of the fluid charge and current.

Following our analytical analysis, we will further investigate some classic cases that arise in compressible flow and plasmas using numerical simulation and postprocessing to reveal the nature of the source terms qualitatively.

4.4.1 Couette Flow Solution

The classic two-dimensional Couette flow problem is sketched in Figure 4.2. A viscous fluid is trapped between two plates; the upper plate is moving at some velocity U . For a Newtonian fluid, a linear velocity profile results. The viscous contribution behaves as a source term in this case.

If we assume the flow is steady, laminar and incompressible, and that no pressure gradient is present, and if the temperature gradient is small such that the coefficient of viscosity is a constant, then the well known

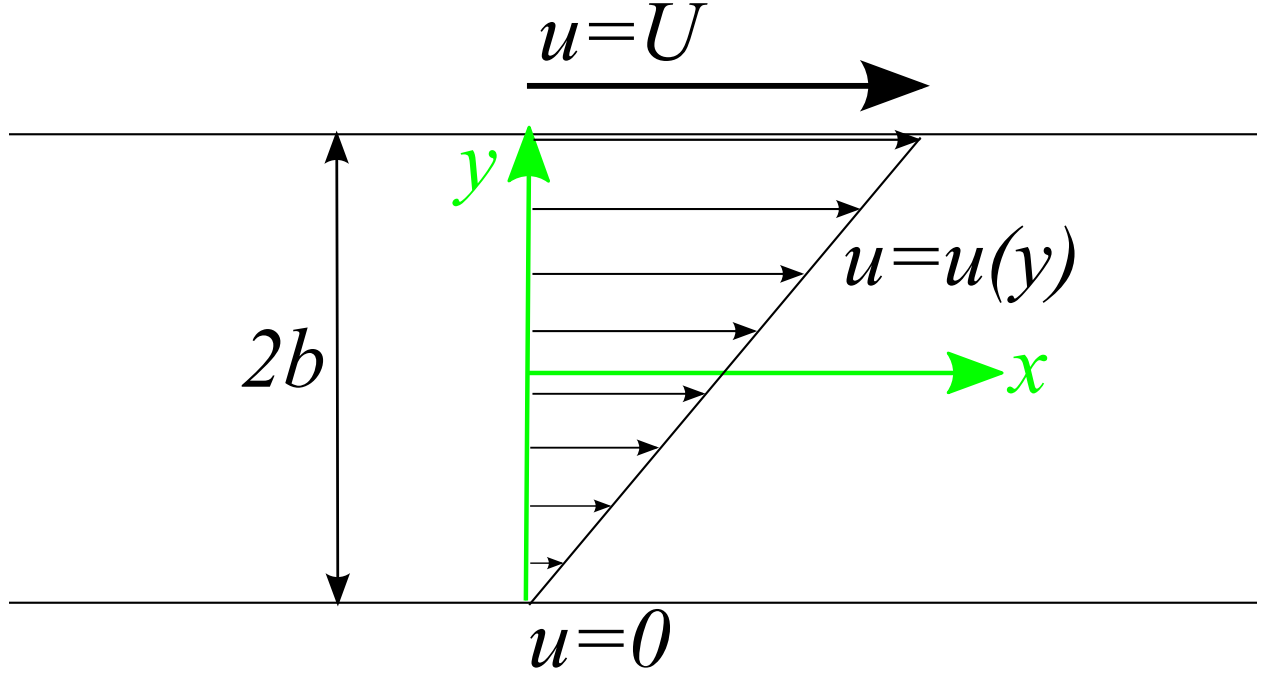


Figure 4.2: A diagram of the usual configuration for Couette flow. Coordinate system is shown in green. The velocity vanishes at the lower plate, $u(-b) = 0$, and matches the velocity U of the upper plate at $y = b$, $u(b) = U$. [7]

solution [7] is given as a linear profile,

$$u(y) = \frac{U}{2b} (y + b), \quad -b \leq y \leq +b \quad (4.31)$$

where the coordinate system is taken as that shown in Figure 4.2. The Maxwell equations in this case will reduce to

$$\nabla \cdot \boldsymbol{\omega} = 0 \quad (4.32)$$

$$\nabla \cdot \boldsymbol{\zeta} = \varrho_F \quad (4.33)$$

$$\nabla \times \boldsymbol{\zeta} = 0 \quad (4.34)$$

$$u^2 \nabla \times \boldsymbol{\omega} = \mathbf{j}_F \quad (4.35)$$

The viscous term is included in the sources. The vorticity, $\boldsymbol{\omega} = \omega_z \hat{\mathbf{z}}$, and Lamb vector, $\boldsymbol{\zeta} = \boldsymbol{\omega} \times \mathbf{u} = \zeta_y \hat{\mathbf{y}}$,

may be calculated directly knowing this result,

$$\omega_z = -\frac{du}{dy} = -\frac{U}{2b} \quad (4.36)$$

and

$$\zeta_y = \omega_z u = -\frac{U^2}{4b^2} (y + b) \quad (4.37)$$

Once the fields are known, the sources may be calculated,

$$\varrho_F = \nabla \cdot \boldsymbol{\zeta} = \frac{d\zeta_y}{dy} = -\frac{U^2}{4b^2} \quad (4.38)$$

and

$$\mathbf{j}_F = 0 \quad (4.39)$$

since the vorticity is constant everywhere. Hence, the charge is a constant throughout the domain, and the current density is zero.

To construct a solution approach to Couette flow using the Maxwell equations, we would consider a case in which we have a knowledge of the charge and current density, ϱ_F and \mathbf{j}_F . As noted, in this case the charge is a constant, and the current density is zero in the interior of the flow. To solve this problem, we may simply integrate over the Gauss law for ζ_y ,

$$\zeta_y = \int \varrho_F dy \quad (4.40)$$

An equivalent approach may be taken to determine the vorticity; the Ampere-Maxwell equation will reveal that the derivative of the vorticity is zero, in which case the vorticity is a constant. From a knowledge of this, we may reconstruct the velocity field using the drift relation, $\mathbf{u} = (\boldsymbol{\zeta} \times \boldsymbol{\omega}) / |\boldsymbol{\omega}|^2$. In the x direction, we will have

$$u = \frac{\zeta_y}{\omega_z} \quad (4.41)$$

And applying this to our particular problem, we have

$$u = \frac{U^2 / (4b^2)}{U / (2b)} (y + b) = \frac{U}{2b} (y + b) \quad (4.42)$$

Although this is an extremely simple problem, it emphasizes the basic process of how the fluid is deter-

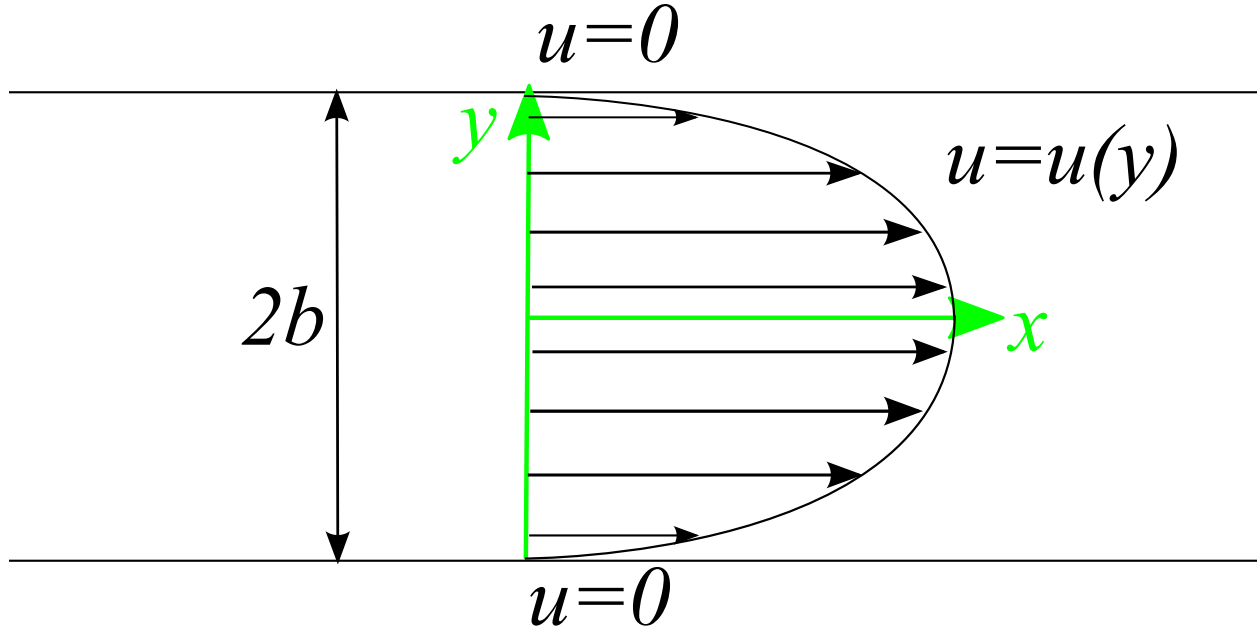


Figure 4.3: A diagram of the usual configuration for fully developed duct flow. The coordinate system is shown in green. The diameter of the duct is $2b$. At both solid surfaces, the no slip boundary condition is applied, $u(b) = u(-b) = 0$. A parabolic velocity profile results. [6, 7]

mined by its fields. Furthermore, it reveals that the form of the source terms for the case of a relative motion between the solid boundaries in a simple geometry consists of a constant charge.

4.4.2 Duct Flow Solution

A second example of inhomogeneous incompressible flow is two-dimensional duct flow. Figure 4.3 shows the usual setup for the duct flow problem. We assume the flow is steady, incompressible, viscous and laminar. A constant pressure gradient is assumed to drive the flow, $P = dp/dx = \text{const}$. The traditional solution, using the geometry in Figure 4.3, reveals a parabolic velocity profile for the fully-developed case,

$$u = A(b^2 - y^2), \quad -b \leq y \leq +b \quad (4.43)$$

where $A = P/(2\mu)$, where μ is the coefficient of viscosity. The velocity profile is sketched in Figure 4.3.

With the solution in hand, we may construct the fields, $\omega = \omega_z \hat{z}$ and $\zeta = \zeta_y \hat{y}$,

$$\omega_z = -\frac{du}{dy} = 2Ay \quad (4.44)$$

and

$$\zeta_y = \omega_z u = 2A^2 y (b^2 - y^2) \quad (4.45)$$

And we may show that the velocity field may be reconstructed using the drift relation given in equation 4.41,

$$u = \frac{\zeta_y}{\omega_z} = \frac{2A^2 y (b^2 - y^2)}{2Ay} = A (b^2 - y^2) \quad (4.46)$$

A point of concern surfaces here: along the line $y = 0$, the vorticity vanishes, and hence the drift relation becomes indeterminant along this line; thus, equation 4.46 is only technically valid when $y \neq 0$. The application of l'Hôpital's rule circumvents this issue and allows the calculation of the correct velocity at $y = 0$. The sources ϱ_F and \mathbf{j}_F are presented in Figure 4.4. From the fields, the fluid source terms may be directly calculated,

$$\varrho_F = \nabla \cdot \boldsymbol{\zeta} = \frac{d\zeta_y}{dy} = 2A^2 (b^2 - 3y^2) \quad (4.47)$$

and

$$\mathbf{j}_F = u^2 \nabla \times \boldsymbol{\omega} = u^2 \frac{d\omega_z}{dy} \hat{\mathbf{x}} = 2A^3 [b^2 - y^2]^2 \hat{\mathbf{x}} \quad (4.48)$$

The form of these source terms are presented in Figure 4.5.

Next, we consider some numerical solution approaches to solving the fluid velocity equipped only with a knowledge of the sources given in equations 4.47 and 4.48. While Couette flow presented only a simple problem, duct flow permits us to practice some more advanced solution approaches. We specifically attempt the following solution approaches to arrive at a fluid velocity:

- *Solution Approach A.* This approach is a check on the drift velocity, and is not truly a solution approach; instead, the exact form of the vorticity is taken as that given in equation 4.44 (it is assumed known, and is not solved for in this approach). The Lamb vector is calculated by directly integrating over the Gauss law, using the form of equation 4.40 and the form of ϱ_F given in equation 4.47, which is considered given. Once ζ_y is known, the velocity is reconstructed using the drift relation given in equation 4.41.
- *Solution Approach B. Reconstructive iteration for velocity u .* In this approach, we first solve the Gauss law using the interpolated form of the charge, as in Solution Approach A. Then we iteratively solve the Ampere-Maxwell law for the vorticity using the current density expression in equation 4.48 and

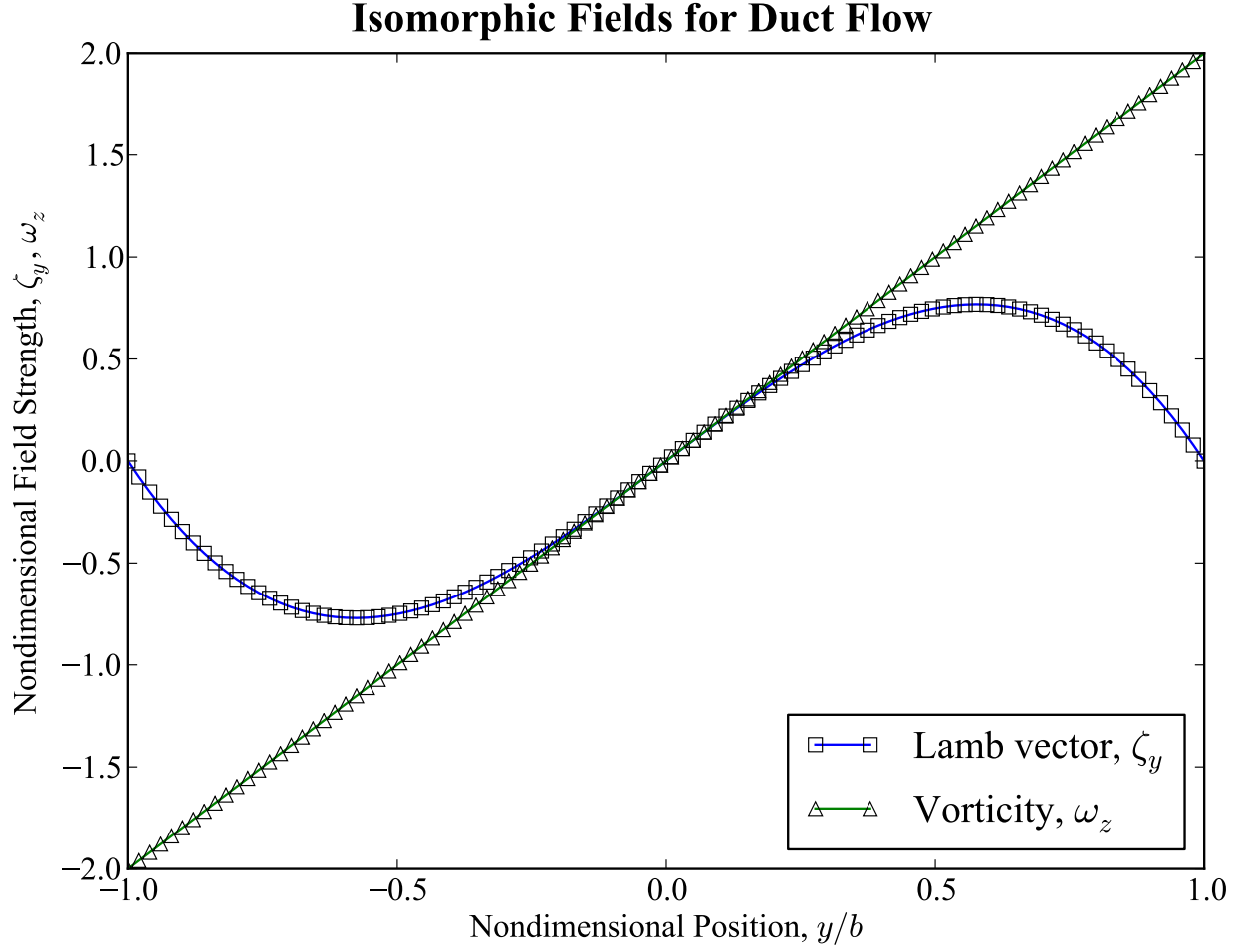


Figure 4.4: A plot of the Lamb vector, ζ_y , and vorticity, ω_z , for duct flow.

the average square of the velocity,

$$\langle u^2 \rangle \frac{d\omega_z}{dy} = \mathbf{j}_F \quad (4.49)$$

The velocity is then reconstructed from the Lamb vector, ζ_y , and the vorticity, ω_z , using the drift relation, as given in equation 4.41. Finally, the average velocity square, $\langle u^2 \rangle$, is recalculated from the updated velocity field. When the average square of the velocity across the whole domain converges to within some tolerance (10^{-5} was typically used), the convergence is considered complete.

- *Solution Approach C. Bounded-domain Green's function solution.* The use of Green's functions is pervasive throughout electrostatics. Since our problem lends itself directly to such a framework, we may explore a solution approach utilizing the same method. Since the curl of the Lamb vector must be zero for a steady problem, $\nabla \times \zeta = 0$, this implies that the Lamb vector may be expressed as a gradient

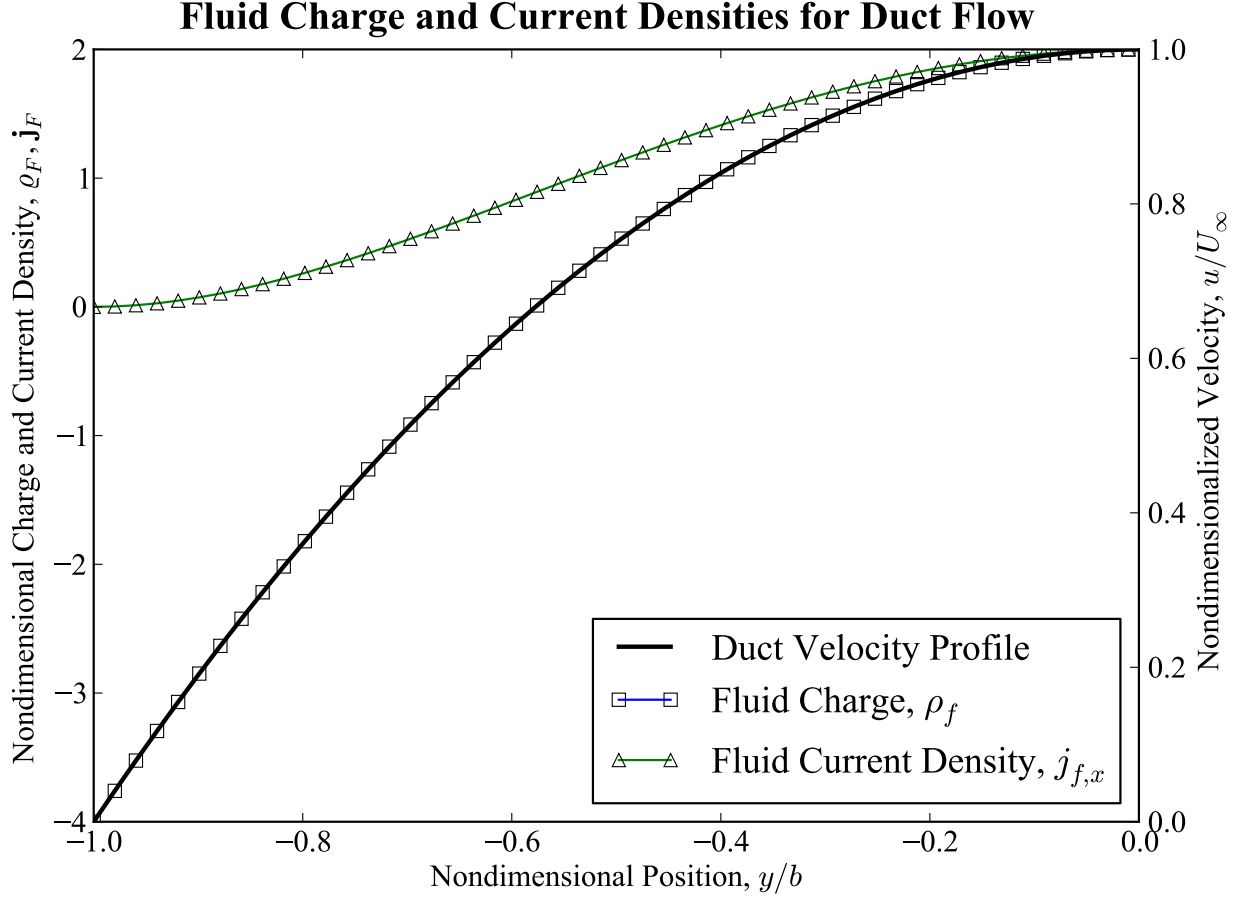


Figure 4.5: A plot of the nondimensional fluid charge and current density for the duct flow problem. The analytical form of the velocity, as given in equation 4.43, is shown for comparison. Only half of the domain is shown; here the solid wall is at $y = -1$ and the centerline is at $y = 0$.

of a scalar potential function, $-\nabla\psi$. Substitution into the Gauss law yields a Poisson equation,

$$-\nabla^2\psi = -\frac{d^2\psi}{dy^2} = \varrho_F(y) \quad (4.50)$$

We use the form of ϱ_F given in equation 4.47 here. To solve this inhomogeneous problem, we construct a Green's function. We consider the domain of the duct to be a bounded one-dimensional domain, $-b \leq y \leq b$, with boundary conditions $u(b) = u(-b) = 0$. The Green's function, $G(y; y')$ is defined to satisfy the corresponding problem with only a point source,

$$-\frac{d^2G}{dy^2} = \delta(y - y') \quad (4.51)$$

subject to the boundary conditions $G(0; y') = 0$ and $G(L; y') = 0$, and where $\delta(y - y')$ is the Dirac

delta distribution. Applying Green's identity,

$$\int_{-b}^b \left\{ \psi(y) \frac{d^2 G}{dy^2} - G(y; y') \frac{d^2 \psi}{dy^2} \right\} dy' = \left[\psi(y) \frac{dG}{dy} - G(y; y') \frac{d\psi}{dy} \right]_{-b}^b \quad (4.52)$$

By direct substitution of equations 4.50 and 4.51 into equation 4.52, and extinguishing all terms on the right-hand side by application of the boundary conditions for ψ and G , we have

$$\int_{-b}^b \{ \psi(y) \delta(y - y') \} dy' = \int_{-b}^b G(y; y') \varrho_F dy' \quad (4.53)$$

Integrating over the Dirac delta distribution, we have $\int \psi(y') \delta(y - y') dy' = \psi(y)$ by the integration property of the Dirac delta. Rearranging for $\psi(y)$, we have

$$\psi(y) = \int_{-b}^b G(y; y') \varrho_F dy' \quad (4.54)$$

To determine the specific form of $G(y; y')$ for this bounded-domain problem, we must first solve equation 4.51 at all points except where $y = y'$; this special case may be treated using the jump conditions of the Green's function, $G(y'^-; y') = G(y'^+; y')$ and $dG/dy|_{y'+} - dG/dy|_{y'-} = \int \delta(y - y') dy' = 1$. Applying these conditions, the form of the Green's function for this problem is

$$G(y; y') = \begin{cases} \frac{y}{2b} (2b - y'), & y < y' \\ \frac{y'}{2b} (2b - y), & y > y' \end{cases} \quad (4.55)$$

As expected, the Green's function displays the usual property of symmetry between y and y' . With the Green's function known and the form of the source term ϱ_F given by its form in equation 4.47, we may directly construct the potential $\psi(y)$ via equation 4.54. In our numerical solution, Gauss-Legendre quadrature was used to integrate the kernel over the domain. Once this potential is known, we must know what it represents to reconstruct the velocity. In this case, ψ represents the kinetic energy of the flow, since the pressure gradient is constant. So, we may calculate the velocity as $u(y) = \sqrt{2\psi(y)}$. Notice that this approach circumvents the use of equation 4.41 to reconstruct the velocity; this will prove important when we discuss the results.

- *Solution Approach D. Method of images.* As a final approach to solve the duct flow system, we attempt to approximate it using the method of images for electrostatics. The method of images takes advantage of the uniqueness of a solution to pose an equivalent but easier problem with an identical solution, typically by adding fictitious charge in regions where the solution is not desired, to force the boundary conditions to be true. We select a slightly different choice of coordinate system extending over $y > 0$, where the solid wall is located at $y = 0$. It suffices to consider the domain to the centerline, since we anticipate that the solution will be symmetric. We construct an equivalent but simpler problem with the same boundary conditions by insisting on the presence of a fictitious charge

positioned a distance $y^* = -y$ away on the opposite side of the solid wall. To calculate the solution, we construct a Green's function, but including the fictitious charge contributions in addition to the ones in the domain of interest. We can once again formulate our problem as a Poisson equation as in equation 4.50; however, the auxiliary equation for the Green's function will contain both the real and fictitious charge contributions,

$$-\nabla^2 G(y; y') = -\delta(y - y') + \delta(y - y^*) \quad (4.56)$$

and our solution $\psi(y)$ can be calculated in a similar manner to the method discussed in Solution Approach C. The major difference in this approach is that equation 4.56 implies a different Green's function for the solution integral. Our new Green's function for the method of images will be [101] (following a similar approach to that described for Solution Approach C)

$$G(y; y') = -\frac{1}{2}|y - y'| + \frac{1}{2}|y - y^*| \quad (4.57)$$

Notice that this choice of the Green's function correctly satisfies the boundary condition at the wall, since here $G(0; y') = -(1/2)(y' - y^*)$. Since $y' = -y^*$, this vanishes at $y = 0$. Since $G(y; y')$ is now known, and the charge is given by equation 4.47, we may integrate both in equation 4.54 to get ψ , and once again calculate the velocity u from ψ in the same way as Solution Approach C.

These solution approaches were implemented in a simple Python simulation using the expressions for the source terms given in equations 4.47 and 4.48. The equations were solved in a nondimensional form, such that $b = 1$ and $A = 1$. The one-dimensional domain was discretized into 100 nodes for the calculation. The solutions determined using these approaches are presented in Figure 4.6. Due to symmetry, only half of the domain is shown, with the wall at $y = -1$ and the centerline at $y = 0$. We can see that the solution approaches generally agree. Observe that the solution approaches A and B fail near the centerline; this is expected, given their reliance on the drift relation, equation 4.41. Since the centerline $y = 0$ is technically irrotational and $\omega_z = 0$ along it, the velocity cannot be reconstructed at this point. This problem was not encountered in the Couette flow case, because Couette flow is fully vortical. This exposes a possible serious limitation to reconstructive schemes using the drift relation; regions of irrotationality are questionable for the validity of reconstructing the velocity vector in this region using equation 4.41; however, in this case, l'Hôpital's rule allows us to successfully circumvent this problem, and the correct velocity may be calculated along $y = 0$. Notice that solution methods C and D do not seem to have any such issue; in fact, the maximum error for both Green's function approaches is within 0.1%. Therefore, the bounded domain Green's function approach and the method of images provide excellent accuracy to resolving the correct solution. The solution approaches using reconstructive methods are very reasonable in the vortical regions of the duct (Solution Methods A and B achieved an error of 0.2% and 0.9%, respectively, in the vortical region) but near the centerline, where the vorticity goes to zero, the error increases due to their reliance on the drift relation

(Solution Methods A and B achieve an error of 2% and 100%, respectively, at the centerline). Although Solution Method A achieves a reasonable amount of error for the duct flow problem, the results are generally unpredictable and depend on the problem.

4.4.3 Blasius Boundary Layer Flow Solution

We now endeavor to study a problem that is much more complicated than the previous examples. The problem of viscous, laminar boundary layer evolution of an incompressible fluid across a flat plate is a well known problem with a theoretical solution [148] that matches very well to experimental data. The study of incompressible boundary layer flow also leads directly to the theory and study of compressible boundary layer flow. Here we study the incompressible form; we construct some source models from the known exact solution, and illustrate some solution procedures for this example.

If the flow is steady, incompressible, and laminar, and if the temperature gradient is small such that the transport properties may be assumed to be constant, then the continuity and momentum equations describing the flow may be written as

$$\nabla \cdot \mathbf{u} = \frac{\partial u}{\partial x} + \frac{\partial v}{\partial y} = 0 \quad (4.58)$$

$$u \frac{\partial u}{\partial x} + v \frac{\partial u}{\partial y} = \nu \frac{\partial^2 u}{\partial y^2} \quad (4.59)$$

where $\nu = \mu/\rho$ is the kinematic coefficient of viscosity. Since the temperature gradient is small, the flow is considered isothermal. A simple scaling argument may be constructed to show that the thickness of the boundary layer, $\delta(x)$, scales as

$$\delta(x) \sim \sqrt{\frac{\nu x}{U_\infty}} \quad (4.60)$$

Here U_∞ is the freestream velocity. Since there is no characteristic length scale in the x direction, the equations permit a similarity solution by transforming into the similarity plane, as sketched in Figure 4.7. We introduce the similarity variable $\eta = y/\delta(x) = y\sqrt{(U_\infty x)/\nu}$. By transforming into the similar plane, we may solve the equations in just η , and the resulting solution is a two-dimensional solution in x and y after inverse-transforming back to physical space. A generalized streamfunction may be constructed, $f(\eta)$, which automatically satisfies the continuity equation 4.58; the normalized velocity will be defined as $u/U_\infty = f'(\eta) = df/d\eta$, where we use the prime notation to denote differentiation with respect to the similarity variable. This approach was historically introduced by Blasius [148]; by substituting these quantities and transformations into the momentum equation, we are rewarded with the celebrated Blasius equation,

$$f''' + \frac{1}{2}ff'' = 0 \quad (4.61)$$

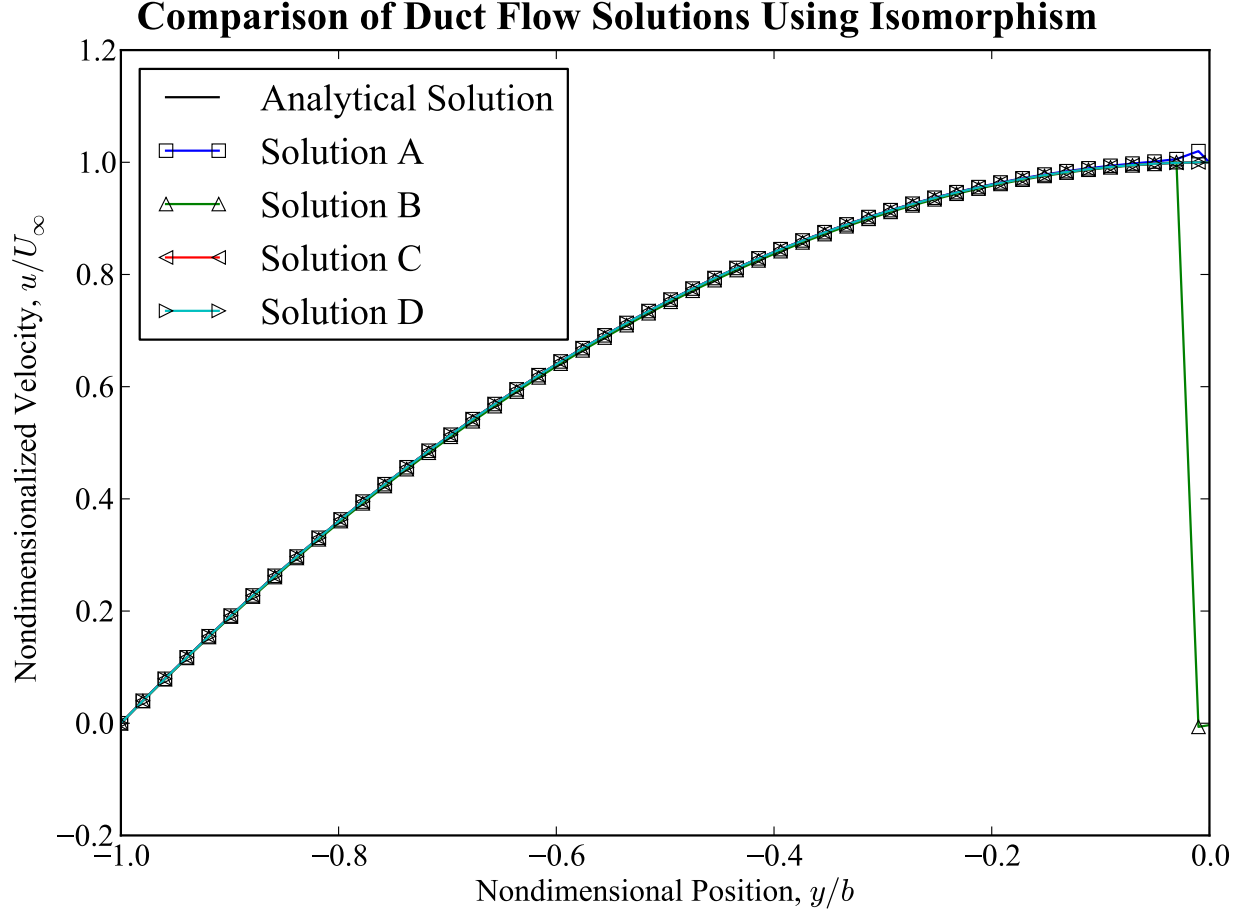


Figure 4.6: Plot of the different solution methods described in the text compared to the analytical duct velocity profile. Only half of the domain is shown for clarity, with the solid wall at $y = -1$ and the centerline at $y = 0$; the solution is symmetric across $y = 0$. Solution Methods A and B are reconstructive, using equation 4.41 to calculate the velocity, whereas Solution Methods C and D use Green's function approaches to solve for the potential. Solution Methods A and B achieve errors of 0.2% and 0.9% in the vortical region ($y < -0.1$), but reach errors of 2% and 100% in the center, since the vorticity vanishes and equation 4.41 becomes indeterminant. l'Hôpital's rule may be applied here to calculate the correct values of the velocity at the centerline. Solution Methods C and D achieve very low error (less than hundreds of a percent) across the entire domain.

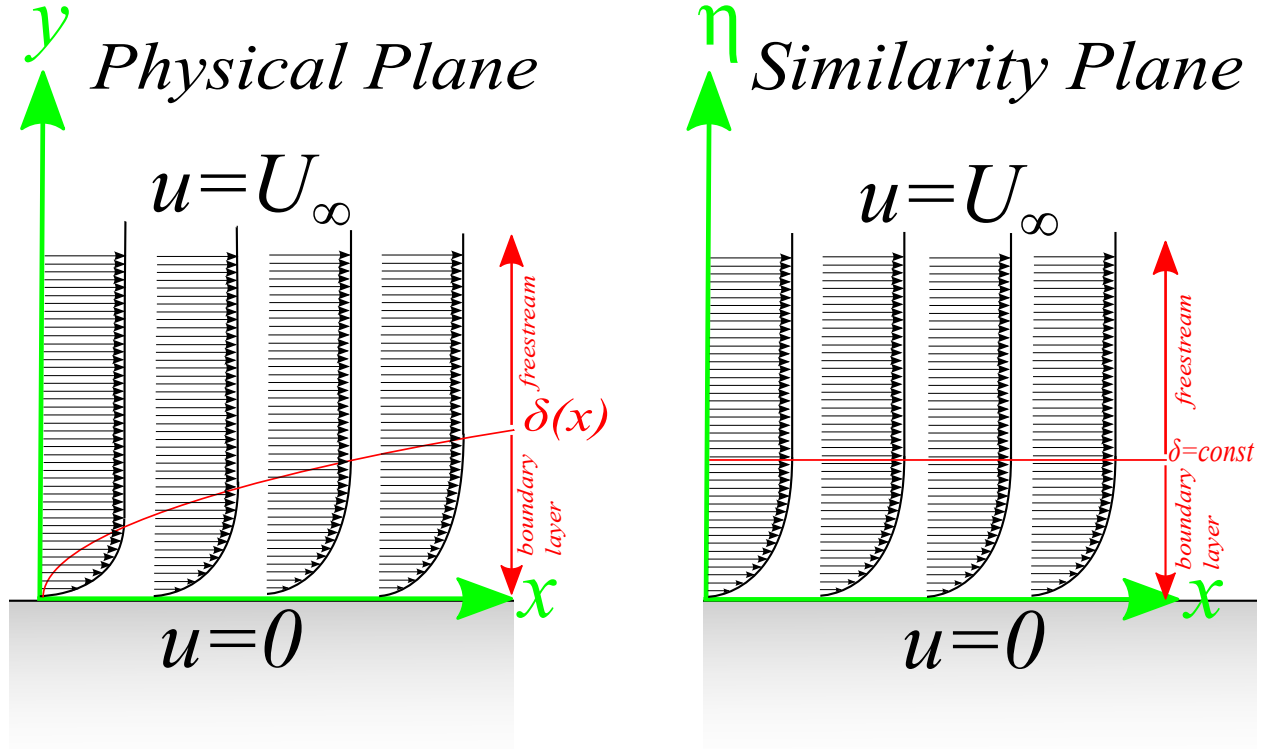


Figure 4.7: Diagram of the Blasius boundary layer flow problem. In the physical plane, the flow is two-dimensional, but the problem admits a similarity solution in the similarity plane. The quantity $\delta(x)$ denotes the boundary layer thickness. [6]

with boundary conditions $f(0) = f'(0) = 0$ and $f' \rightarrow 1$ as $\eta \rightarrow \infty$. This is a nonlinear, third-order ordinary differential equation that may be numerically solved using straightforward techniques. The solution has been recalculated using the shooting method in a simple Python script, and the results are shown in Figure 4.8. From this similarity solution, the appropriate velocity profile anywhere in the physical domain can be determined by transformation to the physical plane.

The fields may be calculated knowing that $u/U_\infty = f'$. The vorticity, $\omega = \omega_z \hat{z}$, is

$$\omega_z = -\frac{du}{dy} = -U_\infty \left(\frac{d\eta}{dy} \right) \frac{d}{d\eta} \left(\frac{u}{U_\infty} \right) \quad (4.62)$$

$$= -U_\infty \sqrt{\frac{U_\infty x}{\nu}} \frac{d}{d\eta} (f') \quad (4.63)$$

$$= -U_\infty \sqrt{\frac{U_\infty x}{\nu}} f'' \quad (4.64)$$

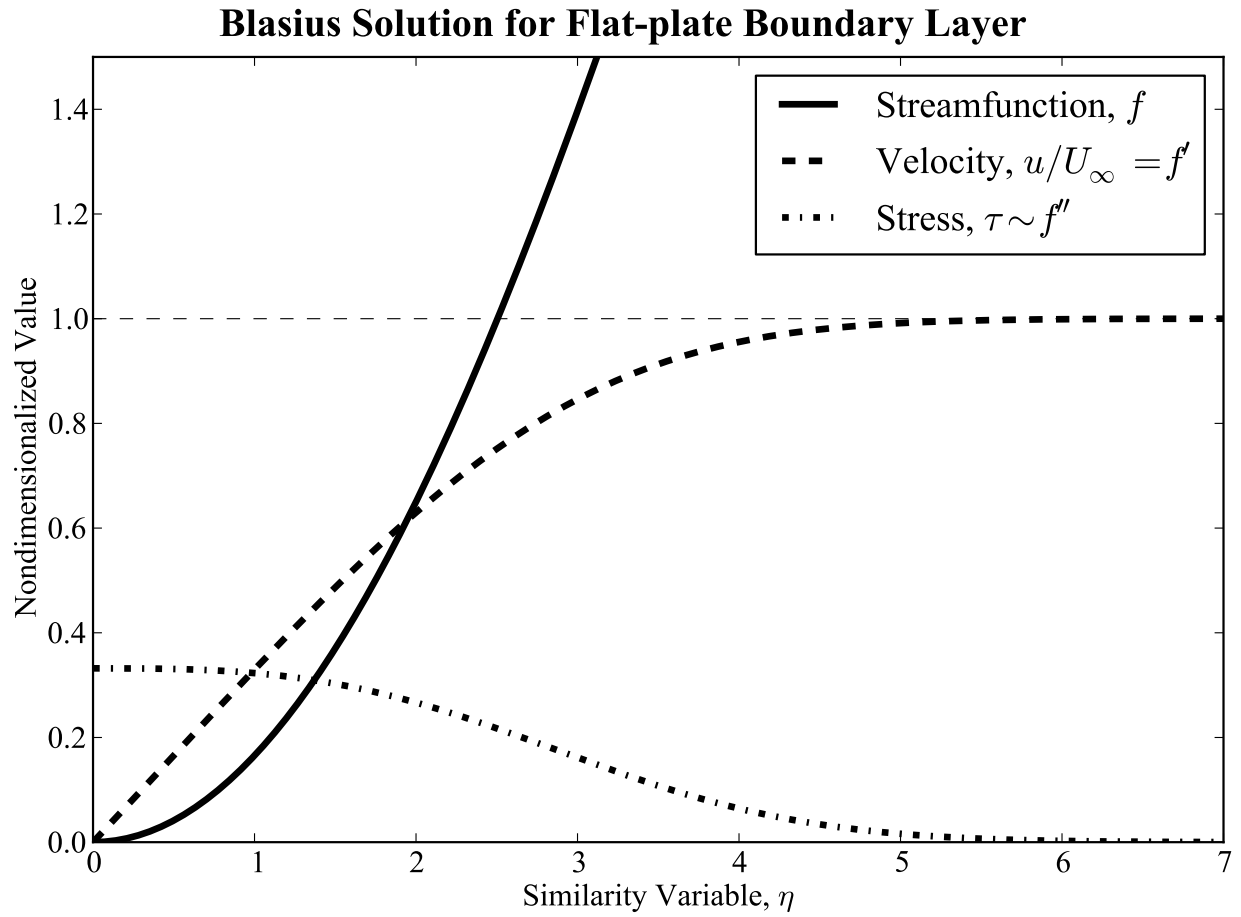


Figure 4.8: The classic numerical solution to the Blasius equation, equation 4.61. This solution was computed using the shooting method in a Python code.

The Lamb vector, $\zeta = \zeta_y \hat{y}$, will be

$$\zeta_y = \omega_z u = \left(-U_\infty \sqrt{\frac{U_\infty x}{\nu}} f'' \right) (U_\infty f') \quad (4.65)$$

$$= -U_\infty^2 \sqrt{\frac{U_\infty x}{\nu}} f' f'' \quad (4.66)$$

From these, the form of the charge and current density may be calculated,

$$\nabla \cdot \zeta = \varrho_F = \frac{d\zeta_y}{dy} = -U_\infty^2 \sqrt{\frac{U_\infty x}{\nu}} \left(\frac{d\eta}{dy} \right) \frac{d}{d\eta} (f' f'') \quad (4.67)$$

$$\varrho_F = -U_\infty^2 \left(\frac{U_\infty x}{\nu} \right) \left((f'')^2 + f' f''' \right) \quad (4.68)$$

and

$$\mathbf{j}_F = u^2 \nabla \times \boldsymbol{\omega} = u^2 \left(\frac{d\omega_z}{dy} \right) \quad (4.69)$$

$$= (U_\infty f')^2 \left(\frac{d\eta}{dy} \right) \frac{d}{d\eta} \left(-U_\infty \sqrt{\frac{U_\infty x}{\nu}} f'' \right) \quad (4.70)$$

$$= -U_\infty^2 \left(\frac{U_\infty x}{\nu} \right) \left((f')^2 f''' \right) \quad (4.71)$$

The fields, ζ_y and ω_z , are shown in Figure 4.9. The fields were calculated both directly from equations 4.62 and 4.65 and differenced from the velocity vector; both approaches agreed. The analytical expressions for the source terms, given in equations 4.67 and 4.69 are shown in Figure 4.10, along with a tenth-order polynomial fit¹ to these expressions. The coefficients for the polynomial fit are presented in Table 4.1. In the solution approaches explored below, the polynomial fit to the source terms was used.

With a knowledge of the source terms, we may broach the question of how to calculate numerical solutions for Blasius boundary layer flow by leveraging the isomorphic equations instead. The same solution approaches (analogous to those applied for duct flow) are utilized here:

- *Solution approach A.* This once again was not a true solution approach; the vorticity was taken as given from equation 4.62. The Lamb vector, ζ_y , was calculated by directly integrating the Gauss law, given the interpolated form of the charge density. The velocity was calculated using the drift relation given in equation 4.41. This permitted a check on the drift relation, although the vorticity was assumed to be known in this case.
- *Solution approach B. Reconstructive iteration approach.* In this approach, the Lamb vector was first calculated by integrating the Gauss law given the form of the interpolated charge density. Next, the vorticity was calculated using an iterative scheme identical to that for duct flow, where the Ampere-

¹Tenth-order polynomials were chosen because any less order tended to show some disagreement at the wall, which could introduce violations to the no-slip condition when applying the solution methods discussed below.

Table 4.1: Coefficients for a tenth-order polynomial fit for the Blasius charge distribution.

k	α_k
0	0.109661
1	0.0129543
2	-0.0573069
3	0.0853625
4	-0.0879662
5	0.0408102
6	-0.00915218
7	0.000930392
8	-0.00001244
9	-4.83213e-6
10	2.68597e-7

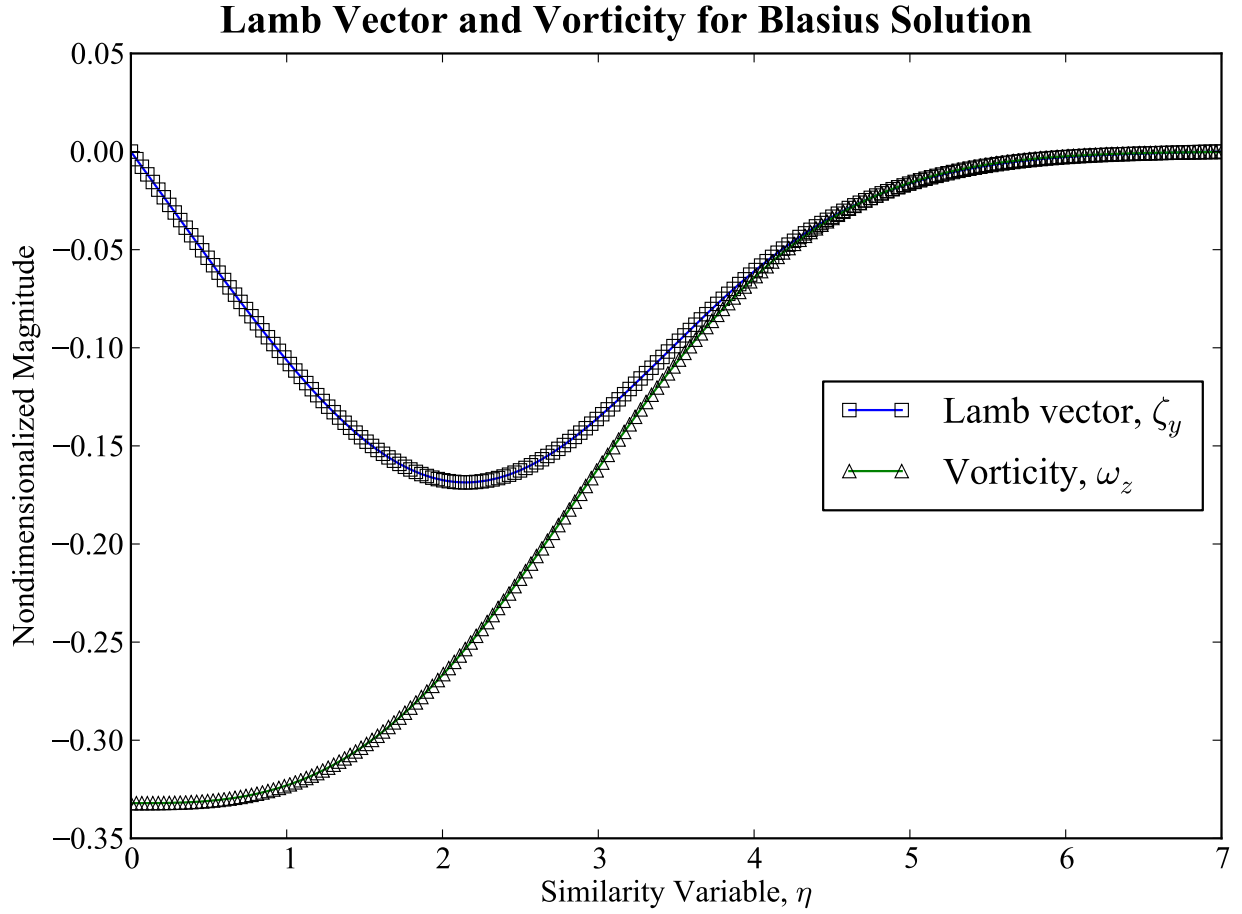


Figure 4.9: The calculated Lamb vector, ζ_y , and vorticity, ω_z , for the Blasius solution. Differencing the solution directly and using the expressions given in equations 4.65 and 4.62 give identical results.

Comparison of Boundary Layer Solutions Using Isomorphism

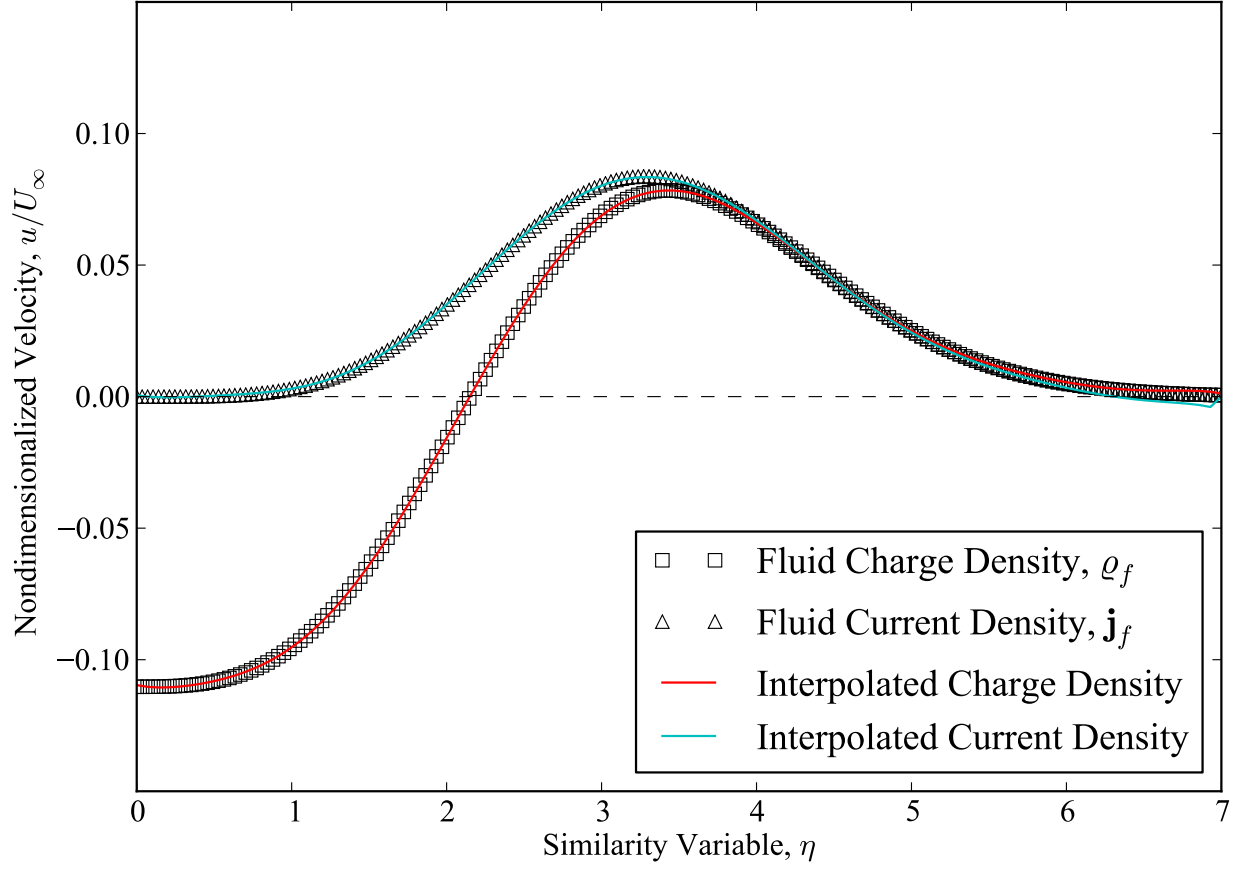


Figure 4.10: The calculated source terms, ϱ_F and $j_{F,x}$, for Blasius layer flow. These results qualitatively agree with Marmanis' results for turbulent, incompressible flow [108, 109], although the source terms are closer to the wall in turbulent flows since the velocity profile is flatter. In the freestream, the flow becomes homogeneous, and no source terms appear.

Maxwell equation was solved for vorticity, the drift relation was used to update the velocity field, and the average velocity was recalculated using the new field. The iteration was terminated once the average velocity converged; a tolerance of 10^{-5} was used for determining convergence.

- *Solution approach C. Bounded-domain Green's function.* This approach followed the same bounded-domain approach used for duct flow; we take advantage of the fact that $\nabla \times \zeta = 0$ to formulate a Poisson equation for a potential,

$$-\nabla^2 \psi(\eta) = \varrho_F \quad (4.72)$$

We may solve this equation by constructing a Green's function that satisfies the auxiliary equation,

$$-\nabla^2 G(\eta; \eta') = \delta(\eta - \eta') \quad (4.73)$$

where we wish to solve the equation in the semi-infinite domain $\eta > 0$. The application of a bounded-domain approach to solve a semi-infinite problem is questionable, but as long as the domain is considered larger than the boundary layer itself (i.e., if we have some upper-limit estimate, L , that exceeds the boundary layer thickness, $L > \delta(x)$) then we should still resolve the solution within this region. The wall is placed at $\eta = 0$. Application of Green's identity yields

$$\int_0^L \{ \psi(\eta) \nabla^2 G(\eta; \eta') - G(\eta; \eta') \nabla^2 \psi(\eta') \} d\eta' = \left[\psi(\eta) \frac{dG}{d\eta} - G(\eta; \eta') \frac{d\psi}{d\eta} \right]_0^L \quad (4.74)$$

Here the appropriate boundary conditions are $\psi(0) = 0$, $\psi(L) = 1/2$ (which assumes that the velocity has reached the freestream value at L), and corresponding homogeneous conditions for the Green's function, $G(0) = 0$ and $G(L) = 0$. Applying these, we have

$$\int_0^L \{ \psi(\eta) \nabla^2 G(\eta; \eta') - G(\eta; \eta') \nabla^2 \psi(\eta') \} d\eta' = \frac{1}{2} \frac{dG}{d\eta} \Big|_L \quad (4.75)$$

Direct substitution of equations 4.72 and 4.73 into equation 4.75 gives

$$-\int_0^L \psi(\eta) \delta(\eta - \eta') d\eta' + \int_0^L G(\eta; \eta') \varrho_F(\eta') d\eta' = \frac{1}{2} \frac{dG}{d\eta} \Big|_L \quad (4.76)$$

Again integrating over the Dirac delta distribution, $\int_0^L \psi(\eta) \delta(\eta - \eta') d\eta' = \psi(\eta)$, and rearranging to solve for $\psi(\eta)$, we have

$$\psi(\eta) = \int_0^L G(\eta; \eta') \varrho_F(\eta') d\eta' - \frac{1}{2} \frac{dG}{d\eta} \Big|_L \quad (4.77)$$

We must calculate the Green's function by solving equation 4.73; we once again take advantage of the

jump conditions as discussed in the duct flow section, and our Green's function is

$$G(\eta; \eta') = \begin{cases} \frac{\eta}{L} (L - \eta'), & \eta < \eta' \\ \frac{\eta'}{L} (L - \eta), & \eta > \eta' \end{cases} \quad (4.78)$$

Using the symmetry property of the Green's function, the derivative term $dG/d\eta|_L$ in equation 4.77 will be

$$\left. \frac{dG}{d\eta} \right|_{\eta=L} = \left. \frac{dG}{d\eta'} \right|_{\eta'=L} = \frac{d}{d\eta'} \left[\frac{\eta}{L} (L - \eta') \right] = -\frac{\eta}{L} \quad (4.79)$$

and substitution of this into equation 4.77 yields

$$\psi(\eta) = \int_0^L G(\eta; \eta') \varrho_F(\eta') d\eta' + \frac{\eta}{2L} \quad (4.80)$$

Equipped with a knowledge of the Green's function (equation 4.78), the integral form of the solution (equation 4.80), and the interpolated polynomial form of the charge density, ϱ_F , we may numerically integrate the solution over the bounded domain $0 < \eta < L$. For this investigation, we took $L = 7$, which includes the entire boundary layer within it. The integration was performed numerically using Gauss-Legendre quadrature. In Section 4.4.4, we also examine the construction of a closed-form solution using this approach.

- *Solution approach D. Method of images.* As discussed earlier, the application of the method of image charges can often be exploited for electrostatic problems with great success. In this case, we demonstrate the application of this technique to Blasius boundary layer flow. We place a fictitious charge on the other side of the solid wall (which is positioned at $\eta = 0$), a distance $\eta^* = -\eta$ away from the point η of consideration. The sum of the charges ensures that the boundary condition is met at the wall. The auxiliary equation for the Green's function now possesses the contribution from both the real and fictitious charges,

$$-\nabla^2 G(\eta; \eta') = \delta(\eta - \eta') - \delta(\eta - \eta^*) \quad (4.81)$$

Solving this equation for the Green's function [101], we have

$$G(\eta; \eta') = -\frac{1}{2} |\eta - \eta'| + \frac{1}{2} |\eta - \eta^*| \quad (4.82)$$

Following a similar analysis as that provided above, our solution may be written as

$$\psi(\eta) = \int_0^\infty G(\eta; \eta') \varrho_F(\eta') d\eta' \quad (4.83)$$

where the Green's function is provided in equation 4.82 and the charge density, ϱ_F , is given by its

interpolated polynomial expression. We integrated up to $\eta = 7$, which includes the entire boundary layer and at which point the charge density has fallen to zero.

These solution approaches were applied to the Blasius boundary layer problem; the results are shown in Figure 4.11. At first glance, one immediately notes that the solution approaches A and B failed in the freestream region. This is expected, since the drift relation becomes indeterminate in this region; hence, we again see limitations surface in using reconstructive schemes that calculate the velocity field using the drift relation, since it is only strictly valid in vortical region (approximately $\eta < 5$). Solution approaches C and D achieved remarkable accuracy, less than 0.1% from the accepted Blasius solution. The bounded-domain solution actually turned out to be slightly better than the method of images approach, although the domain was treated as a bounded domain.

4.4.4 Closed-form Blasius Solution Using a Bounded-Domain Green's Function Approach

It is worth pointing out that, while the method of images and bounded-domain approaches were performed numerically, the equations permit a closed-form solution that may be accomplished using rather straightforward mathematics. Suppose the specific form of the charge density takes the form as a tenth-order polynomial (the same used in the interpolations above),

$$\varrho_F = \sum_{k=0}^{10} \alpha_k \eta^k \quad (4.84)$$

with the coefficients, α_k , presented in Table 4.1. The integral form of the solution $\psi(\eta)$ is given by equation 4.80. Substituting equation 4.84 in for the charge density, $\varrho_F(\eta')$, we have

$$\psi(\eta) = \int_0^L G(\eta; \eta') \sum_{k=0}^{10} \alpha_k \eta'^k d\eta' + \frac{\eta}{2L} \quad (4.85)$$

We now directly substitute the Green's function in equation 4.78 into our integration; since the treatment near $\eta = \eta'$ requires care, we may split the integration up at this point,

$$\psi(\eta) = \int_0^\eta \frac{\eta'}{L} (L - \eta) \sum_{k=0}^{10} \alpha_k \eta'^k d\eta' + \int_\eta^L \frac{\eta}{L} (L - \eta') \sum_{k=0}^{10} \alpha_k \eta'^k d\eta' + \frac{\eta}{2L} \quad (4.86)$$

Distributing the integration, we have

$$\begin{aligned} \psi(\eta) = & \int_0^\eta \eta' \sum_{k=0}^{10} \alpha_k \eta'^{k-1} d\eta' - \frac{\eta}{L} \int_0^\eta \sum_{k=0}^{10} \alpha_k \eta'^k d\eta' + \\ & \eta \int_\eta^L \sum_{k=0}^{10} \alpha_k \eta'^{k-1} d\eta' - \frac{\eta}{L} \int_\eta^L \eta' \sum_{k=0}^{10} \alpha_k \eta'^k d\eta' + \frac{\eta}{2L} \end{aligned} \quad (4.87)$$

Comparison of Boundary Layer Solutions Using Isomorphism

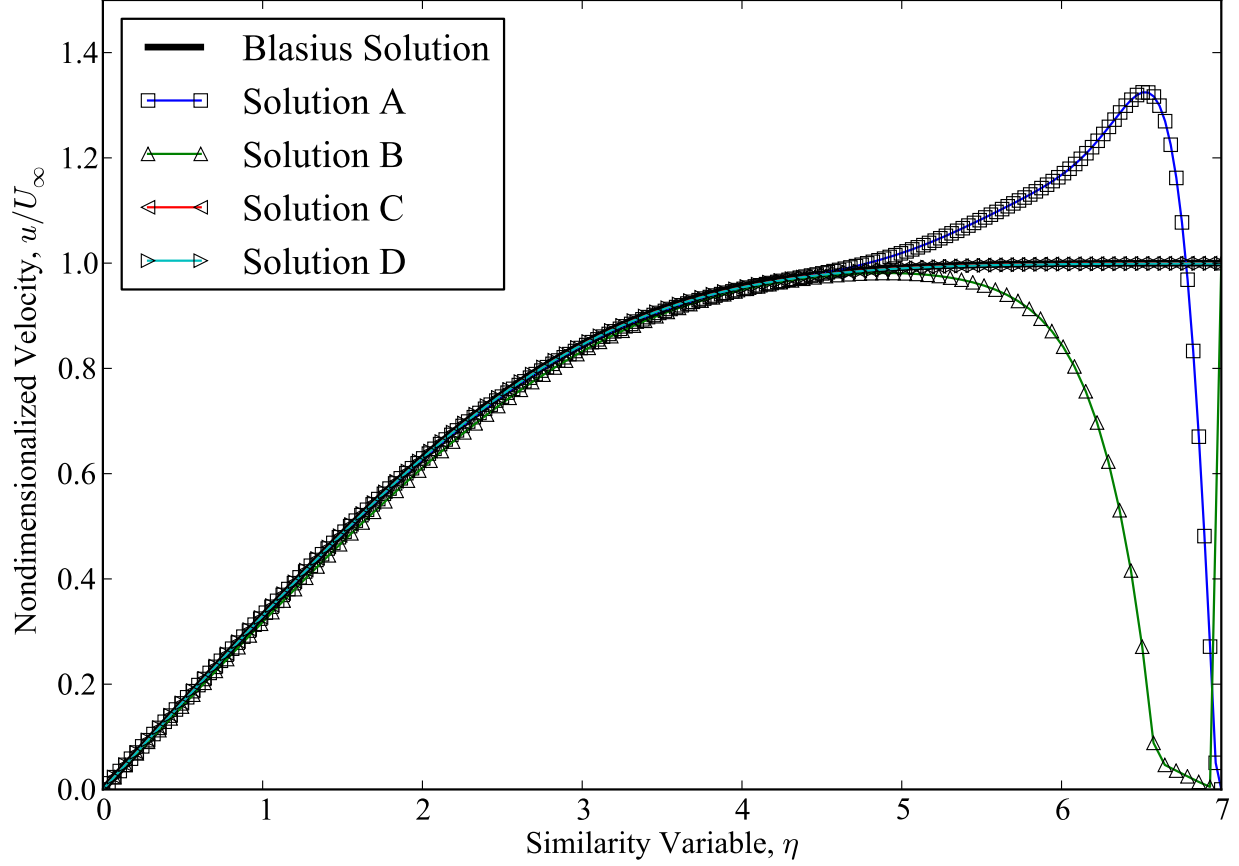


Figure 4.11: Blasius solution calculated using the isomorphic equations with a given charge distribution. Four different solution methods were attempted: (A) a check on the drift relation, (B) an iterative scheme that reconstructs the velocity by solving for Lamb vector and vorticity and using the drift relation, (C) a bounded-domain Green's function approach for calculating the kinetic energy, and (D) a method of images approach. The reconstructive schemes failed in the irrotational region, since the drift relation becomes indeterminant as $\omega \rightarrow 0$. Methods (C) and (D) matched remarkably well, with error much less than 1%.

We are further permitted to exchange the integration with the summation, which yields

$$\psi(\eta) = \sum_{k=0}^{10} \alpha_k \left\{ \int_0^\eta \eta'^{k+1} d\eta' - \frac{\eta}{L} \int_0^\eta \eta'^{k+1} d\eta' + \eta \int_\eta^L \eta'^k d\eta' - \frac{\eta}{L} \int_\eta^L \eta'^{k+1} d\eta' \right\} + \frac{\eta}{2L} \quad (4.88)$$

While this expression is cumbersome, the integrations involve only polynomials, and so are rather straightforward. Integrating yields

$$\psi(\eta) = \sum_{k=0}^{10} \alpha_k \left\{ \frac{L-\eta}{L} \left(\frac{\eta^{k+2}}{k+2} \right) + \eta \left(\frac{L^{k+1}}{k+1} - \frac{\eta^{k+1}}{k+1} \right) - \frac{\eta}{L} \left(\frac{L^{k+2}}{k+2} - \frac{\eta^{k+2}}{k+2} \right) \right\} + \frac{\eta}{2L} \quad (4.89)$$

Some manipulation reveals

$$\psi(\eta) = \sum_{k=0}^{10} \alpha_k \left\{ (\eta L^{k+1} - \eta^{k+2}) \left(\frac{1}{k+1} - \frac{1}{k+2} \right) \right\} + \frac{\eta}{2L} \quad (4.90)$$

Since $\psi(\eta)$ represents the kinetic energy per unit mass, $\psi(\eta) = u^2/2$, we may solve for the velocity vector as

$$u(\eta) = \sqrt{\frac{\eta}{L} + 2 \sum_{k=0}^{10} \alpha_k (\eta L^{k+1} - \eta^{k+2}) \left(\frac{1}{k+1} - \frac{1}{k+2} \right)} \quad (4.91)$$

This closed form expression for the velocity is plotted against the numerical solution (from Solution Method C in Figure 4.11) in Figure 4.12. If we choose $\eta = L$, we see that the solution given in equation 4.91 becomes exactly $u(\eta) = 1$. Hence, equipped with source term information, the field equations permit closed-form solutions in much the same way as classical electrodynamics. Other more exotic techniques could also be employed, such as multipole expansions or similar numerical approaches, such as Yee's algorithm.

Although Blasius boundary layer flow represents a problem that already has a solution, these approaches demonstrate the feasibility of applying approaches borrowed from classical electrodynamic to solve such flows in a very similar manner to the treatment of electric and magnetic fields. Also, through our investigation of Couette, duct and Blasius flow, we have collected three simple source terms for fluids that may be *superposed* with other fluid or electric charge to construct more complicated flows for fluids or plasmas.

4.4.5 Gasdynamic and Magnetohydrodynamic Charge from Numerical Simulations

For cases when analytic expressions are not available for constructing simple source models, we may resort to numerical simulation and postprocessing. A particularly interesting case to investigate is the source behavior of shock waves. Although we will not perform an in-depth quantitative investigation, we will build to our intuition of the sources by examining the behavior of the charge for an oblique shock.

Consider inviscid, supersonic flow impinging upon a wedge at some fixed angle; this will establish an oblique shock wave. The incoming freestream Mach number, wedge angle and shock angle are all related. To

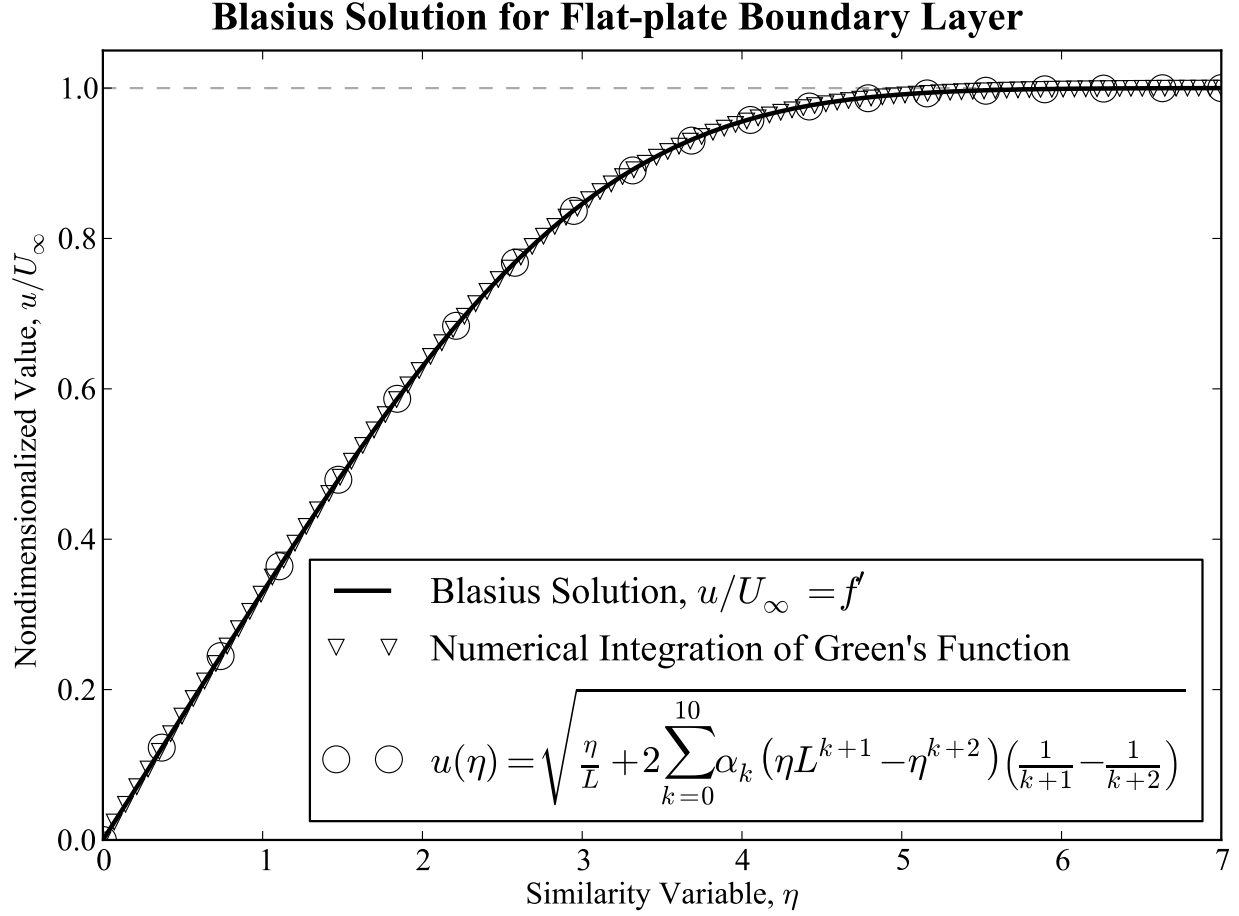


Figure 4.12: Comparison of the accepted Blasius velocity profile (computed numerically using the shooting method), and the numerical and closed-form (equation 4.91) solutions obtained using the bounded-domain Green’s function approach. This approach requires some estimated upper limit that bounds the boundary layer, L . It is not necessary that L be the boundary layer thickness, $\delta(x)$, simply that $\delta(x) < L$. Here, $L = 7$.

visually depict the form of the gasdynamic charge, we calculated a numerical solution to this problem for an incoming flow of air at Mach number $M = 2.5$, to a wedge of angle of $\theta = 15^\circ$. The domain was rectangular, $[0, 1.7] \times [0, 0.8]$ respectively, and was populated with a fully unstructured triangular mesh consisting of 36,389 triangular control volumes, as shown in Figure 4.13. The same numerical procedure described later in Chapter 5 was used, except with no electromagnetics present.

The solution was evolved unsteadily until a steady-state condition was reached. The final solution is shown in Figure 4.14. Behind the shock, the expected Mach number should be 1.87, and the shock angle is predicted to be 36.9° [149]. In the solution presented in Figure 4.14, the smallest Mach number behind the shock is 1.85 (this was the largest observed deviation from the theoretical value), and the shock angle was measured visually to be 36.5° ; this is within 1.4% and 1.2% of the theoretical values, respectively.

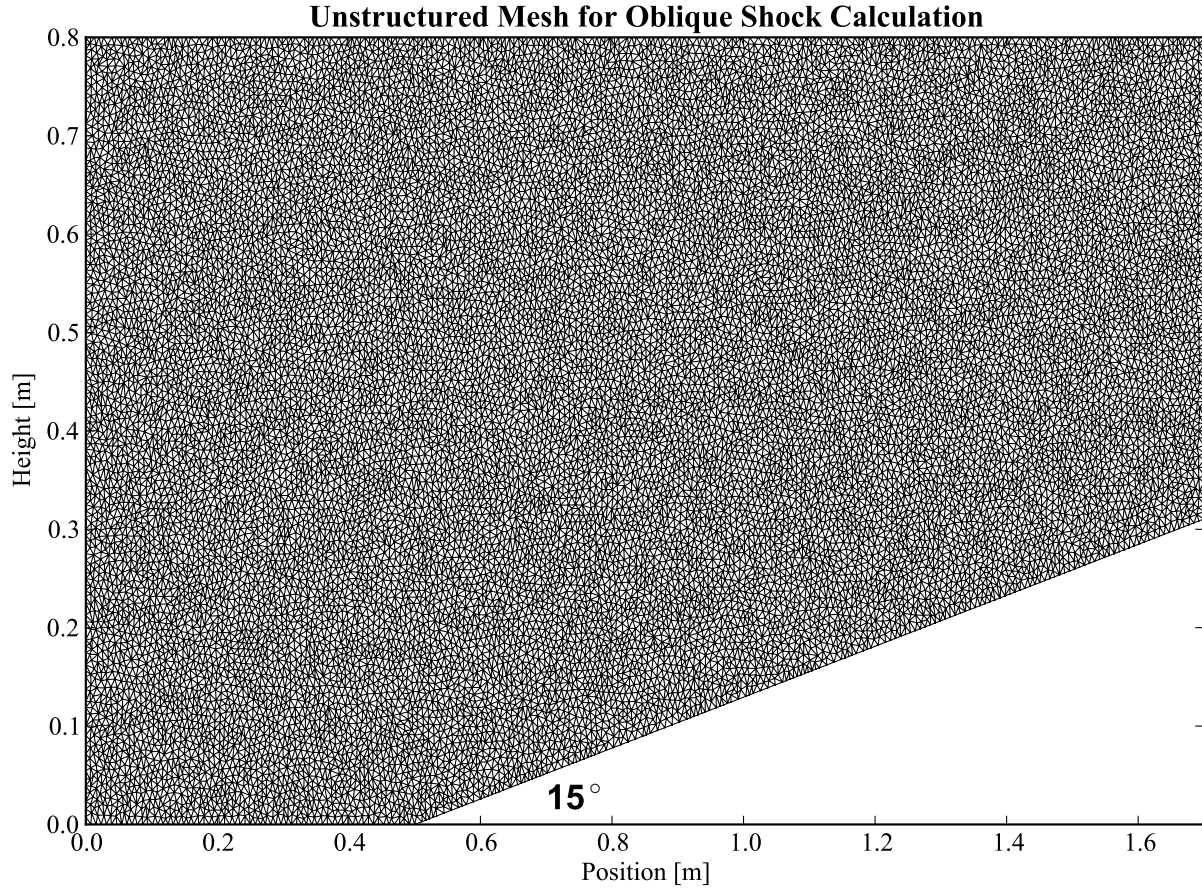


Figure 4.13: Unstructured mesh used for calculating the oblique shock. The mesh is composed of 36,389 elements.

Once the solution was calculated, the gasdynamic charge was postprocessed in its microscopic form. The result is shown in Figure 4.15. The shock itself possesses a characteristic structure of microscopic charge in its vicinity. In Figure 4.16, a convolving average was performed using the test function given in equation 3.33 and an averaging radius of $R = 5\Delta x = 0.158m$.

The convolved form of the gasdynamic charge shows that the shock could be approximated by *representing it as a surface of charge*. This is analogous to an interface between materials in electrodynamics, where the material properties cause a discontinuous jump in the normal component of the electric field and the tangential component of the magnetic field. We derived similar boundary conditions in Section 3.5.3, where we showed that the same conditions apply at boundary interfaces for ζ_α and Ω_α .

An effort was also made to qualitatively explore the form of the source terms for plasmas of interest. Particularly, we examined the postprocessing of source data from the Orzsag-Tang magnetohydrodynamic vortex problem [142] and the hydrodynamic Kelvin-Helmholtz problem [150]. These problems represent

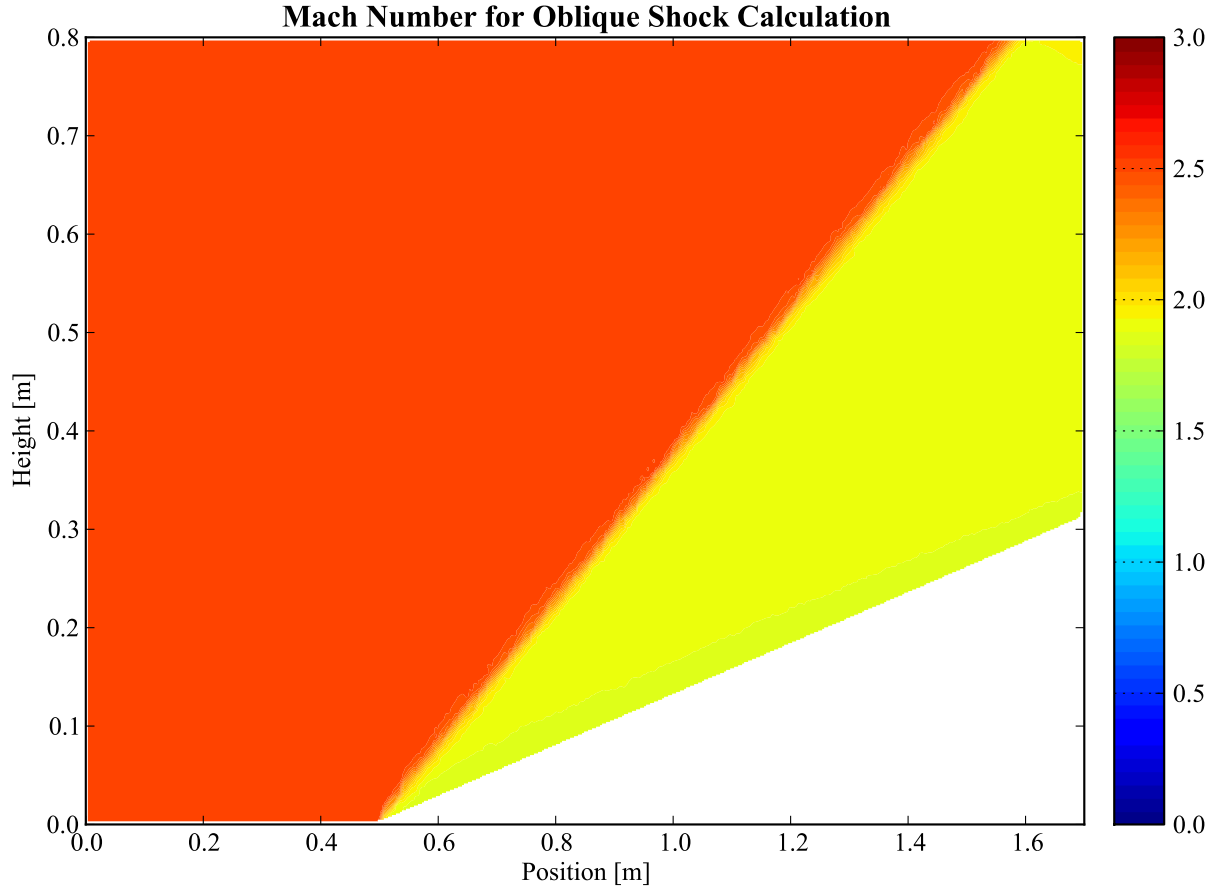


Figure 4.14: Mach number of the oblique shock solution after a steady-state condition was reached. The Mach number left of the shock is 2.5, while the Mach number behind the shock reaches a minimum of 1.848 along the lower boundary (a slight dip in the solution occurs here), while the oblique shock relations yield a downstream Mach number of 1.874; this is within 1.4% of the theoretical value. The angle of the oblique shock was measured visually to be 36.5° , while the predicted shock angle is 36.9° ; this is within 1.2%.

unsteady inviscid, compressible plasma evolution with instabilities and turbulence. The postprocessed data is at least representative of what we can expect the plasma source term data to resemble.

The Orszag-Tang and Kelvin-Helmholtz problems are described in much more detail in Sections 6.5 and 6.4. Both were performed using structured grids. The initial conditions and simulation parameters for the postprocessed source terms were identical to those presented in these two respective sections. The numerical formulation used for simulation was that described in Chapter 5. In Figure 4.17, we see an abundance of charge structures propagating through the domain. These structures arise due to the time-varying compressive nature of the medium, propagating shocks, and spatial arrangement of the enthalpy. A convolved average of this data is presented in Figure 4.18, where we see that the propagating shocks contribute significant charges, while most of the small-scale charge has been averaged out. However, several

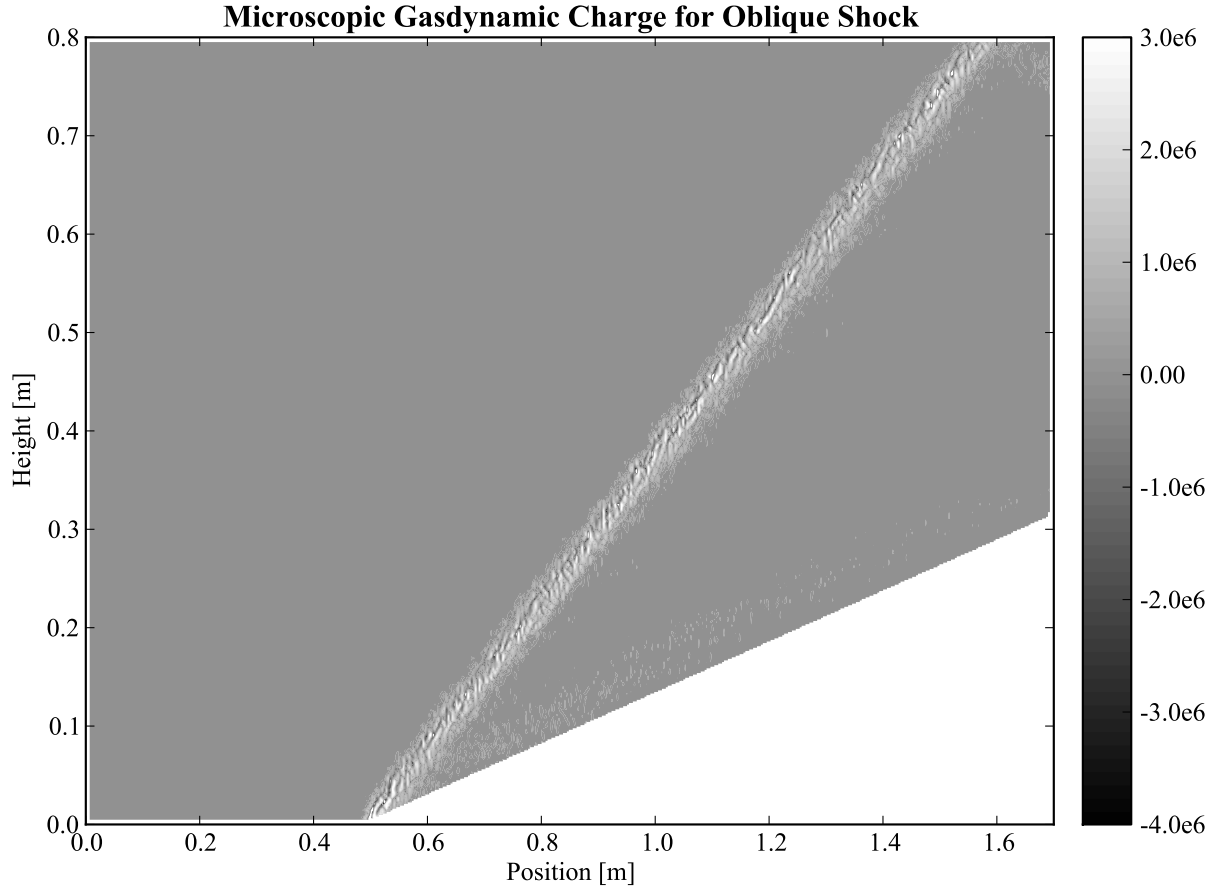


Figure 4.15: The microscopic gasdynamic charge for the oblique shock problem.

of the significant flow structures are associated with the small-scale charge structures, and empirical models of this problem would require predicting the time evolution of these small-scale charges.

The Kelvin-Helmholtz instability reveals an expected charge distribution near sharp gradients in density (see Figure 4.19). There is little microscopic charge that is filtered out by the convolving average (see Figure 4.20). The simulations of the Orszag-Tang and Kelvin-Helmholtz flows reveal that time-dependent phenomena would be difficult to construct accurate source models for simulation, since the charge must evolve correctly over time. For time-varying simulations using empirical data, one would need a charge model that would reflect the evolving behavior of the charge data. Since this involves significant data collection and modeling, it was not attempted here and remains to be examined in future work. It is also clear that time-evolving plasmas will demand more detailed empirical models; whereas in the oblique shock case, we seek a steady-state solution and therefore the time-dependent contributions to the charge do not appear in the final solution, we must include these contributions accurately in a time-dependent problem. This represents

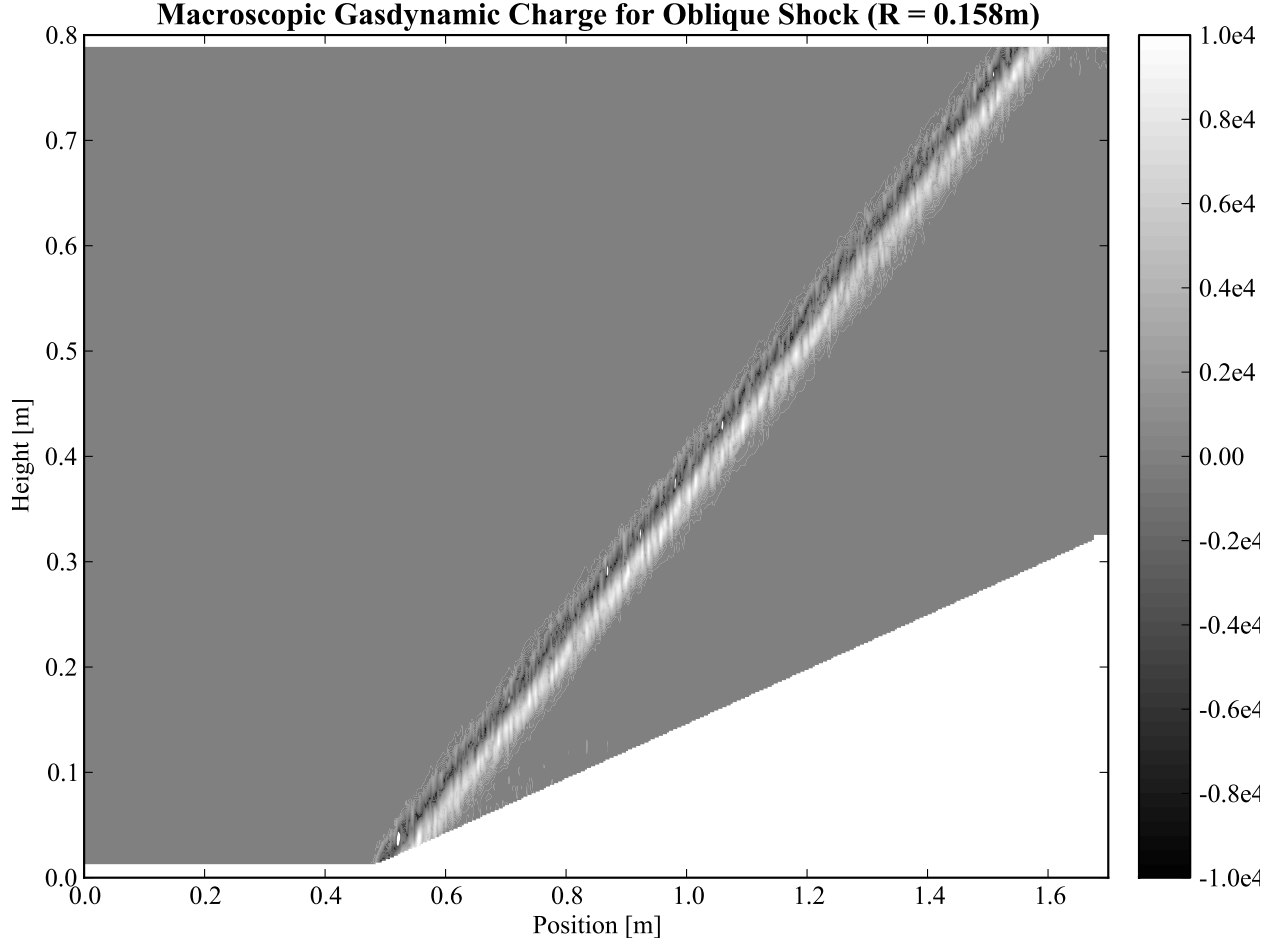


Figure 4.16: A convolved macroscopic gasdynamic charge distribution for the oblique shock problem. The averaging length here was $R = 5\Delta x \sim 0.158m$. The region of charge near the shock is thinner and more uniform than the microscopic charge presented in Figure 4.15. This investigation implies that the charge at a shock could potentially be treated as a surface of charge, similar to an interface with a discontinuous jump in classical electrodynamics.

a significant challenge to modeling plasmas using empirical formulations of the source terms, since the time dependency would have to be somehow anticipated within the source model. Steady-state solutions are much more readily constructable, since no time-dependence of the source behavior is required. This is a realm of modeling that would enjoy superior improvement using iterative or reconstructive approaches, if the reconstruction were successful.

4.5 Summary of Solution Approaches

The homogeneous approach is direct and mathematically convenient; there may be physical cases where this assumption is valid. When it is, the source terms vanish, and a set of ‘vacuum’ equations may be

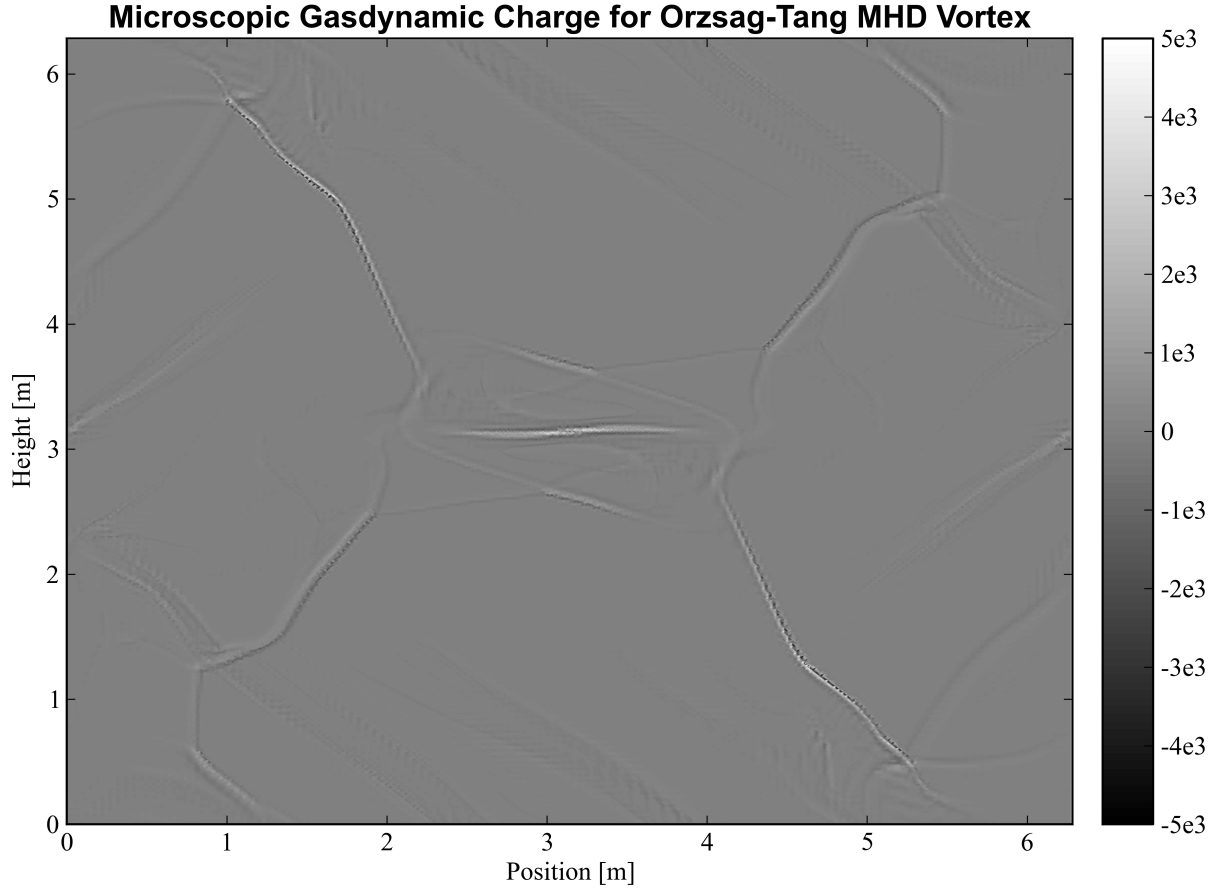


Figure 4.17: The microscopic form of the generalized charge for the Orzsag-Tang MHD vortex problem. The charge is intrinsically time-dependent, and so is changing each timestep.

solved instead. A homogeneous set of wave equations result that predict the evolution of waves in the generalized fields. We were able to show using the homogeneous approximation that the usual collection of magnetohydrodynamic waves are included in these generalized waves.

Inhomogeneous wave equations exist, but require more investigation.

For incompressible fluids, we examined three cases with known analytical solutions, and predicted the quantitative form of the source terms for these cases. These represent valuable starting points for future work in which these source terms may be superposed to study more complicated flow. Notice that, in the cases studied, we needed the solution to the problem beforehand, to determine the form of the source terms. Once the source terms were discovered and assumed to be known, we illustrated several creative approaches to solving these fluid problems by considering techniques from classical electrodynamics, including iterative schemes, Green's function approaches, and the method of images. It is anticipated that a library of these source terms could serve as building blocks for more complicated flows; the superposition of these charges

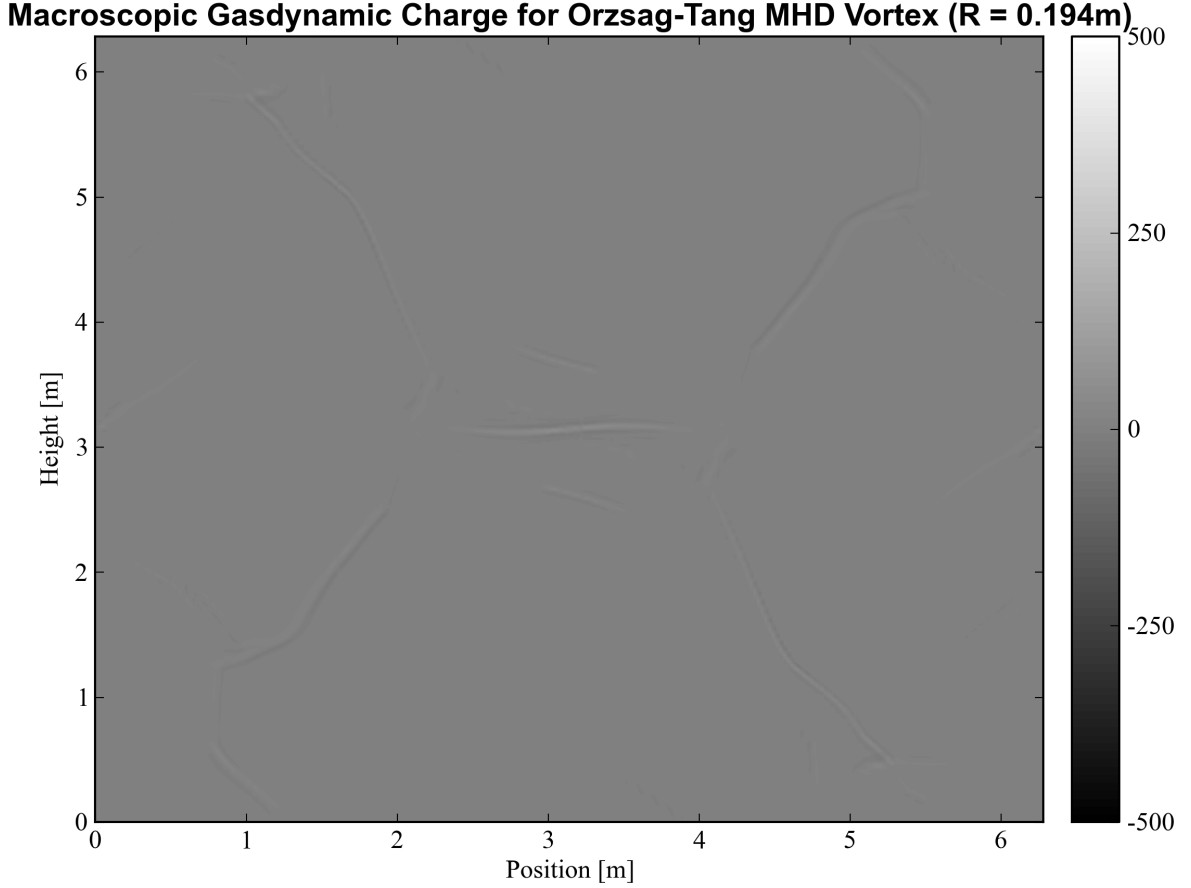


Figure 4.18: The macroscopic, convolved charge distribution for the Orzsag-Tang MHD vortex problem. The averaging length here was $R = 3\Delta x \sim 0.194m$. Notice that the small-scale noise and ripples have been averaged out; only the surface charge due to shocks remain, similar to that seen in the oblique shock source data.

and currents would then allow for determining numerical and closed-form solutions to more complicated problems without requiring that we solve the problem first to discover the form of the sources. If efficient iterative schemes were discovered, this would also significantly help, as the source terms could be solved in tandem with the fields as they were converged to physically correct values for complicated fluid and plasma problems.

We also successfully demonstrated that both numerical and closed-form solution approaches can be applied. It is anticipated that these approaches would be much more successful if efficient iterative methods were discovered that could be exploited to solve fluid and plasma problems without requiring an accretion of empirical building-block models. However, at present, the approach of accumulating fundamental empirical models that may be reused to construct solutions to more complicated flow problems represents a more

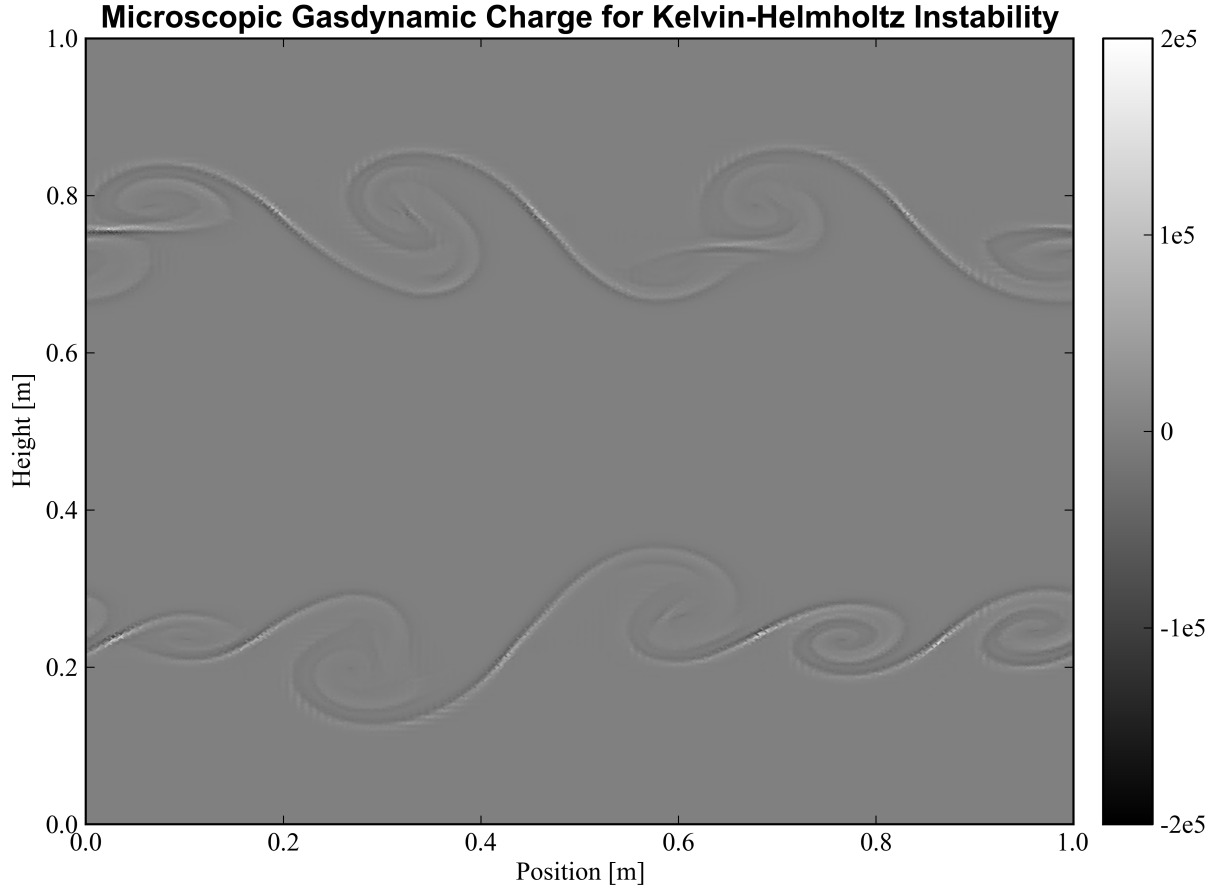


Figure 4.19: The microscopic charge distribution from a Kelvin-Helmholtz hydrodynamic instability.

promising methodology for utilizing the isomorphism.

For the more relevant problems of compressible fluids and plasmas, more source data is needed before the empirical modeling approach will become sustainable for efficiently calculating solutions. The difficulty in constructing these source models can easily be perceived by the silence in the literature for addressing these issues, even after several repeated attempts to exploit the Maxwell form of fluid dynamic equations for several different investigations. Marmanis' work was perhaps the most successful of these endeavors, as it did in fact lay out source data for turbulent flow, and this was used to demonstrate remarkable accuracy in predicting turbulent mean flow solutions; however, compressible and plasma approaches [110, 119, 121, 135] have not yet shown such models and have only presented theories of how this approach could be utilized. The results in this chapter represent an advance in our understanding and utilization of these source models, and the Blasius solution predicted qualitatively agrees with data that Marmanis presents, although the two have been examined for different cases. One can easily see from the examples presented above how the gathering

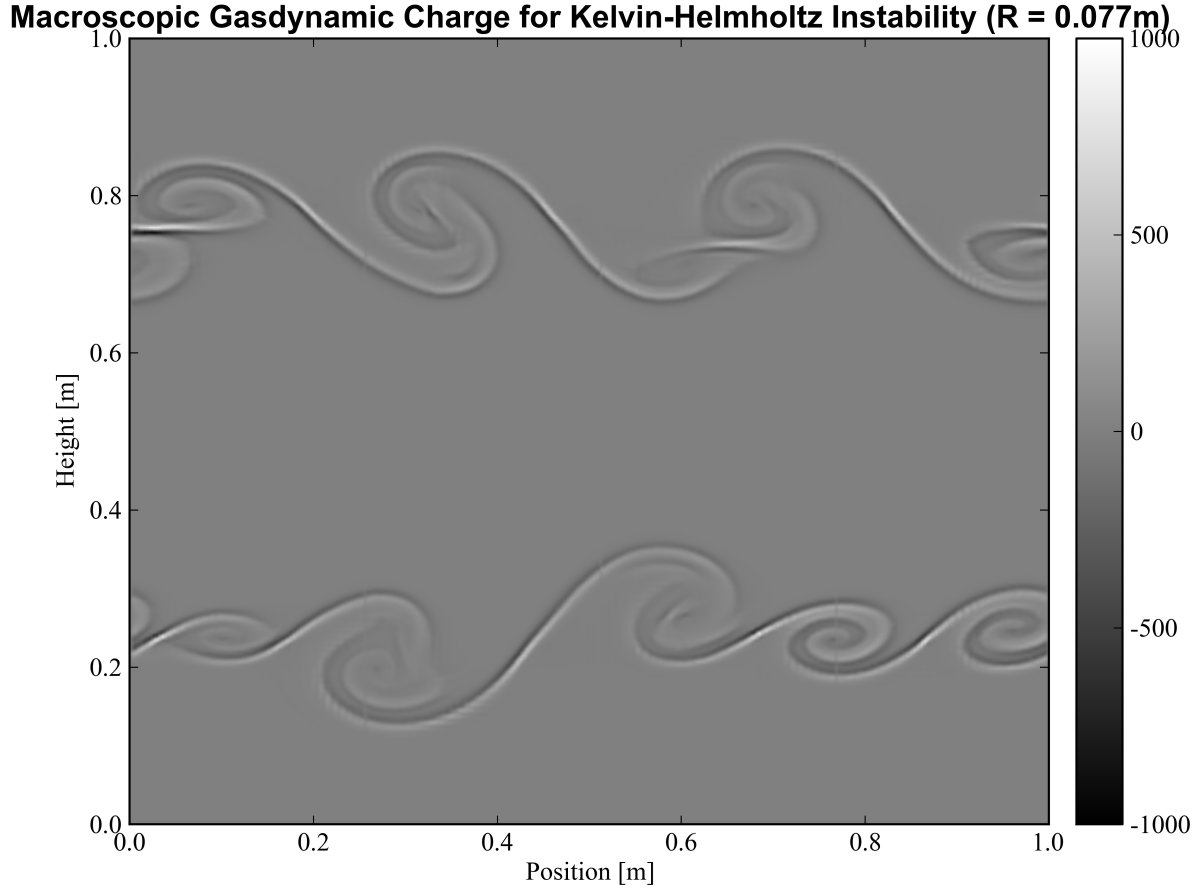


Figure 4.20: The convolved charge distribution for a Kelvin-Helmholtz hydrodynamic instability. The convolved form is not much different in structure from the microscopic form. The charge appears along the boundary between the high- and low-density fluids. The averaging length used here was $R = 0.077\text{m}$.

of these source models could be a daunting process; however, once these simple models were obtained, it would make the solution of more complicated models much more feasible.

Chapter 5

A Strong Conservative Finite Volume Framework for Plasma Simulations

“The average human male is about sixty percent water. Far as we’re concerned, that’s a little extravagant. So if you feel a bit dehydrated in this next test, that’s normal. We’re gonna hit you with some jet engines and see if we can’t get you down to twenty or thirty percent.”

Cave Johnson [1]

5.1 Motivation and State of the Art

Numerical simulation for gasdynamics and electromagnetics has a very rich history that cannot be covered in an in-depth fashion here. For brevity, we will not address this significantly, but the interested reader is referred to LeVeque [151, 152], Toro [153], Wesseling [154], Hirsch [155], Anderson [156], Ferziger and Peric [157] and Fletcher [158, 159] for comprehensive discussions of numerical approaches for compressible and incompressible flows, and to Jackson [5], Sadiku [160], Landau, Paez and Bordeianu [100], Taflove [161], and Van Reinen [162] for reviews of electrodynamic simulations. Most pertinent to our review here is the seminal work by Godunov in 1959 [163], which birthed the Godunov class of solvers, also referred to as Riemann solvers. Godunov’s scheme proposed discretizing the computational domain into a series of *Riemann problems* (discussed below) to solve gasdynamic problems with discontinuities and shocks. Although Godunov’s original method is more of a museum piece compared to modern Riemann solver approaches, it attracted interest towards the field of shock-capturing numerical schemes, and a series of subsequent variants appeared that improved upon the idea, including van Leer’s HLL solver [164], Toro’s contact-corrected HLLC solver [165], and Roe’s method [11], taking advantage of an approximate form of the Riemann problem.

The application of these approaches quickly propagated into the numerical simulation of plasmas. Zachary

and Collelazz [166], Brio and Wu [145], Dai and Woodward [167], and Cargo and Gallice [168] developed Roe-type finite volume solvers for magnetohydrodynamics. Brio and Wu’s success in demonstrating the superior efficiency and accuracy of the Roe scheme for MHD over other typical finite volume approaches (such as the Lax-Friedrichs method) set a timbre for the community of MHD numerical simulation that continues to this day. Other Riemann solver approaches have been implemented with great success as well; Honkkila and Janhunen [169], Janhunen [170], Gurski [171], and Li [172] have explored Harten-Lax-van Leer (HLL) schemes for MHD. Flux vector splitting is not directly applicable to the MHD equations, since they are not homogeneous of degree one with respect to the state vector; however, MacCormack [46, 48] and Jiang and Wu [142] found successful ways of circumventing this problem. In more recent work, flux splitting schemes such as the Advected Upstream Splitting Method (AUSM) and the related Energy-Convective Upwind and Split Pressure (E-CUSP) methods have been applied to magnetohydrodynamics as well [173–176].

Godunov schemes have also been applied to Maxwell’s equations with great success. Shang and Fithen [143], Shang and Gaitonde [177], Munz, Schneider and Voß [178], Munz, Ommes and Schneider [103], and Shankar, et al. [179, 180], Weber [181], and Vinokur and Yarrow [182] have produced a wealth of information surrounding how to apply these finite volume methods for the solution of Maxwell’s equations. This foundation has proved valuable for the development of plasmadynamic solvers, which have taken advantage of these approaches [59, 73–76].

By comparison to the vast amount of literature surrounding the MHD model, the fully coupled models introduced in Chapter 2 have received relatively little attention until the last decade or so. Early attempts to solve the fully coupled systems examined their utility for aerospace applications. MacCormack, et. al’s work [47–49, 84, 85, 87, 89] has explored solving the fully coupled single-fluid system with displacement current. This work has applied Steger-Warming flux vector splitting to investigate MHD augmentation in scramjet performance and electromagnetic mitigation of blunt-body shocks during re-entry. Originally, this work discovered electromagnetic effects that could lead to unstarts of the MHD-augmented scramjet system that were not seen using the MHD model [84], but ultimately the cause was found to be an issue in the divergence cleaning [84]. Eventually, MacCormack migrated to using a potential formulation for the electrodynamic equations, coupled to the fluid equations. [49] D’Ambrosio and Giordano [8] worked on comparisons of the MHD system (called in their work the simplified magnetofluiddynamic model, SMFD) to the fully coupled single-fluid system (what they refer to as the full magnetofluiddynamic system, FMFD). Their work also introduced coupling to finite rate chemical kinetics for the purpose of simulating strong hypersonic shocks [49, 50, 93]. Their work identified some of major problems in resolving the disparity between the different speeds of the system [8, 93].

A separate vein of recent literature parallels the work by MacCormack, D’Ambrosio, and Giordano. Li, et al [59, 60, 64, 95, 96], Merkle, et al. [97, 183] and Moeller, et al. [61, 62, 98, 184] introduced a means of resolving the displacement current in the GEMS code, which was originally produced at the University of Tennessee Space Institute [185]. This allowed the single-fluid model in Table 2.3 to be calculated with chemical reaction,

turbulence modeling and zonal parallelization [59,60]. The approach was applied to simulate an arc heater at the Arnold Engineering Development Center [95], but suffered stiffness and stability problems due to the large currents involved. Subsequent numerical simulations of the early transient startup period of pulsed plasma thrusters, which involves the formation of current across a capacitor (inherently involving the appearance of a displacement current) proved successful [59–61,98], but once again, large currents caused stability issues for long-term simulations of the evolution of the pulsed plasma thruster.

The application of Riemann solvers to the full two-fluid plasma model has been explored by Hakim, et al. [76,77], Shumlak, et al. [74,75], Srinivasan, et al. [186], and Loverich, et al. [73,187]. These investigations have explored the application of finite volume methods using the Roe scheme and discontinuous Galerkin methods for solving the two-fluid system, and have specifically investigated lower-hybrid drift instabilities [77], magnetic reconnection rates in the geospace environment [75,76], and high-energy-density simulations [73,76,77,187]. All of this work reported stiffness and stability problems encountered in resolving the behavior of the plasma, particularly due to the fact that the two-fluid model intrinsically captures the Hall effect; therefore, it is necessary to resolve the light speed time scale. When large conductivities are encountered and long durations are required, enormous stiffness can occur, and stability constraints push the maximum stable timestep much lower than either the physical timesteps or the Courant timestep. Since large conductivities are ubiquitous to plasmas of engineering interest, this represents a potential limitation of the two-fluid model. The application of two-fluid solvers including chemical reaction, viscosity, and heat transfer have also been investigated by Miura and Groth [188] and Lonkar, et al. [83] for applications in electric propulsion and plasma actuator modeling.

At present, then, the numerical solution of the single-fluid model is characterized by solution approaches that incorporate chemical reaction, viscous and heat transfer effects for hypersonic flight and propulsion, and focus on capturing charge separation effects, displacement current and electromagnetic waves for applications in hypersonic flight and propulsion and for re-entry modeling. The two-fluid model is characterized by both finite volume and discontinuous Galerkin schemes, and some success has been seen in implementing chemical reaction, viscosity and heat transfer in the two-fluid model. From the perspective of applications, most groups have tended to cite either aerospace applications for electric propulsion, hypersonic flight and propulsion, or high-energy-density plasma instabilities and oscillations as the motivating factor for migrating to these models. In the case of electric propulsion, the presence of high-conductivity plasma exhausting to vacuum represents a wide range of conductivities involved; as pointed out by Li, et al. [59], the pulsed plasma thruster and many such propulsion systems involve capacitive-driven plasmas, which, during early transient periods, can only complete the circuit via a displacement current that is otherwise not permitted to exist in the MHD model. Another place where the full Maxwell system would be valuable is in the study of the communications blackout; the propagation of an electromagnetic wave into a non-neutral plasma sheath requires a more physically correct model to capture the behavior of such a process than MHD allows. In the case of instabilities and oscillations, these small-scale oscillations can influence or determine the overall

stability and long-term instability behavior of high-energy-density plasmas, and therefore must be captured correctly if the long-term solution is desired.

One common problem that has been encountered by all of this work for solving the single-fluid and two-fluid systems is the disparity encountered between the timescales involved. Highly disparate speeds indicate a very high condition number for matrix problems, and thus frequently become ill-conditioned for numerical solution. Exacerbating this problem for both systems is the presence of enormous source terms, which threaten the stability of the simulation. The previous work has indicated that the maximum *stable* timestep can be much, much lower than the minimum required timestep needed to resolve the smallest speed. Therefore, the stiffness is compounded not only by the presence of the disparity in eigenvalues, but also due to numerical stability requirements, which may not have any physical significance. As pointed out by all groups working on these systems, they represent computationally intense problems. [48, 59, 75]

5.2 Objective

Having established the state of the art, it is clear that, while the single-fluid and two-fluid models capture more detailed physics that may be essential to resolving the correct evolution of the plasma, stiffness and stability issues plague the approach when conductivities become large and when long durations (usually associated with resolving fluid reactions) are required. Due to the applications of interest, we may frequently encounter either of these two conditions that cause the systems to become stiff and unstable. Therefore, it behooves us to find a means of improving the stability and stiffness of the equations without compromising the quality of the physics captured by these systems.

This next investigation explores such an improvement for modeling plasmas. The objective here is to introduce a reformulation of the coupled fluid system into a *strong conservative*, or *flux-coupled*, form, where the exact coupling to the Maxwell equations is now concealed in the solution and flux vectors. Such a formulation was recognized by several authors [59, 92, 94, 189, 190], but no implementation or investigation for comparison has yet been endeavored. By doing so, we eliminate the appearance of explicit source terms to the fluid equations, which strain the numerical solution considerably.

The new strong conservative approach takes advantage of the conservation form of Maxwell’s equations in order to remove the explicit appearance of the Lorentz force and Ohmic dissipation term in favor of derivatives of the Poynting propagation vector, Maxwell stress tensor and electromagnetic energy. This allows these quantities to be united in the solution and flux terms. The disadvantage to doing this is that it significantly alters the eigenstructure of the equations, which is prerequisite for several trusted finite volume flux schemes.

In this investigation, we specifically performed the following:

- The new Jacobians and corresponding eigenstructure for the strong conservative approach were derived, and are presented in Appendix A.5. This development builds off of the uncoupled eigenstructure for

the Navier-Stokes and Maxwell equations (presented in Appendices A.2 and A.3, but contributes a new coupling term. The new eigenvalues and eigenvectors were checked to fully diagonalize the strong conservative system.

- An approximate Riemann solver approach based on Roe’s method was constructed. This approach depends on the new eigenvectors of the strong conservative system. To validate both the eigenvectors and Riemann solver approach, a different approach was also tested using the Advected Upstream Splitting Method (AUSM), which does not require a knowledge of the eigenvectors. Both approaches were executed on validation test problems. The results show very good agreement, with only expected differences.
- The source-coupled and strong conservative systems were both executed on some validation problems with known solutions. Both of these approaches are capable of capturing the low- and high-conductivity limits of the electromagnetic fields, due to the inclusion of the time-varying electric field, and charge separation effects due to the inclusion of a net macroscopic charge. The strong conservative form is significantly more stable when intermediate to high conductivities appear in the computational domain, and also demonstrates better accuracy in the validation tests explored.
- Finally, as posed in the introduction, the original intent of this study was to improve the two-fluid plasma system. It is shown that the strong conservative reformulation of the equations is not possible for the two-fluid equations without some modification or simplifying assumption.

5.3 Single-fluid Source-coupled Form

We presented the form of the single-fluid model coupling the Navier-Stokes and full Maxwell equations in Table 2.3. This model assumes the flow is of an inviscid, calorically and thermally perfect gas. The electrical conductivity has been assumed to take the form of a scalar; a more advanced conductivity model, viscosity and heat transfer can always be implemented with appropriate modification to these equations. For clarity, we repeat the form of the fluid equations solved in this framework here,

$$\frac{\partial \varrho}{\partial t} + \nabla \cdot (\varrho \mathbf{u}) = 0 \quad (5.1)$$

$$\frac{\partial}{\partial t} (\varrho \mathbf{u}) + \nabla \cdot (\varrho \mathbf{u} \mathbf{u} + \hat{\mathbf{l}} p) = \varrho_e \mathbf{E} + \mathbf{j}_e \times \mathbf{B} \quad (5.2)$$

$$\frac{\partial \mathcal{E}}{\partial t} + \nabla \cdot ([\mathcal{E} + p] \mathbf{u}) = \mathbf{j}_e \cdot \mathbf{E} \quad (5.3)$$

This assumes a coupling to the Maxwell equations through the presence of a Lorentz body force term and Ohmic heating term. We may write these equations coupled to the Maxwell equations in the following form,

$$\frac{\partial \mathbf{U}}{\partial t} + \nabla \cdot \mathbf{F} = \mathbf{H} \quad (5.4)$$

where

$$\mathbf{U} = \begin{bmatrix} \varrho \\ \varrho \mathbf{u} \\ \mathcal{E} \\ \mathbf{B} \\ \mathbf{E} \end{bmatrix}, \quad \mathbf{F} = \begin{bmatrix} \varrho \mathbf{u} \\ \varrho \mathbf{u} \mathbf{u} + \hat{\mathbf{I}} p \\ [\mathcal{E} + p] \mathbf{u} \\ \hat{\mathbf{c}} \mathbf{u} \mathbf{r} \mathbf{l}(\mathbf{E}) \\ -c_0^2 \hat{\mathbf{c}} \mathbf{u} \mathbf{r} \mathbf{l}(\mathbf{B}) \end{bmatrix}, \quad \mathbf{H} = \begin{bmatrix} 0 \\ \varrho_e \mathbf{E} + \mathbf{j}_e \times \mathbf{B} \\ \mathbf{j}_e \cdot \mathbf{E} \\ \mathbf{0} \\ -\mathbf{j}_e / \epsilon_0 - \varrho_e \mathbf{u} \end{bmatrix} \quad (5.5)$$

Here $\hat{\mathbf{I}} = \delta_{ik}$ is the identity matrix. Our notation $\nabla \cdot (\hat{\mathbf{c}} \mathbf{u} \mathbf{r} \mathbf{l}(\mathbf{E})) = \nabla \cdot (\hat{\mathbf{I}} \times \mathbf{E})$ should be taken to mean $\partial_l \epsilon_{ijk} \delta_{jl} E_k = \epsilon_{ijk} \partial_j E_k$, where ∂_l is the index form of ∇ and ϵ_{ijk} is the Levi-Civita tensor.

Equations 5.4 and 5.5 represents the customary form of the coupled system. Observe that the coupling is entirely mitigated to the source vector, \mathbf{H} ; we will hence refer to this formulation as the *source-coupled* formulation to distinguish it from the new formulation we will be testing. If we examine the source vector for each system, it is clear that the source terms for the fluid system threaten the stability of our numerical simulation; the dependency on the electromagnetic variables indicates that the sources will vary on the time scale of the electromagnetics, which is much faster than the fluid time scales; thus, the sources will appear as an extremely rapid fluctuation to the fluid equations. When the conductivity becomes large, the magnitude of these rapid fluctuations strain the equations, and an excessively small timestep is necessary to avoid numerical instabilities. Often, the maximum *stable* timestep is much lower than the Courant timestep, and simulations incur very large performance drawbacks and excessive computational times needed to resolve the solution accurately.

5.4 Conservation Form of Maxwell's Equations

In the source-coupled formulation in equations 5.4 and 5.5, it would be preferable to recast the source terms into derivatives that could be united on the left-hand side. Such a *strongly conservative* formulation could potentially enjoy much more robustness and stability. In order to do so, we must cast the Lorentz body force and Ohmic dissipation terms into a form amenable to the left-hand side of the equations. Details of this approach have been noted by Giordano [190], D'Amobrosio and Giordano [92, 94], Kulikovskii [189], and Li, et al. [59], but this approach has not actually been investigated or validated.

We begin by transforming the Lorentz force term into a conservation form. Substituting Ampere's law (equation 2.11) in for the total current density \mathbf{j}_e in the $\mathbf{j}_e \times \mathbf{B}$ term, and substituting Gauss' law (equation 2.9) in for the total charge density ϱ_e , we have

$$\varrho_e \mathbf{E} + \mathbf{j}_e \times \mathbf{B} = \epsilon_0 \mathbf{E} (\nabla \cdot \mathbf{E}) + \frac{1}{\mu_0} \left\{ -\frac{1}{c_0^2} \frac{\partial \mathbf{E}}{\partial t} + \nabla \times \mathbf{B} \right\} \times \mathbf{B} \quad (5.6)$$

Applying the product rule to $\partial \mathbf{E} / \partial t$ and adding the divergence of \mathbf{B} (since $\nabla \cdot \mathbf{B} = 0$), we have

$$\varrho_e \mathbf{E} + \mathbf{j}_e \times \mathbf{B} = \frac{1}{\mu_0} \left\{ -\frac{1}{c_0^2} \frac{\partial}{\partial t} (\mathbf{E} \times \mathbf{B}) + \frac{1}{c_0^2} (\mathbf{E} \nabla \cdot \mathbf{E} - \mathbf{E} \times \nabla \times \mathbf{E}) + \mathbf{B} \nabla \cdot \mathbf{B} - \mathbf{B} \times \nabla \times \mathbf{B} \right\} \quad (5.7)$$

Now, we turn our attention to the Ohmic dissipation. If we again substitute Ampere's law in for the total current density, we have

$$\mathbf{j}_e \cdot \mathbf{E} = \mathbf{E} \cdot \frac{1}{\mu_0} \left[-\frac{1}{c_0^2} \frac{\partial \mathbf{E}}{\partial t} + \nabla \times \mathbf{B} \right] \quad (5.8)$$

Applying the vector identity $\nabla \cdot (\mathbf{A} \times \mathbf{B}) = \mathbf{B} \cdot \nabla \times \mathbf{A} - \mathbf{A} \cdot \nabla \times \mathbf{B}$,

$$\mathbf{j}_e \cdot \mathbf{E} = -\frac{1}{\mu_0} \left\{ \frac{1}{c_0^2} \frac{\partial \mathbf{E}}{\partial t} \cdot \mathbf{E} + \frac{\partial \mathbf{B}}{\partial t} \cdot \mathbf{B} + \nabla \cdot (\mathbf{E} \times \mathbf{B}) \right\} \quad (5.9)$$

We now introduce the following electromagnetic quantities:

1. The Poynting propagation vector,

$$\mathbf{S}^{EM} = \frac{1}{\mu_0} \mathbf{E} \times \mathbf{B} \quad (5.10)$$

2. The electromagnetic energy density,

$$\mathcal{E}^{EM} = \frac{1}{2\mu_0} \left\{ \frac{\mathbf{E} \cdot \mathbf{E}}{c_0^2} + \mathbf{B} \cdot \mathbf{B} \right\} \quad (5.11)$$

3. The Maxwell stress tensor,

$$\hat{\boldsymbol{\Sigma}}^{EM} = \Sigma_{\mu\nu}^{EM} = \frac{1}{\mu_0} \left\{ \frac{E_\mu E_\nu}{c_0^2} + B_\mu B_\nu \right\} - \delta_{\mu\nu} \mathcal{E}^{EM} \quad (5.12)$$

and, after some manipulation, equations 5.7 and 5.9 reduce to the following identities:

$$\varrho_e \mathbf{E} + \mathbf{j}_e \times \mathbf{B} = -\frac{1}{c_0^2} \frac{\partial \mathbf{S}^{EM}}{\partial t} + \nabla \cdot \hat{\boldsymbol{\Sigma}}^{EM} \quad (5.13)$$

$$\mathbf{j}_e \cdot \mathbf{E} = -\frac{\partial \mathcal{E}^{EM}}{\partial t} - \nabla \cdot \mathbf{S}^{EM} \quad (5.14)$$

5.5 Single-fluid Strong Conservative Form

Having derived the identities in equations 5.13 and 5.14, we can now apply them to equations 5.2 and 5.3 in order to reduce the fluid equations to a set of *strongly conservative*, or *flux-coupled*, equations free of explicit source terms. This application yields the following set of strongly conservative fluid equations,

$$\frac{\partial \varrho}{\partial t} + \nabla \cdot (\varrho \mathbf{u}) = 0 \quad (5.15)$$

$$\frac{\partial}{\partial t} \left(\varrho \mathbf{u} + \frac{1}{c_0^2} \mathbf{S}^{EM} \right) + \nabla \cdot \left(\varrho \mathbf{u} \mathbf{u} + \hat{\mathbf{l}} p - \hat{\Sigma}^{EM} \right) = 0 \quad (5.16)$$

$$\frac{\partial}{\partial t} (\mathcal{E} + \mathcal{E}^{EM}) + \nabla \cdot ([\mathcal{E} + p] \mathbf{u} + \mathbf{S}^{EM}) = 0 \quad (5.17)$$

which are the continuity, total momentum, and total energy equations, respectively. Now, the conservative form for the flux-coupled system can be expressed by writing

$$\frac{\partial \mathbf{U}_F}{\partial t} + \nabla \cdot \mathbf{F}_F = \mathbf{H}_F \quad (5.18)$$

with

$$\mathbf{U}_F = \begin{Bmatrix} \varrho \\ \varrho \mathbf{u} + \mathbf{S}^{EM}/c_0^2 \\ \mathcal{E} + \mathcal{E}^{EM} \\ \mathbf{B} \\ \mathbf{E} \end{Bmatrix}, \quad \mathbf{F}_F = \begin{Bmatrix} \varrho \mathbf{u} \\ \varrho \mathbf{u} \mathbf{u} + \hat{\mathbf{l}} p - \Sigma^{EM} \\ [\mathcal{E} + p] \mathbf{u} + \mathbf{S}^{EM} \\ \hat{\mathbf{curl}}(\mathbf{E}) \\ -c_0^2 \hat{\mathbf{curl}}(\mathbf{B}) \end{Bmatrix}, \quad \mathbf{H}_F = \begin{Bmatrix} 0 \\ \mathbf{0} \\ 0 \\ \mathbf{0} \\ -\mathbf{j}_e/\epsilon_0 - \varrho_e \mathbf{u} \end{Bmatrix} \quad (5.19)$$

Observe that the coupling is now entirely contained in the solution vector, \mathbf{U} , and the flux vector, \mathbf{F} . The system is now homogeneous for the fluid equations. It is our proposal that this system is numerically more stable than the source-coupled system of equations; hence, we should be able to achieve a higher maximum stable timestep using equations 5.18 and 5.19 than using equations 5.4 and 5.5.

5.6 Overview of the Numerical Formulation

Our system of equations for any of the above models may generically be written as

$$\frac{\partial \mathbf{U}}{\partial t} + \nabla \cdot \mathbf{F} = \mathbf{H} \quad (5.20)$$

where the solution, flux and source vectors, \mathbf{U} , \mathbf{F} , and \mathbf{H} , respectively, are given by either equation 5.5 or 5.19, depending on the system of interest. Our goal is to discretize this equation and solve it numerically.

The first-order form of equation 5.20 is amenable to the finite volume approach, in which a volume integration is used to cast the equation in to integral form. The advantage here lies within the application of Gauss' divergence theorem to the volume integral of the flux term; the flux across the surface can then be treated as a surface integral instead. By constructing a numerical flux scheme, we may predict the flux across each interface adjoining the control volumes that comprise the mesh and capture shocks, discontinuities and steep gradients.

We will consider two approaches to discretizing the systems; in the first, we construct a Riemann solver approach that implements the Roe scheme to calculate the numerical flux across the faces of each adjoining volume. Despite the successes of the Roe scheme, it requires a detailed understanding of the eigenstructure of the governing equations; this can be seen as a drawback, since often complicated systems of equations may have a very large and complicated eigenstructure. To implement this approach, we derived the new eigenstructure for the flux-coupled strong conservative system (presented in Appendix A.5), which is shown to be much more complicated than the source-coupled form. To validate the Roe method and the new eigenstructure, we also explored the application of the Advected Upstream Splitting Method (AUSM), which does not require a knowledge of the eigenstructure. Both approaches were implemented in an implicit scheme that permits larger timesteps and enjoys better stability for the disparity in the eigenvalues.

In Section 5.7, we first cover the basic groundwork of systems of conservation laws; this section is provided for those unfamiliar with the foundation of the finite volume and Riemann solver approaches, and borrows heavily from [151, 153]. In Section 5.8, we discuss the finite volume method itself in general, and then we specifically investigate its formulation in this investigation in Section 5.9, where we detail the implicit scheme. We address divergence cleaning for multiple dimensions in Section 5.10. Following this, in Sections 5.11 and 5.12, we discuss the Roe approximate Riemann solver and AUSM flux schemes, respectively; finally, in Section 5.14, we present details regarding the solver algorithm employed. In Appendix ??, Sections A.2, A.3, A.4 and A.5 have been provided to supplement the remainder of this chapter; they present the mathematical details of the Navier-Stokes, Maxwell, source-coupled and strong conservative coupled formulations, respectively, which are required in the discussion below.

5.7 Systems of Hyperbolic Conservation Laws

Generally, we refer to a *conservation law* as a first-order partial differential equation that may be written in the form

$$\frac{\partial \mathbf{U}}{\partial t} + \nabla \cdot \mathbf{F}(\mathbf{U}) = 0 \quad (5.21)$$

which represents a four-divergence in spacetime. Here, U is a scalar quantity of interest, and $\mathbf{F}(U) \in \mathbb{R}^D$ is the associated flux of U in D spatial dimensions. By integrating over a volume and applying Gauss' law to the divergence term, this equation physically couples the change of the quantity U within the volume to the rate of flux of the quantity, $\mathbf{F}(U)$, through the surface bounding the volume. The finite volume method takes advantage of this continuity form of the equations to develop a discretization that preserves the conservative variable, U , across the a control surface that bounds two adjoining control volumes. If the domain is discretized into a mesh of control volumes, the conservative variable may be updated in each control volume by considering the flux moving in and out across each bounding face.

When m different equations are present, we can rewrite equation 5.21 into a system of conservation laws. Furthermore, when a *source term*, or forcing function, \mathbf{H} , is present on the right-hand side, our equations more correctly become *balance equations*, and a system of m generic balance equations may be written as

$$\frac{\partial \mathbf{U}}{\partial t} + \nabla \cdot \mathbf{F}(\mathbf{U}) = \mathbf{H}(\mathbf{U}) \quad (5.22)$$

where $\mathbf{U} \in \mathbb{R}^m$ is the *solution vector*, $\mathbf{F} \in \mathbb{R}^{m \times D}$ is the *flux vector*, and $\mathbf{H} \in \mathbb{R}^m$ is the *source vector* for a problem in D spatial dimensions. The flux and source vectors are considered known functions of the solution vector. We consider the solution vector \mathbf{U} as our unknown, and wish to solve equation 5.22. Before explaining the numerical procedure, we will need at least a rudimentary understanding of the mathematical character of equation 5.22, upon which we will briefly elaborate.

5.7.1 Quasilinear Form, Jacobian, Eigenstructure

It is more revealing to pose equation 5.22 into a *quasilinear* form, which exposes the underlying structure of the system of equations. Applying the chain rule of calculus, we may rewrite the divergence of the flux term as

$$\nabla \cdot \mathbf{F} = \frac{\partial \mathbf{F}}{\partial x_k} = \frac{\partial \mathbf{F}}{\partial \mathbf{U}} \frac{\partial \mathbf{U}}{\partial x_k} = \hat{\mathbf{A}} \nabla \cdot \mathbf{U} \quad (5.23)$$

where $\hat{\mathbf{A}} = \partial \mathbf{F} / \partial \mathbf{U} \in \mathbb{R}^{m \times m}$ is the *Jacobian* of equation 5.22. The associated form of equation 5.22 with the Jacobian matrix is the *quasilinear form*,

$$\frac{\partial \mathbf{U}}{\partial t} + \hat{\mathbf{A}} \frac{\partial \mathbf{U}}{\partial x_k} = \mathbf{H}(\mathbf{U}) \quad (5.24)$$

The Jacobian matrix has a set of eigenvalues, denoted $\lambda^{(p)}$, $p \in \{1, \dots, m\}$, associated with it, which satisfy the *characteristic polynomial*,

$$\det(\hat{\mathbf{A}} - \lambda \mathbf{I}) = 0 \quad (5.25)$$

where $\hat{\mathbf{I}} \in \mathbb{R}^{m \times m}$ is the identity matrix and \det is the matrix determinant. The Jacobian is also characterized by a set of eigenvectors, which may be distinguished between *left* and *right* eigenvectors. The right eigenvectors of $\hat{\mathbf{A}}$, denoted $\mathbf{K}^{(p)}$, $p \in \{1, \dots, m\}$, are a set of m column vectors that satisfy the relationship

$$\hat{\mathbf{A}}\mathbf{K}^{(p)} = \lambda^{(p)}\mathbf{K}^{(p)} \quad (5.26)$$

The left eigenvectors, denoted $\mathbf{L}^{(p)} \in \mathbb{R}^m$, $p \in \{1, \dots, m\}$, are a set of m row vectors that satisfy the relationship

$$\mathbf{L}^{(p)T}\hat{\mathbf{A}} = \lambda^{(p)}\mathbf{L}^{(p)T} \quad (5.27)$$

Recall that eigenvectors are only specified up to an arbitrary multiplicative constant. For the remainder of the dissertation, whenever we simply say *eigenvectors*, we will imply right eigenvectors, unless otherwise noted.

We may introduce the definition of a left and right *eigenmatrix*¹ for equation 5.22, which is composed of rows of left eigenvectors (columns of right eigenvectors),

$$\hat{\mathbf{K}} = \left\{ \mathbf{K}^{(p)} \right\}, p \in \{1, \dots, m\} \quad (5.28)$$

$$\hat{\mathbf{L}} = \left\{ \mathbf{L}^{(p)} \right\}, p \in \{1, \dots, m\} \quad (5.29)$$

The left and right eigenmatrices can generally be chosen such that

$$\hat{\mathbf{K}} = \hat{\mathbf{L}}^{-1} \quad (5.30)$$

and, of course, the converse,

$$\hat{\mathbf{L}} = \hat{\mathbf{K}}^{-1} \quad (5.31)$$

This requires that the eigenvectors form linearly independent sets in the eigenmatrices.

The diagonal matrix of eigenvalues, denoted, $\hat{\mathbf{\Lambda}}$, can be written as

$$\hat{\mathbf{\Lambda}} = \text{Diag} \left\{ \Lambda^{(p)} \right\}, p \in \{1, \dots, m\} = \begin{pmatrix} \Lambda^{(1)} & 0 & \dots & 0 & 0 \\ 0 & \Lambda^{(2)} & \dots & 0 & 0 \\ \vdots & \vdots & \ddots & \vdots & \vdots \\ 0 & 0 & \dots & \Lambda^{(m-1)} & 0 \\ 0 & 0 & \dots & 0 & \Lambda^{(m)} \end{pmatrix} \quad (5.32)$$

¹...for lack of a better term. There seems to be no consistent name or notation for this matrix, despite its consistent appearance and importance.

and the following relationships hold,

$$\hat{\mathbf{A}}\hat{\mathbf{K}} = \hat{\mathbf{K}}\hat{\mathbf{\Lambda}} \quad (5.33)$$

$$\hat{\mathbf{L}}\hat{\mathbf{A}} = \hat{\mathbf{\Lambda}}\hat{\mathbf{L}} \quad (5.34)$$

We are now in a position to introduce the notion of diagonalization, which exposes the characteristic structure of equation 5.22. The Jacobian, $\hat{\mathbf{A}}$, is said to be *diagonalizable* if there exists some matrix $\hat{\mathbf{X}}$ such that

$$\hat{\mathbf{X}}^{-1}\hat{\mathbf{A}}\hat{\mathbf{X}} = \hat{\mathbf{\Lambda}} \quad (5.35)$$

If the Jacobian matrix $\hat{\mathbf{A}}$ is diagonalizable, and the eigenvalues contained in $\hat{\mathbf{\Lambda}}$ are all real such that $\hat{\mathbf{\Lambda}} \in \mathbb{R}^{m \times m}$, then equation 5.22 is said to be *hyperbolic*, and the matrix $\hat{\mathbf{X}}$ here must be the right eigenmatrix, $\hat{\mathbf{K}}$, to satisfy relations 5.33 and 5.34. Thus, for a hyperbolic set of conservation laws,

$$\hat{\mathbf{K}}^{-1}\hat{\mathbf{A}}\hat{\mathbf{K}} = \hat{\mathbf{L}}\hat{\mathbf{A}}\hat{\mathbf{K}} = \hat{\mathbf{\Lambda}} \quad (5.36)$$

We may also project the left and right eigenvectors on this expression in order to obtain

$$\hat{\mathbf{K}}\hat{\mathbf{\Lambda}}\hat{\mathbf{K}}^{-1} = \hat{\mathbf{K}}\hat{\mathbf{\Lambda}}\hat{\mathbf{L}} = \hat{\mathbf{A}} \quad (5.37)$$

5.7.2 The Scalar Linear Advective Wave Equation

One of the simplest forms of equation 5.22 is a scalar, constant-coefficient assumption of the form

$$\frac{\partial w}{\partial t} + \lambda \frac{\partial w}{\partial x} = 0 \quad (5.38)$$

Here w is our scalar unknown, and λ is an associated speed. This equation has a single eigenvalue, λ ; as discussed in the previous section, this equation is hyperbolic if $\lambda \in \mathbb{R}$. Suppose it is supplied with some initial condition, $w(x, t = 0) = w_0(x)$, which is some initial spatial profile of w . To solve this problem, we consider an initial point in space, x_0 , and the value of w at that point. If we follow a path through time, $x(t)$, from x_0 , and if we now consider our unknown function to be a function only of time, i.e., $w(x, t) = w(x(t), t)$, then we can reduce this partial differential equation to an ordinary differential equation. Along the path $x(t)$, the rate of change of the scalar solution w will be (via the total differential)

$$\frac{dw}{dt} = \frac{\partial w}{\partial t} + \frac{\partial w}{\partial x} \frac{dx}{dt} \quad (5.39)$$

But the speed dx/dt is just the speed of propagation, $dx/dt = \lambda$. Thus, the rate of change of w along $x(t)$ is

$$\frac{dw}{dt} = \frac{\partial w}{\partial t} + \lambda \frac{\partial w}{\partial x} = 0 \quad (5.40)$$

Hence, *the solution w is constant along $x(t)$* . Since the eigenvalue λ is constant everywhere, the initial condition profile, $w_0(x)$, just translates along x with speed λ , so at any given time t the solution to equation 5.38 will be

$$w(x, t) = w(x - \lambda t, 0) = w_0(x - \lambda t) \quad (5.41)$$

5.7.3 Characteristics and the General Solution of the Linear Cauchy Problem

With the solution of the linear advective equation in hand, we may consider the general Cauchy problem for a quasilinear hyperbolic problem. Suppose that we are faced with the task of solving the following problem,

$$\begin{aligned} \frac{\partial \mathbf{U}}{\partial t} + \hat{\mathbf{A}} \frac{\partial \mathbf{U}}{\partial x} &= 0, \\ \mathbf{U}(x, t=0) &= \mathbf{U}_0(x), \quad -\infty < x < \infty, \quad t \geq 0 \end{aligned} \quad (5.42)$$

To solve equation 5.42, consider projecting the left eigenmatrix, $\hat{\mathbf{K}}^{-1}$, onto the equation,

$$\frac{\partial}{\partial t} (\hat{\mathbf{K}}^{-1} \mathbf{U}) + \hat{\mathbf{K}}^{-1} \hat{\mathbf{A}} \frac{\partial \mathbf{U}}{\partial x} = 0 \quad (5.43)$$

But since, by equation 5.37, we know $\hat{\mathbf{K}}^{-1} \hat{\mathbf{A}} = \hat{\mathbf{K}}^{-1} \hat{\mathbf{K}} \hat{\mathbf{\Lambda}} \hat{\mathbf{K}}^{-1} = \hat{\mathbf{\Lambda}} \hat{\mathbf{K}}^{-1}$, we have

$$\frac{\partial}{\partial t} (\hat{\mathbf{K}}^{-1} \mathbf{U}) + \hat{\mathbf{\Lambda}} \frac{\partial}{\partial x} (\hat{\mathbf{K}}^{-1} \mathbf{U}) = 0 \quad (5.44)$$

If we take our unknown now to be the new projected solution vector, $\mathbf{W} = \hat{\mathbf{K}}^{-1} \mathbf{U}$, then we have effectively transformed our solution into a new problem,

$$\frac{\partial \mathbf{W}}{\partial t} + \hat{\mathbf{\Lambda}} \frac{\partial \mathbf{W}}{\partial x} = 0 \quad (5.45)$$

If we write this in an indexed form,

$$\frac{\partial W^{(p)}}{\partial t} + \lambda^{(p)} \frac{\partial W^{(p)}}{\partial x} = 0 \quad (5.46)$$

where $p \in \{1, \dots, m\}$. This reveals that equation 5.45 is just a system of *decoupled* scalar linear advective equations, each propagating at its own speed, $\lambda^{(p)}$. Since we have already determined the solution to a single

linear advective wave equation (cf. equation 5.41), each equation may be solved in the same manner,

$$W^{(p)}(x, t) = W^{(p)}(x - \lambda^{(p)}t, t = 0) = W_0^{(p)}(x - \lambda^{(p)}t) \quad (5.47)$$

where $p \in \{1, \dots, m\}$. The quantities \mathbf{W} are the *characteristics* of equation 5.42. Having computed all components of \mathbf{W} , the final solution \mathbf{U} may be calculated by transforming back,

$$\mathbf{U} = \hat{\mathbf{K}} \mathbf{W}(x, t) = \sum_{p=1}^m W^{(p)}(x, t) \mathbf{K}^{(p)} \quad (5.48)$$

where $\mathbf{K}^{(p)}$ is the p^{th} column right eigenvector. Equation 5.48 is an eigenvector expansion of the conservative variables, \mathbf{U} ; given the characteristics, $W^{(p)}$, which represent the coefficients of the expansion, we have effectively constructed an exact solution to the quasilinear Cauchy problem posed in equations 5.42.

While classical solutions of differential equations usually insist that the data be sufficiently smooth and differentiable, an intriguing aspect of equation 5.48 is that it applies even in cases where the data is discontinuous. In the next section, we take advantage of this property to construct the solution to the Riemann problem, which includes an intrinsic discontinuity in the initial condition.

5.7.4 The Riemann Problem

Anticipating the development of a Riemann solver, we discuss the Riemann problem, which represents a fundamental special case of equation 5.22. This problem reminiscent of the behavior of piecewise-constant data in a mesh, particularly between two different control volumes; it therefore becomes an integral part of the solver development later for the Roe flux scheme. The Riemann problem is generally posed as a Cauchy problem for a given system of equations in the form of equation 5.22, where a discontinuity is established in the initial conditions,

$$\begin{aligned} \frac{\partial \mathbf{U}}{\partial t} + \hat{\mathbf{A}} \frac{\partial \mathbf{U}}{\partial x} &= 0, \\ \mathbf{U}(x, t = 0) = \mathbf{U}_0(x) &= \begin{cases} \mathbf{U}_L, & x < 0 \\ \mathbf{U}_R, & x > 0 \end{cases} \\ -\infty < x < \infty, & \quad t \geq 0 \end{aligned} \quad (5.49)$$

The initial conditions for a scalar system and the propagation of waves for a system of m equations and the structure of the solution are sketched in Figure 5.1, and a more detailed visualization of the construction of the solution is presented in Figure 5.2. The solution admits a series of m waves, each possessing an eigenvalue $\lambda^{(p)}$. We expect that the solution on the left of the left-most wave must be the \mathbf{U}_L , and correspondingly, the solution to the right of the right-most wave must be \mathbf{U}_R . As per our discussion for solving the general Cauchy problem, we may write the left and right state vectors as eigenfunction expansions,

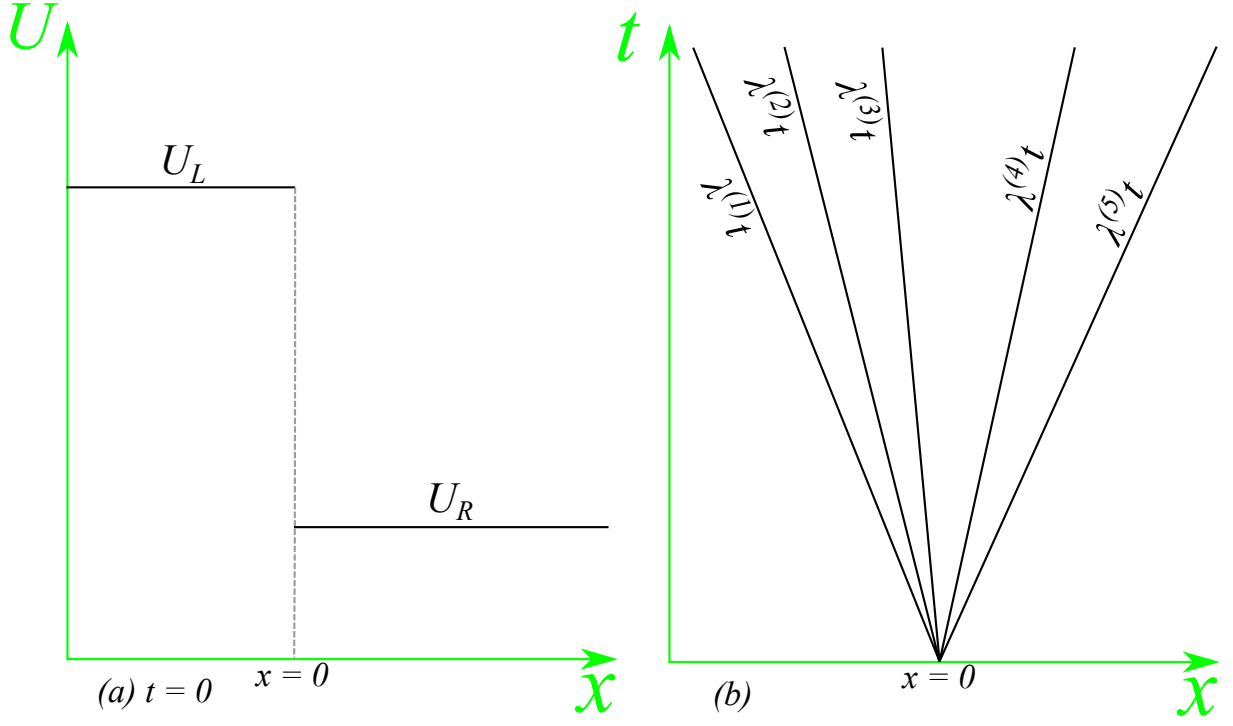


Figure 5.1: Schematic of the classic Riemann problem. (a) The initial condition for a scalar system; there is a discontinuity at $x = 0$. The initial data is U_L for $x < 0$ and U_R for $x > 0$. (b) The propagation of the waves for a system of m conservation laws; m different waves result. In this figure, $m = 5$; the black lines trace the m characteristic lines, $x = \lambda^{(p)}t$.

$$\mathbf{U}_L = \sum_{p=1}^m W_L^{(p)} \mathbf{K}^{(p)}, \quad \mathbf{U}_R = \sum_{p=1}^m W_R^{(p)} \mathbf{K}^{(p)} \quad (5.50)$$

where $W_L^{(p)}$ and $W_R^{(p)}$ represent the characteristics of the initial conditions, and $p \in \{1, \dots, m\}$. For any point in the domain, (x, t) , the quantity x/t will fall between two eigenvalues λ_H and λ_{H+1} , such that $\lambda_H < x/t < \lambda_{H+1}$. Then the superposed solution to the Riemann problem may be written as

$$\mathbf{U}(x, t) = \sum_{p=H+1}^m W_L^{(p)} \mathbf{K}^{(p)} + \sum_{p=1}^H W_R^{(p)} \mathbf{K}^{(p)} \quad (5.51)$$

which simply means that crossing the p^{th} characteristic implies a jump in the solution's characteristic, $W^{(p)}$, from the left state, $W_L^{(p)}$, to the right state, $W_R^{(p)}$ (see Figure 5.2). This can be more clearly understood by rewriting equation 5.51 in terms of the *difference* in the characteristics,

$$\left(W_R^{(p)} - W_L^{(p)} \right) \mathbf{K}^{(p)} = \alpha^{(p)} \mathbf{K}^{(p)} \quad (5.52)$$

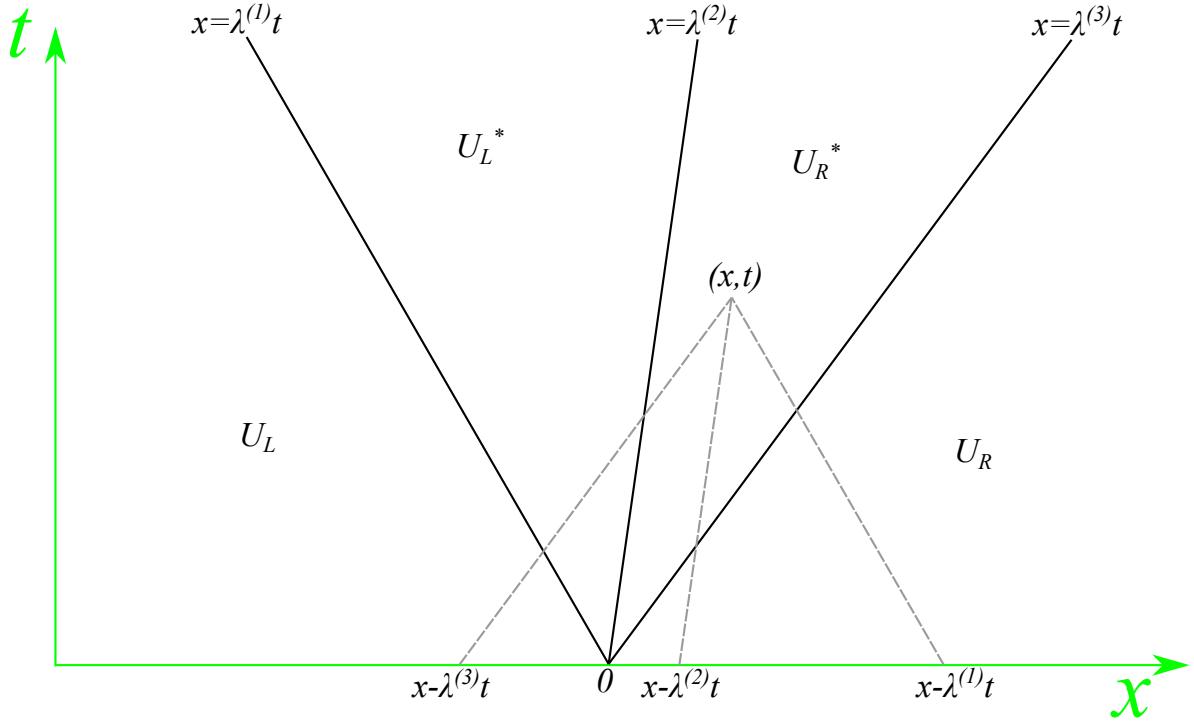


Figure 5.2: An example of constructing the solution to the Riemann problem for $m = 3$. Tracing back along the characteristics, we determine $W^{(p)}$ from the initial conditions. The solution \mathbf{U} is constant in each sector. The general solution is $\mathbf{U}(x, t) = \sum_{p=H+1}^m W_L^{(p)} \mathbf{K}^{(p)} + \sum_{p=1}^H W_R^{(p)} \mathbf{K}^{(p)}$, where $\lambda_H < x/t < \lambda_{H+1}$. The left-most and right-most sectors are known (given in the initial conditions); they are $\mathbf{U}_L = \sum_{p=1}^m W_L^{(p)} \mathbf{K}^{(p)}$ and $\mathbf{U}_R = \sum_{p=1}^m W_R^{(p)} \mathbf{K}^{(p)}$, respectively. In the sector \mathbf{U}_L^* , the $p = 1$ characteristic has been crossed, but not the second two, so $H = 1$, and the solution is $\mathbf{U}_L^* = W_R^{(1)} \mathbf{K}^{(1)} + W_L^{(2)} \mathbf{K}^{(2)} + W_L^{(3)} \mathbf{K}^{(3)}$. In Sector \mathbf{U}_R^* , the first two characteristics have been crossed, but not the third; here, $H = 2$, and the solution in this region is $\mathbf{U}_R^* = W_R^{(1)} \mathbf{K}^{(1)} + W_R^{(2)} \mathbf{K}^{(2)} + W_L^{(3)} \mathbf{K}^{(3)}$. [151]

where we have introduced the *decomposition coefficient*, $\alpha^{(p)} = W_R^{(p)} - W_L^{(p)}$. Equation 5.52 is known as the *Rankine-Hugoniot jump condition*. In this sense, the full solution is given as

$$\Delta \mathbf{U} = \mathbf{U}_R - \mathbf{U}_L = \sum_{p=1}^m \alpha^{(p)} \mathbf{K}^{(p)} \quad (5.53)$$

Here, the Riemann data $\Delta \mathbf{U}$ is known given the initial conditions, and it is expected that the eigenvectors are known from the Jacobian matrix $\hat{\mathbf{A}}$ given the system of equations in equation 5.49. The solution of the Riemann problem is now equivalent to determining the decomposition coefficients, $\alpha^{(p)}$, $p \in \{1, \dots, m\}$. Equation 5.53 may be viewed as a linear system of equations that can be solved to determine these coefficients. In summary, we see from equation 5.53 that, for the quasilinear case, solving the Riemann problem involves decomposing the jump $\Delta \mathbf{U}$ into eigenvectors of the Jacobian matrix.

All of the above discussion has been preparatory to our explanation of the numerical scheme applied for this investigation. Equipped with a rudimentary understanding of the character of equation 5.22 based on a knowledge of its eigenvalues and eigenmatrices, we can construct a numerical scheme that will solve the systems as identified above.

5.8 The Finite Volume Method

Finite volume numerical schemes are attractive to scientists and engineers due to their exceptional ability to conserve physical quantities and to correctly capture shocks, discontinuities and steep gradients. This method takes advantage of the mathematical structure of systems of hyperbolic conservation laws; we have provided a more detailed discussion of the general theory of systems of conservation laws and their structure in the previous section. In the following, it will be presumed that the reader has some familiarity with these mathematics. More detailed information is available in the classic references [151, 153].

The primary ingredients in formulating a finite volume numerical scheme is

- Application of the divergence theorem to the flux term in the governing equations,
- Development of a semi-discretized equation,
- Implementation of a numerical flux approximation, and
- Application of a time integration scheme to discretize and evolve the governing equations

The finite volume approach takes advantage of the integral formulation of equation 5.22. We begin by integrating over an arbitrary domain, Ω . The divergence theorem may be applied to the integral of the flux divergence, which produces a surface integral, which leads to the weak form [151]

$$\int_{\Omega} \frac{\partial \mathbf{U}}{\partial t} d\Omega + \oint_{\partial\Omega} \mathbf{F} \cdot \mathbf{n} dA = \int_{\Omega} \mathbf{H} d\Omega \quad (5.54)$$

where $\partial\Omega$ and dA are understood to be the associated bounding surface and infinitesimal boundary area of the volume, Ω . Since the mesh is not moving, the integration and differentiation may be exchanged in the first term, $\int_{\Omega} \partial/\partial t (\cdot) d\Omega_D = d/dt \int_{\Omega} (\cdot) d\Omega_D$.

Let us suppose that the domain Ω represents a very small control volume bounded by a finite set of boundary faces denoted \mathcal{F} , as shown in Figure 5.3. We may approximate the solution vector, \mathbf{U} , as being roughly constant within this control volume, if it is sufficiently smaller than the length scale of interest. In this case, we may perform the integration for the solution vector and source term vector trivially, since $\int_{\Omega} \mathbf{U} d\Omega \approx \mathbf{U} \int_{\Omega} d\Omega = \mathbf{U} \cdot V$, where we adopt the notation V to denote the volume contained within the domain Ω . If there are a finite number of faces contained in \mathcal{F} , then the surface integration becomes a summation, and equation 5.54 now becomes

$$\frac{d\mathbf{U}}{dt} + \frac{1}{V} \sum_{j \in \mathcal{F}} \mathbf{F}_j(\mathbf{U}_j) \cdot \mathbf{n}_j A_j = \mathbf{H} \quad (5.55)$$

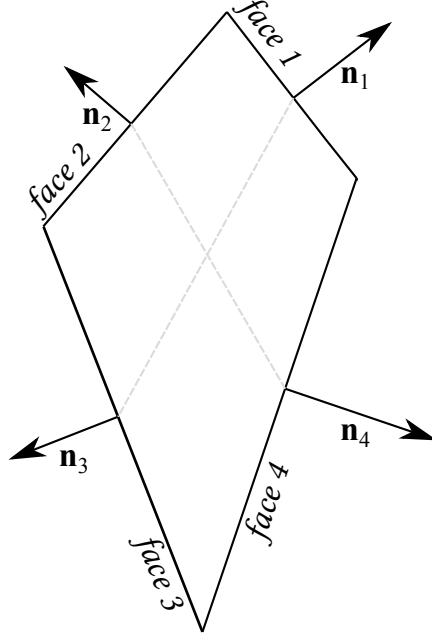


Figure 5.3: A sample two-dimensional control volume bounded by four sides. If faces were indexed by an integer j , then all four faces could be specified as $j \in \{1, \dots, 4\}$; the corresponding faces bounding the volume would be $\mathcal{F} = \{1, 2, 3, 4\}$. The \mathbf{n}_j represents the normal unit vectors for $j \in \{1, 2, 3, 4\}$.

Here, the index j is used to denote that the quantity is calculated at the face j . Again, the set \mathcal{F} is understood to contain faces that bound the domain Ω . We introduce the notion of *residual*, which is defined as

$$\mathbf{R}(\mathbf{U}) = \mathbf{H}(\mathbf{U}) - \frac{1}{V} \sum_{j \in \mathcal{F}} \mathbf{F}_j(\mathbf{U}_j) \cdot \mathbf{n}_j A_j \quad (5.56)$$

and we may now pose equation 5.55 in the *semi-discretized form*,

$$\frac{d\mathbf{U}}{dt} = \mathbf{R}(\mathbf{U}) \quad (5.57)$$

We can envision that a large domain Ω_D could be discretized into a mesh of such approximate control volumes, Ω_k , where the index k is used to denote a set of several such small control volumes; if we have N_Ω different control volumes in the domain, then $k \in \{1, \dots, N_\Omega\}$. Then equation 5.57 must be temporally discretized and solved at each of these control volumes to gather a set of solution vectors \mathbf{U}_k , $k \in \{1, \dots, N_\Omega\}$ on each control volume. Our numerical solution is then comprised of the collection of solution vectors available in each control volume, \mathbf{U}_k .

Two further details remain for us to fully specify the numerical scheme: first, a means of integrating equation 5.57 in time is needed to time-march the solution vector \mathbf{U} ; second, the value of the flux at the bounding face, $\mathbf{F}_j(\mathbf{U}_j)$, must be given a prescription, particularly since we do not technically have solution data \mathbf{U}_j available at the face (we are only keeping track of the solutions \mathbf{U}_k in the volumes).

5.9 Dual-time Implicit Scheme

To advance the solution vector \mathbf{U} in time, we need to numerically integrate the semi-discretized equation, equation 5.57. This could be done in any number of fashions. A simple forward-difference scheme, or more advanced explicit methods taking advantage of Runge-Kutta integration schemes or predictor-corrector methods such as the MacCormack or Adams-Bashforth methods [146] could be implemented with simplicity.

Instead of choosing an explicit approach, an implicit method is much more appropriate. Our motivation is particularly based on the large disparity expected in the eigenvalues, and furthermore, implicit schemes generally tend to stabilize stiff source terms. Implicit schemes can also frequently be shown to be unconditionally stable, in which case large timesteps are available, since they are not restricted to the Courant-Friedrichs-Lewis condition. This permits us to solve the equations in a much more efficient manner for most problems of interest.

In this investigation, the dual-time technique² was selected for the plasmadynamic solvers. This technique has been used to great success for a number of fluid problems. There are also numerous advantages to using this technique that will be discussed shortly.

To introduce the dual-time approach, we start again from our system of m conservation laws, as posed in equation 5.22; before performing the volume integration over a domain Ω , however, we first add a new time derivative of a vector \mathbf{Q} in a fictitious time scale, τ ,

$$\frac{\partial \mathbf{Q}}{\partial \tau} + \frac{\partial \mathbf{U}}{\partial t} + \nabla \cdot \mathbf{F} = \mathbf{H} \quad (5.58)$$

where \mathbf{Q} is a state vector that we will specify momentarily. It is clear that equation 5.58 is exactly equal to equation 5.22 when the vector \mathbf{Q} reaches a steady-state equilibrium in the pseudotime,

$$\frac{\partial \mathbf{Q}}{\partial \tau} = 0 \quad (5.59)$$

We place the following constraints on our choice of the vector \mathbf{Q} :

- We must be able to update the physical (solution, flux, and source) vectors by iterating \mathbf{Q} in τ ; that is, we must be able to write the solution, flux and source vectors as functions of this vector, and
- We would ideally like to choose the \mathbf{Q} that converges fastest with the least amount of error in the physical vectors.

²also known as the *fictitious time method* or *pseudo-time method*

In this approach, we start with equation 5.58, and we want the solution to equation 5.22. This will only ever happen when the condition 5.59 is true. We solve equation 5.58 for the vector \mathbf{Q} evolving in the new time scale τ , and each iteration we update the solution, flux and source vectors, $\mathbf{U}(\mathbf{Q})$, $\mathbf{F}(\mathbf{Q})$, and $\mathbf{H}(\mathbf{Q})$. When we reach a steady-state in τ , the derivative $\partial\mathbf{Q}/\partial\tau$ no longer contributes to equation 5.58, so the solution vector we have iterated to in the dual-time now satisfies equation 5.22 exactly. Numerically, we must settle for forcing the change in \mathbf{Q} to fall below some specified tolerance, but this error tends to be much smaller than the error introduced by our approximation for $\mathbf{F}(\mathbf{Q})$ and $\mathbf{H}(\mathbf{Q})$.

After integrating over the k^{th} control volume Ω_k and introducing the residual in the same way as in the previous subsection, our new semi-discretized equation for the dual-time form is

$$\frac{d\mathbf{Q}_k}{d\tau} = \mathbf{R}_k(\mathbf{Q}_k) - \frac{d\mathbf{U}_k}{dt} \quad (5.60)$$

where k once again is an index indicating the control volume Ω_k being the k^{th} volume in the mesh. The residual \mathbf{R}_k is identical to that given in the last subsection in equation 5.56. Once the condition 5.59 is met, our semi-discretized equation is identical to equation 5.57.

To discretize the physical time derivative, we apply a second-order-accurate three-point difference. The solution vectors for the previous two physical timesteps are indicated as \mathbf{U}'_k and \mathbf{U}''_k , respectively. The discretization of the pseudotime derivative is performed using an Euler implicit discretization. Introducing the physical timestep as Δt and the pseudo-timestep as $\Delta\tau$, and using the superscript n to indicate the iteration in the pseudotime, we have

$$\frac{\mathbf{Q}_k^{n+1} - \mathbf{Q}_k^n}{\Delta\tau} = \mathbf{R}_k^{n+1} - \frac{(\frac{3}{2}\mathbf{U}_k^{n+1} - 2\mathbf{U}'_k + \frac{1}{2}\mathbf{U}''_k)}{\Delta t} \quad (5.61)$$

where $\mathbf{R}_k^{n+1} = \mathbf{R}_k(\mathbf{Q}^{n+1})$. We must now collect the $n+1$ terms in order to develop a matrix equation that can be solved at each k^{th} volume. To do so, we introduce the following linearizations,

$$\mathbf{Q}_k^{n+1} = \mathbf{Q}_k^n + \Delta\mathbf{Q}_k^n \quad (5.62)$$

$$\mathbf{U}_k^{n+1} = \mathbf{U}_k^n + \frac{\partial\mathbf{U}_k^n}{\partial\mathbf{Q}_k^n} \Delta\mathbf{Q}_k^n \quad (5.63)$$

$$\mathbf{R}_k^{n+1} = \mathbf{R}_k^n + \frac{\partial\mathbf{R}_k^n}{\partial\mathbf{Q}_k^n} \Delta\mathbf{Q}_k^n \quad (5.64)$$

and equation 5.61 now becomes, after collecting the unknown update vector $\Delta\mathbf{Q}_k^n$,

$$\left\{ \frac{1}{\Delta\tau} \hat{\mathbf{r}} + \frac{3}{2} \frac{1}{\Delta t} \frac{\partial\mathbf{U}_k^n(\mathbf{Q}_k^n)}{\partial\mathbf{Q}_k^n} - \frac{\partial\mathbf{R}_k^n(\mathbf{Q}_k^n)}{\partial\mathbf{Q}_k^n} \right\} \Delta\mathbf{Q}_k^n = \mathbf{R}_k^n(\mathbf{Q}_k^n) - \frac{(\frac{3}{2}\mathbf{U}_k^n - 2\mathbf{U}'_k + \frac{1}{2}\mathbf{U}''_k)}{\Delta t} \quad (5.65)$$

where we have introduced the Jacobian matrices $\hat{\mathbf{F}} \in \mathbb{R}^{m \times m}$, $\partial \mathbf{U}(\mathbf{Q})/\partial \mathbf{Q} \in \mathbb{R}^{m \times m}$ and $\partial \mathbf{R}(\mathbf{Q})/\partial \mathbf{Q} \in \mathbb{R}^{m \times m}$. These depend on the system of equations, and we have given their full form in Appendices A.4.4 and A.5.4 for the source-coupled and strong conservative systems, respectively. Equation 5.65 has the form $\hat{\mathbf{a}}\mathbf{x} = \mathbf{b}$, and is solved using a Gauss-Seidel matrix inverter for the update vector $\Delta \mathbf{Q}_k^n$. The vectors \mathbf{Q}_k^{n+1} , $\mathbf{U}_k^{n+1}(\mathbf{Q})$ and $\mathbf{R}_k^{n+1}(\mathbf{Q})$ are then updated via equations 5.62 through 5.64. This process is iterated until the vector $\Delta \mathbf{Q}_k^n$ falls below some specified tolerance, at which point the steady-state solution has been reached in τ , and the term $\partial \mathbf{Q}/\partial \tau$ drops out of equation 5.58. Tolerances between 10^{-4} and 10^{-9} were tested, and showed good convergence and agreement.

There are several advantages to be gained by solving equation 5.22 in this fashion:

- Even if equation 5.22 approaches diffusive or steady-state limits, equation 5.58 is *always* hyperbolic in τ ; we can thus solve problems for all cases using a unified hyperbolic approach.
- Since \mathbf{Q} will not add anything to the final solution in the steady-state limit in τ , we may choose \mathbf{Q} to be whatever is convenient; they need not be conservative variables like \mathbf{U} .
- Choosing the primitive variables or some other convenient choice of \mathbf{Q} significantly alleviates the form of the Jacobian matrices $\hat{\mathbf{F}}$, $\partial \mathbf{U}(\mathbf{Q})/\partial \mathbf{Q}$, and $\partial \mathbf{R}(\mathbf{Q})/\partial \mathbf{Q}$.
- The physical time derivative can be shown to always behave as a sink (it will never act as a source) [59]; this tends to stabilize the equations numerically and accelerates the convergence.
- In the limit that $\Delta \tau \rightarrow \infty$, equation 5.65 is identical to the Newton's method for systems of equations [75]. However, the Newton iteration method can be very sensitive to initial conditions; adding the fictitious time derivative allows for a higher-order method of resolving the nonlinear convergence regime before linear convergence is reached.
- In the simplest case, $\hat{\mathbf{F}} = \partial \mathbf{U}/\partial \mathbf{Q}$. But again taking advantage of the irrelevance of \mathbf{Q} in the limit of the dual-time steady-state, we need not retain this form of $\hat{\mathbf{F}}$. Instead, changing this matrix may act to *precondition* the system, allowing faster convergence in τ . Wesseling [154] gives examples of this approach for weakly compressible systems, where the eigenvalues are highly disparate. Li, et al. [59] offers a preconditioning scheme for the coupled Maxwell and Navier-Stokes equations, which introduces a preconditioning parameter, β . In the dual-time, τ , the eigenvalue of Ampere's law becomes βc_0 . The parameter β is chosen depending on the local electrical conductivity; if the conductivity is low, the correct eigenvalue must be used, so $\beta = 1$. When the electrical conductivity is large, however, the diffusive limit is effectively reached, and virtually no wave contributions are provided; in this case, we may choose a value of β that modifies the eigenvalue to a lower value, which considerably accelerates the convergence with little loss in accuracy [59]. In this way, the correct eigenvalue is used in the low-conductivity limit, whereas a smaller value is chosen when the wave contributions are very small. Note that the correct eigenvalue is always used in the physical derivatives and source vector, as well

as the other equations in the dual-time. We follow [59] to choose this parameter as

$$\beta = \left\{ \frac{1}{\mu_0 \sigma c_0 L} \right\}^n \quad (5.66)$$

where σ is the local electrical conductivity, L is an appropriate length scale and n is a power, typically between 0.5 to 2.

In this investigation, the vector \mathbf{Q} was chosen as the primitive variable vectors,

$$\mathbf{Q} = \begin{pmatrix} \varrho & \mathbf{u} & p & \mathbf{B} & \mathbf{E} \end{pmatrix} \quad (5.67)$$

We will take \mathbf{Q} now to always refer to the primitive vector. Since the solution and primitive vectors are related via a one-to-one transformation, any dependency on \mathbf{U} can be exchanged now for \mathbf{Q} and vice versa. Thus, we will use \mathbf{U} and \mathbf{Q} interchangeably for the remainder of this chapter, since one can always be determined from the other. The matrix $\hat{\mathbf{F}}$ was taken as a one-parameter preconditioning matrix as given by Li, et al. [59]. Test cases were run and showed an improved rate of convergence for both the source-coupled and strong conservative approaches using this preconditioning scheme.

5.10 Divergence Cleaning

Recall from Section 2.1.5 that the Gauss laws for the electric and magnetic fields represent divergence constraints. Only solutions to the equations that obey these constraints may be admitted as physical solutions. Discretization of the Maxwell equations in multiple dimensions tends to allow error to accumulate in the divergences unless action is taken to prevent this; this buildup of error allows unphysical solutions to the Maxwell equations to develop. Two different approaches were explored for divergence cleaning, as outlined below.

5.10.1 Brackbill-Barnes Divergence Cleaning

The first approach utilized is the common Brackbill-Barnes approach [191], which requires the solution of a Poisson equation. After the solution update for a single timestep, an iterative process is started, wherein we first calculate the numerical monopole field, $\mathcal{M}(\mathbf{x})$,

$$\mathcal{M}(\mathbf{x}) = \nabla \cdot \mathbf{B} \quad (5.68)$$

A Poisson equation is solved for a correction potential, $\Psi(\mathbf{x})$, with the monopoles acting as the source,

$$-\nabla^2 \Psi(\mathbf{x}) = \mathcal{M}(\mathbf{x}) \quad (5.69)$$

Once the correction potential has been determined, the magnetic field may be corrected by subtracting the gradient of the correction potential,

$$\mathbf{B} \rightarrow \mathbf{B} - \nabla \Psi(\mathbf{x}) \quad (5.70)$$

This approach has been frequently used in magnetohydrodynamic simulations to constrain the divergence of the magnetic field. An equivalent approach can also be applied for the electric field, except that the source term must be careful to exclude the contributions of the charge density that is physically present. This iterative procedure is performed until the maximum divergences in the domain, $|\nabla \cdot \mathbf{B}|$ and $|\nabla \cdot \mathbf{E} - \varrho_e/\epsilon_0|$, were less than some set tolerance. Tolerances between 10^{-2} and 10^{-4} were used and showed good agreement.

5.10.2 Lagrange Multiplier Approach (Perfectly Hyperbolic Maxwell Equations) Divergence Cleaning Approach

The second approach explored is the *perfectly hyperbolic Maxwell equations*, or sometimes called the Lagrange multiplier approach, in which two extra fields, Ψ_B and Ψ_E , are introduced to Maxwell equations [103]. The divergence constraints are rewritten in hyperbolic form with time derivatives of these fields, and they are coupled to the Faraday and Ampere-Maxwell laws via gradients that are added. Once this is performed, the Maxwell equations are effectively rewritten in the form

$$\frac{\partial \mathbf{B}}{\partial t} + \nabla \times \mathbf{E} + \xi \nabla \Psi_B = 0 \quad (5.71)$$

$$\frac{\partial \mathbf{E}}{\partial t} - c_0^2 \nabla \times \mathbf{B} + c_0^2 \chi \nabla \Psi_E = -\mathbf{j}_e/\epsilon_0 \quad (5.72)$$

$$\frac{1}{\xi c_0^2} \frac{\partial \Psi_B}{\partial \tau} + \nabla \cdot \mathbf{B} = 0 \quad (5.73)$$

$$\frac{1}{\chi} \frac{\partial \Psi_E}{\partial \tau} + \nabla \cdot \mathbf{E} = \varrho_e/\epsilon_0 \quad (5.74)$$

Here ξ and χ are dimensionless parameters that effectively represent the strength of the cleaning. Notice that the time derivative of the new divergence fields, Ψ_B and Ψ_E , have been relegated to the dual-time only. This provides an iterative solution procedure that is updated during the dual-time implicit iteration to relax the full solution to the next timestep while retaining a clean divergence. In this approach, the Maxwell equations now become a system of eight equations (Faraday, Ampere-Maxwell, and the two hyperbolized advective equations 5.73 and 5.74) with eight unknowns (\mathbf{E} , \mathbf{B} , Ψ_B and Ψ_E). Equations 5.73 and 5.74 are now hyperbolic equations that can be easily incorporated into our solution approach. The new hyperbolic equations effectively propagate the numerical error accumulation out of the domain at some speed that is specified via the strengths χ and ξ . Whereas the Brackbill-Barnes approach fixes the divergence error below a tolerance, this approach relies on the specification of the speed; larger speeds will result in cleaner divergence, but since the speed now appears in the eigenvalues, high speeds can slow the simulation down, since the new

waves in Ψ_B and Ψ_E must be resolved. Thus, enforcing a stronger constraint costs more simulation time.

5.11 Roe Approximate Riemann Solver Flux Scheme

A prescription for calculating the flux at a face, \mathbf{F}_j , remains to be identified in our formulation. In terms of our original equation, equation 5.22, the flux vector is really a known function of the solution vector, $\mathbf{F}(\mathbf{Q})$, but since we only have solution data available in the control volumes, we do not know the formulation for \mathbf{Q}_j at the face j . The Courant-Friedrich-Lewis condition guarantees that, in a small amount of time, the waves have only propagated a small distance away, so we anticipate calculating an approximation to \mathbf{F}_j as a function of the left and right state vectors, $\mathbf{F}_j \approx \mathbf{F}_j(\mathbf{Q}_L, \mathbf{Q}_R)$. The obvious temptation is to calculate an arithmetic average for the flux based on the two state vectors in the volumes that share face j ,

$$\mathbf{F}_j = \frac{1}{2} (\mathbf{F}_L + \mathbf{F}_R) = \frac{1}{2} (\mathbf{F}(\mathbf{Q}_L) + \mathbf{F}(\mathbf{Q}_R)) \quad (5.75)$$

where L and R denote the *left* and *right* volumes (the two volumes adjoined to the face j). We always define L and R in the sense that the normal vector on the face points from L to R . This naïve approach is elegantly simple, but does not work. As best summarized by LeVeque [151], “Unfortunately, this method is generally unstable for hyperbolic problems and cannot be used, even if the time step is small enough that the CFL condition is satisfied.” Equation 5.75 tends to introduce numerical instabilities that quickly sabotage the solution approach. A simple solution for this problem, therefore, is unlikely to work.

Godunov’s scheme, which historically serves as the basis of all Riemann solver approaches, suggested the novel idea of considering the numerical solution to be equivalent to a piecewise constant set of data, where the solution is a constant value, \mathbf{U}_k , in each control volume. Regarding the solution in this manner allows us to examine the local region around a face j and its surrounding left and right adjoining volumes; it becomes apparent that the region there resembles a Riemann problem (see Figure 5.4) in the local vicinity of the face j , where the left and right state vectors, \mathbf{Q}_L and \mathbf{Q}_R , serve as the initial left and right data for equation 5.49. Godunov’s proposal was to solve the problem as a series of Riemann problems, one at each face, and calculate the updated solution in each volume as the average of the new contributed waves propagated into the volume from each bounding face.

The original Godunov scheme proposed solving the Riemann problem exactly; for nonlinear problems such as those encountered in fluid dynamics, this can be difficult. While a closed-form solution to the Riemann problem for a nonlinear problem does not exist, an iterative approach can be constructed that permits an arbitrary level of precision to be achieved. However, this manner of computing the Riemann solution is computationally expensive, and the solution turns out to only be necessary for adding sufficient diffusion to the unstable flux scheme in equation 5.75. A variety of alternative proposals that followed Godunov’s idea but improve upon the accuracy and efficiency of the solution method have been introduced; this body of work is collectively termed *Godunov methods*, or *Riemann solvers*.

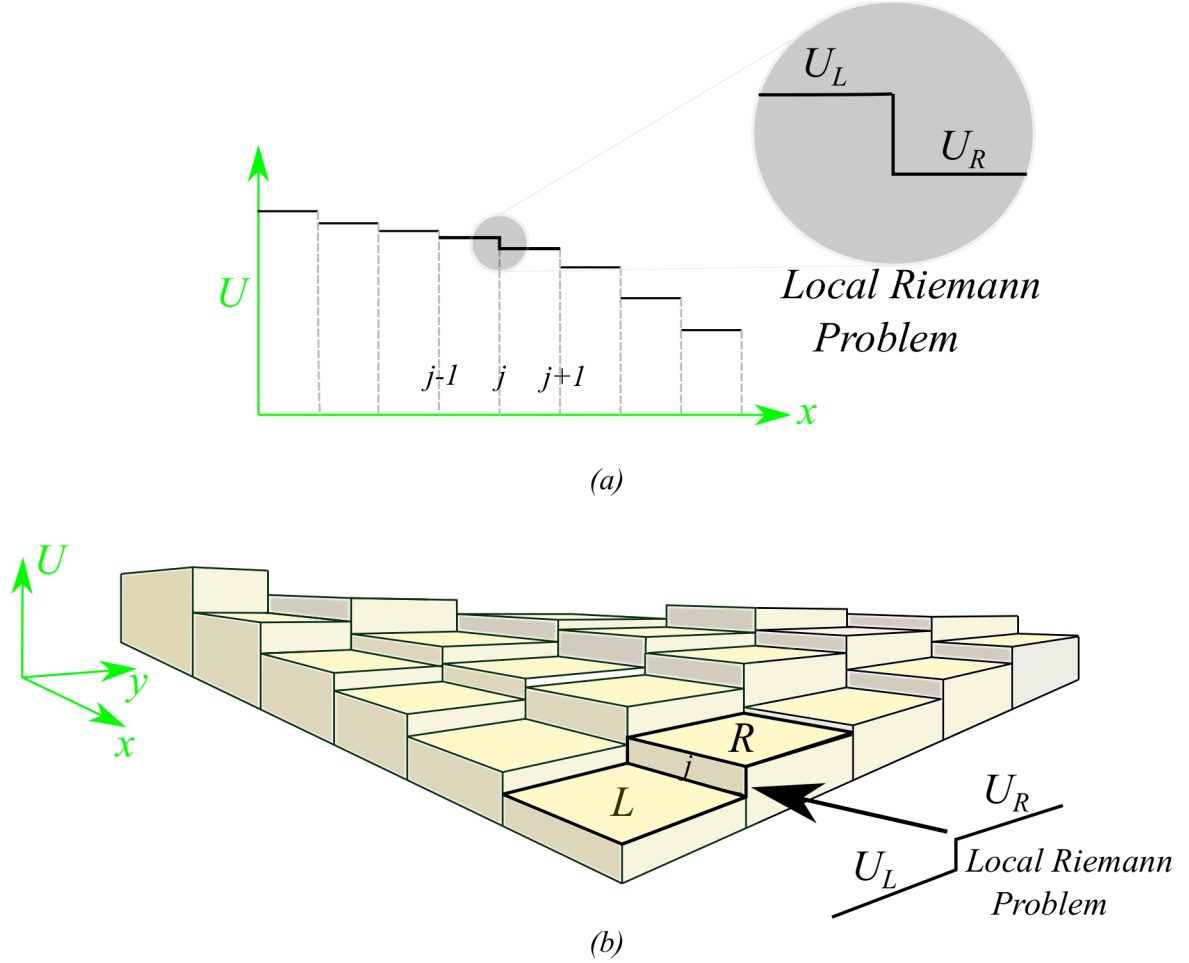


Figure 5.4: Godunov methods treat the discretized mesh of solution vectors \mathbf{U}_k as a series of Riemann problems. (a) In a one-dimensional mesh, considering the solution vector \mathbf{U}_k to be piecewise constant across the mesh (constant in each separate volume k), we see that the face adjoining two volumes (face j in the figure) may be regarded as a Riemann problem, where the solution data in the two volumes represents the left and right data, \mathbf{U}_L and \mathbf{U}_R , respectively. (b) The extrapolation of this scheme to multiple dimensions holds as well. In this two-dimensional example, the quadrilateral mesh of piecewise constant data \mathbf{U}_k forms a Riemann problem in the direction normal to a given face j .

In 1981, Roe [11] proposed a much faster approach that has enjoyed popularity from its inception to the present. It suggests that the governing system of equations, given in equation 5.22, be approximated locally at each face as a *constant-coefficient* quasilinear problem,

$$\frac{\partial \mathbf{U}}{\partial t} + \hat{\mathbf{A}} \frac{\partial \mathbf{U}}{\partial x_k} = 0 \quad (5.76)$$

Here $\hat{\mathbf{A}}$ is a *constant* Jacobian matrix (referred to as the *Roe matrix*) that approximates the local value of the exact Jacobian, $\hat{\mathbf{A}}(\mathbf{Q})$. Since equation 5.76 is a constant-coefficient problem, the eigenvector expansion

for the Riemann solution presented in equation 5.53 is valid, and thus we calculate an *exact* solution to an *approximate* (linearized) Riemann problem. This tends to alleviate the expense required for calculating the Riemann solution without sacrificing much accuracy. At each face in the computational mesh, $\hat{\mathbf{A}}$ is recalculated as a function of some appropriate average of the left and right state vectors, $\hat{\mathbf{A}} = \hat{\mathbf{A}}(\underline{\mathbf{Q}})$, where $\underline{\mathbf{Q}} = \underline{\mathbf{Q}}(\mathbf{Q}_L, \mathbf{Q}_R)$ is an average that will be discussed momentarily. Once the approximate form of the matrix is known, Roe suggested calculating the flux at the face using a modification of equation 5.75,

$$\mathbf{F}_j(\mathbf{Q}_L, \mathbf{Q}_R) = \frac{1}{2}(\mathbf{F}_L + \mathbf{F}_R) - \frac{1}{2} \sum_{p=1}^m \underline{\alpha}^{(p)} |\underline{\lambda}^{(p)}| \underline{\mathbf{K}}^{(p)} \quad (5.77)$$

where $p \in \{1, \dots, m\}$. Here the underbar indicates that the quantity is derived from the Roe matrix, $\hat{\mathbf{A}}(\underline{\mathbf{Q}})$, and thus will depend on $\underline{\mathbf{Q}}$. The quantities $\underline{\lambda}^{(p)}$ and $\underline{\mathbf{K}}^{(p)}$ are the eigenvalues and eigenvectors of the Roe matrix $\hat{\mathbf{A}}$, respectively, and $\underline{\alpha}^{(p)}$ are the solutions to the linearized Riemann problem,

$$\Delta \mathbf{U} = \mathbf{U}_R - \mathbf{U}_L = \sum_{p=1}^m \underline{\alpha}^{(p)} \underline{\mathbf{K}}^{(p)} \quad (5.78)$$

This is just the application of the results from equation 5.53 to the approximate problem in equation 5.76 with initial data \mathbf{U}_L and \mathbf{U}_R provided by the state vectors in the left and right volumes. This is shown diagrammatically in Figure 5.4.

For the Roe flux given in equation 5.77, we therefore need the eigenvalues, $\underline{\lambda}^{(p)}$, eigenvectors, $\underline{\mathbf{K}}^{(p)}$, and decomposition coefficients, $\underline{\alpha}^{(p)}$, with $p \in \{1, \dots, m\}$. Notice that the approximate Jacobian itself, $\hat{\mathbf{A}}$, is not explicitly required. Often, it suffices to construct a *Roe-averaged* set of values, denoted $\underline{\mathbf{Q}} = \underline{\mathbf{Q}}(\mathbf{Q}_L, \mathbf{Q}_R)$, from which the eigenvalues, eigenvectors and decomposition coefficients may be calculated directly. The derivation of the correct form of $\underline{\mathbf{Q}}$ is not trivial; in a stroke of brilliance, Roe suggested the construction of a *parameter vector* to determine a sufficient averaging scheme, which will not be discussed here; details of this approach are provided in [11]. Such an approach was given by Roe for the equations of inviscid gasdynamics, and other examples have followed in the literature. If the system of equations is linear (such as the Maxwell equations), then the Roe-averaged quantities can reduce to arithmetically averaged quantities; for nonlinear problems, the average usually involves a more complicated construction. In practice, once the form of the Roe-averaged values $\underline{\mathbf{Q}}$ are known, the eigenvalues, eigenvectors and decomposition coefficients are often determined analytically from the Roe-averaged state vector, $\underline{\mathbf{Q}}$.

With this information, the basic algorithm for calculating the Roe flux can be summarized as follows, given the left and right state vectors, \mathbf{Q}_L and \mathbf{Q}_R :

1. Calculate the Roe-averaged values from the left and right states, $\underline{\mathbf{Q}}$.
2. Calculate the averaged eigenvalues, $\underline{\lambda}^{(p)}$, $p \in \{1, \dots, m\}$, given the Roe-averaged values, $\underline{\mathbf{Q}}$.
3. Calculate the averaged right eigenvectors, $\underline{\mathbf{K}}^{(p)}$, $p \in \{1, \dots, m\}$, given the Roe-averaged values, $\underline{\mathbf{Q}}$.
4. Calculate the decomposition coefficients, $\underline{\alpha}^{(p)}$, $p \in \{1, \dots, m\}$, that satisfy equation 5.78.

5. Use $\underline{\lambda}^{(p)}$, $\underline{\mathbf{K}}^{(p)}$, $\underline{\alpha}^{(p)}$, \mathbf{Q}_L and \mathbf{Q}_R to calculate \mathbf{F}_j , as per equation 5.77.

In the following, we discuss the development of each of these steps for the source-coupled and strong conservative systems. The large forms of the matrices involved precludes their appearance directly in the dissertation text, but each system's full Jacobians, eigenvalues, and eigenvectors have been included in the appendix. In Appendix A.2, we present this information for the uncoupled Navier-Stokes equations, and in Appendix A.3, we present the same information for the Maxwell equations. Appendix A.5 shows the corresponding form for the strong conservative form. Below, we address these by using a block matrix representation of the coupled systems.

5.11.1 Jacobian Matrix

To implement the Roe scheme, the exact form of the Jacobian matrix, $\hat{\mathbf{A}}$, must first be determined. Roe scheme approaches have already been developed for the uncoupled, independent systems of the three-dimensional, inviscid Navier-Stokes equations and full Maxwell equations; the information for each of these uncoupled systems is presented in Appendices A.2 and A.3, respectively. In the case that the system is coupled, we anticipate that a block system can be composed that includes both contributes. We will assume that the matrix can be written as

$$\hat{\mathbf{A}} = \begin{pmatrix} \hat{\mathbf{A}}_f & \hat{\mathbf{A}}_c \\ \hat{\mathbf{0}} & \hat{\mathbf{A}}_m \end{pmatrix} \quad (5.79)$$

where $\hat{\mathbf{A}}_f$ and $\hat{\mathbf{A}}_m$ are the usual normal-projected Jacobian matrices for the fluid and Maxwell systems, respectively; here $\hat{\mathbf{A}}_c$ is a coupling term that is either zero (in the case of the source-coupled form), or very complicated (in the case of the strong conservative form). For the strong conservative form, the term $\hat{\mathbf{A}}_c$ serves as the point of coupling in the fluid equations to the Maxwell system. In the source-coupled form, the coupling is fashioned in the source terms, so no coupling matrices are necessary. Notice that if the system is source-coupled, the block matrix allows treatment of the flux calculation in an uncoupled fashion, since the coupling will be provided in the time integration update through the residual, \mathbf{R} . The coupling matrix, $\hat{\mathbf{A}}_c$, was calculated for the strong conservative form using symbolic manipulation software. Its size precludes its appearance directly in the text, but has been included in the Appendix A.5.1.

5.11.2 Eigenvalues

The source-coupled and strong conservative forms enjoy identical eigenvalues, since the presence of the coupling matrix in the strong conservative form, $\hat{\mathbf{A}}_c$, only affects off-diagonal terms and does not contribute to the characteristic polynomial. For both systems, the diagonal matrix of eigenvalues can be expressed as

$$\hat{\Lambda} = \begin{pmatrix} \hat{\Lambda}_f & \hat{\mathbf{0}} \\ \hat{\mathbf{0}} & \hat{\Lambda}_m \end{pmatrix} \quad (5.80)$$

where $\hat{\Lambda}_f$ and $\hat{\Lambda}_m$ are the fluid and Maxwell eigenvalues, given in equations A.57 and A.80, respectively.

5.11.3 Eigenvectors

An analysis of the eigenvectors for the source-coupled and strong conservative forms reveal a similar block structure,

$$\hat{\mathbf{K}} = \begin{pmatrix} \hat{\mathbf{K}}_f & \hat{\mathbf{K}}_c \\ \hat{\mathbf{0}} & \hat{\mathbf{K}}_m \end{pmatrix} \quad (5.81)$$

where $\hat{\mathbf{K}}_f$ and $\hat{\mathbf{K}}_m$ are the usual fluid and Maxwell eigenvectors, given in equations A.61 and A.85, respectively, and $\hat{\mathbf{K}}_c$ is a new set of coupling eigenvectors. For the source-coupled system, this new coupling matrix is zero, $\hat{\mathbf{K}}_c \rightarrow \hat{\mathbf{0}}$, and the flux calculation can be treated as a block system; for the strong conservative form, the matrix $\hat{\mathbf{K}}_c$ is nonzero, and can be very complicated. The eigenvectors were also derived using the symbolic manipulation software Mathematica [192], and verified to fully diagonalize the system of equations; their full form is shown in Appendix A.5.3.

5.11.4 Solutions to the Riemann Problem

The decomposition coefficients, $\underline{\alpha}$, must be calculated for the source-coupled and strong conservative forms for the Roe flux scheme by solving equation 5.78 for each respective system. For the source-coupled form, the Riemann problem is still represented in a block system, and equation 5.78 can be solved straightforwardly, as the Riemann problem itself is not coupled (once again, the coupling enters through the residual during the pseudo-time integration). In this case, we get the typical decomposition coefficients for each respective system, as presented in Appendices A.2.4 and A.3.4 for the fluid and Maxwell systems, respectively.

Calculating the decomposition coefficients for the strong conservative form is much more difficult. Due to the presence of the new coupling eigenvectors, the system of equations represented in equation 5.78 is a nontrivial system of equations. We confirmed that an analytical solution exists, per symbolic manipulation software, but were unable to convert the solution into a form feasible for implementation; furthermore, the size of the solution would have considerably slowed down the execution of the solver with the number of extra terms added. To circumvent this difficulty, we approximated the decomposition coefficients by using the same set for the source-coupled form. Although this is an approximation, we confirmed that the additional terms in the correct form for the strong conservative decomposition coefficients were of order $1/c_0^2$ and $1/c_0^3$; it is expected that these terms will contribute little to the actual value of the decomposition coefficients while severely complicating both the implementation and execution time. Therefore, the same set of decomposition coefficients were used in both the source-coupled and strong conservative forms. The validation test results, presented in Chapter 6, indicate that this assumption is reasonable.

5.12 Advected Upstream Splitting Method (AUSM) Flux Scheme

The Roe scheme described in the previous section involves a lot of complicated calculations and detailed information. To validate the new eigenstructure for the strong conservative form, the approximations of the decomposition coefficients, and the new Roe method itself, we also constructed a flux scheme using the AUSM technique described by Liou and Steffan [12, 193, 194]. This approach does not require the Jacobian matrices or eigenstructure, and so can be used to verify the Roe scheme results for the strong conservative approach. Furthermore, the AUSM family of schemes offers several potential advantages over Riemann solver approaches: it guarantees entropy conservation and positivity preservation, is carbuncle-free, is relatively easy to implement, and requires much less execution time per cycle for calculation than the Roe method [12]. Alternative flux-splitting methods related to AUSM, such as the Energy-Convective Upwind and Split Pressure (E-CUSP) method, could also be applied. Our goal is still the same here: to develop an approximation for \mathbf{F}_j at face j as a function of the left and right state vectors, \mathbf{Q}_L and \mathbf{Q}_R .

The AUSM scheme has been reviewed elsewhere [12, 147]; although the presentation of the definitions used in the algorithm usually resembles the unstacking of Russian matryoshka dolls, we repeat the basic algorithm here, primarily following [147]. As an example, we begin by considering the three-dimensional equations of inviscid gasdynamics. The essence of the method is captured in the assumption that the flux may fundamentally be split in to the *advective* and *pressure* (or sometimes the *linear* and *nonlinear*) terms,

$$\mathbf{F}(\mathbf{Q}) = \mathbf{F}^{(A)}(\mathbf{Q}) + \mathbf{F}^{(P)}(\mathbf{Q}) \quad (5.82)$$

where $\mathbf{F}^{(A)}$ and $\mathbf{F}^{(P)}$ are the advective and pressure fluxes, respectively. The flux vector for the three-dimensional inviscid Navier-Stokes equations can be written relative to face j 's normal vector, \mathbf{n}_j , as

$$\mathbf{F} = \begin{bmatrix} \varrho \mathbf{u} \cdot \mathbf{n}_j \\ \varrho u \mathbf{u} \cdot \mathbf{n}_j + p n_x \\ \varrho v \mathbf{u} \cdot \mathbf{n}_j + p n_y \\ \varrho w \mathbf{u} \cdot \mathbf{n}_j + p n_z \\ \varrho H \mathbf{u} \cdot \mathbf{n}_j \end{bmatrix} = \mathbf{u} \cdot \mathbf{n}_j \begin{bmatrix} \varrho \\ \varrho u \\ \varrho v \\ \varrho w \\ \varrho H \end{bmatrix} + p \begin{bmatrix} 0 \\ n_x \\ n_y \\ n_z \\ 0 \end{bmatrix} = M \begin{bmatrix} \varrho a \\ \varrho a u \\ \varrho a v \\ \varrho a w \\ \varrho a H \end{bmatrix} + p \begin{bmatrix} 0 \\ n_x \\ n_y \\ n_z \\ 0 \end{bmatrix} \quad (5.83)$$

Here, we have split the flux into the advective and pressure fluxes, each containing those respective terms; we have also recast the advective flux in terms of the Mach number, $M = \mathbf{u} \cdot \mathbf{n}_j / a$, where a is the local speed of sound; n_x , n_y , and n_z should be understood to be components of the normal vector, \mathbf{n}_j . The AUSM scheme proposes approximating the flux at face j as

$$\mathbf{F}_j = \widehat{\mathbf{F}}^{(A)} + \widehat{\mathbf{F}}^{(P)} \quad (5.84)$$

where the $\widehat{\mathbf{F}}^{(A)}$ and $\widehat{\mathbf{F}}^{(P)}$ are the upwinded advective and pressure fluxes; they may be defined as

$$\widehat{\mathbf{F}}^{(A)} = \widehat{M} \begin{cases} \begin{bmatrix} \rho a \\ \rho a u \\ \rho a v \\ \rho a w \\ \rho a H \end{bmatrix}_L, & \widehat{M} \geq 0 \\ \begin{bmatrix} \rho a \\ \rho a u \\ \rho a v \\ \rho a w \\ \rho a H \end{bmatrix}_R, & \widehat{M} < 0 \end{cases} \quad (5.85)$$

and where

$$\widehat{\mathbf{F}}^{(P)} = \widehat{p} \begin{pmatrix} 0 & n_x & n_y & n_z & 0 \end{pmatrix}^T \quad (5.86)$$

In these expressions, we impose the following definitions:

$$\widehat{M} = M_L^+ + M_R^- \quad (5.87)$$

and

$$\widehat{p} = p_L^+ + p_R^- \quad (5.88)$$

The expressions M^\pm and p^\pm can take many different forms. In this work, we use the following definitions,

$$M^\pm = M_4^\pm = \begin{cases} M_1^\pm(M), & |M| \geq 1 \\ M_2^\pm(M) (1 \mp 2M_2^\mp(M)), & \text{else} \end{cases} \quad (5.89)$$

$$p^\pm = p_5^\pm = \begin{cases} (1/M) M_1^\pm(M), & |M| \geq 1 \\ M_2^\pm(M) [(\pm 2 - M) \mp 3M M_2^\mp(M)], & \text{else} \end{cases} \quad (5.90)$$

with

$$M_1^\pm = \frac{1}{2} (M \pm |M|) \quad (5.91)$$

$$M_2^\pm = \pm \frac{1}{4} (M \pm 1)^2 \quad (5.92)$$

Given the forms of M^\pm and p^\pm , the values \widehat{M} and \widehat{p} can be calculated, and these are used to construct the

upwinded advective and pressure fluxes, $\hat{\mathbf{F}}^{(A)}$ and $\hat{\mathbf{F}}^{(P)}$. Finally, the flux approximation \mathbf{F}_j is assembled by summing these two contributions. With reference to our previous discussion regarding the unstable flux average in equation 5.75, we note that the AUSM flux can be written in the form

$$\mathbf{F}_j = \frac{1}{2}\widehat{M} \begin{bmatrix} \rho a \\ \rho a u \\ \rho a v \\ \rho a w \\ \rho a H \end{bmatrix}_L + \begin{bmatrix} \rho a \\ \rho a u \\ \rho a v \\ \rho a w \\ \rho a H \end{bmatrix}_R - \frac{1}{2}|\widehat{M}| \begin{bmatrix} \rho a \\ \rho a u \\ \rho a v \\ \rho a w \\ \rho a H \end{bmatrix}_R - \begin{bmatrix} \rho a \\ \rho a u \\ \rho a v \\ \rho a w \\ \rho a H \end{bmatrix}_L + \widehat{p} \begin{bmatrix} 0 \\ n_x \\ n_y \\ n_z \\ 0 \end{bmatrix} \quad (5.93)$$

This is clearly not a simple modification of equation 5.75, but rather the left and right flux averages are weighted by the Mach number [195]; the additional terms serve as a numerical dissipation to counter the instabilities in the flux average.

So far, we have only considered the uncoupled Navier-Stokes equations. In the case of the source-coupled formulation, this discussion suffices for the AUSM method, since the coupling is relegated to the sources. However, for the strong conservative form, the appearance of new terms in the flux vectors complicate the scheme slightly. There are actually several approaches that could be used for incorporating the new flux terms. For example, the Maxwell stress tensor could be considered a pressure term (in the magnetohydrodynamic limit, the stress tensor reduces to the magnetic pressure), and thus could be split into the pressure term, while the remaining terms are included in the advective term. An alternative approach might be to consider a separate, new flux term added to the advective and pressure split fluxes, which contains the electromagnetic flux terms. For this investigation, several variations of these methods were explored, but it was discovered that more detailed and complicated splitting schemes did not significantly improve the accuracy or speed; therefore, the simplest approach was taken. In this approach, we split the new strong conservative flux terms into a new vector. This means that the Navier-Stokes flux is now written as in equation 5.83, but with an additional flux vector containing the new coupling contributions,

$$\begin{aligned} \mathbf{F} &= \begin{bmatrix} \rho \mathbf{u} \cdot \mathbf{n}_j \\ \rho u \mathbf{u} \cdot \mathbf{n}_j + p n_x - \Sigma_{xx}^{EM} n_x - \Sigma_{xy}^{EM} n_y - \Sigma_{xz}^{EM} n_z \\ \rho v \mathbf{u} \cdot \mathbf{n}_j + p n_y - \Sigma_{xy}^{EM} n_x - \Sigma_{yy}^{EM} n_y - \Sigma_{yz}^{EM} n_z \\ \rho w \mathbf{u} \cdot \mathbf{n}_j + p n_z - \Sigma_{xz}^{EM} n_x - \Sigma_{yz}^{EM} n_y - \Sigma_{zz}^{EM} n_z \\ \rho H \mathbf{u} \cdot \mathbf{n}_j + S_x^{EM} n_x + S_y^{EM} n_y + S_z^{EM} n_z \end{bmatrix} \\ &= M \begin{bmatrix} \rho a \\ \rho a u \\ \rho a v \\ \rho a w \\ \rho a H \end{bmatrix} + p \begin{bmatrix} 0 \\ n_x \\ n_y \\ n_z \\ 0 \end{bmatrix} - \begin{bmatrix} 0 \\ \Sigma_{xx}^{EM} n_x + \Sigma_{xy}^{EM} n_y + \Sigma_{xz}^{EM} n_z \\ \Sigma_{xy}^{EM} n_x + \Sigma_{yy}^{EM} n_y + \Sigma_{yz}^{EM} n_z \\ \Sigma_{xz}^{EM} n_x + \Sigma_{yz}^{EM} n_y + \Sigma_{zz}^{EM} n_z \\ -(S_x^{EM} n_x + S_y^{EM} n_y + S_z^{EM} n_z) \end{bmatrix} \end{aligned} \quad (5.94)$$

where we have added a new vector on the right containing the coupling terms ($\hat{\mathbf{\Sigma}}^{EM}$ and \mathbf{S}^{EM} are again the Maxwell stress tensor and Poynting vector, respectively) for the strong conservative form. While upwinding this new flux vector was attempted, it did not significantly improve the accuracy or speed over simply using the previous timestep's calculations for the electromagnetic fields, \mathbf{E} and \mathbf{B} . Therefore, for the investigations presented, simply calculating the new term from the most recent field calculations was used and added to couple the Navier-Stokes system to the Maxwell equations.

Since the Maxwell equations do not change form between the source-coupled and strong conservative systems, it is neither necessary nor helpful to modify the Maxwell solver scheme. The Maxwell equations were solved using the Roe scheme when the AUSM scheme was applied to the strong conservative form.

5.13 Boundary Conditions

For the validation test cases presented in Chapter 6, simple boundary conditions were needed for simulation. For the fluid system, either periodic, inflow, outflow or inviscid slip boundary conditions could be applied. For the Maxwell equations, either periodic, transmissive or perfectly conducting boundary conditions were available. The boundary conditions were treated by constructing ghost volumes interfacing to the boundaries of the computational mesh. If a control volume k possesses a face j that lies on the surface of the computational domain, a ghost volume labelled m is assigned as the right volume to the face j , such that $\mathcal{V}_j = \{L, R\} = \{k, m\}$. The state vector for the ghost volume, \mathbf{Q}_m , was determined by the choice of boundary condition. The calculation of the flux across the face, \mathbf{F}_j , and subsequent change to the boundary volume residual, \mathbf{R}_k , was calculated in the same way as interior volumes. The inflow condition prescribed a fixed \mathbf{Q}_m for the ghost volume (it could be changed during simulation to ramp the inflow). The different boundary conditions are detailed in the following subsections.

5.13.1 Periodic Boundary Conditions

Periodic conditions are useful for exploring problems in instability and turbulence [151]. These conditions will be applied in Chapter 6 for the magnetohydrodynamic Kelvin-Helmholtz instability and Orszag-Tang turbulence problems. In this case, the domain is considered topologically connected, such that information leaving one side of the computational domain is taken as an inflow from the opposite side. In this case, the ghost volume m is identical to the topologically connected opposite volume, and $\mathbf{Q}_m = \mathbf{Q}_R$ is taken as the state vector in this connected volume.

5.13.2 Transmissive Outflow and Inviscid Wall Boundary Conditions

Transmissive outflow of waves out of the computational domain is significant, since it permits a smaller computational domain than the full physical setup to be modeled [151]; however, successful transmission of waves out of the domain without numerical reflection is an active research problem [196], particularly for

Maxwell's equations. Typically, perfectly-matched layers (PMLs) or absorbing boundary conditions (ABCs) can be applied to minimize the numerical reflections as electromagnetic waves exit the domain, but these conditions are not perfect. For the investigations here, simple transmissive (Neumann) conditions sufficed, and any reflected numerical waves were small. In the future, more advanced transmissive conditions are planned for study. The condition used for the validations insists that the gradient of \mathbf{Q} across the face j is zero, which means that the ghost volume state vector is $\mathbf{Q}_m = \mathbf{Q}_R = \mathbf{Q}_L$. For the fluid, the outflow was assumed to be supersonic. Inviscid wall conditions could further be applied by first assuming the boundary was transmissive, and then subtracting the residual in the boundary cell, \mathbf{R}_k , associated with the normal velocity, $\mathbf{u} \cdot \mathbf{n}_j$. This subtraction is after the residual accumulation (which uses the transmissive condition for the boundary), and before the time integration to the next timestep.

5.14 Putting It All Together: Meshing, Interpolation, Gradient Reconstruction and Solver Algorithm

Now that the essential ingredients for the finite volume solver have all been discussed, we may lay out the finer details of unstructured meshing, the application of interpolation and gradient reconstruction, and the overall algorithm.

We can extend our notation introduced so far to discuss data structures representing arbitrary geometries. We consider the computational domain, Ω_D , to be discretized into a set of *nodes*, *faces*, and *volumes*. Nodes represent single points in the geometry; faces are represented as collections of points to form a bounding surface between two control volumes, and the volumes are defined by closed sets of bounding faces. We keep our present indexing, using j to represent some face and k to represent some control volume, and introduce an index i for nodes. Thus, $i \in \{1, \dots, N_N\}$, $j \in \{1, \dots, N_F\}$, and $k \in \{1, \dots, N_\Omega\}$, where N_N , N_F , and N_Ω represents the maximum number of nodes, faces, and volumes, respectively, that comprise the mesh. The index will now always dictate what data structure a quantity belongs to, so, for example, \mathbf{F}_j belongs on face j , \mathbf{U}_k belongs on volume k , etc. Each data structure possesses a position vector, \mathbf{r} , pointing to its physical position (for faces and volumes, it points to the centroid). Vectors between two elements may be denoted using two indices; for example, the distance from face j to its L volume may be written $\mathbf{r}_{Lj} = \mathbf{r}_L - \mathbf{r}_j$. We must further introduce the notion of *connectivity sets*; a connectivity set is denoted using the calligraphic letters \mathcal{N} , \mathcal{F} , \mathcal{V} , and \mathcal{B} , for connected nodes, faces, volumes and neighboring structures of the same type, respectively. Thus, any node i has a set of mother volumes, \mathcal{V}_i , and mother faces, \mathcal{F}_i , and neighbor nodes, \mathcal{B}_i , which are connected via faces that share node i . Similarly, a control volume k has a set of daughter nodes, \mathcal{N}_k , daughter faces, \mathcal{F}_k , and a set of neighboring control volumes that share a common face, \mathcal{B}_k . Faces contain a set of daughter nodes, \mathcal{N}_j , and a list of volumes adjoined to the face, $\mathcal{V}_j = \{L, R\}$. Only two volumes, L and R , are ever permitted to be attached to any face j . The volumes L and R are chosen such that the normal vector on the face, \mathbf{n}_j , points from L to R . For boundary faces, the associated adjoining

volumes will be a singleton, $\mathcal{V}_j = \{L\}$, and the normal vector is redefined consistently with this. The volume in any control volume k is denoted V_k , and the area of any face j is denoted A_j . We will further make use of the notation $|\mathcal{N}|$ to indicate the size of the set \mathcal{N} . To assist the reader, Figure 5.5 and Table 5.1 have been provided, which diagram the associated data and their nomenclature for each data structure.

The solution update procedure proceeds as follows. The state vector, \mathbf{Q}_k , is known from the last timestep (or initial conditions), and has the form

$$\mathbf{Q} = \left(\varrho \quad \mathbf{u} \quad p \quad \mathbf{B} \quad \mathbf{E} \quad \Psi_B \quad \Psi_E \right)^T \quad (5.95)$$

where Ψ_B and Ψ_E are the divergence fields for the Lagrange multiplier approach to cleaning the divergence. To disable divergence cleaning, the associated speeds may be set to zero. The residual on the first dual-time iteration, $\mathbf{R}_k^{n=0}$, is zeroed, and the old solutions from the previous two timesteps are recorded, \mathbf{U}'_k and \mathbf{U}''_k . Boundary faces are assigned ghost volume data for their right volume, R , depending on their associated boundary condition. We traverse the faces j , $j \in \{1, \dots, N_F\}$, and on each determine the left and right state vectors, \mathbf{Q}_{jL} and \mathbf{Q}_{jR} , to be used for the flux scheme (either Roe or AUSM). The left and right state vectors are interpolated from the values of \mathbf{Q}_L and \mathbf{Q}_R using the method discussed below to achieve higher accuracy. Once the flux scheme has been used to determine the flux at the face j , \mathbf{F}_j , we subtract this flux contribution from the residual in the left volume, \mathbf{R}_L^n , and we add the same amount to the right volume, \mathbf{R}_R^n . In this way, the flux is conserved across the face. We then traverse the control volumes k , $k \in \{1, \dots, N_\Omega\}$, and solve the matrix equation 5.65 at each volume k . The dual-time iteration involves the process described in Section 5.9, wherein the Jacobian matrices are calculated, the state vector is updated in the dual-time, the solution and source terms (and also possibly the flux terms) are updated as functions of the state vector \mathbf{Q} using the linearization in equations 5.62 through 5.64. We tried both updating the flux vector, \mathbf{F}_j^n , throughout the dual-time iteration, and also explicitly computing it before the dual-time iteration; a difference in accuracy was not found in the validation test problems, and the execution time required was lower if the flux was computed explicitly beforehand. The dual-time process is iterated until the dual-time derivative drops out of equation 5.58, which occurs when the update vector, $\Delta\mathbf{Q}_k$, falls below a tolerance. Tolerances in the range of 10^{-4} to 10^{-9} were tested and showed good agreement. If the Brackbill-Barnes approach is used for divergence cleaning, the speeds for the Lagrange equations are set to zero, and the Poisson solve is performed after the solution update at the end of the timestep.

In order to improve the spatial accuracy of the solver, a high-order spatial reconstruction scheme was implemented. This consisted of an interpolation scheme for weighting the volume data, \mathbf{U}_k , to the nodes, \mathbf{U}_i , and faces, \mathbf{U}_j . The interpolation occurred before the solution update procedure each timestep. Once the solution data was interpolated to the nodes and faces, the gradient data in each volume, $\nabla\mathbf{Q}_k$, could be computed using a Green-Gauss gradient reconstruction method. The volume gradient data would be necessary for the calculation of diffusive fluxes, such as viscous terms in the Navier-Stokes equations. Fur-

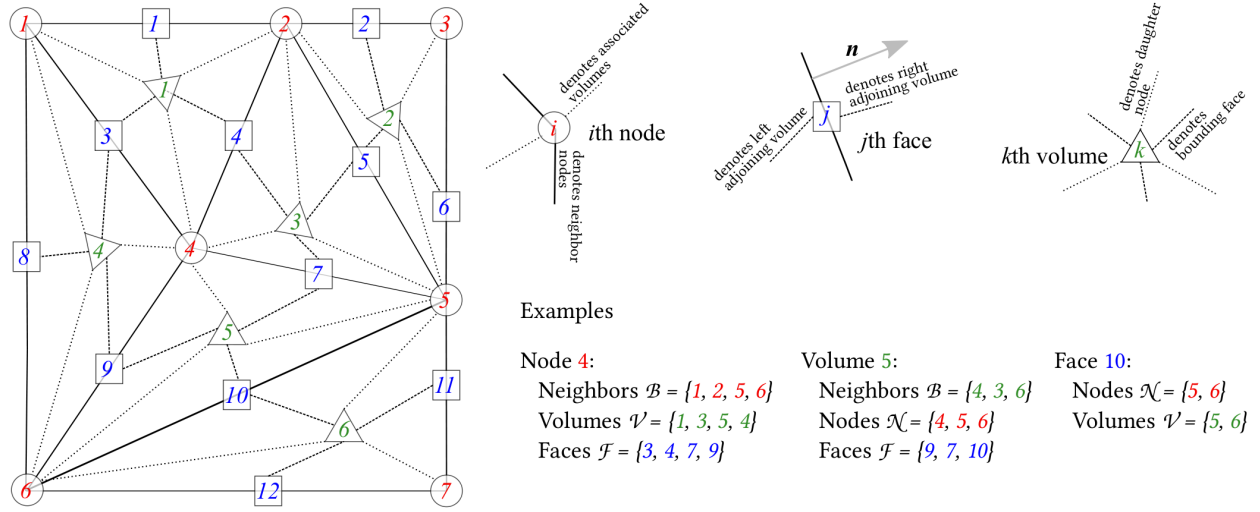


Figure 5.5: A diagrammatic sketch of connectivity within the mesh. An example two-dimensional mesh is shown on the left, composed of triangles (shown in solid lines). Elements are indicated for nodes as red indices in circles, for faces as blue indices in squares, and for volumes as green indices in triangles. Connectivity between the different elements are shown via dashed lines. Elements are not restricted to triangular in shape; each element can carry as many constituent edges and nodes as memory permits.

thermore, after the volume gradient data, $\nabla \mathbf{Q}_k$, was available, the gradient data on each face, $\nabla \mathbf{Q}_j$ could be determined in a face j by applying flux limiting schemes to the volume gradient data in the left and right adjoining volumes, $\nabla \mathbf{Q}_L$ and $\nabla \mathbf{Q}_R$. With the limited face gradient data, a MUSCL-based interpolation scheme [197] could be applied at each face j to improve the accuracy of the left and right state vectors. The new, interpolated vectors are denoted \mathbf{Q}_{jL} and \mathbf{Q}_{jR} , and are interpolated from the raw left and right state data, $\nabla \mathbf{Q}_L$ and $\nabla \mathbf{Q}_R$.

To interpolate the solution data to the nodes and faces, the solution \mathbf{Q} was interpolated to each node i based on the solution data for its mother volumes, \mathbf{Q}_k , $k \in \mathcal{V}_i$. A weighted-area interpolation scheme was used, which involves the construction of the precomputed geometric matrices

$$\mathbf{r}_{ik} = \mathbf{r}_i - \mathbf{r}_k \quad (5.96)$$

$$\hat{\mathbf{G}}_{ik} = \frac{(\mathbf{r}_{ik} - \mathbf{r}_i)(\mathbf{r}_{ik} - \mathbf{r}_i)}{[\max(\mathbf{r}_{ik} - \mathbf{r}_i)]^2} \quad (5.97)$$

$$\mathbf{c}_{ik} = \hat{\mathbf{G}}_{ik}^{-1} \mathbf{r}_{ik} \quad (5.98)$$

for $k \in \mathcal{V}_i$. These matrices can be precomputed and stored on each node i . The actual weight for any node i and volume $k \in \mathcal{V}_i$, is then given by

$$w_{ik} = 1 - \mathbf{c}_{ik} \cdot \mathbf{r}_{ik} \quad (5.99)$$

Table 5.1: Nomenclature of mesh data structures.

Data structure	Notation	Associated Data	
		Notation	Description
Nodes	N_i	\mathbf{r}_i	position vector
		\mathbf{U}_i	solution vector at node
		\mathcal{V}_i	set of associated mother volumes
		\mathcal{F}_i	set of associated mother faces
		\mathcal{B}_i	set of neighboring nodes
Faces	F_j	\mathbf{r}_j	centroid position vector
		\mathbf{U}_j	solution vector as face
		$\nabla \mathbf{U}_j$	gradient of solution vector at face
		\mathcal{V}_j	adjoining volumes connected to this face (only two)
		\mathcal{N}_j	set of associated daughter nodes
		\mathbf{r}_{jk}	set of vectors from face centroid to adjoining volumes (only two)
		A_j	area of face
		\mathbf{n}_j	normal vector of face
Volumes	Ω_k	\mathbf{r}_k	centroid position vector
		\mathbf{U}_k	solution vector at volume centroid
		$\nabla \mathbf{U}_k$	gradient of solution vector at centroid
		\mathbf{R}_k	residual at centroid
		\mathcal{N}_k	set of associated daughter nodes
		\mathcal{F}_k	set of associated daughter faces
		\mathcal{B}_k	set of neighboring control volumes
		V_k	volume of control volume

and the solution vector on the node i is then given as

$$\mathbf{Q}_i = \frac{\sum_{k \in \mathcal{V}_i} w_{ik} \mathbf{Q}_k}{\sum_{k \in \mathcal{V}_i} w_{ik}} \quad (5.100)$$

The value \mathbf{Q}_j can be computed for this algorithm using the arithmetic average of the solution data \mathbf{Q}_i for the associated nodes, \mathcal{N}_j ,

$$\mathbf{Q}_j = \frac{1}{|\mathcal{N}_j|} \sum_{i \in \mathcal{N}_j} \mathbf{Q}_i \quad (5.101)$$

Once the solution data \mathbf{Q}_i is known, an explicit Green-Gauss integration for $\nabla \mathbf{Q}_k$ is constructed using the integral of the gradient,

$$\int_{\Omega_k} \nabla \mathbf{Q}_k d\Omega_k = \int_{\Omega_k} \nabla \cdot (\mathbf{Q}_k \hat{\mathbf{i}}) d\Omega_k = \oint_{\partial \Omega_k} \mathbf{Q}_j \hat{\mathbf{i}} \cdot \mathbf{n} dA \approx \sum_{j \in \mathcal{F}_k} \mathbf{Q}_j \mathbf{S}_j \quad (5.102)$$

such that

$$\nabla \mathbf{Q}_k = \frac{1}{V_k} \sum_{j \in \mathcal{F}_k} \mathbf{Q}_k \mathbf{S}_j \quad (5.103)$$

where $\mathbf{S}_j = A_j \hat{\mathbf{i}} \cdot \mathbf{n}_j$ is a geometric vector that may be computed and stored on each face j before simulation. With the volume gradient data, $\nabla \mathbf{Q}_k$, the gradient at the face j , $\nabla \mathbf{Q}_j$, may be calculated by applying a *flux-limiting* scheme to the left and right volume gradients, $\nabla \mathbf{Q}_j = \text{limiter}(\nabla \mathbf{Q}_k)$, $k \in \mathcal{V}_j$. Flux limiting ensures that shocks and discontinuities are resolved without dispersive error. Here, the minmod [198] and van Albada [199] flux limiters were implemented; either may be applied during simulation, depending on the user's choice. Once the limited form of $\nabla \mathbf{Q}_j$ is known, the left and right state vectors at the face j are interpolated, $\mathbf{Q}_{jL} = \mathbf{Q}_L + \nabla \mathbf{Q}_j \cdot \mathbf{r}_{Lj}$ and $\mathbf{Q}_{jR} = \mathbf{Q}_R + \nabla \mathbf{Q}_j \cdot \mathbf{r}_{Rj}$, are passed to the flux scheme (either Roe or AUSM) to calculate the flux, \mathbf{F}_j , at the face j . This permits at least second-order spatial accuracy of the solution approach; more detailed or iterative variants can also be introduced with this framework.

Chapter 6

Validation Tests for the Strong Conservative Formulation

“All these science spheres are made of asbestos, by the way. Keeps out the rats. Let us know if you feel a shortness of breath, a persistent dry cough or your heart stopping. Because that’s not part of the test. That’s asbestos.”

Cave Johnson [1]

In this section, we present the validation tests run for the strong conservative and source-coupled systems. Our primary interest is to compare the performance and accuracy and performance of the source-coupled and strong conservative approaches, and to compare the accuracy of the Roe and AUSM formulations for the strong conservative solver. For consistency, only structured meshes were used for the results presented, although fully unstructured meshes were also explored.

6.1 Brio and Wu Plasma Shock Riemann Problem

The Brio and Wu plasma shock problem [145] has become a classic benchmark for validating high-conductivity plasma simulations. The problem is analogous to the Sod gasdynamic shock tube problem, except that an additional discontinuity is applied in the magnetic field. When the conductivity is high, the plasma should demonstrate the typical variety of waves expected in magnetohydrodynamic plasmas. Both the Roe and AUSM methods were applied to this test problem; the Roe results are presented here.

The same nondimensional initial conditions and simulation parameters are used here that appears in the literature, so that a direct comparison between the approaches may be made. The computational domain is a one-dimensional region of nondimensional unit length, $x \in [0, 1]$, divided into 1,600 elements. The initial

conditions are taken as

$$\mathbf{Q}(x, t = 0) = \begin{cases} \mathbf{Q}_{\text{left}}, & x < 0.5 \\ \mathbf{Q}_{\text{right}}, & x \geq 0.5 \end{cases} \quad (6.1)$$

where

$$\mathbf{Q}_{\text{left}} = \begin{cases} \varrho = 1 \\ \mathbf{u} = \mathbf{0} \\ p = 1 \\ \mathbf{B} = (0.75, 1, 0) \\ \mathbf{E} = \mathbf{0} \end{cases}, \quad \mathbf{Q}_{\text{right}} = \begin{cases} \varrho = 0.125 \\ \mathbf{u} = \mathbf{0} \\ p = 0.1 \\ \mathbf{B} = (0.75, -1, 0) \\ \mathbf{E} = \mathbf{0} \end{cases} \quad (6.2)$$

The specific heat ratio is assumed to be a constant and is chosen as $\gamma = 2$. Although this is an unrealistic choice for the specific heat ratio, it was historically chosen because it permitted an analytical form for the Roe averaging for the MHD equations [145]; it is still commonly chosen for benchmarking against Brio and Wu's solution [145]. Following the literature [75], we choose $c_0 = 100$, $\mu_0 = 1$, and by the Weber relation, we have $\epsilon_0 = 10^{-4}$. In order to test a physically correct scenario, values of $c_0 = 10^3, 10^4, 10^5$ and 10^6 were also tested; $c_0 = 10^6$ corresponds to a realistic disparity between the fluid and light speeds, and showed identical results to $c_0 = 100$.

The solution is dependent on assigned scalar conductivity, σ . In the limit that the conductivity becomes infinitely large, the magnetic field becomes diffusive, and our solution should agree with the MHD solution. However, when the conductivity is small, the solution should approach the wave limit for the magnetic field. The wave phenomena is not captured by the MHD model, but is captured by the single-fluid model we are considering.

To begin, the conductivity was first set to zero everywhere in the domain. This results in pure, uncoupled wave propagation in the fluid and electromagnetics. The result is depicted in Figure 6.1, where the fluid exhibits the Sod shock tube solution (the initial hydrodynamic data is identical to the Sod shock tube problem), and the magnetic field propagates purely as a wave. In Figure 6.1, due to their large propagation speed, the electromagnetic waves have already propagated out of the domain, which is why the magnetic field is zero. In Figure 6.2, we show the electromagnetic wave propagation at early simulation times.

The MHD limit of the solution for high conductivity could be reached with a conductivity of $\sigma = 10^6$. The solution is considered after ten light transit times, which is a nondimensional time of $t = 0.10$. This is the same time for which the classic solution is presented in [145], which allows for a direct comparison. The solution at this time using the source-coupled and strong conservative form is shown in Figure 6.3. Both solutions clearly converge to the MHD solution, but the source-coupled solution possesses several source-induced oscillations, whereas the strong conservative solution achieves remarkable accuracy to the expected solution. It should be noted that, although both solutions were assigned the same criteria for convergence,

Table 6.1: A comparison of the performance of the source-coupled and strong conservative formulations for the Brio and Wu problem.

Formulation	Total Execution Time (s)	Avg. Time Spent per Timestep (s)	Avg. Number of Dual-time iterations
Source-coupled	1,650	0.031	17.4
Strong conservative	331.6	0.0062	3.0

the strong conservative approach achieved this solution in approximately 20% of the time required for the source-coupled solution. A detailed comparison of the performance times on identical machines is presented in Table 6.1. The strong conservative solver could also be applied at a larger CFL number before experiencing stability difficulties; a $CFL = 0.5$ based on the speed of light could be achieved, while a CFL of only 0.2 could be stably used for the source-coupled scheme. The typical variety of magnetohydrodynamic waves are present, depicted in Figure 6.3; note, however, that the correct speeds are resolved using the fully coupled model, even though the Alfvénic speeds were not used as eigenvalues in this simulation (only the fluid eigenvalues and the speed of light were used). This demonstrates fidelity to the expected MHD solution using the full equations.

When the conductivity is increased, mixed wave and diffusion behavior results. For low conductivities, this introduces damping to the electromagnetic waves that would otherwise exhibit pure propagation. This effect can be clearly seen in Figure 6.4, where the tangential magnetic field is plotted for different conductivities in four early timesteps. A comparison of the magnetic field at the same final time with different conductivities is shown in Figure 6.5; here, in the vacuum case, the magnetic field behaves as a wave, and has already propagated out of the computational domain before this final time.

6.2 Jiang and Wu Plasma Shock Riemann Problem

The second test problem is a hypersonic magnetohydrodynamic problem investigated by Jiang and Wu [142]. This problem is similar to the Brio and Wu problem, except that a large pressure ratio is established, such that a compressive shock moving at Mach 15.5 is produced. The Roe strong conservative and source-coupled solvers were selected for this test problem. The problem has an analytical solution calculated by Brio and Wu [145] and Jiang and Wu [142]. The computational domain is once again a one-dimensional region of unit nondimensional length, $x \in [0, 1]$, this time divided into 200 elements. The initial conditions are given as

$$\mathbf{Q}(x, t = 0) = \begin{cases} \mathbf{Q}_{\text{left}}, & x < x_0 \\ \mathbf{Q}_{\text{right}}, & x \geq x_0 \end{cases} \quad (6.3)$$

Uncoupled Brio and Wu Solution

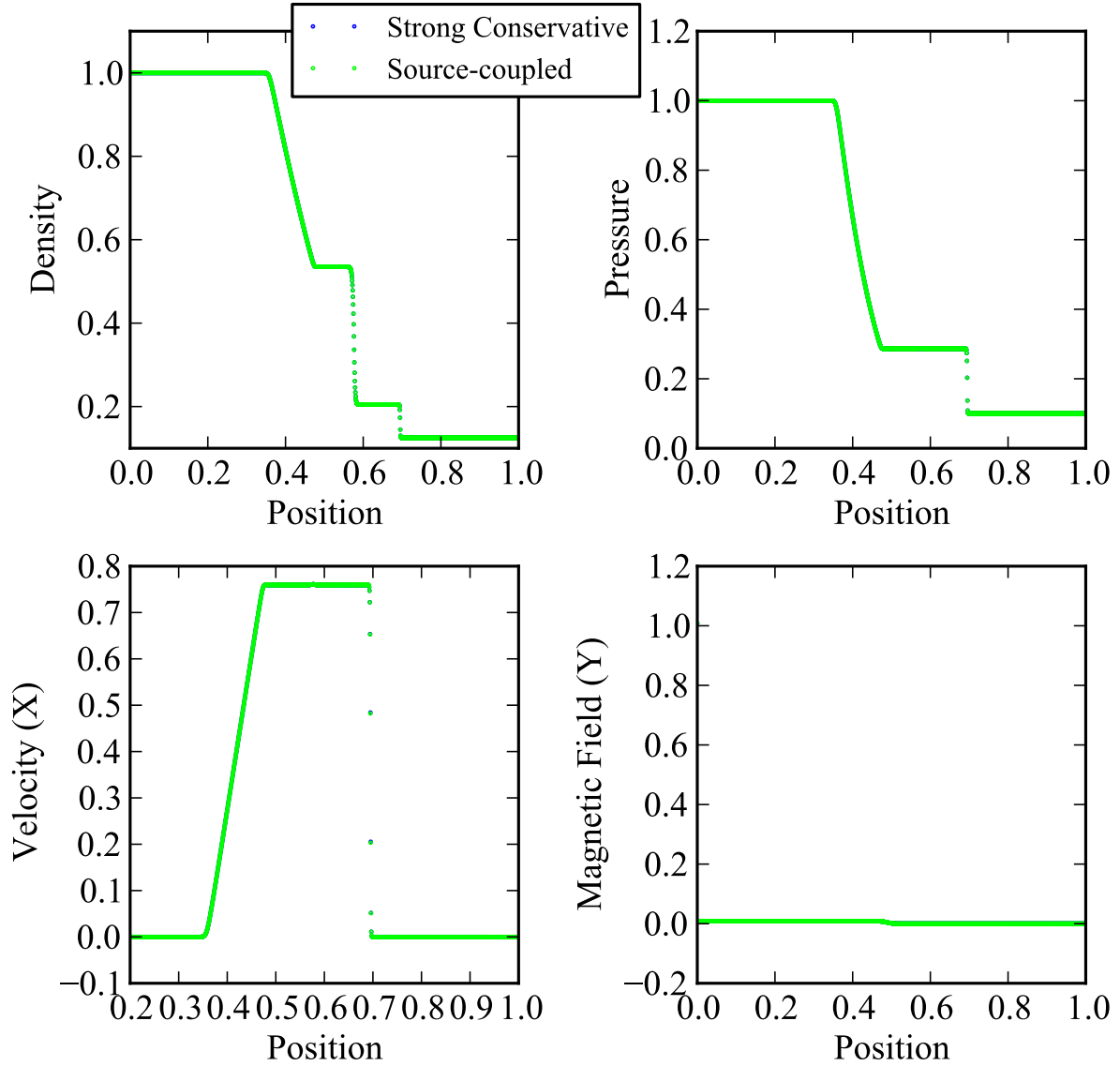


Figure 6.1: Solution to the one-dimensional Brio and Wu problem [145] using the source-coupled and strong conservative flux-coupled solutions at $t = 0.10$. The system was uncoupled here ($\sigma = 0$). The solutions lie on top of each other. No magnetic field is visible because it has already propagated out of the domain (see Figure 6.2 for visualizations of the early wave motion.)

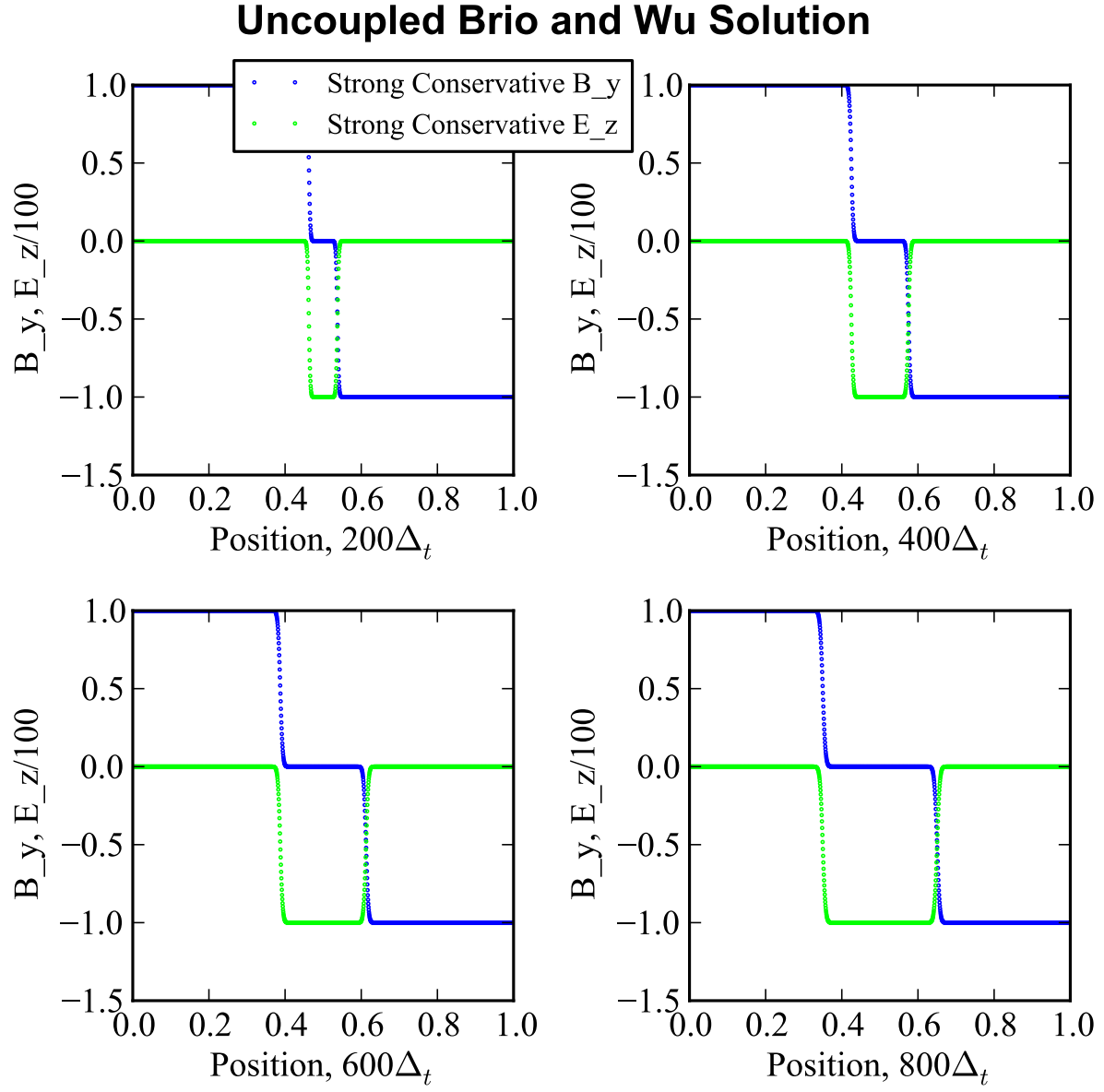


Figure 6.2: Wave propagation of the tangential fields at $200\Delta t$, $400\Delta t$, $600\Delta t$ and $800\Delta t$ for the Brio and Wu problem [145]. The electric field has been scaled down by $1/c_0$ to fit.

Brio and Wu Solution in One Dimension

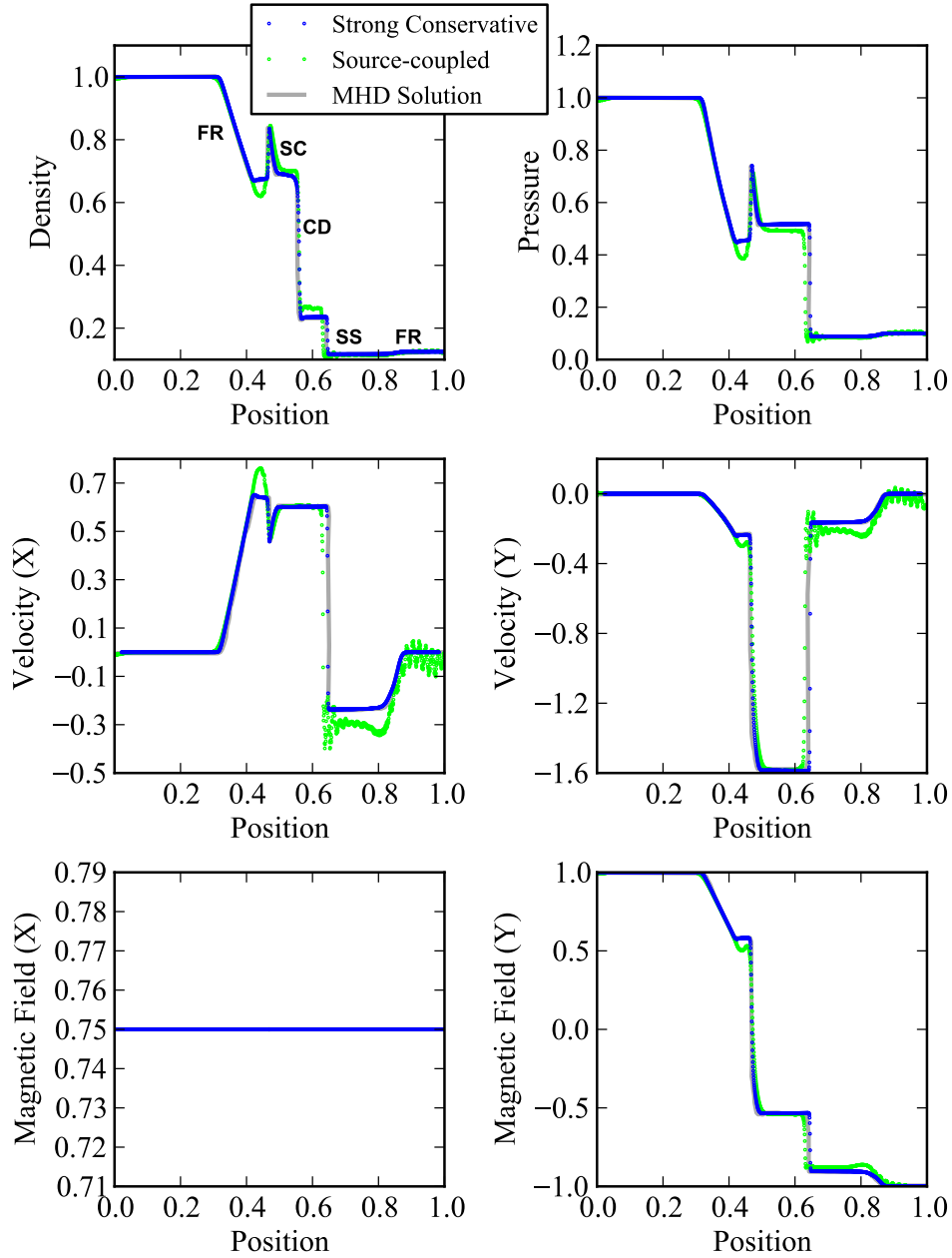


Figure 6.3: Solution to the one-dimensional Brio and Wu problem [145] using the source-coupled and strong conservative flux-coupled solutions. The accepted magnetohydrodynamic solution is also shown. The waves are denoted in the density plot: two fast rarefaction waves (FR), a slow compound wave (SC), a contact discontinuity (CD), and a slow shock wave (SS). The MHD solution (gray solid line) is almost exactly underneath the strong conservative solution (blue points).

Early Wave/Diffusive Behavior for Different Conductivities

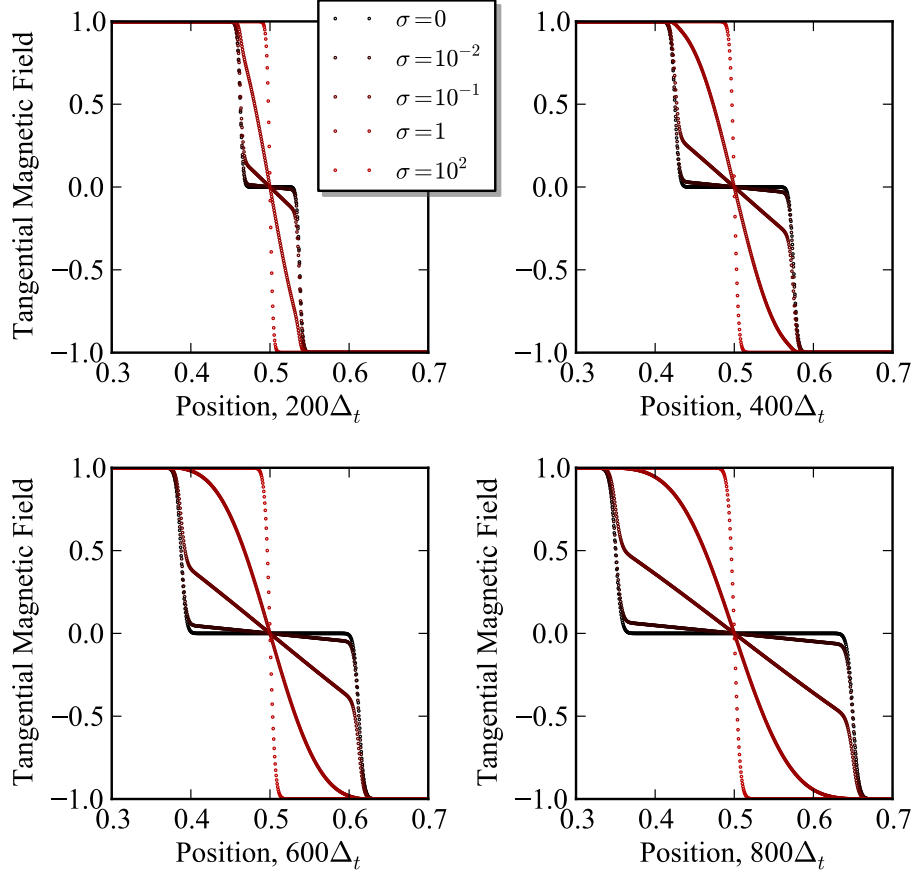


Figure 6.4: Early wave/diffusion behavior for different conductivities in the Brio and Wu problem [145]. Redder curves indicate a higher conductivity.

where

$$\mathbf{Q}_{\text{left}} = \begin{cases} \varrho = 1 \\ \mathbf{u} = \mathbf{0} \\ p = 1000 \\ \mathbf{B} = (0, 1, 0) \\ \mathbf{E} = \mathbf{0} \end{cases}, \mathbf{Q}_{\text{right}} = \begin{cases} \varrho = 0.125 \\ \mathbf{u} = \mathbf{0} \\ p = 0.1 \\ \mathbf{B} = (0, -1, 0) \\ \mathbf{E} = \mathbf{0} \end{cases} \quad (6.4)$$

For this problem, we used both the source-coupled and strong conservative form. The computational domain was taken as $\Omega = [-1, 1]$ with 200 control volumes. The initial discontinuity was set up in the middle of the computational domain, at $x_0 = 0$. The simulation is run until a nondimensional time of $t = 0.012$. The speed of light was again taken as $c = 100$ following the literature [75], although the speed of light was

Tangential Magnetic Field for Different Conductivities

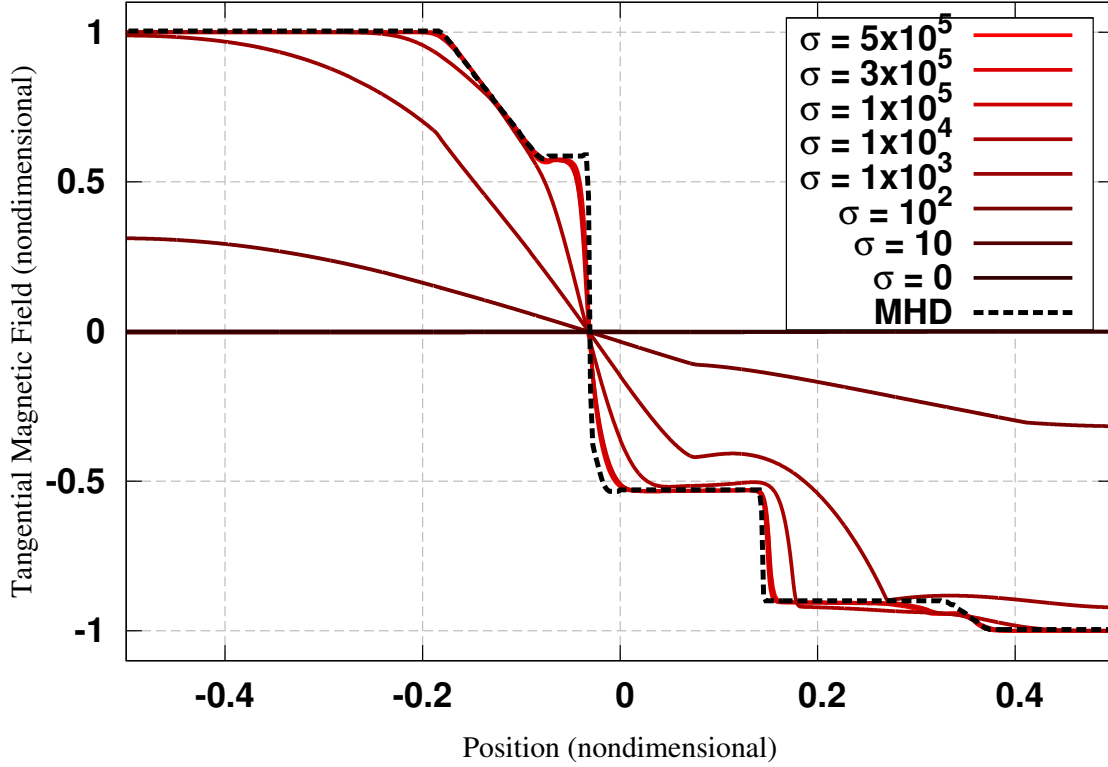


Figure 6.5: The tangential magnetic field at the final simulation time $t = 0.10$ for different conductivities in the Brio and Wu problem [145]. Redder curves indicate a higher conductivity. In the $\sigma = 0$ case, the waves have already propagated out of the domain by this late in the simulation.

also tested for the same range described for the Brio and Wu problem, up to 10^6 , and showed identical results.

The solution to this Riemann problem was calculated very accurate by both the strong conservative and source-coupled forms (see Figure 6.6). There are small oscillations present in the source-coupled form, presumably due to the source terms. The strong conservative form suffered no such oscillations, and falls almost exactly on top of the accepted solution [142]. However, while the accuracy was agreeable between the two approaches, the difference in the amount of time required to resolve these solutions at identical solutions is surprising. A comparison of the time required to calculate each solution is presented in Table 6.2, which shows that the strong conservative form offered an improvement of almost two orders of magnitude over the execution time required for the source-coupled formulation. Note that the maximum stable CFL of the strong conservative form was not used here; both simulations were limited to the same number of cycles at the same CFL, chosen to match a stable CFL for the source-coupled form. The maximum CFL for the

Table 6.2: A comparison of the performance of the source-coupled and strong conservative formulations for the Jiang and Wu problem.

Formulation	Total Execution Time (s)	Avg. Time Spent per Timestep (s)	Avg. Number of Dual-time iterations
Source-coupled	116.7	0.09774	571
Strong conservative	1.42	0.00119	6

strong conservative form based on the speed of light was approximately 0.5. The source-coupled form was tested to be stable for a CFL as large as 0.2.

6.3 Mixed Wave/Diffusion Test: Radio Wave Propagation in Plasma

The coupled Navier-Stokes and Maxwell equations permit a higher-fidelity investigation of low-conductivity plasmas and gases. The interaction of electromagnetic waves and plasmas is of significant interest, as discussed in Chapter 1. In this section, we further explore the capabilities of the new solution approach for resolving electromagnetic wave propagation in the vacuum limit, MHD limit and the mixed case of both wave and diffusion phenomena occurring.

Li, et al. [59] provide a one-dimensional test case based on the telegrapher’s equation that demonstrates the capabilities to capture both the wave and diffusion limits of the electromagnetics. This test was performed using SI units for the dimensions, instead of using nondimensional data. The one-dimensional domain is one meter in length, $x \in [0, 1]$ m, divided into 1,000 elements, with a constant plasma electrical conductivity, σ , chosen to be a specific value; three values are presented here: a vacuum case ($\sigma = 0$ mho/m), 10^{-2} mho/m, and 10^{-1} mho/m. For initial conditions, the electromagnetic fields are set to zero everywhere. At $t = 0$, a step magnetic field is imposed on the left boundary ($x = 0$ m). This condition is enforced for all time. Depending on the conductivity in the one-meter region, different effects are expected to be seen. If the conductivity is zero (vacuum case), then we expect the step magnetic field to propagate as a wave traveling at the physically correct speed of light. If the conductivity is increased slightly, then we expect to see some mixture of wave and diffusion behavior occur in the low-conductivity domain. If we continue to increase the conductivity, we eventually expect to see agreement with the MHD theory.

For the same one-dimensional case, we may calculate an MHD analytical solution by assuming that the field may only diffuse. This solution is [59]

$$B_z = B_0 \left\{ 1 - \operatorname{erf} \left(\frac{x}{2} \sqrt{\frac{\mu_0 \sigma}{t}} \right) \right\} \quad (6.5)$$

where B_0 is the magnitude of the boundary step (taken as unity here), x is the position, and t is the current

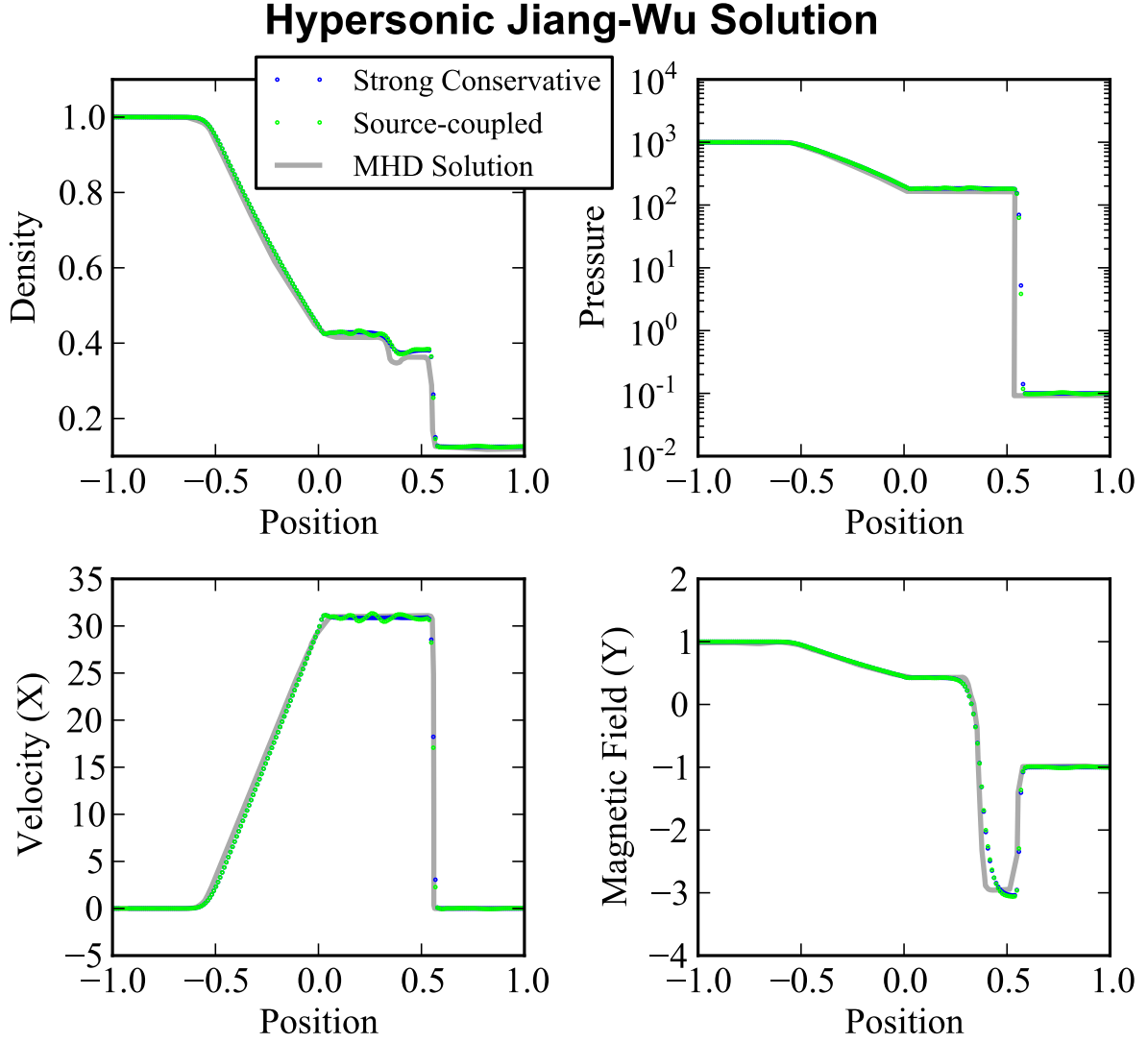


Figure 6.6: Solutions to the Jiang and Wu hypersonic MHD problem [142, 145], using the source-coupled formulation and the strong conservative formulation, and a comparison to the analytical MHD solution. Both source-coupled and strong conservative solutions are on top of the analytical solution.

time. This solution provides the instantaneous profile of the magnetic field for the magnetic diffusion approximation.

In Figure 6.7, we present solutions as calculated using the new strong conservative formulation. In Figure 6.7a, the conductivity of the one-meter domain is zero, and we see complete propagation of the step magnetic field into the domain, depicted by plotting the magnetic field in the domain for five times. By 3.33ns, the wave impinges on the far right of the one-meter domain, which is expected according to the speed of light. In Figure 6.7b, the simulation with $\sigma = 10^{-2}\text{mho/m}$ is presented for the same times. For a comparison, the MHD solution according to equation 6.5 is presented as dashed lines for the same times. It is evident that the two calculations do not agree for low electrical conductivity. This is because of the inclusion of the displacement current in the strong conservative calculation. The displacement current introduces a wave contribution to the solution that propagates as a front; however, unlike the vacuum case, there is now damping due to the diffusion contribution. Clearly, the MHD solution is not valid for this conductivity; it does not correctly capture the wave contribution of the magnetic field. Finally, in Figure 6.7c, we present the case of $\sigma = 10^{-1}\text{mho/m}$; the plots are shown for the same times as the other graphs. We still see some small wave contribution present in the first depicted time, $t = 0.66\text{ns}$, but the diffusion has severely damped this wave. The maximum difference in this first time is 0.04T between the numerical solution including the wave behavior and the MHD analytical solution in equation 6.5. For all later times, the calculated solution agrees with the MHD analytical solution to within 1.5% error. For larger conductivities, we expect the magnetic field to more closely match the MHD behavior, with virtually no wave contributions present. For the lower-conductivity tests, the MHD solution fails to correctly resolve the true nature of the magnetic field, but the numerical solution approach has demonstrated agreement to the correct physical nature of both the wave and diffusion limits.

Further qualitative assessments were also pursued to verify that both low-conductivity and high-conductivity behavior could be resolved in the same computational domain. While these tests have no direct comparison to justify their accuracy, we clearly expect the physical limits to be correctly observed as the electrical conductivity ranges from zero to very large. For these tests, a one-dimensional domain of meter length, $x \in [0, 1]\text{m}$, was divided into a vacuum region for $x < 0.5\text{m}$, and a plasma slab of finite, nonzero electrical conductivity for $x > 0.5\text{m}$. A 1GHz sinusoidal pulse in E_z of amplitude 10^5V/m was launched into the vacuum region from the left boundary ($x = 0\text{m}$). The results of the radio wave impinging on the plasma depended on the value of the conductivity assigned to the plasma region, $x > 0.5\text{m}$. In Figure 6.8, we present waterfall plots of three different tested plasma conductivities: in column (a), the plasma region was actually also set to vacuum ($\sigma = 0\text{mho/m}$), so we expect pure propagation without any interaction. In column (b), the conductivity was $\sigma = 10^{-1}\text{mho/m}$, and we see mixed wave and diffusion behavior of the magnetic field in the plasma region; a reflected wave propagates back towards the left boundary. In column (c), the conductivity was $\sigma = 1\text{mho/m}$, and much stronger diffusion is encountered in the plasma region. Higher conductivities were also tested, and showed the development of a skin effect on the plasma slab region.

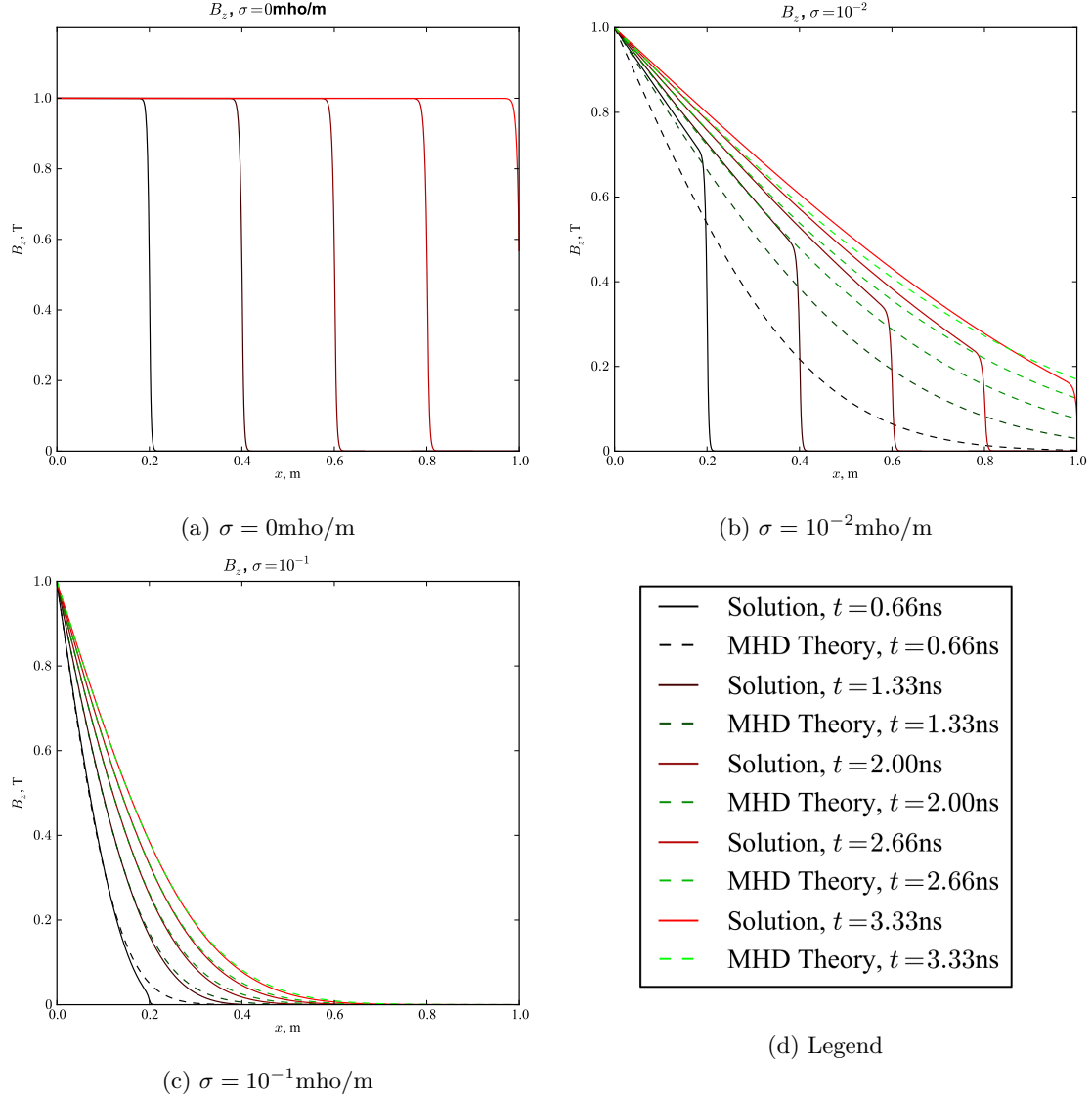


Figure 6.7: One-dimensional simulation where $B_z = 1.0$ is imposed on the left boundary ($x = 0\text{m}$) for all time. (a) The vacuum ($\sigma = 0\text{mho/m}$) test. The wave impinges on the right of the domain ($x = 1\text{m}$) at $t = 3.33\text{ns}$, indicating pure wave propagation. (b) The $\sigma = 10^{-2}\text{mho/m}$ test. Mixed wave and diffusion behavior of the magnetic field results. For comparison, the one-dimensional analytical solution for the pure diffusion (MHD) magnetic field is shown for identical times. Here, the MHD solution is suspect, because the displacement current is significant. (c) The $\sigma = 10^{-1}\text{mho/m}$ test. The magnetic field exhibits more diffusion than wave behavior. At $t = 0.66\text{ns}$, some wave contribution is present, but is severely damped by the diffusion. The remaining four times agree very closely with the expected MHD solution.

While this is a qualitative assessment of the interaction of an electromagnetic wave and a finite-conductivity plasma region, it demonstrates that both low- and high-conductivity regions can be simulated within the same computational domain.

Radio Wave Propagation Into a Plasma Slab

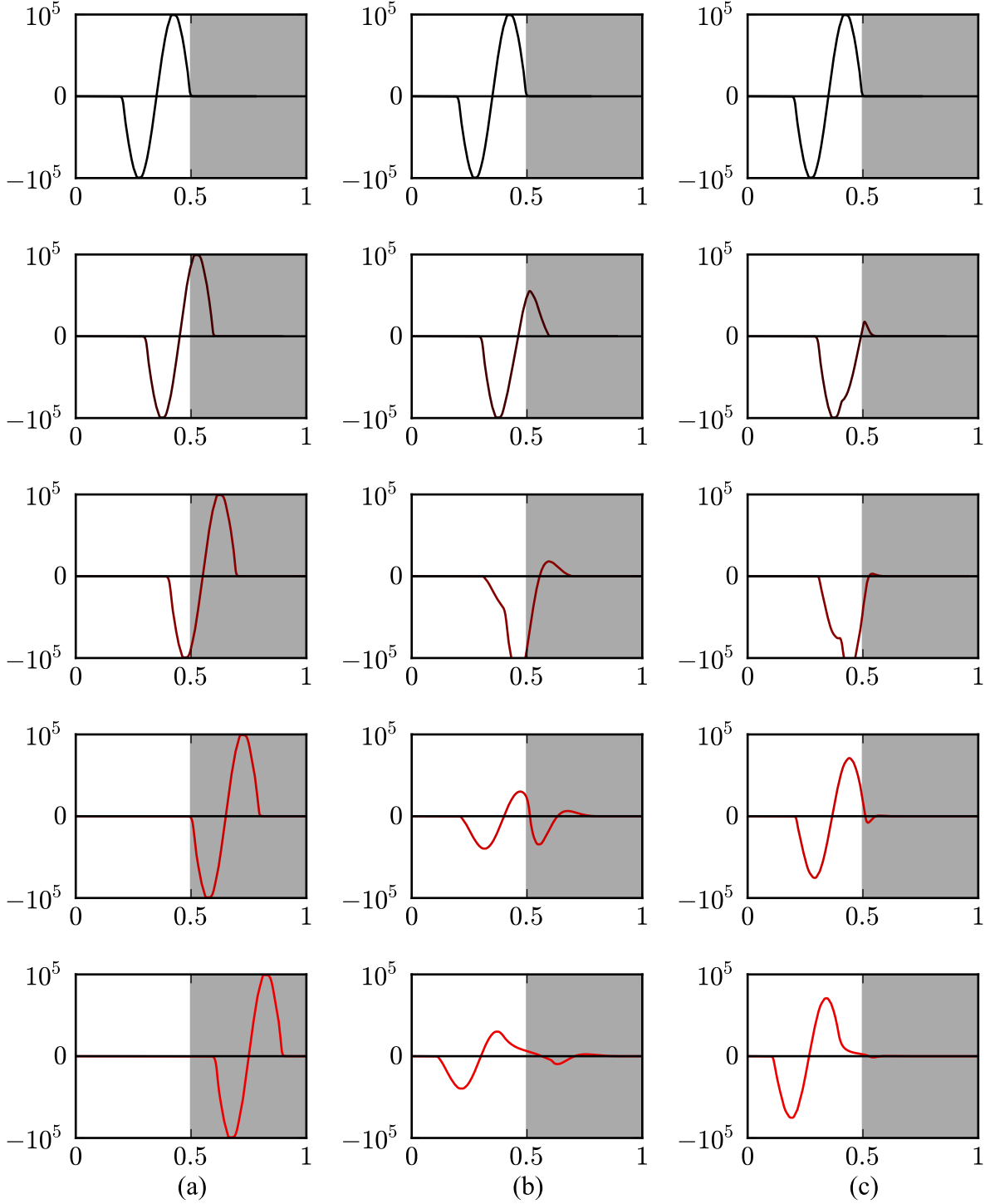


Figure 6.8: Radio wave propagation through vacuum region ($x < 0.5\text{m}$) impinging on a plasma slab of finite conductivity ($x > 0.5\text{m}$, depicted in gray). The conductivity is (a) vacuum ($\sigma = 0\text{mho/m}$), (b) $\sigma = 10^{-1}\text{mho/m}$, (c) $\sigma = 1\text{mho/m}$. Times (starting with top and ending with bottom plot) are 1.67ns, 2.00ns, 2.33ns, 2.67ns, and 3.00ns, respectively.

6.4 Kelvin-Helmholtz Instability with Applied Magnetic Field

In addition to plasma turbulence, it is desirable to explore plasma instability with this strong conservative approach, since it permits the inclusion of a greater deal of physics that could play an important role in the long-term behavior of a plasma. An example of an application where this is important is the Hall effect thruster, which is known to degrade in performance due to the presence of plasma oscillations. These oscillations generally cannot be captured via the existing MHD framework.

While a detailed investigation of plasma stability for Hall effect thrusters is postponed to future work, it suffices to consider a simple example of instabilities arising in a plasma. In this case, we examine the Kelvin-Helmholtz instability for a compressible, inviscid medium, with and without a magnetic field present. Without the magnetic field, the simulation is purely hydrodynamic, which gives rise to a chaotic flow. The presence of the magnetic field tends to suppress the short-wavelength instabilities, and a much less chaotic structure emerges.

For this simulation, we only use the AUSM flux scheme on a 256×256 mesh grid. The domain is $[0, 1] \times [0, 1]$, with periodic boundaries. The middle region (between $y > 0.25$ and $y < 0.75$) is comprised of a high-density ($\varrho = 2$) fluid, while the remainder of the domain is a low-density ($\varrho = 1$) fluid. The pressure everywhere was set to $p = 2.5$. The higher-density flow is set to move to the right with speed $u = 1$, and the low-density flow is set to move at a speed of $u = -1$, establishing a relative velocity between the two flows. The flow direction is a small perturbation in the x and y velocities was initialized on the surface interfaces between the two fluids, with a magnitude scale of 0.01. The same perturbation was used in both the hydrodynamic and magnetohydrodynamic cases.

In Figure 6.9, the density calculations in the domain are presented. The left column presents the hydrodynamic simulation; the right column presents results at the same times immersed in a weak magnetic field (initially a uniform field of $B_x = 0.35$), which stabilizes the flow. It is clear that two different structures emerge in the long-term behavior of these two simulations, due to the presence of the magnetic field.

6.5 Orszag-Tang Plasma Turbulence Problem

Plasma turbulence plays an important role in several engineering cases. Oscillations and micro-instabilities in many applications can quickly lead to turbulence. In plasmas, turbulence can arise in inviscid situations, due to compressions of the magnetic field influencing the flow.

The Orszag-Tang magnetohydrodynamic problem was initially conceived of as a direct-simulation test problem for incompressible MHD flows [200]; it was later extended to the compressible domain to validate compressible solvers [142]. It remains a standard turbulence problem for plasma solvers today [176]. The problem involves a periodic two-dimensional square domain, $[0, 2\pi] \times [0, 2\pi]$, discretized typically on a 192×192 quadrilateral mesh. In this investigation, different mesh sizes of 64×64 , 128×128 , 192×192 and

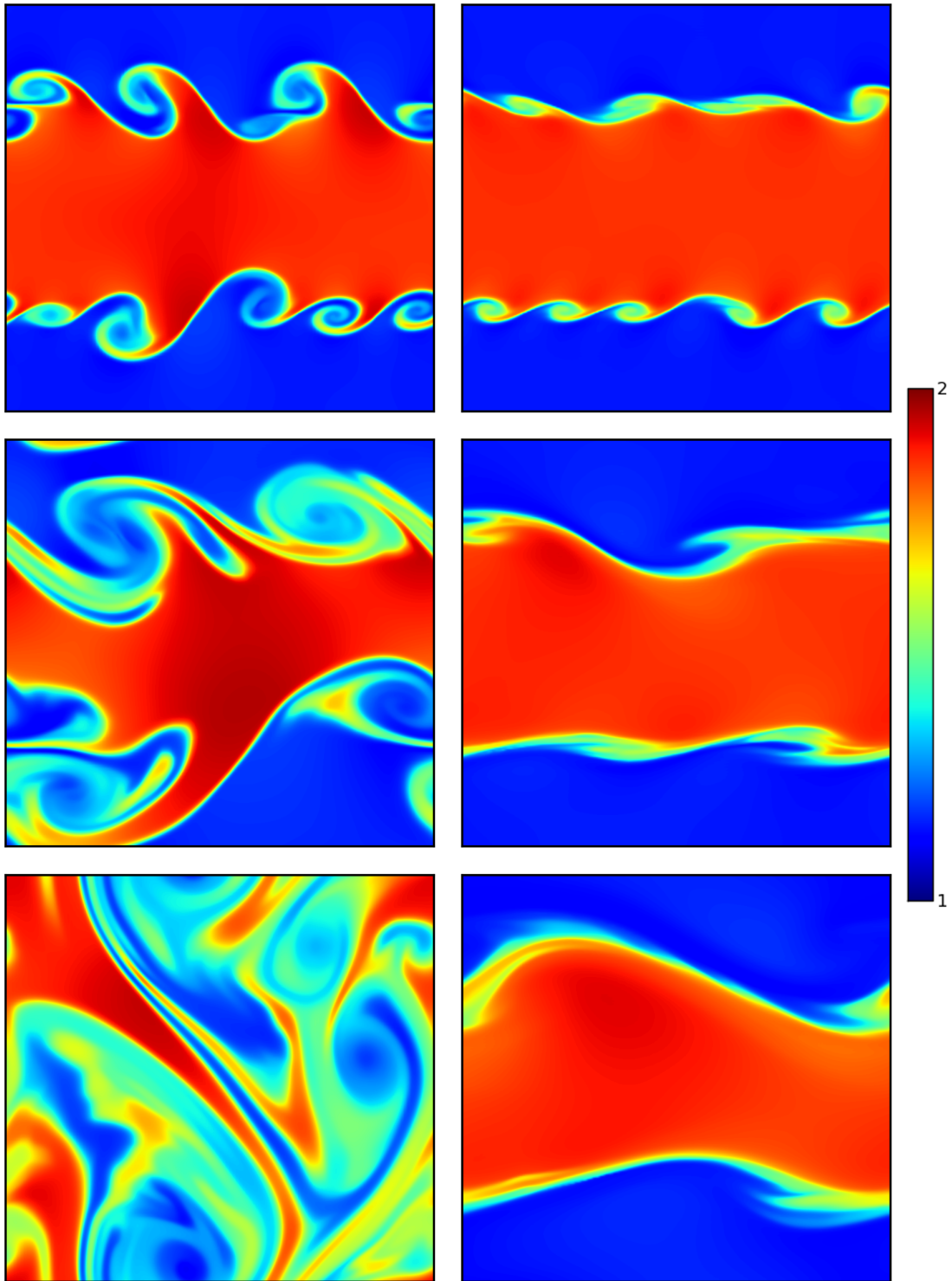


Figure 6.9: A visual depiction of the evolution of the Kelvin-Helmholtz instability without (left column) and with (right column) a weak applied magnetic field (initially uniform $B_x = 0.3$). Times (from top to bottom) are approximately $t = 1.5, 3.0, 5.8$. The presence of the magnetic field suppresses the small-wavelength instabilities and tends to stabilize the flow.

256×256 were simulated using both the Roe and AUSM strong conservative schemes. The values are once again treated in a nondimensional fashion to facilitate comparison to existing literature; the initial conditions are set up with a vortex condition as specified in [142, 176],

$$\mathbf{Q}(x, y, t = 0) = \begin{cases} \varrho = \gamma^2 \\ p = \gamma \\ \mathbf{u} = (-\sin(y), \sin(x), 0) \\ \mathbf{B} = (-\sin(y), \sin(2x), 0) \\ \mathbf{E} = \mathbf{0} \end{cases} \quad (6.6)$$

The specific heat ratio is taken as a constant $\gamma = 5/3$. The final nondimensional simulation time is typically taken as $t = 3.0$. The simulation was performed using a $CFL = 0.7$, $CFL = 0.7$, $CFL = 0.5$, and $CFL = 0.3$, for the 64×64 , 128×128 , 192×192 and 256×256 grids, respectively.

A typical result that agrees very well with the accepted solution is shown in Figure 6.10, which used the 256×256 grid; spatial contour plots of density and pressure are shown, and vector plots of the velocity and magnetic field are depicted. For clarity, only every ninth vector was plotted. The initial vortex interacts with the magnetic field and causes a series of shocks and discontinuities to result [142], which demonstrates the formation of a turbulent plasma flow. A visual comparison of the density and pressure MHD calculations from [142] and the new density and pressure calculations using the Roe strong conservative solver on the 256×256 grid is presented in Figure 6.11. An example of the time evolution of the turbulent flow for longer simulation times is presented in Figure 6.12.

Grid resolution tests demonstrate the convergence of the solution as the grid size is improved. The 192×192 and 256×256 grids tend to agree very well with each other for both the AUSM and Roe methods; the Roe method provided a more consistent calculation across the four different grid sizes tested (see Figure 6.13) while the AUSM method had much less consistent results; particularly, the solution suffered terrible accuracy on the 64×64 grid size (see Figure 6.14).

6.6 Magnetohydrodynamic Rotor Problem

The MHD rotor problem suggested by Brackbill [201] and Balsara and Spicer [202] tests the solver's capabilities for capturing strong torsional Alfvén waves propagating within the domain. A rapidly spinning dense fluid is immersed in a light surrounding fluid and an ambient, initially uniform magnetic field, and both fluids are assigned the same electrical conductivity. The presence of the magnetic field permits a medium for angular momentum to be delivered to the ambient fluid from the rotating dense fluid through Alfvénic propagation [202]. The strong conservative Roe method was applied to this problem. The computational domain is $[-1/2, 1/2] \times [-1/2, 1/2]$, and was discretized on grid meshes of size 64×64 , 128×128 , 192×192 , and 256×256 . Boundary conditions were all transmissive. The nondimensional initial conditions are taken

Orszag-Tang Solution Using the Strong Conservative Roe Scheme

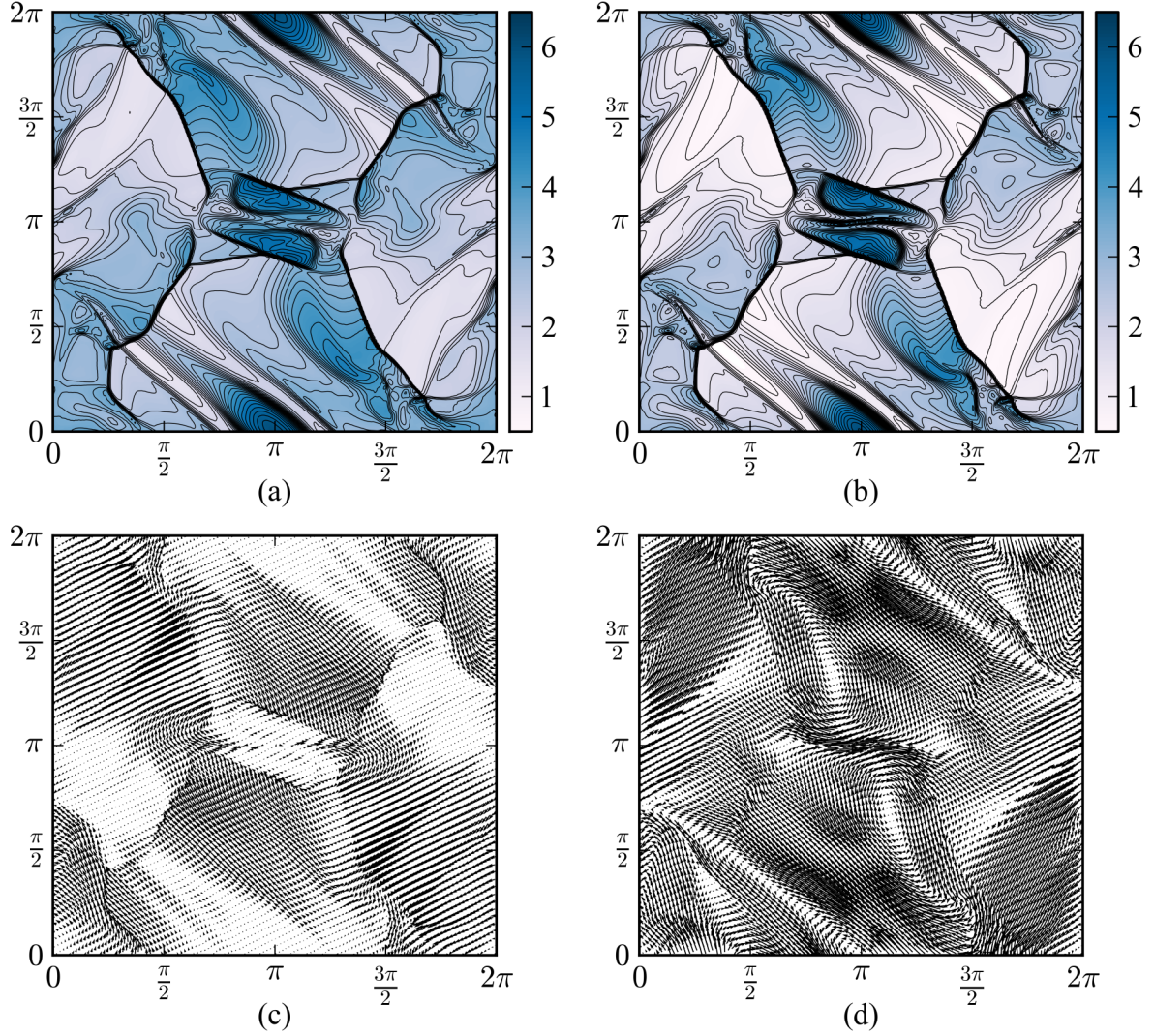


Figure 6.10: Two-dimensional spatial contour plots of (a) density, and (b) pressure, and two-dimensional vector plots of (c) velocity field, and (d) magnetic field for the Orszag-Tang problem [142] calculated at the final time $t = 3.0$. The vector plots present only every ninth vector, to make the plot more visible. This solution was calculated on the 256×256 grid, and agrees well with the accepted magnetohydrodynamic solution [142].

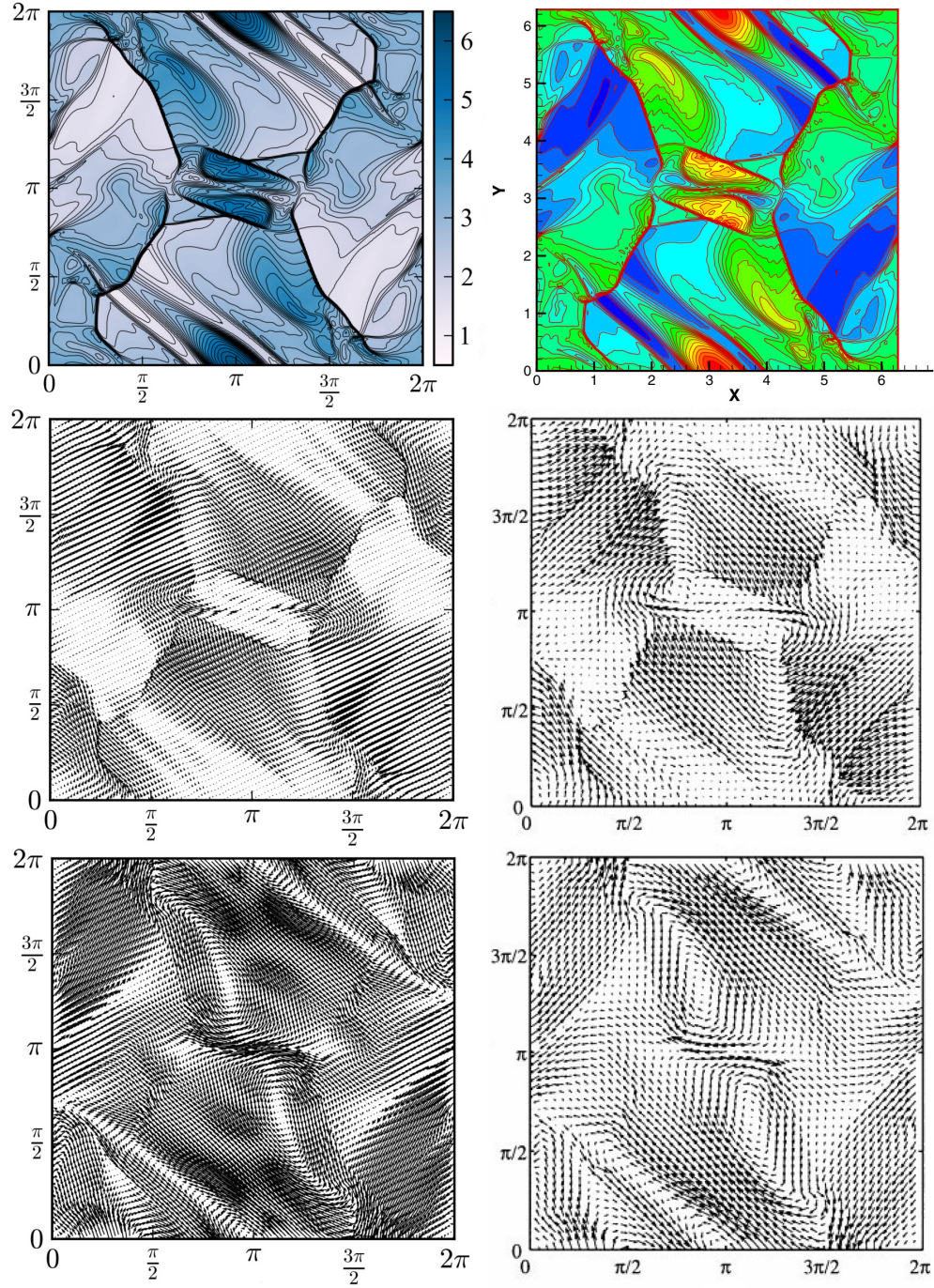


Figure 6.11: A visual comparison of the strong conservative Roe solution on 256×256 grid (left column) to the MHD solution on comparable grid size (right column). The top comparison shows density contour plots; the middle comparison shows vector plots of the velocity field; the bottom comparison shows vector plots of the magnetic field. Contour levels and vector densities were not matched to the MHD solution, although the minimum and maximum contour levels were the same as those used in MHD solutions. The MHD density plot is reprinted from [176] with permission from Elsevier; the MHD vector plots are reprinted from [142] with permission from Elsevier.

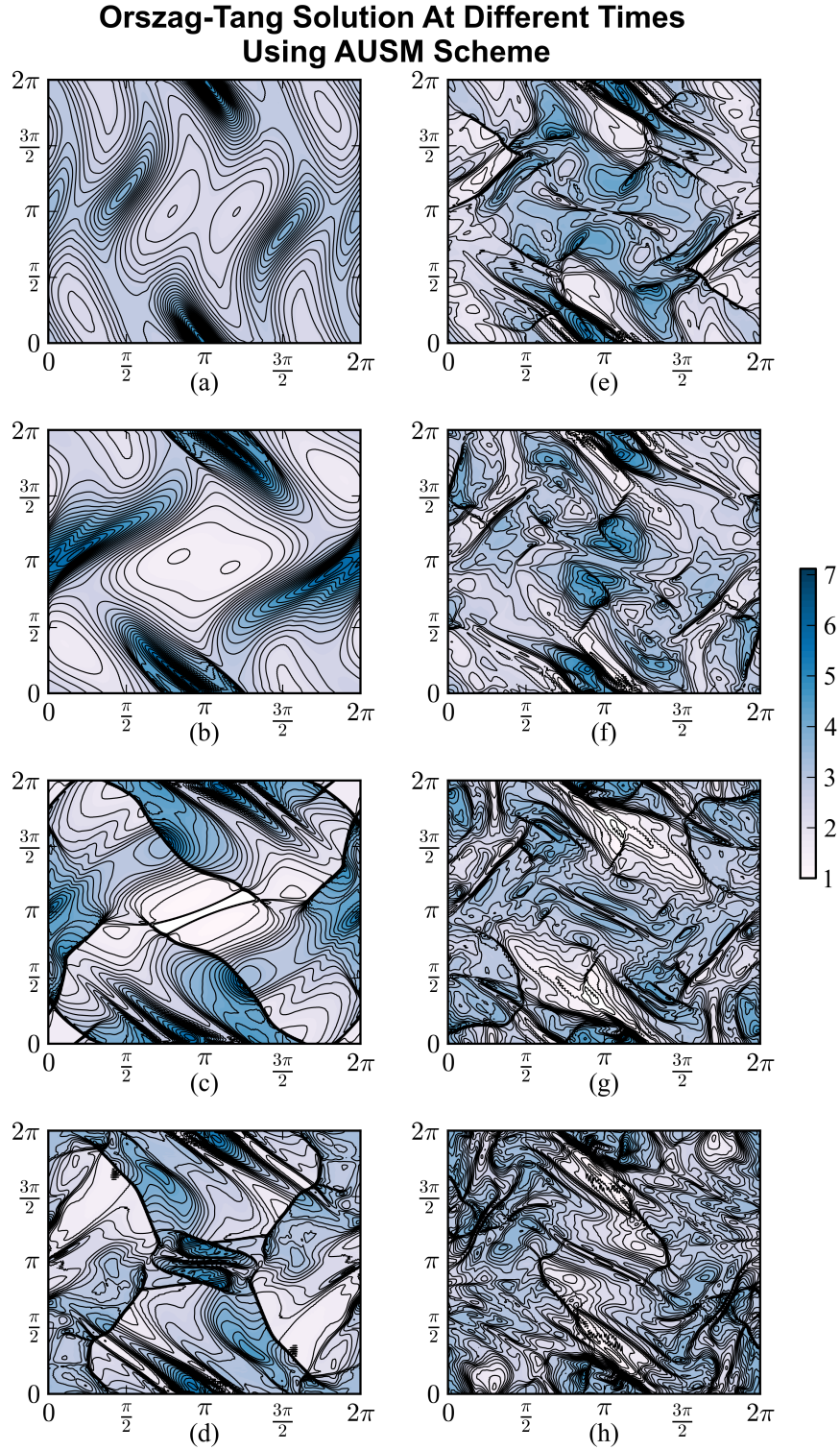


Figure 6.12: This simulation was run using the AUSM strong conservative scheme on the 256×256 grid, but was run for much longer to see the long-term development of turbulence. Times are $t =$ (a) 0.5, (b) 1.0, (c) 2.0, (d) 3.0, (e) 4.0, (f) 5.0, (g) 6.0, (h) 7.0.

Orszag-Tang Solution Using the Strong Conservative Roe Scheme

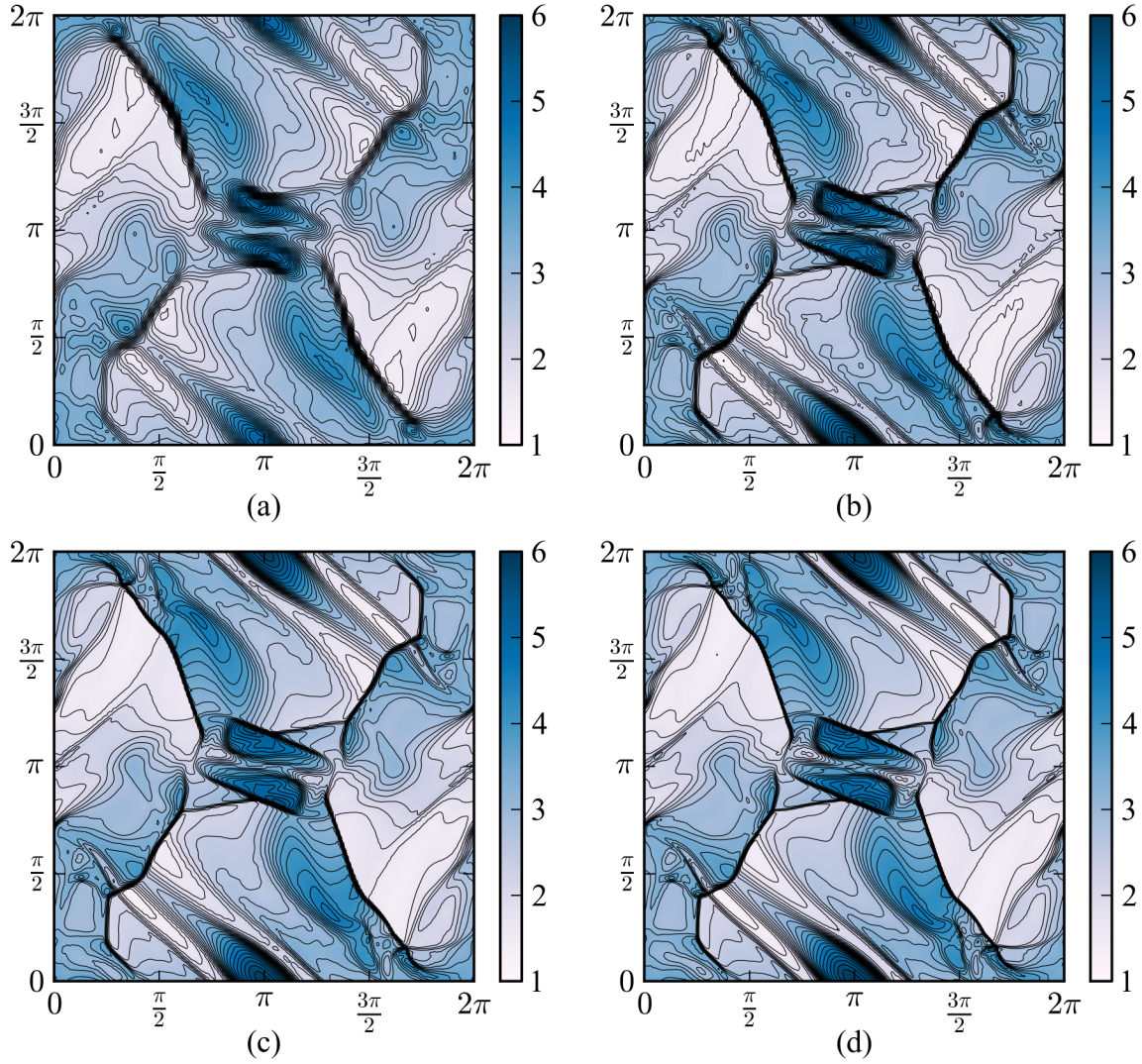


Figure 6.13: Two-dimensional contour plot of the density for the Orszag-Tang vortex solution [142] calculated at time $t = 3.0$ for different grid meshes. (a) 64×64 . (b) 128×128 . (c) 192×192 . (d) 256×256 .

Orszag-Tang Solution Using the Strong Conservative AUSM Scheme

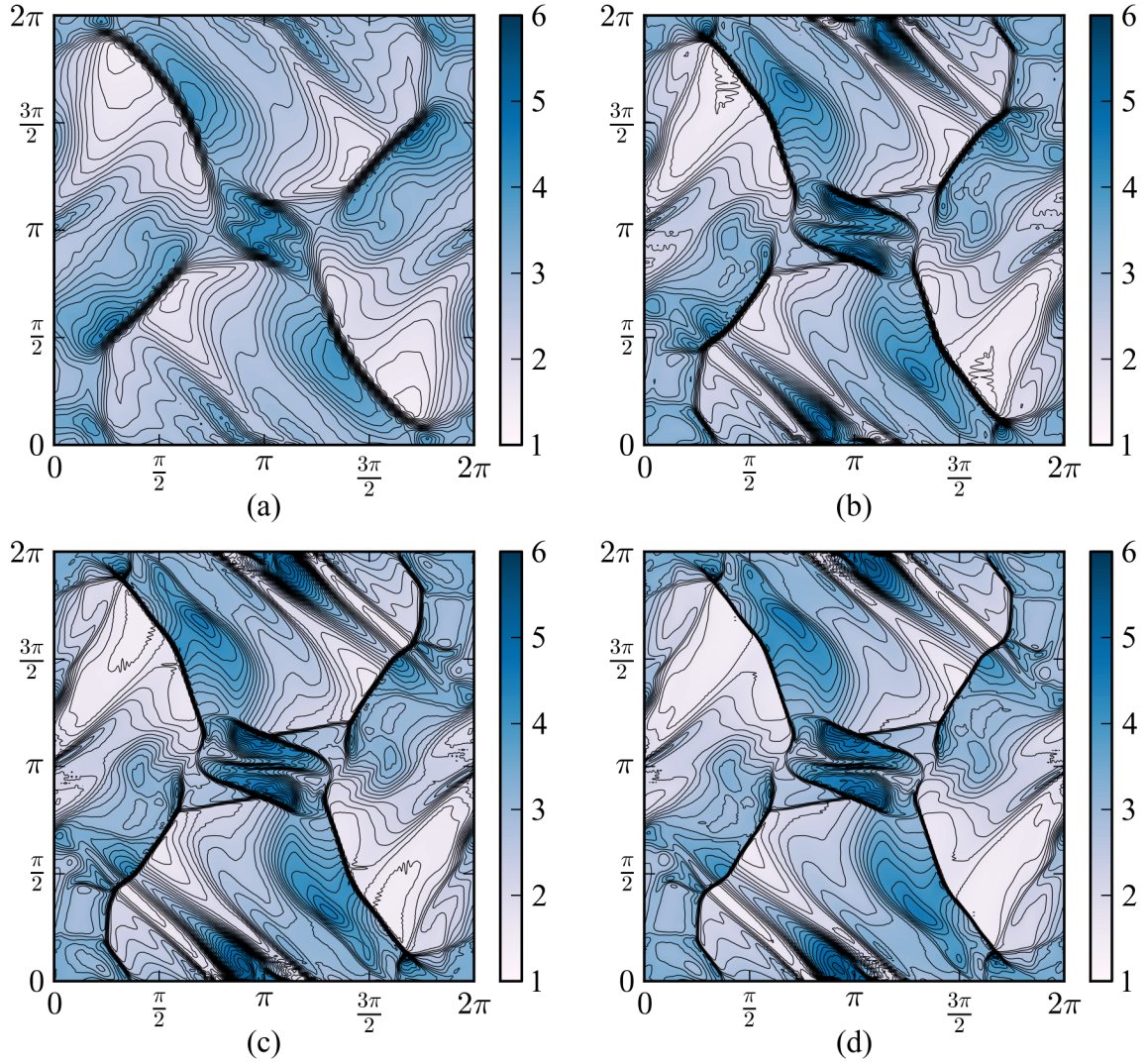


Figure 6.14: Two-dimensional contour plot of the density for the Orszag-Tang vortex solution [142] calculated at time $t = 3.0$ for different grid meshes. (a) 64×64 . (b) 128×128 . (c) 192×192 . (d) 256×256 .

as

$$\mathbf{Q}(x, y, t = 0) = \begin{cases} \varrho = 1 + 9f(r) \\ p = 1 \\ u = \begin{cases} -2f(r)y/0.1, & r < 0.1 \\ -2f(r)y/r, & r \geq 0.1 \end{cases} \\ v = \begin{cases} 2f(r)x/0.1, & r < 0.1 \\ 2f(r)x/r, & r \geq 0.1 \end{cases} \\ w = 0 \\ \mathbf{B} = (5/\sqrt{4\pi}, 0, 0) \\ \mathbf{E} = \mathbf{0} \end{cases} \quad (6.7)$$

where

$$f(r) = \begin{cases} 1, & r < 0.1 \\ (200/3)(0.115 - r), & 0.1 \leq r \leq 0.115 \\ 0, & r > 0.115 \end{cases} \quad (6.8)$$

Here $r^2 = x^2 + y^2$; the dense fluid is contained within $r < 0.1$, and the ambient fluid is in the region $r > 0.115$. The intermediate region between the two is given a tapered linear interpolation to smooth the data [176]. The specific heat ratio was taken as $\gamma = 5/3$. The final nondimensional simulation time was taken as $t = 0.15$.

Contour spatial plots of the density and pressure and vector plots of the velocity and magnetic fields are presented in Figure 6.15. Only every eighteenth vector is shown, to improve clarity. The presence of angular momentum transmitted through the Alfvénic torsional waves and imparted to the ambient fluid as angular momentum is visible, and the solution matches well to the accepted magnetohydrodynamic solutions [201, 202]; a visual comparison of the density calculations using the MHD theory in [176] and the new strong conservative approach are shown in Figure 6.16. A comparison of the pressures for the different grid sizes (Figure 6.17) shows that the solution has not fully converged on the lower-resolution meshes. In the higher-resolution cases (192×192 and 256×256), the solution is almost identical, and agrees very well to the accepted solutions.

The rotor problem was repeated using different conductivities, to confirm that the solution approach resolves both the low- and high-conductivity limits of the magnetic field. With an uncoupled case of no conductivity ($\sigma = 0$), no Alfvén waves resulted, and the magnetic field remained its initial uniform value for the entirety of the simulation. The dense fluid rotating within the ambient fluid caused a Kelvin-Helmholtz instability to develop, as expected. It is well known that the presence of a magnetic field tends to suppress such instabilities, which is why no such instability develops in the conductive case of the rotor problem. Raising the conductivity allowed the magnetic field to respond to the fluid, and tended to stabilize it.

Rotor Solution Using the Strong Conservative Roe Scheme

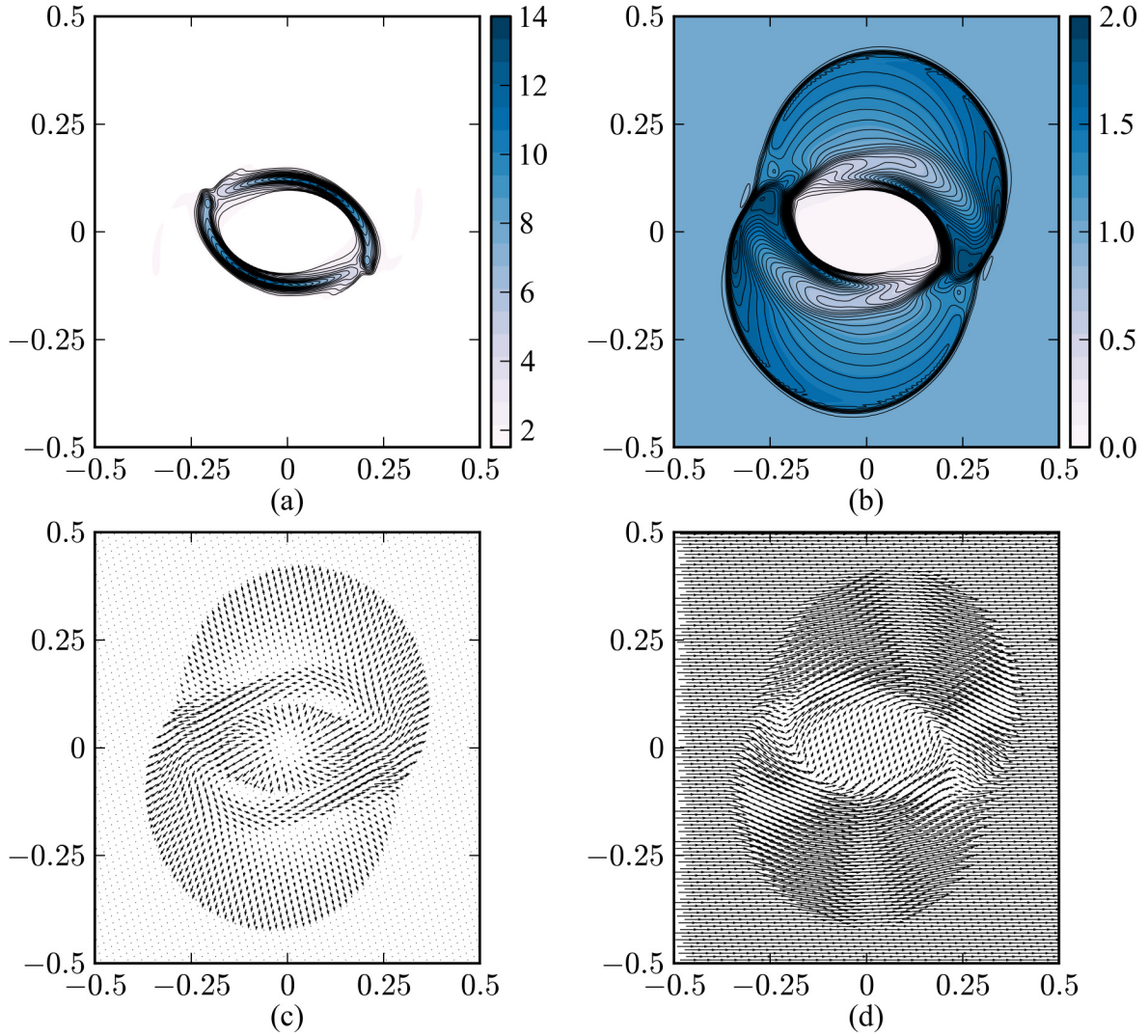


Figure 6.15: Spatial contour plots of the (a) density and (b) pressure, and vector plots of the (c) velocity field and (d) magnetic field at the final solution time of $t = 0.15$ using the 256×256 grid. The solution matches very well to the accepted MHD solutions [176, 202]. Torsional Alfvén waves transmit the angular momentum of the dense rotor to the ambient fluid. Only every eighteenth vector is shown to improve visibility.

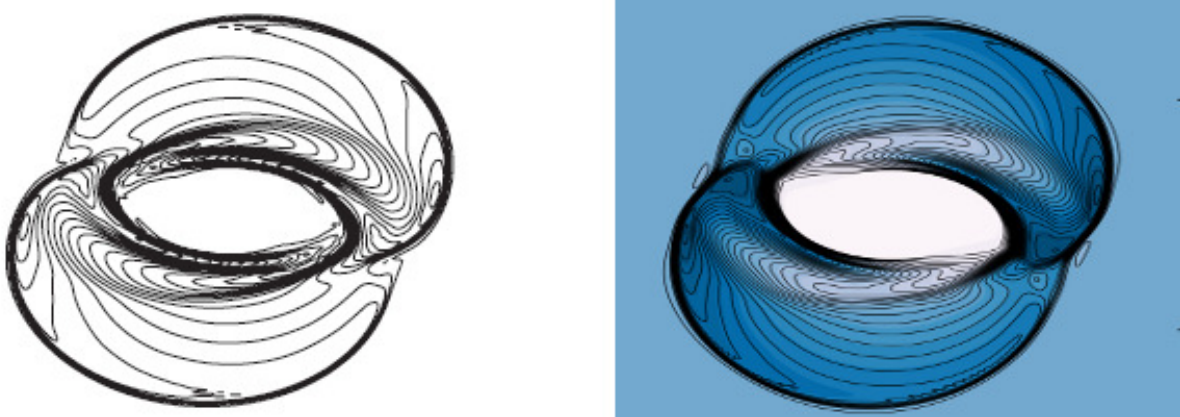


Figure 6.16: A visual comparison of (left) the pressure calculated using the MHD theory [176] and (right) the pressure calculated by the new fully coupled strong conservative Roe solver. Left image is reprinted from [176], with permission from Elsevier.

6.7 Comparisons Between Source-coupled and Strong Conservative Schemes

To compare the source-coupled and strong conservative formulation, the Riemann problems discussed in Sections 6.1 and 6.2 were run side by side using each formulation. Both formulations were run using the same Courant number, which was taken as the lower of the maximum stable Courant numbers for the strong conservative and source-coupled forms. Simulation attempts for two-dimensional problems using the source-coupled method were also attempted, but could not be converged in a reasonable amount of time for this investigation.

A comparison of the strong conservative and source-coupled formulations reveals a significant improvement in both accuracy and performance using the new strong conservative approach for the test cases explored. For the Riemann problems explored, convergence of the source-coupled form required far more (sometimes an order of magnitude more) iterations in the dual-time formulation than the strong conservative form. The average time per cycle increases with the number of dual-time iterations required to converge the values. Particularly in the Brio and Wu problem, and less so but still present in the Jiang and Wu problem, it is clear that the strong conservative form achieved a more accurate solution. In both problems, the source-coupled form reveals strong oscillations in the converged solution; it is known that these oscillations can be induced by the presence of unstable source terms.

Furthermore, the maximum stable Courant limit for the strong conservative form is much higher than the source-coupled form, since the strong conservative form enjoys better stability. This permits a much faster simulation without compromising accuracy in the converged solution. The Riemann problems discussed in

Rotor Solution Using the Strong Conservative Roe Scheme

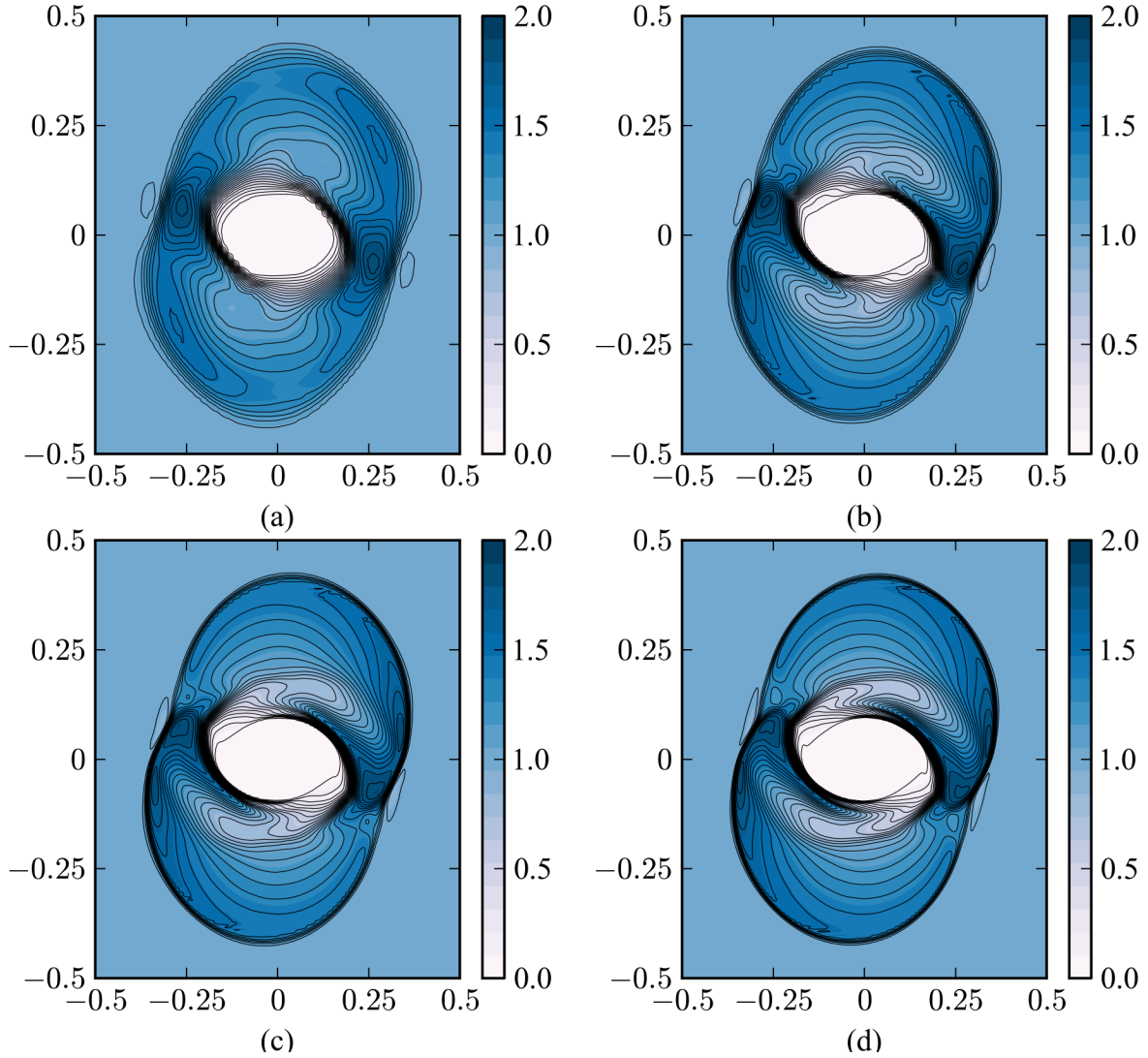


Figure 6.17: A comparison of the pressure calculated for the MHD rotor solution using grid size (a) 64×64 , (b) 128×128 , (c) 192×192 , and (d) 256×256 . The lower-resolution solutions show several regions where the solution depends on the grid size. The higher-resolution meshes show consistent agreement of the solution.

Sections 6.1 and 6.2 were executed using the same Courant number for both formulations, but the strong conservative form was also run at higher Courant numbers, and identical results were obtained. Coupled with less time spent per cycle, this indicates that the strong conservative form provides a much more efficient approach for resolving the same equations as the source-coupled formulation.

6.8 Comparisons Between Roe and AUSM Flux Schemes

The two flux scheme implementations for the strong conservative form facilitates a validation of the approaches against each other; we expect that both implementations should resolve the same results, since the system of equations and initial and boundary conditions are the same. We will primarily compare the results for the the Orszag-Tang magnetohydrodynamic vortex problem in Section 6.5.

Image differences were performed between contour plots printed at the same size, levels, data, and at the same time. The image differences are presented in Figure 6.18 for the Orszag-Tang vortex problem. All grid sizes tested (64×64 , 128×128 , 192×192 , and 256×256) are presented. From Figure 6.18, we can tell that the Roe and AUSM schemes exhibited more difference on the smallest grid. The AUSM solution looks noticeably different from the accepted solution at the smallest grid, while the smallest grid Roe solution looks much more similar. Thus, more disagreement is seen between the Roe and AUSM methods for the coarse mesh. The gray ‘X’ in the 64×64 grid represents a noticeable departure in calculated wave speeds between the Roe and AUSM schemes. However, as the grid resolution is increased, we see markedly better comparison between the two solutions. There is still a small difference in the positions of the shocks; this is presumably due to the higher diffusion added by the AUSM scheme, which tends to be slightly less accurate than the Roe method [12]. However, the AUSM scheme was noted to perform much faster than the Roe method as well. The AUSM scheme achieved a maximum stable CFL for the Orszag-Tang problem of $CFL = 0.5$, while the Roe method could only be executed using $CFL = 0.3$ under identical conditions. Not only is the CFL different, but a single Roe cycle literally takes more execution time than an AUSM cycle, due to the need to calculate the eigenvalues, eigenvectors and decomposition coefficients; the elegance of the AUSM scheme requires less time to compute a similar solution. Therefore, the AUSM method provides a faster method than Roe with at least comparable accuracy to the Roe method at higher grid resolutions, while the Roe method suffices well for lower grid resolutions, but takes longer, especially at higher grid resolutions.

6.9 A Strong Conservative Form for the Two-fluid Plasma Model

Initially, the strong conservative form was explored to find benefit for the two-fluid plasma model. It was hoped at the outset of this exploration that we could take advantage of the strong conservative reformulation for the two-fluid plasma equations, since previous investigations have shown that severe stability problems can be encountered for the numerical solution of the two-fluid plasma equations. Furthermore, the presence

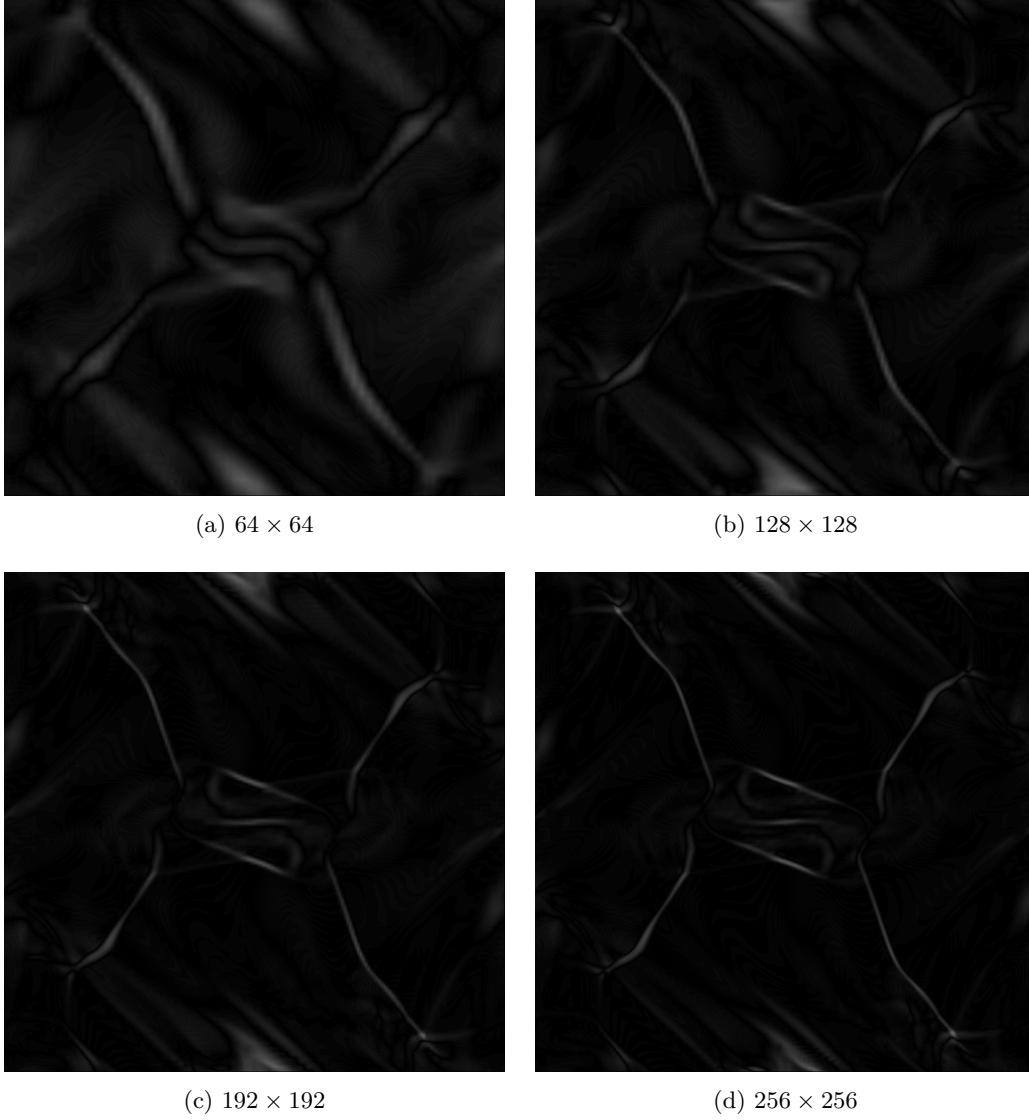


Figure 6.18: Image differences of the Roe and AUSM schemes for the Orszag-Tang magnetohydrodynamic vortex problem, as discussed in Section 6.5. The images were produced as 1024×1024 -pixel contour plots at identical levels, color map, time, and figure placement. The images were subtracted in grayscale color space. Subfigures here show different grid resolutions: (a) 64×64 , (b) 128×128 , (c) 192×192 , and (d) 256×256 . It is clear from subfigure (a) that, at low grid resolutions, the Roe and AUSM approaches differ. In these low-res cases, the Roe method proved much more accurate to the expected grid-independent solution. As the grid resolution is increased, the Roe and AUSM methods agree more and more closely, although the execution time for the Roe method becomes excessive compared to the AUSM scheme. In the highest grid resolution tested in subfigure (d), we see that there is a slight discrepancy in the locations of the shocks. This is suspected to be a diffusion issue with the AUSM scheme, since the AUSM method adds more diffusion across shocks than the Roe method.

of strong oscillations in numerical solutions of the two-fluid plasma equations has been observed [75–77], but it is not fully understood whether these oscillations are the result of numerical (artificial) or physical

phenomena.

Unfortunately, the strong conservative approach cannot directly be applied to eliminate the presence of source terms in the two-fluid model. This is due to the definition of the Lorentz body force and Ohmic heating terms in each moment set; recalling from Table 2.2 the form of the Lorentz body force and Ohmic heating terms, the quantities $(e_\alpha/m_\alpha)(\varrho_\alpha \mathbf{E} + \varrho_\alpha \mathbf{u} \times \mathbf{B})$ and $(e_\alpha/m_\alpha) \mathbf{u} \cdot \mathbf{E}$ represent the explicit sources. However, the conservative form of the Maxwell equations, identified in equations 5.13 and 5.14, only apply to the *total* current and charge, and therefore cannot be equated to these expressions. It is possible to substitute the total current and charge into these two-fluid sources by recognizing equations 2.108 and 2.109 in Table 2.2, but these introduce new quantities that must be left as explicit source terms while part of the coupling is mitigated to the flux and solution vectors. Recasting the two-fluid equations in this way could potentially allow for some moment sets to be written in terms of quantities that are less stiff (we could, for example, recast the electron equations with ion source terms; since the ion quantities change slowly, these would represent less stiff sources for the electron equations) but generally this involves introducing the reverse effect in at least one set of moment equations.

A further possibility is that the mass ratio happens to be fortuitous. If this is the case, then the charge-to-mass ratios of the different species may be convenient to express as multiples of the total current. For example, in a positron-electron plasma, where the mass ratio is unity, a factor of two emerges in equations 2.108 and 2.109. This might allow for the application of the identities 5.13 and 5.14 in equations 2.102 for the two-fluid case, but this is a limiting special case of the equations with a very convenient mass ratio. Since the identities could not generally be applied to the equations, we instead decided to focus on the single-fluid model, which certainly allows for the reformulation into a strong conservative set of equations. It is hoped that future work might find a means of implementing such a flux-coupled scheme for the two-fluid system; this could potentially allow a significant speedup in solving the equations for stiff systems.

Chapter 7

Discussion, Conclusions, Future Directions

“Cake, and grief counseling, will be available at the conclusion of the test.”

GLaDOS [1]

In this chapter, a review of our objective and a demonstration that we have in fact met this objective, and a summary of the findings from both investigations will be presented.

7.1 Review of the Objective

The objective that we posed at the beginning of this dissertation was to advance the state of the art in our capabilities to model plasmas. The advance here was twofold; first, we insisted on using models that capture more of the underlying physics of the plasma that are not permitted in MHD simulations (due to the magnetic diffusion approximation), which allows us to address the issues discussed in Chapter 1, and to improve the efficiency with which these solutions may be constructed. Currently, simulations of the single-fluid and two-fluid fully-coupled models discussed in Chapter 2 incurs major stiffness and stability constraints, and this limits our capabilities to solve these equations with only modest effort.

To improve our situation, in Chapter 3, we investigated an approach that takes advantage of a mathematical relationship between the two-fluid equations and the Maxwell equations of electrodynamics. We showed that this results in a set of isomorphic field equations, which are mathematically identical to Maxwell’s equations, but with intrinsically different physical source terms. If source term data were more readily available, we showed in Chapter 4 that the equations can be solved using classic techniques from electromagnetic theory. However, the deficit of available overshadows this approach, and more source term data needs to be harvested. Acquiring more source term models beyond what was provided in Chapter 4 was not seen as feasible for this dissertation project. Other possibilities, such as an iterative solution, also exist, but were not

rewarding avenues of research in this investigation due to their increased execution time and poor efficiency of constructing the solution.

To deal with the lack of source term data, in Chapter 5, we constructed a numerical solver to attempt performing simulations of known plasma problems so that the data may be postprocessed. This led to a separate investigation in which we reposed the Navier-Stokes equations in a strong conservative form to improve the stability of the equations, and it was shown in Chapter 6 that this method was very successful for the fully-coupled single-fluid model, and that it is intractable for the two-fluid model. The computed test cases and their results for the strong conservative single-fluid model coupled to the full Maxwell equations showed a significant improvement in performance and accuracy against the comparable solutions using the traditional source-coupled formulation. Derivations of the new eigenstructure were presented, which allowed for the construction of a Roe-based Riemann solver approach. This was validated against the Advected Upstream Splitting Method, which does not require a knowledge of the new eigenvectors.

Although the isomorphic approach succeeds in our demonstrations of solving the new field equations, it is limited by data availability and, in some cases, ill-posed reconstructive schemes for transforming the generalized fields back into the primitive variable set. The drift relation breaks down in non-vortical parts of the plasma. Using a potential formulation for the equations instead and constructing Green's function solutions succeeded in circumventing this problem, but requires a different means of reconstructing the primitive data. We introduced some simple source models which could be used as building blocks for more complicated problems. The strong conservative solver was used to qualitatively explore the form of the source terms, but ultimately, the strong conservative approach independently succeeded in our stated objective, which was to develop an analysis method for predicting general plasma fluid-electrodynamic interactions, in a much more straightforward way than the isomorphic approach.

Below, we review our findings and contributions to the state-of-the-art in both of these investigations. We then discuss future directions that this work is expected to take.

7.2 Summary of Findings

We summarize our findings for our two investigations as follows:

7.2.1 Findings for the Two-fluid Isomorphism

The investigation exploring the two-fluid isomorphism may be summarized as follows:

- There exists an equivalent set of equations for a two-fluid plasma in the form of Maxwell's equations for classical electrodynamics. The electric and magnetic fields are supplanted by the *generalized Lamb vector*, ζ_α , and the *generalized vorticity*, Ω_α , respectively, which become the new central dynamical variables in this framework.

- The isomorphism introduces an analogous set of source terms for the two-fluid plasma, the *generalized charge density*, ϱ_α , and the *generalized current density*, \mathbf{j}_α , which include both electric charge and current density contributions as well as new *fluid* charge and current densities. Although the form of the generalized source terms is achieved analytically, due to the nature of Maxwell's equations, we must either know the fields and solve for the sources or know the sources and solve for the fields. Iterative approaches for solving the equations, at present, do not seem promising.
- Of these two stated problem types for the Maxwell equations, we considered the latter to be more representative of attempting to solve a given flow field problem. However, a knowledge of the sources must be possessed. We would ideally like to construct empirical models to simple forms of the source terms, which can then be used as building blocks for more complicated problems. To discover the form of the sources, we examined three simple steady, incompressible fluid problems and determined the form of the source terms for these cases; we illustrated some solution approaches taking advantage of the isomorphism. We also demonstrated some qualitative postprocessing of the source terms for compressible fluids and plasmas to show the general nature of the sources for these cases.
- From the solution approaches tested, numerical reconstructive schemes that rely on the drift relation are limited to vortical regions of the flow that possess some generalized vorticity. The Green's function approach and method of images, which were borrowed from electrostatics, were applied with remarkable accuracy to solve the problems.
- Homogeneous solutions, where the source terms vanish, result in wave equations in the generalized fields. We showed that the typical variety of magnetohydrodynamic waves can be recovered.

7.2.2 Findings for Comparison of Strong Conservative and Source-coupled Forms

- A strong conservative formulation is possible for the single-fluid equations of motion. These equations retain the exact coupling to the Maxwell system in the solution and flux vectors, rather than appearing as explicit source terms.
- The fully-coupled model was validated against several problems. Low-conductivity and electromagnetic wave propagation tests as well as high-conductivity magnetic diffusion limit tests were solved by discretizing and numerically simulating these equations.
- This strong conservative flux-coupled approach provided a more stable simulation than the traditional source-coupled approach in the validation test cases explored. Since a higher maximum stable timestep can be achieved, the simulation performance was substantially increased. Accuracy was also improved, since source-induced oscillations vanished. The most significant improvement occurs in cases where large currents are expected, since the magnitude of the source terms increase with increasing conductivity; cases where essentially magnetohydrodynamic behavior may occur somewhere within the computational domain typically strain the source-coupled formulation, but can be resolved with modest effort using the strong conservative formulation.

- Both the AUSM and Roe approximate Riemann solver approaches compared increasingly well with increasing grid density. For the most refined grids explored, the most prominent distinction was in slight differences in shock location. This is presumed to be due to the addition of more diffusion by the AUSM flux than the Roe flux.
- We were originally interested in applying this technique to the two-fluid plasma model to relieve the form of the source terms; however, this is not generally possible without either additional assumptions, simplification in the mass ratio, or an alternate form of the equations. This is due to the definition of the coupling terms in the Lorentz force and Ohmic dissipation for each species. As an example of this, we were able to present a numerical solution to the Brio and Wu problem [145] for a positron-electron plasma, where the mass ratio is unity; however, in the general case, this approach will not work.

7.3 Contributions to the State-of-the-Art

The above results present a set of isomorphic field equations that extend the previous work of Marmanis [108, 109], Kambe [110], Mahajan [121] and others to explore the utility for constructing solutions to two-fluid plasmas. The new isomorphism permits a full set of Maxwell equations describing the plasma flow, although, to solve for the fields, source term information must also be provided. This unites different threads of literature that have examined this approach for fluid dynamics [108–110, 116, 117] and plasmas [118, 119, 121]. Furthermore, we have explored the nature of the source terms for simplified fluid flow problems, which has fashioned simple models that may be superposed in the cases of more complicated flow patterns. We showed that this could be used to calculate reconstructive solutions (in regions where the drift relation, equation 3.80, does not fail) and Green’s function solutions. Also, if sufficient models for the source terms are known, then closed-form solutions can also be calculated; we presented a closed-form solution for Blasius boundary layer flow that demonstrates the utility of the approach. The drawback, as discussed in Chapter 4, is the lack of source term data available with which to calculate the generalized fields from the Maxwell equations. The exploration for more source term models is relegated as future work, since the framework and demonstration of the feasibility of the approach have been presented.

Our second approach extended the numerical capabilities for solving plasma models that include the full Maxwell equations. We started with the intent to apply this strong conservative approach to the two-fluid equations, which could substantially alleviate the computationally intense calculation, but we showed that this method is not directly applicable to the two-fluid equations. Instead, we applied it to the single-fluid reduction of the two-fluid equations, retaining the full Maxwell equations, and, for the validation test cases explored, a substantial improvement in execution time and accuracy was observed for problems where the current became large. The failure of the source-coupled form to adequately handle large currents agrees with previous investigations [59–61, 95, 98], but is handled gracefully and with only modest effort by the new strong conservative form presented and explored in this dissertation. This permits us to explore the

applications discussed in Chapter 1 using a framework that requires less effort and execution time than the state-of-the-art approaches.

7.4 Future Directions

The construction of the isomorphism, explication of some of its ramifications, and unification between the present and previous work has been accomplished here; however, this topic is unbounded, and several very impressive ideas may be readily drawn from it for future investigations.

Clearly, the gathering and classification of source term models for the field equations is necessary for the real utility in this framework to emerge. Source term data could be gathered analytically or by numerical simulation, as shown, or also by experiment. We focused on simple models in this work because a collection of simple models provides a foundation for constructing more complicated models. Introduction of a sufficient number of models would allow engineers to superpose these models in domains of interest, and calculate the resulting fields from the equations.

However, several more imaginative approaches could also be envisioned. If source term models for the Riemann problem were constructed, an alternative approach to solve the fluid equations could be developed by considering faces between volumes to radiate charges and currents. This would permit a Maxwell solution, given a knowledge of how much charge and current was emitted at each face and each timestep. This would provide an alternative approach to the Riemann solver approach, albeit a similar conceptual idea. However, the solution of the Maxwell equations would be much simpler to implement, and less expensive to update, given sufficient models for the Riemann charge and current.

Any development of an iterative scheme for the isomorphic field equations would represent a significant step forward. The biggest advantage of an iterative scheme is that empirical models may not be necessary for the source terms; the sources are instead treated as part of the unknown set in this approach, and both sources and fields are converged in an approximate manner. Our investigation did not yield any fruitful results in this pursuit, which motivated our focus on empirical modeling instead.

Another road to exploiting the isomorphism may be to give up on finite volume simulations altogether. Variational schemes that take advantage of the Lagrangian formulation could potentially offer another avenue of development that might provide a superior approach for determining the evolution of the plasma. One could attempt to solve the equations purely using Galerkin spectral methods or with perturbation expansions. One can see that several different paths are possible for continuing this work in an effort to improve the expense associated with a numerical simulation of the two-fluid system.

The second part of this dissertation focused on the development of a strong conservative numerical solution procedure and solver for predicting plasma fluid-electrodynamic field interactions, and the demonstration of this technique over the traditional approach was presented. The most disappointing facet of this work was that this method was not obviously or directly applicable to the two-fluid system. While the demonstration

of this technique for the single-fluid model represents a significant improvement in our capabilities to model plasmas, a significant expansion of this work would be to show a way of furthering the mileage of the two-fluid model by a similar means of eliminating source terms while retaining coupling. This does not seem immediately possible due to the formulation of the model in terms of species charge and current densities, while the identities presented in section 5.4 holds for the total charge and current densities.

The solver developed during this dissertation also has a broad future for its expansion and utility. We have focused primarily on the numerical scheme in this dissertation; the application of the solver for varying problems such as our motivating examples in Chapter 1 represents a near-term effort that will be continued. Although validation of the solver has been presented here that clearly demonstrates its capabilities, verification cases that compare the predicted solutions to experimental data require further investigation. Current ongoing efforts will apply the method to pulsed plasma thrusters and scramjet propulsion models with magnetohydrodynamic augmentation.

7.5 Concluding Remarks

The formation and exploitation of analogies and isomorphisms has played a significant role in the progression of our understanding. This dissertation has participated in this advance by constructing such an analogy in the field structure of fluid dynamics and electrodynamics. In addition to introducing the extended formalism for a plasma, this has also found an intersection in the previous work investigating analogies in fluid dynamics, plasmas, and electrodynamics. The exploitation of this isomorphism depends on the availability of data, but allows a very different perspective of fluids and plasmas from the perception of classical electrodynamics. As Maxwell observed, “it is a good thing to have two ways of looking at a subject, and to admit that there are two ways of looking at it.” The benefit of the isomorphism ultimately may not lie in its utility as much as its valuable departure from the classic approach of thinking about fluids and plasmas.

The value of the strong conservative approach succeeded more acutely in what we had set out to accomplish, and has more direct utility for our motivating problems of interest. It has long been argued that a conservative equation is numerically superior to a non-conservative expression [156], and this work has provided valuable evidence that this may be true.

It is sincerely hoped that the problems discussed in Chapter 1 are ultimately realized. It is truly hoped that when they are, this dissertation is perceived as nothing more than a humble step forward in this collective endeavor, a small bastion that buttresses our incipient tower of knowledge.

Bibliography

- [1] Valve Corporation, “Portal 2TM,” 2011.
- [2] O. Heaviside, “Electromagnetic induction and it’s propagation,” *The Electrician*, 1885 – 1887.
- [3] O. Heaviside, “Electromagnetic waves, the propagation of potential and the electromagnetic effects of a moving charge,” *The Electrician*, 1888 – 1889.
- [4] J. C. Maxwell and W. D. Niven, *The Scientific Papers of James Clerk Maxwell*. No. v. 1 in Cambridge Library Collection - Physical Sciences, Cambridge University Press, 2011.
- [5] J. D. Jackson, *Classical Electrodynamics*. John Wiley & Sons, Inc., third ed., 1999.
- [6] F. White, *Viscous fluid flow*. McGraw Hill Series in Mechanical Engineering, McGraw-Hill Professional Publishing, 1991.
- [7] T. Kambe, *Elementary Fluid Mechanics*. World Scientific Publishing Company Incorporated, 2007.
- [8] D. D’Ambrosio and D. Giordano, “Electromagnetic Fluid Dynamics for Aerospace Applications,” *Journal of Thermophysics and Heat Transfer*, vol. 21, no. 2, pp. 284–302, 2007.
- [9] T. N. Foundation, “The nobel prize in physics 1970,” May 2013.
- [10] P. M. Bellan, *Fundamentals Of Plasma Physics*. Cambridge University Press, 2006.
- [11] P. L. Roe, “Approximate Riemann solvers, parameter vectors, and difference schemes,” *Journal of Computational Physics*, vol. 43, pp. 357–372, Oct. 1981.
- [12] M. S. LIOU and C. J. STEFFEN, “A NEW FLUX SPLITTING SCHEME,” *JOURNAL OF COMPUTATIONAL PHYSICS*, vol. 107, pp. 23–39, July 1993.
- [13] D. Swanson, *Plasma Waves*. Plasma Physics, Institute of Physics Publishing, 2003.
- [14] E. Holt and R. Haskell, *Foundations of plasma dynamics*. Macmillan, 1965.
- [15] G. W. Sutton and A. Sherman, *Engineering Magnetohydrodynamics*. Dover Publications, Inc., 1965.
- [16] T. Boyd and J. Sanderson, *The Physics of Plasmas*. Cambridge University Press, 2003.
- [17] R. Hazeltine and F. Waelbroeck, *The Framework of Plasma Physics*. Frontiers in Physics, Westview Press, Advanced Book Program, 2004.
- [18] C. Kittel, *Introduction to solid state physics*. Wiley, 1996.
- [19] A. Aleksandrov, L. Bogdankevich, and A. Rukhadze, *Principles of plasma electrodynamics*. Springer series in electrophysics, Springer-Verlag, 1984.

- [20] J. S. Shang, "Recent research in magneto-aerodynamics," *PROGRESS IN AEROSPACE SCIENCES*, vol. 37, pp. 1–20, Jan. 2001.
- [21] J. R. Roth, D. M. Sherman, and S. P. Wilkinson, "Electrohydrodynamic Flow Control with a Glow-Discharge Surface Plasma," *AIAA Journal*, vol. 38, pp. 1166–1172, July 2000.
- [22] J. R. Roth and X. Dai, "Optimization of the Aerodynamic Plasma Actuator as an Electrohydrodynamic (EHD) Electrical Device," in *44th AIAA Aerospace Sciences Meeting and Exhibit*, Aerospace Sciences Meetings, American Institute of Aeronautics and Astronautics, Jan. 2006.
- [23] J. Huang, T. C. Corke, and F. O. Thomas, "Plasma Actuators for Separation Control of Low-Pressure Turbine Blades," *AIAA Journal*, vol. 44, pp. 51–57, Jan. 2006.
- [24] K. Dennis, Y. Suzen, and N. Uygun, "Simulations of Plasma Flow Control in Low-Pressure Turbines," in *46th AIAA Aerospace Sciences Meeting and Exhibit*, Aerospace Sciences Meetings, American Institute of Aeronautics and Astronautics, Jan. 2008.
- [25] C. Porter, T. McLaughlin, C. Enloe, G. Font, J. Roney, and J. Baughn, "Boundary Layer Control Using a DBD Plasma Actuator," in *45th AIAA Aerospace Sciences Meeting and Exhibit*, Aerospace Sciences Meetings, American Institute of Aeronautics and Astronautics, Jan. 2007.
- [26] J. S. Shang, R. L. Kimmel, J. Menart, and S. T. Surzhikov, "Hypersonic flow control using surface plasma actuator," *JOURNAL OF PROPULSION AND POWER*, vol. 24, no. 5, pp. 923–934, 2008.
- [27] S. Wilkinson, "Oscillating Plasma for Turbulent Boundary Layer Drag Reduction," in *41st Aerospace Sciences Meeting and Exhibit*, Aerospace Sciences Meetings, American Institute of Aeronautics and Astronautics, Jan. 2003.
- [28] T. Jukes, K.-S. Choi, G. Johnson, and S. Scott, "Turbulent Boundary-Layer Control for Drag Reduction Using Surface Plasma," in *2nd AIAA Flow Control Conference*, Fluid Dynamics and Co-located Conferences, American Institute of Aeronautics and Astronautics, June 2004.
- [29] R. Wood, "Aerodynamic Drag and Drag Reduction," in *41st Aerospace Sciences Meeting and Exhibit*, Aerospace Sciences Meetings, American Institute of Aeronautics and Astronautics, Jan. 2003.
- [30] M. Nishihara, D. Gaitonde, and I. Adamovich, "Effect of Nanosecond Pulse DBD Plasma Actuators on Oblique Shocks and on Shock / Boundary Layer Interaction," in *51st AIAA Aerospace Sciences Meeting including the New Horizons Forum and Aerospace Exposition*, Aerospace Sciences Meetings, American Institute of Aeronautics and Astronautics, Jan. 2013.

- [31] S. Leonov, A. Firsov, D. Yarantsev, F. Falempin, and M. Goldfeld, "Plasma Effect on Shocks Configuration in Compression Ramp," in *17th AIAA International Space Planes and Hypersonic Systems and Technologies Conference*, International Space Planes and Hypersonic Systems and Technologies Conferences, American Institute of Aeronautics and Astronautics, Apr. 2011.
- [32] V. Narayanaswamy, L. L. Raja, and N. T. Clemens, "Control of a Shock/Boundary-Layer Interaction by Using a Pulsed-Plasma Jet Actuator," *AIAA Journal*, vol. 50, pp. 246–249, Jan. 2012.
- [33] N. Webb, C. Clifford, and M. Samimy, "Control of Oblique Shock Wave-Boundary Layer Interactions Using Plasma Actuators," in *6th AIAA Flow Control Conference*, Fluid Dynamics and Co-located Conferences, American Institute of Aeronautics and Astronautics, June 2012.
- [34] N. Webb, C. Clifford, and M. Samimy, "An Investigation of the Control Mechanism of Plasma Actuators in a Shock Wave-Boundary Layer Interaction," in *51st AIAA Aerospace Sciences Meeting including the New Horizons Forum and Aerospace Exposition*, Aerospace Sciences Meetings, American Institute of Aeronautics and Astronautics, Jan. 2013.
- [35] G. I. Font, C. L. Enloe, and T. E. McLaughlin, "Plasma Volumetric Effects on the Force Production of a Plasma Actuator," *AIAA Journal*, vol. 48, pp. 1869–1874, Sept. 2010.
- [36] C. Porter, A. Abbas, K. Cohen, T. McLaughlin, and C. L. Enloe, "Spatially Distributed Forcing and Jet Vectoring with a Plasma Actuator," *AIAA Journal*, vol. 47, pp. 1368–1378, June 2009.
- [37] C. L. Enloe, T. E. McLaughlin, R. D. Van Dyken, K. D. Kachner, E. J. Jumper, and T. C. Corke, "Mechanisms and Responses of a Single Dielectric Barrier Plasma Actuator: Plasma Morphology," *AIAA Journal*, vol. 42, pp. 589–594, Mar. 2004.
- [38] C. L. Enloe, T. McLaughlin, G. I. Font, and J. W. Baughn, "Parameterization of Temporal Structure in the Single-Dielectric-Barrier Aerodynamic Plasma Actuator," *AIAA Journal*, vol. 44, pp. 1127–1136, June 2006.
- [39] F. Roveda, J. Shang, and G. Huang, "On Electrodynamic Force of Dielectric Barrier Discharge," in *49th AIAA Aerospace Sciences Meeting including the New Horizons Forum and Aerospace Exposition*, Aerospace Sciences Meetings, American Institute of Aeronautics and Astronautics, Jan. 2011.
- [40] A. Likhanskii, M. Shneider, S. Macheret, and R. Miles, "Modeling of Interaction Between Weakly Ionized Near-Surface Plasmas and Gas Flow," in *44th AIAA Aerospace Sciences Meeting and Exhibit*, Aerospace Sciences Meetings, American Institute of Aeronautics and Astronautics, Jan. 2006.

- [41] A. Likhanskii, V. Semak, M. Shneider, D. Opaitis, R. Miles, and S. Macheret, “Parallel Code Development and Numerical Investigation of Surface Charge Build-Up in DBD Plasma Actuators,” in *46th AIAA Aerospace Sciences Meeting and Exhibit*, Aerospace Sciences Meetings, American Institute of Aeronautics and Astronautics, Jan. 2008.
- [42] D. Orlov, T. Corke, and M. Patel, “Electric Circuit Model for Aerodynamic Plasma Actuator,” in *44th AIAA Aerospace Sciences Meeting and Exhibit*, Aerospace Sciences Meetings, American Institute of Aeronautics and Astronautics, Jan. 2006.
- [43] N. McMullin and D. Snyder, “Numerical Simulation of Plasma-Based Actuator Vortex Control of a Turbulent Cylinder Wake,” in *45th AIAA Aerospace Sciences Meeting and Exhibit*, Aerospace Sciences Meetings, American Institute of Aeronautics and Astronautics, Jan. 2007.
- [44] D. M. Orlov, *Modelling and simulation of single dielectric barrier discharge plasma actuators*. PhD thesis, University of Notre Dame, 2006.
- [45] D. V. Gaitonde and J. Poggie, “Implicit Technique for Three-Dimensional Turbulent Magnetoaerodynamics,” *AIAA Journal*, vol. 41, pp. 2179–2191, Nov. 2003.
- [46] R. MacCormack, “An upwind conservation form method for magnetofluid dynamics,” in *30th Plasmadynamic and Lasers Conference*, Fluid Dynamics and Co-located Conferences, American Institute of Aeronautics and Astronautics, June 1999.
- [47] R. MacCormack, “Simulation of Hypersonic Flow Within a Strong Magnetic Field,” in *45th AIAA Aerospace Sciences Meeting and Exhibit*, Aerospace Sciences Meetings, American Institute of Aeronautics and Astronautics, Jan. 2007.
- [48] R. MacCormack, “Non-Equilibrium Ionized Flow Simulations Within Strong Electro-Magnetic Fields,” in *48th AIAA Aerospace Sciences Meeting Including the New Horizons Forum and Aerospace Exposition*, Aerospace Sciences Meetings, American Institute of Aeronautics and Astronautics, Jan. 2010.
- [49] R. MacCormack, D. D’Ambrosio, D. Giordano, J. K. Lee, and T. Kim, “Plasmadynamic Simulations with Strong Shock Waves,” in *42nd AIAA Plasmadynamics and Lasers Conference*, Fluid Dynamics and Co-located Conferences, American Institute of Aeronautics and Astronautics, June 2011.
- [50] D. D’Ambrosio, D. Giordano, and D. Bruno, “Fully Coupled Maxwell/Navier-Stokes Simulation of Electromagnetic Hypersonics Including Accurate Transport Models,” in *40th AIAA Plasmadynamics and Lasers Conference*, Fluid Dynamics and Co-located Conferences, American Institute of Aeronautics and Astronautics, June 2009.

- [51] C. Park, D. W. Bogdanoff, and U. B. Mehta, "Theoretical Performance of a Magnetohydrodynamic-Bypass Scramjet Engine with Nonequilibrium Ionization," *Journal of Propulsion and Power*, vol. 19, pp. 529–537, July 2003.
- [52] D. V. Gaitonde, "Magnetohydrodynamic Energy-Bypass Procedure in a Three-Dimensional Scramjet," *Journal of Propulsion and Power*, vol. 22, pp. 498–510, May 2006.
- [53] D. V. Gaitonde, "Effect of Hall currents on simulated three-dimensional scramjet with magnetohydrodynamic bypass," *JOURNAL OF PROPULSION AND POWER*, vol. 22, no. 3, pp. 700–703, 2006.
- [54] S. Gupta, J. C. Tannehill, U. B. Mehta, and D. W. Bogdanoff, "Simulation of 3-D Nonequilibrium Seeded Airflow in the NASA Ames MHD Channel," *Journal of Thermophysics and Heat Transfer*, vol. 21, pp. 276–283, Apr. 2007.
- [55] D. V. Gaitonde, "High-Speed Magnetohydrodynamic Flow Control Analyses with Three-Dimensional Simulations," *Journal of Propulsion and Power*, vol. 24, pp. 946–961, Sept. 2008.
- [56] M. Kim, I. D. Boyd, and M. Keidar, "Modeling of Electromagnetic Manipulation of Plasmas for Communication During Reentry Flight," *Journal of Spacecraft and Rockets*, vol. 47, pp. 29–35, Jan. 2010.
- [57] M. Keidar, M. Kim, and I. Boyd, "Electromagnetic Reduction of Plasma Density During Atmospheric Reentry and Hypersonic Flights," *Journal of Spacecraft and Rockets*, vol. 45, pp. 445–453, May 2008.
- [58] R. L. Burton and P. J. Turchi, "Pulsed plasma thruster," *JOURNAL OF PROPULSION AND POWER*, vol. 14, no. 5, pp. 716–735, 1998.
- [59] D. Li, C. Merkle, W. M. Scott, D. Keefer, T. Moeller, and R. Rhodes, "Hyperbolic Algorithm for Coupled Plasma/Electromagnetic Fields Including Conduction and Displacement Currents," *AIAA Journal*, vol. 49, no. 5, pp. 909–920, 2011.
- [60] D. Li, C. Merkle, W. M. Scott, D. Keefer, T. Moeller, and R. Rhodes, "A Hyperbolic Algorithm for Numerical Solutions of Coupled Plasma/EM Fields Including Both Real and Displacement Currents," in *43rd AIAA/ASME/SAE/ASEE Joint Propulsion Conference & Exhibit*, 2007.
- [61] T. Moeller, R. Rhodes, D. Keefer, C. Merkle, and D. Li, "Experimental and computer simulation studies of a pulsed plasma accelerator," in *Plasma Science, 2006. ICOPS 2006. IEEE Conference Record - Abstracts. The 33rd IEEE International Conference on*, p. 91, 2006.

- [62] T. Moeller, D. Keefer, and R. Rhodes, “Experimental pulsed plasma thruster for code evaluation,” in *Plasma Science, 2004. ICOPS 2004. IEEE Conference Record - Abstracts. The 31st IEEE International Conference on*, pp. 302–, 2004.
- [63] D. Rooney, T. Moeller, D. Keefer, R. Rhodes, and C. Merkle, “Experimental and Computer Simulation Studies of a Pulsed Plasma Accelerator,” in *AIAA Joint Propulsion Conference*, 2007.
- [64] D. Li, C. L. Merkle, D. Keefer, T. Moeller, R. Rhodes, and W. M. Scott, “Coupled Electromagnetic/Fluid Dynamic Simulation of Fields Through Plasma and Vacuum,” in *Plasma Science, 2007. ICOPS 2007. IEEE 34th International Conference on*, p. 695, 2007.
- [65] K. Hara, I. Boyd, and V. Kolobov, “One Dimensional Hybrid-Vlasov Simulation of a Hall Thruster,” in *48th AIAA/ASME/SAE/ASEE Joint Propulsion Conference & Exhibit*, Joint Propulsion Conferences, American Institute of Aeronautics and Astronautics, July 2012.
- [66] N. Yamamoto, K. Komurasaki, and Y. Arakawa, “Discharge Current Oscillation in Hall Thrusters,” *Journal of Propulsion and Power*, vol. 21, pp. 870–876, Sept. 2005.
- [67] E. A. D. Marco, E. Coscarelli, and M. Andrenucci, “Electron Dynamics in Hall Thrusters,” in *44th AIAA/ASME/SAE/ASEE Joint Propulsion Conference & Exhibit*, Joint Propulsion Conferences, American Institute of Aeronautics and Astronautics, July 2008.
- [68] D. E. Anton and E. Ahedo, “Low-frequency azimuthal stability analysis of Hall thrusters,” in *48th AIAA/ASME/SAE/ASEE Joint Propulsion Conference & Exhibit*, Joint Propulsion Conferences, American Institute of Aeronautics and Astronautics, July 2012.
- [69] E. A. D. Marco and M. Andrenucci, “Amplifying and Evanescent Waves in Hall Thrusters,” in *44th AIAA/ASME/SAE/ASEE Joint Propulsion Conference & Exhibit*, Joint Propulsion Conferences, American Institute of Aeronautics and Astronautics, July 2008.
- [70] J. Koo and I. Boyd, “Anomalous electron mobility modeling in Hall thrusters,” in *41st AIAA/ASME/SAE/ASEE Joint Propulsion Conference & Exhibit*, Joint Propulsion Conferences, American Institute of Aeronautics and Astronautics, July 2005.
- [71] E. Fossum and L. King, “An Unexamined Collision-less Mechanism for Electron Mobility in Hall Thrusters,” in *45th AIAA/ASME/SAE/ASEE Joint Propulsion Conference & Exhibit*, Joint Propulsion Conferences, American Institute of Aeronautics and Astronautics, Aug. 2009.
- [72] L. C. Steinhauer, “Review of field-reversed configurations,” *Physics of Plasmas*, vol. 18, p. 70501, 2011.

- [73] J. Loverich, A. Hakim, and U. Shumlak, "A Discontinuous Galerkin Method for Ideal Two-Fluid Plasma Equations," *COMMUNICATIONS IN COMPUTATIONAL PHYSICS*, vol. 9, pp. 240–268, Feb. 2011.
- [74] U. Shumlak, R. Lilly, N. Reddell, E. Sousa, and B. Srinivasan, "Advanced physics calculations using a multi-fluid plasma model," *COMPUTER PHYSICS COMMUNICATIONS*, vol. 182, pp. 1767–1770, Sept. 2011.
- [75] U. Shumlak and J. Loverich, "Approximate Riemann solver for the two-fluid plasma model," *Journal of Computational Physics*, vol. 187, pp. 620–638, 2003.
- [76] A. Hakim, J. Loverich, and U. Shumlak, "A high resolution wave propagation scheme for ideal Two-Fluid plasma equations," *JOURNAL OF COMPUTATIONAL PHYSICS*, vol. 219, pp. 418–442, Nov. 2006.
- [77] A. Hakim and U. Shumlak, "Two-fluid physics and field-reversed configurations," *PHYSICS OF PLASMAS*, vol. 14, May 2007.
- [78] L. C. Steinhauer, H. Guo, and A. Ishida, "Computation of equilibria of a flowing two-fluid in two dimensions," *JOURNAL OF FUSION ENERGY*, vol. 26, pp. 207–210, June 2007.
- [79] L. C. Steinhauer and A. Ishida, "Nearby-fluids equilibria. I. Formalism and transition to single-fluid magnetohydrodynamics," *PHYSICS OF PLASMAS*, vol. 13, May 2006.
- [80] L. C. Steinhauer and A. Ishida, "Relaxation of a two-species magnetofluid and application to finite- β flowing plasmas," *Physics of Plasmas*, vol. 5, no. 7, pp. 2609–2622, 1998.
- [81] L. C. Steinhauer, "Formalism for multi-fluid equilibria with flow," *Physics of Plasmas*, vol. 6, no. 7, pp. 2734–2741, 1999.
- [82] L. C. Steinhauer and A. Ishida, "Relaxation of a Two-Specie Magnetofluid," *Physical Review Letters*, vol. 79, no. 18, pp. 3423–3426, 1997.
- [83] A. Lonkar, F. Palacios, R. MacCormack, and J. Alonso, "Multidimensional Simulation of Plasma in Argon through a Shock in Hypersonic Flow," in *43rd AIAA Thermophysics Conference*, Fluid Dynamics and Co-located Conferences, American Institute of Aeronautics and Astronautics, June 2012.
- [84] R. W. Maccormack, "Flow Simulations within Strong Magnetic Fields," No. January, pp. 7–10, 2008.
- [85] R. MacCormack, "Solution of Maxwell's Equations Coupled to the Navier-Stokes Equations," in *40th AIAA Plasmadynamics and Lasers Conference*, Fluid Dynamics and Co-located Conferences, American Institute of Aeronautics and Astronautics, June 2009.

- [86] R. MacCormack, "Numerical Simulation of Aerodynamic Flow Including Induced Magnetic and Electric Fields," in *39th Plasmadynamics and Lasers Conference*, Fluid Dynamics and Co-located Conferences, American Institute of Aeronautics and Astronautics, June 2008.
- [87] R. MacCormack, "Solution of the Equations of Magneto-Fluid Dynamics with Chemical Reaction," in *41st Plasmadynamics and Lasers Conference*, Fluid Dynamics and Co-located Conferences, American Institute of Aeronautics and Astronautics, June 2010.
- [88] R. MacCormack, "Three Dimensional Plasmadynamics Calculations," in *33rd Plasmadynamics and Lasers Conference*, Fluid Dynamics and Co-located Conferences, American Institute of Aeronautics and Astronautics, May 2002.
- [89] R. MacCormack, "Numerical Simulation of Aerodynamic Flow within a Strong Magnetic Field with Hall Current and Ion Slip," in *38th AIAA Plasmadynamics and Lasers Conference*, Fluid Dynamics and Co-located Conferences, American Institute of Aeronautics and Astronautics, June 2007.
- [90] R. MacCormack, "Conservation form method for magnetofluid dynamics," in *39th Aerospace Sciences Meeting and Exhibit*, Aerospace Sciences Meetings, American Institute of Aeronautics and Astronautics, Jan. 2001.
- [91] D. D'Ambrosio, "Numerical prediction of laminar shock/shock interactions in hypersonic flow," in *40th AIAA Aerospace Sciences Meeting & Exhibit*, Aerospace Sciences Meetings, American Institute of Aeronautics and Astronautics, Jan. 2002.
- [92] D. D'Ambrosio and D. Giordano, "Electromagnetic Fluid Dynamics for Aerospace Applications. Part I: Classification and Critical Review of Physical Models," in *35th AIAA Plasmadynamics and Lasers Conference*, Fluid Dynamics and Co-located Conferences, American Institute of Aeronautics and Astronautics, June 2004.
- [93] D. D'Ambrosio and D. Giordano, "Two-Dimensional Numerical Methods in Electromagnetic Hypersonics Including Fully Coupled Maxwell Equations," in *39th Plasmadynamics and Lasers Conference*, Fluid Dynamics and Co-located Conferences, American Institute of Aeronautics and Astronautics, June 2008.
- [94] D. D'Ambrosio, M. Pandolfi, and D. Giordano, "Electromagnetic Fluid Dynamics for Aerospace Applications. Part II: Numerical Simulations Using Different Physical Models," in *35th AIAA Plasmadynamics and Lasers Conference*, Fluid Dynamics and Co-located Conferences, American Institute of Aeronautics and Astronautics, June 2004.

- [95] D. Li, X. Zeng, C. L. Merkle, E. J. Felderman, and J. M. Sheeley, “Coupled Fluid-Dynamic Electromagnetic Modeling of Arc Heaters,” in *37th AIAA Plasmadynamics and Lasers Conference*, 2006.
- [96] D. Li, D. Keefer, R. Rhodes, C. Merkle, K. Kolokolnikov, and R. Thibodeaux, “Analysis of Magnetohydrodynamic Generator Power Generation,” *Journal of Propulsion and Power*, vol. 21, pp. 424–432, May 2005.
- [97] C. Merkle, T. Moeller, R. Rhodes, and D. Keefer, “Computational Simulations of Power Extraction in MHD Channel,” in *40th AIAA Plasmadynamics and Lasers Conference*, Fluid Dynamics and Co-located Conferences, American Institute of Aeronautics and Astronautics, June 2009.
- [98] D. Moeller, T., Rhodes, R., Keefer, D., Merkle, C., Li, “Experimental and Computer Simulation Studies of a Pulsed Plasma Accelerator,” in *33st IEEE International Conference on Plasma Science*, (Traverse City, MI), 2006.
- [99] C. Lian, G. Xia, and C. Merkle, “Impact of Source Terms on Reliability of CFD Algorithms,” in *19th AIAA Computational Fluid Dynamics*, Fluid Dynamics and Co-located Conferences, American Institute of Aeronautics and Astronautics, June 2009.
- [100] R. H. Landau, J. Páez, and C. C. Bordeianu, *A Survey of Computational Physics: Introductory Computational Science*. Princeton University Press, 2011.
- [101] W. Greiner, *Classical*. Classical Theoretical Physics Series, Springer Verlag, 1998.
- [102] B. Thidé, *Electromagnetic Field Theory*. Self-published online at <http://www.plasma.uu.se/CED/Book/>, 2012.
- [103] C. D. Munz, P. Omnes, R. Schneider, E. Sonnendrucker, and U. Voss, “Divergence correction techniques for Maxwell solvers based on a hyperbolic model,” *JOURNAL OF COMPUTATIONAL PHYSICS*, vol. 161, pp. 484–511, July 2000.
- [104] A. D. Sokal, *Monte Carlo Methods in Statistical Physics: Foundations and New Algorithms*. 1996. Lectures at Cargèse Summer School on “Functional Integration: Basics and Applications”.
- [105] E. A. Johnson, *Gaussian-Moment Relaxation Closures for Verifiable Numerical Simulation of Fast Magnetic Reconnection in Plasma*. PhD thesis, University of Wisconsin – Madison, 2011.
- [106] R. Feynman, R. Leighton, M. Sands, and M. Gottlieb, *The Feynman lectures on physics*. The Feynman Lectures on Physics, Pearson/Addison-Wesley, 1963.
- [107] D. H. Towne, *Wave Phenomena*. Addison-Wesley Publishing Company, 1967.

- [108] H. Marmanis, “Analogy between the Navier-Stokes equations and Maxwell’s equations: Application to turbulence,” *Physics of Fluids*, vol. 10, no. 6, pp. 1428–1437, 1998.
- [109] H. Marmanis, *Analogy between the Electromagnetic and Hydrodynamic Equations: Application to Turbulence*. PhD thesis, Brown University, 2000.
- [110] T. Kambe, “A new formulation of equations of compressible fluids by analogy with {M}axwell’s equations,” *Fluid Dynamics Research*, vol. 42, p. 455502, 2010.
- [111] E. T. Whittaker, *A history of the theories of aether and electricity*. Longmans, Green [etc., etc.], 1910.
- [112] D. M. Spiegel, *Innovation in Maxwell’s Electromagnetic Theory*. Cambridge University Press, 1991.
- [113] M. Wise, “The flow analogy to electricity and magnetism, part I: William Thomson’s reformulation of action at a distance,” *Archive for History of Exact Sciences*, vol. 25, no. 1, pp. 19–70, 1981.
- [114] N. J. Nersessian, “Maxwell and ”the Method of Physical Analogy”: Model-based reasoning, generic abstraction, and conceptual change,” in *Essays in the History and Philosophy of Science and Mathematics* (D. Malament, ed.), pp. 129—166, OPEN COURT Publishing Company, 2002.
- [115] H. Helmholtz, “LXIII. On Integrals of the hydrodynamical equations, which express vortex-motion,” *Philosophical Magazine Series 4*, vol. 33, pp. 485–512, Jan. 1867.
- [116] J. G. Logan, “Hydrodynamic Analog of the Classical Field Equations,” *Physics of Fluids*, vol. 5, no. 7, pp. 868–869, 1962.
- [117] J. G. LOGAN, “RAREFIED-GAS FIELD EQUATIONS FOR PLANE SHEAR DISTURBANCE PROPAGATION,” *AIAA Journal*, vol. 1, pp. 1173–1175, May 1963.
- [118] R. J. Thompson and T. M. Moeller, “Classical field isomorphisms in two-fluid plasmas,” *Physics of Plasmas*, vol. 19, no. 8, p. 082116, 2012.
- [119] R. J. Thompson and T. M. Moeller, “A {M}axwell formulation for the equations of a plasma,” *Physics of Plasmas*, vol. 19, no. 1, p. 10702, 2012.
- [120] R. Thompson and T. Moeller, “A Novel Set of Unified Maxwell Equations Describing Both Fluid and Electromagnetic Behavior,” in *43rd AIAA Plasmadynamics and Lasers Conference*, Fluid Dynamics and Co-located Conferences, American Institute of Aeronautics and Astronautics, June 2012.

- [121] S. M. Mahajan, “Temperature-Transformed “Minimal Coupling”: Magnetofluid Unification,” *Physical Review Letters*, vol. 90, p. 35001, Jan. 2003.
- [122] B. A. Bambah, S. M. Mahajan, and C. Mukku, “Yang-Mills Magnetofluid Unification,” *Physical Review Letters*, vol. 97, p. 72301, 2006.
- [123] Z. Yoshida, S. M. Mahajan, T. Mizushima, Y. Yano, H. Saitoh, and J. Morikawa, “Generalized two-fluid equilibria: Understanding RT-1 experiments and beyond,” *Physics of Plasmas*, vol. 17, p. 112507, 2010.
- [124] J. Pino, H. Li, and S. Mahajan, “Relaxed states in relativistic multifluid plasmas,” *Physics of Plasmas*, vol. 17, p. 112112, 2010.
- [125] G. Rousseaux, “On the physical meaning of the gauge conditions of Classical Electromagnetism : the hydrodynamics analogue viewpoint,” *Annales de la Fondation Louis de Broglie*, vol. 28, N02, pp. 261–269, 2003.
- [126] H. Yamada, T. Katano, A. Ishida, and L. C. Steinhauer, “Stability formalism of a flowing two-fluid plasma,” *PHYSICS OF PLASMAS*, vol. 10, pp. 1168–1171, Apr. 2003.
- [127] J. P. Goedbloed, “Variational principles for stationary one- and two-fluid equilibria of axisymmetric laboratory and astrophysical plasmas,” *PHYSICS OF PLASMAS*, vol. 11, pp. L81–L84, Dec. 2004.
- [128] M. J. Lighthill, “On Sound Generated Aerodynamically. I. General Theory,” *Proceedings of the Royal Society of London. Series A. Mathematical and Physical Sciences*, vol. 211, no. 1107, pp. 564–587, 1952.
- [129] M. J. Lighthill, “On Sound Generated Aerodynamically. II. Turbulence as a Source of Sound,” *Proceedings of the Royal Society of London. Series A. Mathematical and Physical Sciences*, vol. 222, no. 1148, pp. 1–32, 1954.
- [130] P. Croaker, N. Kessissoglou, R. Kinns, and S. Marburg, “Fast Low-Storage Method for Evaluating Lighthill’s Volume Quadrupoles,” *AIAA JOURNAL*, vol. 51, pp. 867–884, Apr. 2013.
- [131] J. B. Freund, “A simple method for computing far-field sound in aeroacoustic computations,” *JOURNAL OF COMPUTATIONAL PHYSICS*, vol. 157, pp. 796–800, Jan. 2000.
- [132] M. Kaltenbacher, M. Escobar, S. Becker, and I. Ali, “Numerical simulation of flow-induced noise using LES/SAS and Lighthill’s acoustic analogy,” *INTERNATIONAL JOURNAL FOR NUMERICAL METHODS IN FLUIDS*, vol. 63, pp. 1103–1122, July 2010.
- [133] M. Wang, S. K. Lele, and P. Moin, “Computation of quadrupole noise using acoustic analogy,” *AIAA JOURNAL*, vol. 34, pp. 2247–2254, Nov. 1996.

- [134] G. Russakoff, “No Title,” *American Journal of Physics*, vol. 38, p. 1188, 1970.
- [135] R. Thompson and T. Moeller, “Computational investigations of performance improvements for microlaser ablation plasma thrusters using nozzles,” *Plasma Science, IEEE Transactions on*, vol. 39, no. 11, pp. 2932–2933, 2011.
- [136] R. Thompson and T. M. Moeller, “Computer Simulations of Exothermic Propellants in a Microlaser Ablation Plasma Thruster,” *Journal of Propulsion and Power*, vol. 28, pp. 387–395, Mar. 2012.
- [137] C. Lanczos, *The Variational Principles of Mechanics*. Dover Books On Physics, DOVER PUBN Incorporated, 1970.
- [138] J. Schwinger, L. Deraad, and K. Milton, *Classical Electrodynamics*. Advanced book program, Westview Press, 1998.
- [139] M. Faraday, *Experimental researches in electricity*. No. v. 2 in Experimental Researches in Electricity, Richard and John Edward Taylor, printers and publishers to the University of London, 1844.
- [140] G. Rousseaux, S. Seifer, V. Steinberg, and A. Wiebel, “On the Lamb vector and the hydrodynamic charge,” *Experiments in Fluids*, vol. 42, no. 2, pp. 291–299, 2007.
- [141] R. B. DAHLBURG and J. M. PICONE, “EVOLUTION OF THE ORSZAG-TANG VORTEX SYSTEM IN A COMPRESSIBLE MEDIUM .1. INITIAL AVERAGE SUBSONIC FLOW,” *PHYSICS OF FLUIDS B-PLASMA PHYSICS*, vol. 1, pp. 2153–2171, Nov. 1989.
- [142] G.-S. Jiang and C.-c. Wu, “A High-Order {WENO} Finite Difference Scheme for the Equations of Ideal Magnetohydrodynamics,” *Journal of Computational Physics*, vol. 150, no. 2, pp. 561–594, 1999.
- [143] J. S. Shang and R. M. Fithen, “A comparative study of characteristic-based algorithms for the Maxwell equations,” *JOURNAL OF COMPUTATIONAL PHYSICS*, vol. 125, pp. 378–394, May 1996.
- [144] G. A. Sod, “A survey of several finite difference methods for systems of nonlinear hyperbolic conservation laws,” *Journal of Computational Physics*, vol. 27, no. 1, pp. 1 – 31, 1978.
- [145] M. Brio and C. C. Wu, “An Upwind Differencing Scheme for the Equations of Ideal Magnetohydrodynamics,” *Journal of Computational Physics*, vol. 75, pp. 400–422, 1988.
- [146] A. Quarteroni, R. Sacco, and F. Saleri, *Numerical Mathematics*. Texts in Applied Mathematics, Springer, 2007.

- [147] E. F. Toro and M. E. Vazquez-Cendon, “Flux splitting schemes for the Euler equations,” *COMPUTERS & FLUIDS*, vol. 70, pp. 1–12, Nov. 2012.
- [148] H. Schlichting and K. Gersten, *Boundary-Layer Theory*. Physic and astronomy, MacGraw-Hill, 2000.
- [149] Ames Research Staff, “Equations, tables, and charts for compressible flow,” naca rept. 1135, 1953.
- [150] S. Chandrasekhar, *Hidroynamics and Hidromagnetic Stability*. Dover Books on Physics Series, DOVER PUBN Incorporated, 1961.
- [151] R. J. LeVeque, *Finite Volume Methods for Hyperbolic Problems*. Cambridge Texts in Applied Mathematics, Cambridge University Press, 2002.
- [152] R. J. LeVeque, *Numerical Methods for Conservation Laws*. Lecture Notes in Mathematics, Birkhäuser Verlag AG, 1992.
- [153] E. F. Toro, *Riemann Solvers and Numerical Methods for Fluid Dynamics: A Practical Introduction*. Springer-Verlag Berlin Heidelberg, 2009.
- [154] P. Wesseling, *Principles of Computational Fluid Dynamics*. Springer Series in Computational Mathematics, Springer, 2009.
- [155] C. Hirsch, *Numerical Computation of Internal and External Flows: The Fundamentals of Computational Fluid Dynamics*. No. v. 1, Elsevier Science, 2007.
- [156] J. D. Anderson, *Computational Fluid Dynamics: The Basics With Applications*. McGraw-Hill Series in Aeronautical and Aerospace Engineering, McGraw-Hill Education, 1995.
- [157] J. H. Ferziger and M. Perić, *COMPUTATIONAL METHODS FOR FLUID DYNAMICS.: 2nd edition*. Springer-Verlag GmbH, 1999.
- [158] C. A. J. Fletcher, *Computational Techniques for Fluid Dynamics*. No. v. 1 in Computational Techniques for Fluid Dynamics, Berlin [etc.] : Springer-Verlag, 1991.
- [159] C. A. J. Fletcher, *Computational Techniques for Fluid Dynamics: Specific techniques for different flow categories*. No. v. 2 in Springer series in computational physics, Springer, 2000.
- [160] M. N. O. Sadiku, *Numerical Techniques in Electromagnetics, Second Edition*. Taylor & Francis, 2010.
- [161] A. Taflov and S. C. Hagness, *Computational Electrodynamics: The Finite-Difference Time-Domain Method*. The Artech House antenna and propagation library, Artech House, Incorporated, 2005.

- [162] U. Van Rienen, *Numerical Methods in Computational Electrodynamics: Linear Systems in Practical Applications*. Lecture Notes in Computational Science and Engineering, Springer Verlag, 2001.
- [163] S. K. Godunov, “A Difference Scheme for Numerical Solution of Discontinuous Solution for Hydrodynamic Equations,” *Math. Sbornik*, vol. 47, pp. 271—306, 1959.
- [164] B. Einfeldt, “On Godunov-Type Methods for Gas Dynamics,” *SIAM Journal on Numerical Analysis*, vol. 25, pp. 294–318, Apr. 1988.
- [165] E. F. Toro, M. Spruce, and W. Speares, “Restoration of the contact surface in the HLL-Riemann solver,” *Shock Waves*, vol. 4, no. 1, pp. 25–34, 1994.
- [166] A. L. Zachary and P. Colella, “A higher-order godunov method for the equations of ideal magnetohydrodynamics,” *Journal of Computational Physics*, vol. 99, no. 2, pp. 341–347, 1992.
- [167] W. Dai, “An approximate riemann solver for ideal magnetohydrodynamics,” *Journal of Computational Physics*, vol. 111, no. 2, pp. 354–372, 1994.
- [168] P. Cargo and G. Gallice, “Roe matrices for ideal MHD and systematic construction of roe matrices for systems of conservation laws,” *Journal of Computational Physics*, vol. 136, no. 2, pp. 446–466, 1997.
- [169] V. Honkkila and P. Janhunen, “HLLC solver for ideal relativistic MHD,” *Journal of Computational Physics*, vol. 223, no. 2, pp. 643–656, 2007.
- [170] P. Janhunen, “A Positive Conservative Method for Magnetohydrodynamics Based on HLL and Roe Methods,” *Journal of Computational Physics*, vol. 160, no. 2, pp. 649–661, 2000.
- [171] K. F. Gurski, “An HLLC-type approximate Riemann solver for ideal magnetohydrodynamics,” *SIAM Journal on Scientific Computing*, vol. 25, no. 6, pp. 2165–2187, 2004.
- [172] S. Li, “An HLLC Riemann solver for magneto-hydrodynamics,” *Journal of Computational Physics*, vol. 203, no. 1, pp. 344–357, 2005.
- [173] R. Agarwal, J. Augustinus, and D. Halt, “A comparative study of AUSM and WPS schemes for fluid and MHD flows,” in *30th Plasmadynamic and Lasers Conference*, Fluid Dynamics and Co-located Conferences, American Institute of Aeronautics and Astronautics, June 1999.
- [174] S.-H. Han, J.-I. Lee, and K. H. Kim, “Accurate and Robust Pressure Weight Advection Upstream Splitting Method for Magnetohydrodynamics Equations,” *AIAA Journal*, vol. 47, pp. 970–981, Apr. 2009.

- [175] Y. Shen, G. Zha, and M. Huerta, “E-CUSP Scheme for the Equations of Magnetohydrodynamics with High Order WENO Scheme,” in *49th AIAA Aerospace Sciences Meeting including the New Horizons Forum and Aerospace Exposition*, Aerospace Sciences Meetings, American Institute of Aeronautics and Astronautics, Jan. 2011.
- [176] Y. Shen, G. Zha, and M. A. Huerta, “E-CUSP scheme for the equations of ideal magnetohydrodynamics with high order WENO Scheme,” *JOURNAL OF COMPUTATIONAL PHYSICS*, vol. 231, pp. 6233–6247, Aug. 2012.
- [177] J. S. Shang and D. Gaitonde, “Characteristic-based, time-dependent Maxwell equation solvers on a general curvilinear frame,” *AIAA Journal*, vol. 33, pp. 491–498, Mar. 1995.
- [178] C. D. Munz, R. Schneider, and U. Voss, “A finite-volume method for the Maxwell equations in the time domain,” *SIAM JOURNAL ON SCIENTIFIC COMPUTING*, vol. 22, pp. 449–475, Aug. 2000.
- [179] V. SHANKAR, W. HALL, and A. MOHAMMADIAN, “A CFD-based finite-volume procedure for computational electromagnetics - Interdisciplinary applications of CFD methods,” in *9th Computational Fluid Dynamics Conference*, Fluid Dynamics and Co-located Conferences, American Institute of Aeronautics and Astronautics, June 1989.
- [180] V. SHANKAR, A. MOHAMMADIAN, W. HALL, and R. O. Y. ERICKSON, “CFD spinoff - Computational electromagnetics for radar cross section(RCS) studies,” in *Flight Simulation Technologies Conference and Exhibit*, Guidance, Navigation, and Control and Co-located Conferences, American Institute of Aeronautics and Astronautics, Sept. 1990.
- [181] Y. Weber, K. Hill, and J. Young, “The application of finite-volume, time-domain techniques to EM scattering from cavities and inlets,” in *27th Plasma Dynamics and Lasers Conference*, Fluid Dynamics and Co-located Conferences, American Institute of Aeronautics and Astronautics, June 1996.
- [182] M. VINOKUR and M. YARROW, “Finite-surface method for the Maxwell equations in generalized coordinates,” in *31st Aerospace Sciences Meeting*, Aerospace Sciences Meetings, American Institute of Aeronautics and Astronautics, Jan. 1993.
- [183] C. Merkle, D. Li, and V. Sankaran, “Multi-Disciplinary Computational Analysis in Propulsion,” in *42nd AIAA/ASME/SAE/ASEE Joint Propulsion Conference & Exhibit*, Joint Propulsion Conferences, American Institute of Aeronautics and Astronautics, July 2006.
- [184] T. Moeller; D. Keefer; R. Rhodes; D. Rooney; C. Merkle, “Comparison of Experimental and Computational Simulations Results of a Pulsed Plasma Accelerator,” in *29th International Electric Propulsion Conference, Princeton University, NJ*, 2005.

- [185] X. Zeng, S. Venkateswaran, and C. Merkle, “Designing Dual-Time Algorithms for Steady-State Calculations,” in *16th AIAA Computational Fluid Dynamics Conference*, Fluid Dynamics and Co-located Conferences, American Institute of Aeronautics and Astronautics, June 2003.
- [186] B. Srinivasan and U. Shumlak, “Analytical and computational study of the ideal full two-fluid plasma model and asymptotic approximations for Hall-magnetohydrodynamics,” *Physics of Plasmas*, vol. 18, p. 92113, 2011.
- [187] J. Loverich, “A Finite Volume Algorithm for the Two-Fluid Plasma System in One Dimension,” Master’s thesis, University of Washington, 2003.
- [188] K. Miura and C. Groth, “Development of Two-Fluid Magnetohydrodynamics Model for Non-Equilibrium Anisotropic Plasma Flows,” in *38th AIAA Plasmadynamics and Lasers Conference*, Fluid Dynamics and Co-located Conferences, American Institute of Aeronautics and Astronautics, June 2007.
- [189] A. G. Kulikovskii, N. V. Pogorelov, and A. Y. Semenov, *Mathematical Aspects of Numerical Solution of Hyperbolic Systems*. CRC Press LLC, 2001.
- [190] D. Giordano, “Hypersonic-Flow Governing Equations with Electromagnetic Fields,” in *33rd Plasmadynamics and Lasers Conference*, Fluid Dynamics and Co-located Conferences, American Institute of Aeronautics and Astronautics, May 2002.
- [191] J. U. BRACKBILL and D. C. BARNES, “THE EFFECT OF NONZERO-DEL.B ON THE NUMERICAL-SOLUTION OF THE MAGNETO-HYDRODYNAMIC EQUATIONS,” *JOURNAL OF COMPUTATIONAL PHYSICS*, vol. 35, no. 3, pp. 426–430, 1980.
- [192] Wolfram Research, Inc., *Mathematica Version 9.0.1*. Natick, Massachusetts: Champaign, Illinois, 2013.
- [193] A. L. Scandaliato and M.-S. Liou, “AUSM-Based High-Order Solution for Euler Equations,” *COMMUNICATIONS IN COMPUTATIONAL PHYSICS*, vol. 12, pp. 1096–1120, Oct. 2012.
- [194] M.-S. Liou, “The Evolution of AUSM Schemes,” *DEFENCE SCIENCE JOURNAL*, vol. 60, pp. 606–613, Nov. 2010.
- [195] M.-S. Liou, “Ten years in the making - AUSM-family,” in *15th AIAA Computational Fluid Dynamics Conference*, Fluid Dynamics and Co-located Conferences, American Institute of Aeronautics and Astronautics, June 2001.
- [196] J.-P. Bérenger, “Perfectly matched layer (pml) for computational electromagnetics,” *Synthesis Lectures on Computational Electromagnetics*, vol. 2, no. 1, pp. 1–117, 2007.

- [197] B. van Leer, "Towards the ultimate conservative difference scheme. V. A second-order sequel to Godunov's method," *Journal of Computational Physics*, vol. 32, pp. 101–136, July 1979.
- [198] P. L. Roe, "Characteristic-Based Schemes for the Euler Equations," *Annual Review of Fluid Mechanics*, vol. 18, pp. 337–365, Jan. 1986.
- [199] G. D. van Albada, B. van Leer, and W. W. Roberts Jr., "A comparative study of computational methods in cosmic gas dynamics," *Astron. Astrophysics*, vol. 108, pp. 76–84, Apr. 1982.
- [200] S. ORSZAG and C. TANG, "SMALL-SCALE STRUCTURE OF 2-DIMENSIONAL MAGNETOHYDRODYNAMIC TURBULENCE," *JOURNAL OF FLUID MECHANICS*, vol. 90, no. JAN, pp. 129–143, 1979.
- [201] J. Brackbill, "Fluid modeling of magnetized plasmas," *Space Science Reviews*, vol. 42, no. 1-2, pp. 153–167, 1985.
- [202] D. Balsara and D. Spicer, "A staggered mesh algorithm using high order godunov fluxes to ensure solenoidal magnetic fields in magnetohydrodynamic simulations," *Journal of Computational Physics*, vol. 149, no. 2, pp. 270–292, 1999. cited By (since 1996)197.

Appendix

A.1 Derivation of the Two-fluid Maxwell Equations

This section presents the mathematical details for transforming the two-fluid plasmadynamic equations into a Maxwell form. We start with equation 3.15, in Section 3.3, and calculate the divergence, curl and time derivative of this equation to produce the Gauss, Faraday and Ampere-Maxwell equations, respectively. The final equation, analogous to a statement of no magnetic monopoles, is satisfied by vector identity.

A.1.1 Gauss Laws

The divergence of equation 3.15 is straightforward. We will introduce a new quantity $\varrho_{P,\alpha}$ here; our motivation for doing so will be revealed shortly.

$$\nabla \cdot \zeta_\alpha = \nabla \cdot \left\{ -\frac{\partial \mathbf{P}}{\partial t} - \nabla \mathcal{E}_\alpha^T \right\} \quad (\text{A.1})$$

$$= -\frac{\partial}{\partial t} \nabla \cdot \mathbf{P}_\alpha - \nabla^2 \mathcal{E}_\alpha^T \quad (\text{A.2})$$

$$= -\frac{\partial}{\partial t} \nabla \cdot \left(\mathbf{u}_\alpha + \frac{e_\alpha}{m_\alpha} \mathbf{A} \right) - \nabla^2 \left(H_\alpha + \frac{e_\alpha}{m_\alpha} \phi \right) \quad (\text{A.3})$$

$$= -\frac{\partial}{\partial t} (\nabla \cdot \mathbf{u}_\alpha) - \nabla^2 (H_\alpha) + \frac{e_\alpha}{m_\alpha} \nabla \cdot \left\{ -\frac{\partial \mathbf{A}}{\partial t} - \nabla \phi \right\} \quad (\text{A.4})$$

$$= -\frac{\partial}{\partial t} (\nabla \cdot \mathbf{u}_\alpha) - \nabla^2 (H_\alpha) + \frac{e_\alpha}{m_\alpha} \nabla \cdot \mathbf{E} \quad (\text{A.5})$$

$$\nabla \cdot \zeta_\alpha = -\frac{\partial}{\partial t} (\nabla \cdot \mathbf{u}_\alpha) - \nabla^2 (H_\alpha) + \frac{e_\alpha}{m_\alpha} \frac{\varrho_e}{\epsilon_0} \quad (\text{A.6})$$

$$\nabla \cdot \zeta_\alpha = \varrho_{P,\alpha} \quad (\text{A.7})$$

where we have introduced the simplification

$$\varrho_{P,\alpha} = -\frac{\partial}{\partial t} (\nabla \cdot \mathbf{u}_\alpha) - \nabla^2 H_\alpha + \frac{e_\alpha}{m_\alpha} \frac{\varrho_e}{\epsilon_0} \quad (\text{A.8})$$

The Gauss law for the generalized vorticity may be realized by simple vector identity,

$$\nabla \cdot \boldsymbol{\Omega}_\alpha = \nabla \cdot \nabla \times \mathbf{P}_\alpha = 0 \quad (\text{A.9})$$

A.1.2 Faraday Law

The curl of equation 3.15 is also not a complicated matter. We have

$$\nabla \times \zeta_\alpha = \nabla \times \left\{ -\frac{\partial \mathbf{P}_\alpha}{\partial t} - \nabla \mathcal{E}_\alpha^T \right\} \quad (\text{A.10})$$

$$= -\frac{\partial}{\partial t} \nabla \times \mathbf{P}_\alpha - \nabla \times \nabla \mathcal{E}_\alpha^T \quad (\text{A.11})$$

$$\nabla \times \zeta_\alpha = -\frac{\partial \boldsymbol{\Omega}_\alpha}{\partial t} \quad (\text{A.12})$$

A.1.3 First Ampere-Maxwell Law

The time derivative of equation 3.15 is unfortunately a very tedious calculation. We start by determining it directly, and then manipulate it into the form we seek by continued application of vector identities. Starting by directly differentiating the general Euler equation given by equation 3.15, we have

$$\frac{\partial \zeta_\alpha}{\partial t} = \frac{\partial}{\partial t} \left\{ -\frac{\partial \mathbf{P}_\alpha}{\partial t} - \nabla \mathcal{E}_\alpha^T \right\} \quad (\text{A.13})$$

$$= -\frac{\partial^2 \mathbf{P}}{\partial t^2} - \nabla \frac{\partial \mathcal{E}_\alpha^T}{\partial t} \quad (\text{A.14})$$

$$= -\frac{\partial^2 \mathbf{u}_\alpha}{\partial t^2} - \frac{e_\alpha}{m_\alpha} \frac{\partial^2 \mathbf{A}}{\partial t^2} - \nabla \frac{\partial h_\alpha}{\partial t} - \nabla \frac{\partial}{\partial t} ((1/2) \mathbf{u}_\alpha \cdot \mathbf{u}_\alpha) - \frac{e_\alpha}{m_\alpha} \nabla \phi \quad (\text{A.15})$$

$$= -\frac{\partial^2 \mathbf{u}_\alpha}{\partial t^2} + \frac{\partial}{\partial t} \left[\frac{e_\alpha}{m_\alpha} \left(-\frac{\partial \mathbf{A}}{\partial t} - \nabla \phi \right) \right] - \nabla \frac{\partial h_\alpha}{\partial t} - \nabla \frac{\partial}{\partial t} ((1/2) \mathbf{u}_\alpha \cdot \mathbf{u}_\alpha) \quad (\text{A.16})$$

$$= -\frac{\partial^2 \mathbf{u}_\alpha}{\partial t^2} + \frac{e_\alpha}{m_\alpha} \frac{\partial \mathbf{E}}{\partial t} - \nabla \frac{\partial h_\alpha}{\partial t} - \nabla \frac{\partial}{\partial t} ((1/2) \mathbf{u}_\alpha \cdot \mathbf{u}_\alpha) \quad (\text{A.17})$$

Now we take the gradient of the continuity equation in terms of enthalpy, equation 3.5, and substitute the result in for the third term on the right-hand side,

$$= -\frac{\partial^2 \mathbf{u}_\alpha}{\partial t^2} + \frac{e_\alpha}{m_\alpha} \frac{\partial \mathbf{E}}{\partial t} + \nabla (\mathbf{u}_\alpha \cdot \nabla h_\alpha) + \nabla (a_\alpha^2 \nabla \cdot \mathbf{u}) - \nabla \frac{\partial}{\partial t} ((1/2) \mathbf{u}_\alpha \cdot \mathbf{u}_\alpha) \quad (\text{A.18})$$

We insert the Ampere-Maxwell equation in for the $\partial \mathbf{E} / \partial t$ term,

$$= -\frac{\partial^2 \mathbf{u}_\alpha}{\partial t^2} + \frac{e_\alpha}{m_\alpha} \left\{ -\frac{\mathbf{j}_e}{\epsilon_0} + c_0^2 \nabla \times \mathbf{B} \right\} + \nabla (\mathbf{u}_\alpha \cdot \nabla h_\alpha) + \nabla (a_\alpha^2 \nabla \cdot \mathbf{u}_\alpha) - \nabla \frac{\partial}{\partial t} ((1/2) \mathbf{u}_\alpha \cdot \mathbf{u}_\alpha) \quad (\text{A.19})$$

$$= -\frac{\partial^2 \mathbf{u}_\alpha}{\partial t^2} - \frac{e_\alpha}{m_\alpha} \frac{\mathbf{j}_e}{\epsilon_0} + \frac{e_\alpha}{m_\alpha} c_0^2 \nabla \times \nabla \times \mathbf{A} + \nabla (\mathbf{u}_\alpha \cdot \nabla h_\alpha) + \nabla (a_\alpha^2 \nabla \cdot \mathbf{u}_\alpha) - \nabla \frac{\partial}{\partial t} ((1/2) \mathbf{u}_\alpha \cdot \mathbf{u}_\alpha) \quad (\text{A.20})$$

Now we can split up the term $\nabla (a_\alpha^2 \nabla \cdot \mathbf{u}_\alpha)$,

$$\nabla (a_\alpha^2 \nabla \cdot \mathbf{u}_\alpha) = (\nabla \cdot \mathbf{u}_\alpha) \nabla a_\alpha^2 + a_\alpha^2 \nabla (\nabla \cdot \mathbf{u}_\alpha) \quad (\text{A.21})$$

We can apply the vector identity

$$a_\alpha^2 \nabla (\nabla \cdot \mathbf{u}_\alpha) = a_\alpha^2 \nabla \times \nabla \times \mathbf{u}_\alpha + a_\alpha^2 \nabla^2 \mathbf{u}_\alpha = a_\alpha^2 \nabla \times \boldsymbol{\omega}_\alpha + a_\alpha^2 \nabla^2 \mathbf{u}_\alpha \quad (\text{A.22})$$

to the second term on the right-hand side, which gives us a final form of equation A.20 as

$$\begin{aligned} &= -\frac{\partial^2 \mathbf{u}_\alpha}{\partial t^2} - \frac{e_\alpha}{m_\alpha} \frac{\mathbf{j}_e}{\epsilon_0} + \frac{e_\alpha}{m_\alpha} c_0^2 \nabla \times \nabla \times \mathbf{A} + \nabla (\mathbf{u}_\alpha \cdot \nabla h_\alpha) \\ &\quad + (\nabla \cdot \mathbf{u}_\alpha) \nabla a_\alpha^2 + a_\alpha^2 \nabla \times \boldsymbol{\omega}_\alpha + a_\alpha^2 \nabla^2 \mathbf{u}_\alpha - \nabla \frac{\partial}{\partial t} ((1/2) \mathbf{u}_\alpha \cdot \mathbf{u}_\alpha) \end{aligned} \quad (\text{A.23})$$

We can rewrite this in a simplified form as

$$\frac{\partial \zeta_\alpha}{\partial t} = -\mathbf{j}_\alpha + a_\alpha^2 \nabla \times \boldsymbol{\omega}_\alpha + c_0^2 \nabla \times \left(\frac{e_\alpha}{m_\alpha} \mathbf{B} \right) \quad (\text{A.24})$$

where we have introduced the substitution

$$-\mathbf{j}_\alpha = -\frac{\partial^2 \mathbf{u}_\alpha}{\partial t^2} - \frac{e_\alpha}{m_\alpha} \frac{\mathbf{j}_e}{\epsilon_0} + \nabla (\mathbf{u}_\alpha \cdot \nabla h_\alpha) + (\nabla \cdot \mathbf{u}_\alpha) \nabla a_\alpha^2 + a_\alpha^2 \nabla^2 \mathbf{u}_\alpha - \nabla \frac{\partial}{\partial t} ((1/2) \mathbf{u}_\alpha \cdot \mathbf{u}_\alpha) \quad (\text{A.25})$$

Equation A.24 is still not quite in the form we wish, so we add a term $v_\alpha^2 \nabla \times \boldsymbol{\Omega}_\alpha$, where v_α is some speed that we will choose shortly. Adding this to both sides of equation A.24, we have

$$\frac{\partial \zeta_\alpha}{\partial t} + \mathbf{j}_\alpha = v_\alpha^2 \nabla \times \boldsymbol{\Omega}_\alpha \quad (\text{A.26})$$

where now we have modified our substitution,

$$\begin{aligned} \mathbf{j}_\alpha = & \frac{\partial^2 \mathbf{u}_\alpha}{\partial t^2} - a_\alpha^2 \nabla^2 \mathbf{u}_\alpha + \frac{e_\alpha}{m_\alpha} \frac{\mathbf{j}_e}{\epsilon_0} - \nabla (\mathbf{u}_\alpha \cdot \nabla h_\alpha) - (\nabla \cdot \mathbf{u}_\alpha) \nabla a_\alpha^2 \\ & + \nabla \frac{\partial}{\partial t} ((1/2) \mathbf{u}_\alpha \cdot \mathbf{u}_\alpha) + (v_\alpha^2 - a_\alpha^2) \nabla \times \boldsymbol{\omega}_\alpha + (v_\alpha^2 - c_0^2) \nabla \times \mathbf{B} \end{aligned} \quad (\text{A.27})$$

A.1.4 Second Ampere-Maxwell Law

Although it may initially seem unnecessary, we can derive equation A.26 in a very different fashion. This approach unites the generalized form with the previous incompressible work. We start by taking the time derivative of the generalized Lamb vector, ζ_α ,

$$\frac{\partial \zeta_\alpha}{\partial t} = \frac{\partial}{\partial t} (\boldsymbol{\Omega}_\alpha \times \mathbf{u}_\alpha) = \frac{\partial \boldsymbol{\Omega}_\alpha}{\partial t} \times \mathbf{u}_\alpha + \boldsymbol{\Omega}_\alpha \times \frac{\partial \mathbf{u}_\alpha}{\partial t} \quad (\text{A.28})$$

$$= \mathbf{u}_\alpha \times [\nabla \times (\boldsymbol{\Omega}_\alpha \times \mathbf{u}_\alpha)] + \boldsymbol{\Omega}_\alpha \times \frac{\partial \mathbf{u}_\alpha}{\partial t} \quad (\text{A.29})$$

We can now apply the following vector identity,

$$\mathbf{u}_\alpha \times (\nabla \times \zeta_\alpha) = -\mathbf{u}_\alpha \cdot \zeta_\alpha - \zeta_\alpha \cdot \nabla \mathbf{u}_\alpha - \zeta_\alpha \times (\nabla \times \mathbf{u}_\alpha) + \nabla (\mathbf{u}_\alpha \cdot \zeta_\alpha) \quad (\text{A.30})$$

The curl in the third term on the right-hand side is just the fluid vorticity, $\nabla \times \mathbf{u}_\alpha = \boldsymbol{\omega}_\alpha$. Since \mathbf{u}_α and $\zeta_\alpha = \boldsymbol{\Omega}_\alpha \times \mathbf{u}_\alpha$ are perpendicular, the last term on the right-hand side vanishes. By further recognizing the vector identity

$$\nabla \times (\zeta_\alpha \times \mathbf{u}_\alpha) = \zeta_\alpha \nabla \cdot \mathbf{u}_\alpha - \mathbf{u}_\alpha \cdot \zeta_\alpha + \mathbf{u}_\alpha \cdot \nabla \zeta_\alpha - \zeta_\alpha \cdot \nabla \mathbf{u}_\alpha \quad (\text{A.31})$$

and substituting this into equation A.30 to eliminate the term $-\mathbf{u}_\alpha \cdot \nabla \zeta_\alpha$, equation A.30 now becomes

$$\mathbf{u}_\alpha \times (\nabla \times \zeta_\alpha) = \nabla \times (\mathbf{u}_\alpha \times \zeta_\alpha) - \mathbf{u}_\alpha \nabla \cdot \zeta_\alpha + \zeta_\alpha \nabla \cdot \mathbf{u}_\alpha - 2\zeta_\alpha \cdot \nabla \mathbf{u}_\alpha - \zeta_\alpha \times \omega_\alpha \quad (\text{A.32})$$

Substitution of equation A.32 into equation A.29 yields

$$\frac{\partial \zeta_\alpha}{\partial t} = \nabla \times (\mathbf{u}_\alpha \times \zeta_\alpha) - \mathbf{u}_\alpha \nabla \cdot \zeta_\alpha + \zeta_\alpha \nabla \cdot \mathbf{u}_\alpha - 2\zeta_\alpha \cdot \nabla \mathbf{u}_\alpha - \zeta_\alpha \times \omega_\alpha + \Omega_\alpha \times \frac{\partial \mathbf{u}_\alpha}{\partial t} \quad (\text{A.33})$$

Now the first term on the right-hand side introduces the curl of the generalized vorticity. To see how, we rewrite $\mathbf{u}_\alpha \times \zeta_\alpha = \mathbf{u}_\alpha \times (\Omega_\alpha \times \mathbf{u}_\alpha)$ and apply the vector identity

$$\mathbf{u}_\alpha \times (\Omega_\alpha \times \mathbf{u}_\alpha) = (\mathbf{u}_\alpha \cdot \mathbf{u}_\alpha) \Omega_\alpha - (\mathbf{u}_\alpha \cdot \Omega_\alpha) \mathbf{u}_\alpha \quad (\text{A.34})$$

Thus, the first term on the right-hand side becomes

$$\nabla \times (\mathbf{u}_\alpha \times \zeta_\alpha) = \nabla \times [u_\alpha^2 \Omega_\alpha - (\mathbf{u}_\alpha \cdot \Omega_\alpha) \mathbf{u}_\alpha] \quad (\text{A.35})$$

$$= u_\alpha^2 \nabla \times \Omega_\alpha + \nabla (u_\alpha^2) \times \Omega_\alpha - \nabla \times [(\mathbf{u}_\alpha \cdot \Omega_\alpha) \mathbf{u}_\alpha] \quad (\text{A.36})$$

Substituting this identity into equation A.33, and substituting $\nabla \cdot \zeta_\alpha = \varrho_\alpha$ via equation A.7, we have

$$\begin{aligned} \frac{\partial \zeta_\alpha}{\partial t} + \left\{ \varrho_\alpha \mathbf{u}_\alpha - \zeta_\alpha \nabla \cdot \mathbf{u}_\alpha + 2\zeta_\alpha \cdot \nabla \mathbf{u}_\alpha + \zeta_\alpha \times \Omega_\alpha - \Omega_\alpha \times \frac{\partial \mathbf{u}_\alpha}{\partial t} + \nabla \times [(\mathbf{u}_\alpha \cdot \Omega_\alpha) \mathbf{u}_\alpha] \right\} \\ = u_\alpha^2 \nabla \times \Omega_\alpha \end{aligned} \quad (\text{A.37})$$

or, making a substitution \mathbf{j}'_α , we have

$$\frac{\partial \zeta_\alpha}{\partial t} + \mathbf{j}'_\alpha = u_\alpha^2 \nabla \times \Omega_\alpha \quad (\text{A.38})$$

with

$$\mathbf{j}'_\alpha = \varrho_\alpha \mathbf{u}_\alpha - \zeta_\alpha \nabla \cdot \mathbf{u}_\alpha + 2\zeta_\alpha \cdot \nabla \mathbf{u}_\alpha + \zeta_\alpha \times \Omega_\alpha - \Omega_\alpha \times \frac{\partial \mathbf{u}_\alpha}{\partial t} + \nabla \times [(\mathbf{u}_\alpha \cdot \Omega_\alpha) \mathbf{u}_\alpha] \quad (\text{A.39})$$

Clearly, equation A.38 is in the same form as equation A.26, except that the speed v_α has been chosen as the local fluid velocity, u_α .

We are finally in a position to state the Maxwell equations for the two-fluid dynamical variables, ζ_α and Ω_α . Collecting our results in equations A.7, A.12 and A.26, and identifying by vector identity that the

divergence of the generalized vorticity must always be zero, $\nabla \cdot \Omega_\alpha = \nabla \cdot \nabla \times \mathbf{P}_\alpha \equiv 0$, we have

$$\nabla \cdot \Omega_\alpha = 0 \quad (\text{A.40})$$

$$\nabla \cdot \zeta_\alpha = \varrho_\alpha \quad (\text{A.41})$$

$$\frac{\partial \Omega_\alpha}{\partial t} + \nabla \times \zeta_\alpha = 0 \quad (\text{A.42})$$

$$\frac{\partial \zeta_\alpha}{\partial t} + \mathbf{j}_\alpha = v_\alpha^2 \nabla \times \Omega_\alpha \quad (\text{A.43})$$

where ϱ_α is given by the right-hand side of equation A.7, \mathbf{j}_α is given by equation A.27, and v_α is some speed that we may select. In the case of choosing $v_\alpha = u_\alpha$, we have an alternate form of the current given by equation A.39.

A.2 Jacobians and Eigenstructure of the Navier-Stokes Equations

This section is devoted to providing mathematical details regarding the uncoupled inviscid Navier-Stokes equations. Excellent reviews of these equations and the information covered here is presented in [11, 151, 153, 156]. Here we consider the equations in the form

$$\frac{\partial \varrho}{\partial t} + \nabla \cdot (\varrho \mathbf{u}) = 0 \quad (\text{A.44})$$

$$\frac{\partial}{\partial t} (\varrho \mathbf{u}) + \nabla \cdot (\varrho \mathbf{u} \mathbf{u} + \hat{\mathbf{l}} p) = 0 \quad (\text{A.45})$$

$$\frac{\partial \mathcal{E}}{\partial t} + \nabla \cdot ([\mathcal{E} + p] \mathbf{u}) = 0 \quad (\text{A.46})$$

which represent the conservation of mass, momentum and energy in the fluid. Here ϱ , \mathbf{u} , \mathcal{E} , p , and $\hat{\mathbf{l}}$ are the mass density, velocity vector, total energy, pressure, and identity matrix, respectively. The equation of state is supplied by assuming an ideal gas, $p = \varrho R_{\text{gas}} T$. The total energy is taken as

$$\mathcal{E} = \varrho e + \frac{1}{2} \varrho \mathbf{u} \cdot \mathbf{u} \quad (\text{A.47})$$

where e is the internal energy. We assume the gas is calorically perfect, such that

$$e = \frac{p}{\varrho(\gamma - 1)} \quad (\text{A.48})$$

We may recast these equations into a system of first-order conservation laws,

$$\frac{\partial \mathbf{U}_f}{\partial t} + \nabla \cdot \mathbf{F}_f = 0 \quad (\text{A.49})$$

where

$$\mathbf{U}_f = \begin{Bmatrix} \varrho \\ \varrho \mathbf{u} \\ \mathcal{E} \end{Bmatrix}, \quad \mathbf{F}_f = \begin{Bmatrix} \varrho \mathbf{u} \\ \varrho \mathbf{u} \mathbf{u} + \hat{\mathbf{l}} p \\ [\mathcal{E} + p] \mathbf{u} \end{Bmatrix} \quad (\text{A.50})$$

The subscript f is used to denote that this is the fluid set of equations.

A.2.1 Jacobian Matrix

There are three jacobian matrices for the Navier-Stokes equations (one for each spatial dimension). They are explicitly exposed if we write the system of equations as

$$\frac{\partial \mathbf{U}_f}{\partial t} + \frac{\partial \mathbf{F}_{f,x}}{\partial x} + \frac{\partial \mathbf{F}_{f,y}}{\partial y} + \frac{\partial \mathbf{F}_{f,z}}{\partial z} = 0 \quad (\text{A.51})$$

Recasting this equation into the quasilinear form as discussed in Section 5.7, we have

$$\frac{\partial \mathbf{U}_f}{\partial t} + \hat{\mathbf{A}}_{f,x} \frac{\partial \mathbf{U}_f}{\partial x} + \hat{\mathbf{A}}_{f,y} \frac{\partial \mathbf{U}_f}{\partial y} + \hat{\mathbf{A}}_{f,z} \frac{\partial \mathbf{U}_f}{\partial z} = 0 \quad (\text{A.52})$$

where $\hat{\mathbf{A}}_{f,x} = \partial \mathbf{F}_{f,x} / \partial \mathbf{U}_f$, $\hat{\mathbf{A}}_{f,y} = \partial \mathbf{F}_{f,y} / \partial \mathbf{U}_f$, and $\hat{\mathbf{A}}_{f,z} = \partial \mathbf{F}_{f,z} / \partial \mathbf{U}_f$ are the jacobian matrices. They may be written analytically as

$$\hat{\mathbf{A}}_{f,x} = \begin{Bmatrix} 0 & 1 & 0 & 0 & 0 \\ \hat{\gamma} H - u^2 - a^2 & (3 - \gamma) u & -\hat{\gamma} v & -\hat{\gamma} w & \hat{\gamma} \\ -uv & v & u & 0 & 0 \\ -uw & w & 0 & u & 0 \\ u \left(\frac{\hat{\gamma}}{2} V^2 - H \right) & H - \hat{\gamma} u^2 & -\hat{\gamma} uv & -\hat{\gamma} uw & \gamma u \end{Bmatrix} \quad (\text{A.53})$$

$$\hat{\mathbf{A}}_{f,y} = \begin{Bmatrix} 0 & 0 & 1 & 0 & 0 \\ -uv & v & u & 0 & 0 \\ \hat{\gamma} H - v^2 - a^2 & -\hat{\gamma} u & (3 - \gamma) v & -\hat{\gamma} w & \hat{\gamma} \\ -vw & 0 & w & v & 0 \\ v \left(\frac{\hat{\gamma}}{2} V^2 - H \right) & -\hat{\gamma} uv & H - \hat{\gamma} v^2 & -\hat{\gamma} vw & \gamma v \end{Bmatrix} \quad (\text{A.54})$$

$$\hat{\mathbf{A}}_{f,z} = \begin{Bmatrix} 0 & 0 & 0 & 1 & 0 \\ -uw & w & 0 & u & 0 \\ -vw & 0 & w & v & 0 \\ \hat{\gamma} H - w^2 - a^2 & -\hat{\gamma} u & -\hat{\gamma} v & (3 - \gamma) w & \hat{\gamma} \\ w \left(\frac{\hat{\gamma}}{2} V^2 - H \right) & -\hat{\gamma} uw & -\hat{\gamma} vw & H - \hat{\gamma} w^2 & \gamma w \end{Bmatrix} \quad (\text{A.55})$$

where $\mathbf{u} = (u, v, w)$, $\hat{\gamma} = \gamma - 1$, $V^2 = u^2 + v^2 + w^2$, and H is the total enthalpy, $H = (\mathcal{E} + p)/\varrho$.

We can also express the jacobian matrix for the direction of interest, indicated by the face normal vector, \mathbf{n} , as a normal-projected matrix. This compact representation can be written

$$\hat{\mathbf{A}}_f = \begin{pmatrix} 0 & \mathbf{n} & 0 \\ \frac{\gamma}{2}V^2\mathbf{n} - q\mathbf{u} & \mathbf{u}\mathbf{n} - \hat{\gamma}\mathbf{n}\mathbf{u} + \hat{\mathbf{l}}q & \hat{\gamma}\mathbf{n} \\ q(\hat{\gamma}V^2 - H) & H\mathbf{n} - \hat{\gamma}q\mathbf{u} & \gamma q \end{pmatrix} \quad (\text{A.56})$$

where $\mathbf{n} = (n_x, n_y, n_z)$ represents the normal projection and q is the projection of the velocity onto the normal, $q = \mathbf{u} \cdot \mathbf{n} = un_x + vn_y + wn_z$.

A.2.2 Eigenvalues

The eigenvalues of $\hat{\mathbf{A}}_f$ can be determined analytically as

$$\hat{\Lambda}_f = \text{Diag}\{q - a, q, q, q, q + a\} = \begin{pmatrix} q - a & 0 & 0 & 0 & 0 \\ 0 & q & 0 & 0 & 0 \\ 0 & 0 & q & 0 & 0 \\ 0 & 0 & 0 & q & 0 \\ 0 & 0 & 0 & 0 & q + a \end{pmatrix} \quad (\text{A.57})$$

where $q = \mathbf{u} \cdot \mathbf{n} = un_x + vn_y + wn_z$ and a is the sonic speed, $a^2 = \gamma p / \varrho$.

A.2.3 Eigenvectors

The eigenvectors of $\hat{\mathbf{A}}_f$ can be computed from the jacobian matrices. The *eigenmatrix*, $\hat{\mathbf{K}}_f$, is a matrix composed of column right eigenvectors. There is one eigenmatrix per each dimension. If the Navier-Stokes equations are written with explicit flux terms per each dimension, as in equation A.51, then the three jacobian matrices $\hat{\mathbf{A}}_{f,x}$, $\hat{\mathbf{A}}_{f,y}$, and $\hat{\mathbf{A}}_{f,z}$ will have corresponding eigenmatrices $\hat{\mathbf{K}}_{f,x}$, $\hat{\mathbf{K}}_{f,y}$, and $\hat{\mathbf{K}}_{f,z}$, which are

$$\hat{\mathbf{K}}_{f,x} = \begin{pmatrix} 1 & 1 & 0 & 0 & 1 \\ u - a & u & 0 & 0 & u + a \\ v & v & 1 & 0 & v \\ w & w & 0 & 1 & w \\ H - ua & \frac{1}{2}V^2 & v & w & H + ua \end{pmatrix} \quad (\text{A.58})$$

$$\hat{\mathbf{K}}_{f,y} = \begin{pmatrix} 1 & 0 & 1 & 0 & 1 \\ u & 1 & u & 0 & u \\ v-a & 0 & v & 0 & v+a \\ w & 0 & w & 1 & w \\ H-va & u & \frac{1}{2}V^2 & w & H+va \end{pmatrix} \quad (\text{A.59})$$

$$\hat{\mathbf{K}}_{f,z} = \begin{pmatrix} 1 & 0 & 0 & 1 & 1 \\ u & 1 & 0 & u & u \\ v & 0 & 1 & v & v \\ w-a & 0 & 0 & w & w+a \\ H-aw & u & v & \frac{1}{2}V^2 & H+aw \end{pmatrix} \quad (\text{A.60})$$

If the surface for the flux is on an arbitrary face with associated normal vector \mathbf{n} , then a compact form of the eigenvectors may be written as

$$\hat{\mathbf{K}}_f = \begin{pmatrix} 1 & \mathbf{n} & 1 \\ \mathbf{u} - a\mathbf{n} & \mathbf{a}'_i \mathbf{u} + \mathbf{b}_i & \mathbf{u} + a\mathbf{n} \\ H - qa & \frac{1}{2}V^2 \mathbf{a}'_i + \mathbf{b}_i \cdot \mathbf{u} & H + qa \end{pmatrix} \quad (\text{A.61})$$

where $\mathbf{a}'_i = \mathbf{n} \cdot \mathbf{a}_i$ and $\mathbf{b}_i = \mathbf{n} \times \mathbf{a}_i$, where \mathbf{a}_i are arbitrary spatial basis vectors (in our case, cartesian unit vectors).

A.2.4 Solution to the Linearized Riemann Problem

The Roe scheme requires a form of the decomposition coefficients, $\underline{\alpha}^{(p)}$, for the linearized Riemann problem. If the initial Riemann data consists of a piecewise discontinuous jump centered at $x = 0$,

$$\mathbf{U}(x, t = 0) = \begin{cases} \mathbf{U}_L, & x < 0 \\ \mathbf{U}_R, & x > 0 \end{cases} \quad (\text{A.62})$$

where \mathbf{U}_L and \mathbf{U}_R are known constant state vectors, then the solution, per the discussion in Section 5.7, can be written as an eigenvector expansion,

$$\Delta \mathbf{U} = \mathbf{U}_R - \mathbf{U}_L = \sum_{p=1}^m \alpha^{(p)} \mathbf{K}^{(p)} \quad (\text{A.63})$$

where $p \in \{1, \dots, m\}$ spans the set of m equations, α represents the decomposition coefficients, and $\mathbf{K}^{(p)}$ are the column right eigenvectors. Equation A.63 must be solved for its decomposition coefficients. For the Navier-Stokes equations, the solution may be determined analytically for each dimension. This gives in the

x -direction:

$$\begin{aligned}
\alpha_{f,x}^{(3)} &= \Delta \mathbf{U}_3 - \Delta \mathbf{U}_1 \underline{v} \\
\alpha_{f,x}^{(4)} &= \Delta \mathbf{U}_4 - \Delta \mathbf{U}_1 \underline{w} \\
\alpha_{f,x}^{(2)} &= 2\Delta \mathbf{U}_1 - \frac{\Delta \mathbf{U}_5 + \Delta \mathbf{U}_1 \underline{H} - (\Delta \mathbf{U}_2 \underline{u} + \Delta \mathbf{U}_3 \underline{v} + \Delta \mathbf{U}_4 \underline{w})}{\underline{H} - \frac{1}{2} \underline{V}^2} \\
\alpha_{f,x}^{(1)}, \alpha_{f,x}^{(5)} &= \frac{\pm (\underline{u} \mp \underline{a}) \Delta \mathbf{U}_1 + \Delta \mathbf{U}_2}{2\underline{a}} + \Delta \mathbf{U}_1 - \frac{\alpha_{x,2}}{2}
\end{aligned} \tag{A.64}$$

In the y direction,

$$\begin{aligned}
\alpha_{f,y}^{(2)} &= \Delta \mathbf{U}_2 - \Delta \mathbf{U}_1 \underline{u} \\
\alpha_{f,y}^{(4)} &= \Delta \mathbf{U}_4 - \Delta \mathbf{U}_1 \underline{w} \\
\alpha_{f,y}^{(3)} &= 2\Delta \mathbf{U}_1 - \frac{\Delta \mathbf{U}_5 + \Delta \mathbf{U}_1 \underline{H} - (\Delta \mathbf{U}_2 \underline{u} + \Delta \mathbf{U}_3 \underline{v} + \Delta \mathbf{U}_4 \underline{w})}{\underline{H} + \frac{1}{2} \underline{V}^2} \\
\alpha_{f,y}^{(1)}, \alpha_{f,y}^{(5)} &= \frac{(\pm \underline{v} \mp \underline{a}) \Delta \mathbf{U}_1 + \Delta \mathbf{U}_3}{2\underline{a}} + \Delta \mathbf{U}_1 - \frac{\alpha_{y,3}}{2}
\end{aligned} \tag{A.65}$$

In the z direction,

$$\begin{aligned}
\alpha_{f,z}^{(2)} &= \Delta \mathbf{U}_2 - \Delta \mathbf{U}_1 \underline{u} \\
\alpha_{f,z}^{(3)} &= \Delta \mathbf{U}_3 - \Delta \mathbf{U}_1 \underline{v} \\
\alpha_{f,z}^{(4)} &= 2\Delta \mathbf{U}_1 - \frac{\Delta \mathbf{U}_5 + \Delta \mathbf{U}_1 \underline{H} - (\Delta \mathbf{U}_2 \underline{u} + \Delta \mathbf{U}_3 \underline{v} + \Delta \mathbf{U}_4 \underline{w})}{\underline{H} - \frac{1}{2} \underline{V}^2} \\
\alpha_{f,z}^{(1)}, \alpha_{f,z}^{(5)} &= \frac{(\pm \underline{w} \mp \underline{a}) \Delta \mathbf{U}_1 + \Delta \mathbf{U}_4}{2\underline{a}} + \Delta \mathbf{U}_1 - \frac{\alpha_{z,3}}{2}
\end{aligned} \tag{A.66}$$

where \underline{u} , \underline{v} , \underline{w} , \underline{H} , \underline{a} , and $\underline{V}^2 = \underline{u}^2 + \underline{v}^2 + \underline{w}^2$ are the Roe-averaged velocity components, total enthalpy, sonic speed, and magnitude of the velocity, which are functions of \mathbf{U}_L and \mathbf{U}_R . The appropriate Roe averaging for the inviscid equations is given in [11], and is repeated here:

$$\begin{aligned}
\underline{u} &= \frac{\sqrt{\varrho_L} u_L + \sqrt{\varrho_R} u_R}{\sqrt{\varrho_L} + \sqrt{\varrho_R}} \\
\underline{v} &= \frac{\sqrt{\varrho_L} v_L + \sqrt{\varrho_R} v_R}{\sqrt{\varrho_L} + \sqrt{\varrho_R}} \\
\underline{w} &= \frac{\sqrt{\varrho_L} w_L + \sqrt{\varrho_R} w_R}{\sqrt{\varrho_L} + \sqrt{\varrho_R}} \\
\underline{H} &= \frac{\sqrt{\varrho_L} H_L + \sqrt{\varrho_R} H_R}{\sqrt{\varrho_L} + \sqrt{\varrho_R}} \\
\underline{a} &= \left[(\gamma - 1) \left(\underline{H} - \frac{1}{2} \underline{V}^2 \right) \right]^{1/2}
\end{aligned} \tag{A.67}$$

where $\sqrt{\varrho}$ is understood to be a square root of the mass density.

The eigenvalue and eigenvector matrices presented in equations A.57 and A.61, respectively, were checked

to fully diagonalize the Navier-Stokes system using symbolic mathematical software.

A.3 Jacobians and Eigenstructure of the Maxwell Equations

This section provides mathematical details for the Maxwell equations. Much more complete information is available in [143, 151, 178]. Here, we consider the form of the perfectly hyperbolic Maxwell equations, which includes the numerical fields used for divergence cleaning [178]. One may recover the pure Maxwell set by setting the associated cleaning speeds, χ and γ , to zero, and removing the last two equations. The general equations may be written

$$\frac{\partial \mathbf{B}}{\partial t} + \nabla \times \mathbf{E} + \xi \nabla \Psi_B = 0 \quad (\text{A.68})$$

$$\frac{\partial \mathbf{E}}{\partial t} - c_0^2 \nabla \times \mathbf{B} + c_0^2 \chi \nabla \Psi_E = -\mathbf{j}_e / \epsilon_0 \quad (\text{A.69})$$

$$\frac{1}{\xi c_0^2} \frac{\partial \Psi_B}{\partial \tau} + \nabla \cdot \mathbf{B} = 0 \quad (\text{A.70})$$

$$\frac{1}{\chi} \frac{\partial \Psi_E}{\partial \tau} + \nabla \cdot \mathbf{E} = \varrho_e / \epsilon_0 \quad (\text{A.71})$$

Here \mathbf{E} and \mathbf{B} are the electric and magnetic induction fields, c_0 is the vacuum speed of light, \mathbf{j}_e and ϱ_e are the current and charge density, respectively, and Ψ_B and Ψ_E are the divergence fields, with associated speeds ξ and χ . Notice that the variation of the divergence fields is only permitted in the dual-time; this allows full convergence of equations A.70 and A.71 in the dual-time iteration between timesteps, and restricts the divergence fields from appearing in the physical derivatives.

The equations may be posed in the form of a system of conservation laws as

$$\frac{\partial \mathbf{U}_m}{\partial t} + \nabla \cdot \mathbf{F}_m = \mathbf{H}_m \quad (\text{A.72})$$

where

$$\mathbf{U}_m = \begin{pmatrix} \mathbf{B} \\ \mathbf{E} \\ \Psi_E \\ \Psi_B \end{pmatrix}, \quad \mathbf{F}_m = \begin{pmatrix} \hat{\mathbf{curl}}(\mathbf{E}) + \xi \Psi_B \hat{\mathbf{I}} \\ -c_0^2 \hat{\mathbf{curl}}(\mathbf{B}) + \chi c_0^2 \Psi_E \hat{\mathbf{I}} \\ \chi \mathbf{E} \\ \xi c_0^2 \mathbf{B} \end{pmatrix}, \quad \mathbf{H}_m = \frac{1}{\epsilon_0} \begin{pmatrix} \mathbf{0} \\ \mathbf{j}_e \\ \varrho_e \\ 0 \end{pmatrix} \quad (\text{A.73})$$

where we have rewritten $\nabla \times \mathbf{A}$ into divergence form via a curl operator, $\nabla \cdot \hat{\mathbf{curl}}(\mathbf{A}) = \nabla \cdot (\hat{\mathbf{I}} \times \mathbf{A}) = \partial_l \epsilon_{ijk} \delta_{jl} E_k = \epsilon_{ijk} \partial_j E_k$. The subscript m is used to denote that this is the Maxwell system, to differentiate it from the fluid system.

A.3.1 Jacobian Matrix

There are three jacobian matrices for the Maxwell equations (one for each dimension). If we write the system of equations as

$$\frac{\partial \mathbf{U}_m}{\partial t} + \frac{\partial \mathbf{F}_{m,x}}{\partial x} + \frac{\partial \mathbf{F}_{m,y}}{\partial y} + \frac{\partial \mathbf{F}_{m,z}}{\partial z} = \mathbf{H}_m \quad (\text{A.74})$$

Rewriting equation A.74 into quasilinear form as discussed in Section 5.7, we have

$$\frac{\partial \mathbf{U}_m}{\partial t} + \hat{\mathbf{A}}_{m,x} \frac{\partial \mathbf{U}_m}{\partial x} + \hat{\mathbf{A}}_{m,y} \frac{\partial \mathbf{U}_m}{\partial y} + \hat{\mathbf{A}}_{m,z} \frac{\partial \mathbf{U}_m}{\partial z} = 0 \quad (\text{A.75})$$

where $\hat{\mathbf{A}}_{m,x} = \partial \mathbf{F}_{m,x} / \partial \mathbf{U}_m$, $\hat{\mathbf{A}}_{m,y} = \partial \mathbf{F}_{m,y} / \partial \mathbf{U}_m$, and $\hat{\mathbf{A}}_{m,z} = \partial \mathbf{F}_{m,z} / \partial \mathbf{U}_m$, are given in the form of

$$\hat{\mathbf{A}}_{m,x} = \begin{pmatrix} 0 & 0 & 0 & 0 & 0 & 0 & 0 & \xi \\ 0 & 0 & 0 & 0 & 0 & -1 & 0 & 0 \\ 0 & 0 & 0 & 0 & 1 & 0 & 0 & 0 \\ 0 & 0 & 0 & 0 & 0 & 0 & c^2 \chi & 0 \\ 0 & 0 & c^2 & 0 & 0 & 0 & 0 & 0 \\ 0 & -c^2 & 0 & 0 & 0 & 0 & 0 & 0 \\ 0 & 0 & 0 & \chi & 0 & 0 & 0 & 0 \\ c^2 \xi & 0 & 0 & 0 & 0 & 0 & 0 & 0 \end{pmatrix} \quad (\text{A.76})$$

$$\hat{\mathbf{A}}_{m,y} = \begin{pmatrix} 0 & 0 & 0 & 0 & 0 & 1 & 0 & 0 \\ 0 & 0 & 0 & 0 & 0 & 0 & 0 & \xi \\ 0 & 0 & 0 & -1 & 0 & 0 & 0 & 0 \\ 0 & 0 & -c^2 & 0 & 0 & 0 & 0 & 0 \\ 0 & 0 & 0 & 0 & 0 & 0 & c^2 \chi & 0 \\ c^2 & 0 & 0 & 0 & 0 & 0 & 0 & 0 \\ 0 & 0 & 0 & 0 & \chi & 0 & 0 & 0 \\ 0 & c^2 \xi & 0 & 0 & 0 & 0 & 0 & 0 \end{pmatrix} \quad (\text{A.77})$$

$$\hat{\mathbf{A}}_{m,z} = \begin{pmatrix} 0 & 0 & 0 & 0 & -1 & 0 & 0 & 0 \\ 0 & 0 & 0 & 1 & 0 & 0 & 0 & 0 \\ 0 & 0 & 0 & 0 & 0 & 0 & 0 & \xi \\ 0 & c^2 & 0 & 0 & 0 & 0 & 0 & 0 \\ -c^2 & 0 & 0 & 0 & 0 & 0 & 0 & 0 \\ 0 & 0 & 0 & 0 & 0 & 0 & c^2 \chi & 0 \\ 0 & 0 & 0 & 0 & 0 & \chi & 0 & 0 \\ 0 & 0 & c^2 \xi & 0 & 0 & 0 & 0 & 0 \end{pmatrix} \quad (\text{A.78})$$

These results may be collected into the compact, normal-projected form as

$$\hat{\mathbf{A}}_m = \begin{pmatrix} \hat{\mathbf{0}} & -\hat{\mathbf{curl}}(\mathbf{n}) & \mathbf{0} & \xi\mathbf{n} \\ c_0^2\hat{\mathbf{curl}}(\mathbf{n}) & \hat{\mathbf{0}} & c_0^2\chi\mathbf{n} & \mathbf{0} \\ \mathbf{0} & \chi\mathbf{n} & 0 & 0 \\ \xi c_0^2\mathbf{n} & \mathbf{0} & 0 & 0 \end{pmatrix} \quad (\text{A.79})$$

Here, \mathbf{n} is a normal vector associated with the surface of interest that flux is transported across. It is clear that the normal-projected matrix, $\hat{\mathbf{A}}_m$, is a constant geometric matrix. Since the Maxwell equations (including the divergence fields) constitute a linear system, the Roe matrix is identical to the jacobian matrix presented in equation A.79, and the appropriate Roe average used is the arithmetic average of the fields, $\underline{\mathbf{U}}_m = (\mathbf{U}_L + \mathbf{U}_R)/2$.

A.3.2 Eigenvalues

The eigenvalues of $\hat{\mathbf{A}}_m$ can be determined analytically as

$$\hat{\mathbf{\Lambda}}_m = \text{Diag}\{-c, -c, c, c, -c\chi, c\chi, -c\xi, c\xi\} = \begin{pmatrix} -c & 0 & 0 & 0 & 0 & 0 & 0 & 0 \\ 0 & -c & 0 & 0 & 0 & 0 & 0 & 0 \\ 0 & 0 & c & 0 & 0 & 0 & 0 & 0 \\ 0 & 0 & 0 & c & 0 & 0 & 0 & 0 \\ 0 & 0 & 0 & 0 & -c\chi & 0 & 0 & 0 \\ 0 & 0 & 0 & 0 & 0 & c\chi & 0 & 0 \\ 0 & 0 & 0 & 0 & 0 & 0 & -c\xi & 0 \\ 0 & 0 & 0 & 0 & 0 & 0 & 0 & c\xi \end{pmatrix} \quad (\text{A.80})$$

In the case where the divergence fields are excluded, the typical Maxwell set reduces to six eigenvalues, and the last two equations for the divergence fields are no longer needed,

$$\hat{\mathbf{\Lambda}}_m = \text{Diag}\{-c, -c, c, c, 0, 0\} = \begin{pmatrix} -c & 0 & 0 & 0 & 0 & 0 \\ 0 & -c & 0 & 0 & 0 & 0 \\ 0 & 0 & c & 0 & 0 & 0 \\ 0 & 0 & 0 & c & 0 & 0 \\ 0 & 0 & 0 & 0 & 0 & 0 \\ 0 & 0 & 0 & 0 & 0 & 0 \end{pmatrix} \quad (\text{A.81})$$

A.3.3 Eigenvectors

Since multiplicities are present in the eigenvalues, the eigenvectors are not unique; however, linearly independent eigenvectors may still be constructed by insisting on consistency (the eigenvectors are selected such that similar diagonalized matrices degenerate to the same form as in the cartesian frame [143]). For the cartesian plane, the jacobian matrices $\hat{\mathbf{A}}_{m,x}$, $\hat{\mathbf{A}}_{m,y}$, and $\hat{\mathbf{A}}_{m,z}$ have corresponding eigenmatrices $\hat{\mathbf{K}}_{m,x}$, $\hat{\mathbf{K}}_{m,y}$, and $\hat{\mathbf{K}}_{m,z}$ given in the form of

$$\hat{\mathbf{K}}_{m,x} = \begin{pmatrix} 0 & 0 & 0 & 0 & 0 & 0 & -\frac{1}{c_0} & \frac{1}{c_0} \\ \frac{1}{c_0} & 0 & -\frac{1}{c_0} & 0 & 0 & 0 & 0 & 0 \\ 0 & -\frac{1}{c_0} & 0 & \frac{1}{c_0} & 0 & 0 & 0 & 0 \\ 0 & 0 & 0 & 0 & -c_0 & c_0 & 0 & 0 \\ 0 & 1 & 0 & 1 & 0 & 0 & 0 & 0 \\ 1 & 0 & 1 & 0 & 0 & 0 & 0 & 0 \\ 0 & 0 & 0 & 0 & 1 & 1 & 0 & 0 \\ 0 & 0 & 0 & 0 & 0 & 0 & 1 & 1 \end{pmatrix} \quad (\text{A.82})$$

$$\hat{\mathbf{K}}_{m,y} = \begin{pmatrix} -\frac{1}{c_0} & 0 & \frac{1}{c_0} & 0 & 0 & 0 & 0 & 0 \\ 0 & 0 & 0 & 0 & 0 & 0 & -\frac{1}{c_0} & \frac{1}{c_0} \\ 0 & \frac{1}{c_0} & 0 & -\frac{1}{c_0} & 0 & 0 & 0 & 0 \\ 0 & 1 & 0 & 1 & 0 & 0 & 0 & 0 \\ 0 & 0 & 0 & 0 & -c_0 & c_0 & 0 & 0 \\ 1 & 0 & 1 & 0 & 0 & 0 & 0 & 0 \\ 0 & 0 & 0 & 0 & 1 & 1 & 0 & 0 \\ 0 & 0 & 0 & 0 & 0 & 0 & 1 & 1 \end{pmatrix} \quad (\text{A.83})$$

$$\hat{\mathbf{K}}_{m,z} = \begin{pmatrix} \frac{1}{c_0} & 0 & -\frac{1}{c_0} & 0 & 0 & 0 & 0 & 0 \\ 0 & -\frac{1}{c_0} & 0 & \frac{1}{c_0} & 0 & 0 & 0 & 0 \\ 0 & 0 & 0 & 0 & 0 & 0 & -\frac{1}{c_0} & \frac{1}{c_0} \\ 0 & 1 & 0 & 1 & 0 & 0 & 0 & 0 \\ 1 & 0 & 1 & 0 & 0 & 0 & 0 & 0 \\ 0 & 0 & 0 & 0 & -c_0 & c_0 & 0 & 0 \\ 0 & 0 & 0 & 0 & 1 & 1 & 0 & 0 \\ 0 & 0 & 0 & 0 & 0 & 0 & 1 & 1 \end{pmatrix} \quad (\text{A.84})$$

These eigenvectors may be expressed in a more compact, general normal-projected form as

$$\hat{\mathbf{K}}_m = \left\{ \begin{array}{cccccccc} -\frac{n_y}{c_0} & \frac{n_z}{c_0} & \frac{n_y}{c_0} & -\frac{n_z}{c_0} & 0 & 0 & -\frac{n_x}{c_0} & \frac{n_x}{c_0} \\ \frac{n_x^2+n_z^2}{c_0 n_x} & \frac{n_y n_z}{c_0 n_x} & -\frac{n_x^2+n_z^2}{c_0 n_x} & -\frac{n_y n_z}{c_0 n_x} & 0 & 0 & -\frac{n_y}{c_0} & \frac{n_y}{c_0} \\ -\frac{n_y n_z}{c_0 n_x} & -\frac{n_x^2+n_y^2}{c_0 n_x} & \frac{n_y n_z}{c_0 n_x} & \frac{n_x^2+n_y^2}{c_0 n_x} & 0 & 0 & -\frac{n_z}{c_0} & \frac{n_z}{c_0} \\ -\frac{n_z}{n_x} & -\frac{n_y}{n_x} & -\frac{n_z}{n_x} & -\frac{n_y}{n_x} & -c_0 n_x & c_0 n_x & 0 & 0 \\ 0 & 1 & 0 & 1 & -c_0 n_y & c_0 n_y & 0 & 0 \\ 1 & 0 & 1 & 0 & -c_0 n_z & c_0 n_z & 0 & 0 \\ 0 & 0 & 0 & 0 & 1 & 1 & 0 & 0 \\ 0 & 0 & 0 & 0 & 0 & 0 & 1 & 1 \end{array} \right\} \quad (\text{A.85})$$

This general eigenmatrix, $\hat{\mathbf{K}}_m$, has been checked to fully diagonalize the 8×8 Maxwell system with the divergence fields. In the case that the divergence fields are not included, the Maxwell system reduces to a 6×6 form, and the divergence fields Ψ_E and Ψ_B and their associated equations are not included in the calculation.

A.3.4 Solution to the Riemann Problem

The solution to the linearized Riemann problem is required for the Roe scheme. The Riemann problem is assumed to have piecewise constant initial data in the form

$$\mathbf{U}(x, t = 0) = \begin{cases} \mathbf{U}_L, & x < 0 \\ \mathbf{U}_R, & x > 0 \end{cases} \quad (\text{A.86})$$

where \mathbf{U}_L and \mathbf{U}_R are known constant state vectors, then the solution, per the discussion in Section 5.7, can be written as an eigenvector expansion,

$$\Delta \mathbf{U} = \mathbf{U}_R - \mathbf{U}_L = \sum_{p=1}^m \alpha^{(p)} \mathbf{K}^{(p)} \quad (\text{A.87})$$

where $p \in \{1, \dots, m\}$ spans the set of m equations, α represents the decomposition coefficients, and $\mathbf{K}^{(p)}$ are the column right eigenvectors. Equation A.87 must be solved for its decomposition coefficients. A set of decomposition coefficients will exist in each direction. For the x direction, using $\hat{\mathbf{K}}_{m,x}$, the decomposition

coefficients are

$$\alpha_{m,x}^{(1),(3)} = \frac{1}{2} (\pm c_0 \Delta \mathbf{U}_2 + \Delta \mathbf{U}_6) \quad (\text{A.88})$$

$$\alpha_{m,x}^{(4),(2)} = \frac{1}{2} (\pm c_0 \Delta \mathbf{U}_3 + \Delta \mathbf{U}_5) \quad (\text{A.89})$$

$$\alpha_{m,x}^{(6),(5)} = \frac{1}{2} \left(\pm \frac{\Delta \mathbf{U}_4}{c_0} + \Delta \mathbf{U}_7 \right) \quad (\text{A.90})$$

$$\alpha_{m,x}^{(8),(7)} = \frac{1}{2} (\pm c_0 \Delta \mathbf{U}_1 + \Delta \mathbf{U}_8) \quad (\text{A.91})$$

In the y direction, using $\hat{\mathbf{K}}_{m,y}$, the decomposition coefficients are

$$\alpha_{m,y}^{(3),(1)} = \frac{1}{2} (\pm c_0 \Delta \mathbf{U}_1 + \Delta \mathbf{U}_6) \quad (\text{A.92})$$

$$\alpha_{m,y}^{(2),(4)} = \frac{1}{2} (\pm c_0 \Delta \mathbf{U}_3 + \Delta \mathbf{U}_4) \quad (\text{A.93})$$

$$\alpha_{m,y}^{(6),(5)} = \frac{1}{2} \left(\pm \frac{\Delta \mathbf{U}_5}{c_0} + \Delta \mathbf{U}_7 \right) \quad (\text{A.94})$$

$$\alpha_{m,y}^{(8),(7)} = \frac{1}{2} (\pm c_0 \Delta \mathbf{U}_2 + \Delta \mathbf{U}_8) \quad (\text{A.95})$$

A.4 Jacobians and Eigenstructure of the Source-coupled Navier-Stokes and Maxwell Equations

In this section, we present the usual form of the jacobians, eigenvalues and eigenvectors for the source-coupled form, which has been explored by [8, 47, 59] and, for the two-fluid system, in [75, 76, 187]. The equations are

$$\frac{\partial \mathbf{U}}{\partial t} + \nabla \cdot \mathbf{F} = \mathbf{H} \quad (\text{A.96})$$

where

$$\mathbf{U} = \begin{bmatrix} \varrho \\ \varrho \mathbf{u} \\ \mathcal{E} \\ \mathbf{B} \\ \mathbf{E} \\ \Psi_E \\ \Psi_B \end{bmatrix}, \quad \mathbf{F} = \begin{bmatrix} \varrho \mathbf{u} \\ \varrho \mathbf{u} \mathbf{u} + \hat{\mathbf{I}} p \\ [\mathcal{E} + p] \mathbf{u} \\ \hat{\mathbf{curl}}(\mathbf{E}) + \xi \nabla \Psi_B \\ -c_0^2 \hat{\mathbf{curl}}(\mathbf{B}) + \chi c_0^2 \Psi_E \\ \chi \mathbf{E} \\ \xi c_0^2 \mathbf{B} \end{bmatrix}, \quad \mathbf{H} = \begin{bmatrix} 0 \\ \varrho_e \mathbf{E} + \mathbf{j}_e \times \mathbf{B} \\ \mathbf{j}_e \cdot \mathbf{E} \\ \mathbf{0} \\ -\mathbf{j}_e / \epsilon_0 - \varrho_e \mathbf{u} \\ \varrho_e / \epsilon_0 \\ 0 \end{bmatrix} \quad (\text{A.97})$$

Notice that the coupling between the two systems is restricted entirely to the source vector, \mathbf{H} . This means that the eigenstructure of the equations are fully uncoupled, and coupling occurs only during evaluation of the source term. This permits the jacobians and eigenstructure of this system to be written in a convenient

block matrix form. The divergence cleaning equations have been included; they can be removed by setting $\chi = \xi = 0$ everywhere in the following equations.

A.4.1 Jacobian Matrix

The jacobian matrix is simply a block matrix containing the separate Navier-Stokes and Maxwell jacobians. The jacobian is uncoupled, since the coupling is relegated to the source vector.

$$\hat{\mathbf{A}} = \begin{pmatrix} \hat{\mathbf{A}}_f & \hat{\mathbf{0}} \\ \hat{\mathbf{0}} & \hat{\mathbf{A}}_m \end{pmatrix} \quad (\text{A.98})$$

where $\hat{\mathbf{A}}_f$ and $\hat{\mathbf{A}}_m$ are the fluid and Maxwell jacobian matrices, given in equations A.56 and A.79, respectively.

A.4.2 Eigenvalues

The eigenvalues of the source-coupled equations will be a block matrix comprised of the separate eigenvalues of the Navier-Stokes and Maxwell equations.

$$\hat{\mathbf{\Lambda}} = \begin{pmatrix} \hat{\mathbf{\Lambda}}_f & \hat{\mathbf{0}} \\ \hat{\mathbf{0}} & \hat{\mathbf{\Lambda}}_m \end{pmatrix} \quad (\text{A.99})$$

where $\hat{\mathbf{\Lambda}}_f$ and $\hat{\mathbf{\Lambda}}_m$ are the fluid and Maxwell diagonal eigenvalue matrices, given by equations A.57 and A.80, respectively.

A.4.3 Eigenvectors

The eigenvectors of the source-coupled formulation is a block matrix comprised of the separate eigenmatrices of the Navier-Stokes and Maxwell equations. The eigenvectors are not coupled, since the coupling is relegated to the source vector.

$$\hat{\mathbf{K}} = \begin{pmatrix} \hat{\mathbf{K}}_f & \hat{\mathbf{0}} \\ \hat{\mathbf{0}} & \hat{\mathbf{K}}_m \end{pmatrix} \quad (\text{A.100})$$

where $\hat{\mathbf{K}}_f$ and $\hat{\mathbf{K}}_m$ are the fluid and Maxwell eigenmatrices, given by equations A.61 and A.85, respectively.

A.4.4 Jacobian Matrices for Implicit Scheme

The implicit scheme described in Section 5.9 outlines a procedure for updating the plasmadynamic equations, but requires the calculation of the matrices $\hat{\mathbf{r}}, \partial\mathbf{U}/\partial\mathbf{Q}$ and $\partial\mathbf{R}/\partial\mathbf{Q}$. For simplicity of presentation, we assume that the flux vector, \mathbf{F} , is only updated explicitly every timestep, such that the residual Jacobian becomes $\partial\mathbf{R}/\partial\mathbf{Q} = \partial\mathbf{H}/\partial\mathbf{Q}$. Below, we present the forms of these matrices used in the investigations detailed in

Chapters 5 and 6.

$$\hat{\mathbf{r}} = \begin{bmatrix} 1 & 0 & 0 & 0 & 0 & 0 & 0 & 0 & 0 & 0 & 0 & 0 & 0 \\ u & \varrho & 0 & 0 & 0 & 0 & 0 & 0 & 0 & 0 & 0 & 0 & 0 \\ v & 0 & \varrho & 0 & 0 & 0 & 0 & 0 & 0 & 0 & 0 & 0 & 0 \\ w & 0 & 0 & \varrho & 0 & 0 & 0 & 0 & 0 & 0 & 0 & 0 & 0 \\ V^2/2 & \varrho u & \varrho v & \varrho w & 1/\hat{\gamma} & 0 & 0 & 0 & 0 & 0 & 0 & 0 & 0 \\ 0 & 0 & 0 & 0 & 0 & 1 & 0 & 0 & 0 & 0 & 0 & 0 & 0 \\ 0 & 0 & 0 & 0 & 0 & 0 & 1 & 0 & 0 & 0 & 0 & 0 & 0 \\ 0 & 0 & 0 & 0 & 0 & 0 & 0 & 1 & 0 & 0 & 0 & 0 & 0 \\ 0 & 0 & 0 & 0 & 0 & 0 & 0 & 0 & \beta^{-2} & 0 & 0 & 0 & 0 \\ 0 & 0 & 0 & 0 & 0 & 0 & 0 & 0 & 0 & \beta^{-2} & 0 & 0 & 0 \\ 0 & 0 & 0 & 0 & 0 & 0 & 0 & 0 & 0 & 0 & \beta^{-2} & 0 & 0 \\ 0 & 0 & 0 & 0 & 0 & 0 & 0 & 0 & 0 & 0 & 0 & 1 & 0 \\ 0 & 0 & 0 & 0 & 0 & 0 & 0 & 0 & 0 & 0 & 0 & 0 & 1 \end{bmatrix} \quad (\text{A.101})$$

where $V^2 = u^2 + v^2 + w^2$, $\hat{\gamma} = \gamma - 1$, and β is the preconditioning parameter.

The jacobian matrix $\partial \mathbf{U} / \partial \mathbf{Q}$ is

$$\frac{\partial \mathbf{U}}{\partial \mathbf{Q}} = \begin{bmatrix} 1 & 0 & 0 & 0 & 0 & 0 & 0 & 0 & 0 & 0 & 0 & 0 & 0 & 0 \\ u & \varrho & 0 & 0 & 0 & 0 & 0 & 0 & 0 & 0 & 0 & 0 & 0 & 0 \\ v & 0 & \varrho & 0 & 0 & 0 & 0 & 0 & 0 & 0 & 0 & 0 & 0 & 0 \\ w & 0 & 0 & \varrho & 0 & 0 & 0 & 0 & 0 & 0 & 0 & 0 & 0 & 0 \\ V^2/2 & \varrho u & \varrho v & \varrho w & 1/\hat{\gamma} & 0 & 0 & 0 & 0 & 0 & 0 & 0 & 0 & 0 \\ 0 & 0 & 0 & 0 & 0 & 1 & 0 & 0 & 0 & 0 & 0 & 0 & 0 & 0 \\ 0 & 0 & 0 & 0 & 0 & 0 & 1 & 0 & 0 & 0 & 0 & 0 & 0 & 0 \\ 0 & 0 & 0 & 0 & 0 & 0 & 0 & 1 & 0 & 0 & 0 & 0 & 0 & 0 \\ 0 & 0 & 0 & 0 & 0 & 0 & 0 & 0 & 1 & 0 & 0 & 0 & 0 & 0 \\ 0 & 0 & 0 & 0 & 0 & 0 & 0 & 0 & 0 & 1 & 0 & 0 & 0 & 0 \\ 0 & 0 & 0 & 0 & 0 & 0 & 0 & 0 & 0 & 0 & 1 & 0 & 0 & 0 \\ 0 & 0 & 0 & 0 & 0 & 0 & 0 & 0 & 0 & 0 & 0 & 1 & 0 & 0 \\ 0 & 0 & 0 & 0 & 0 & 0 & 0 & 0 & 0 & 0 & 0 & 0 & 1 & 0 \\ 0 & 0 & 0 & 0 & 0 & 0 & 0 & 0 & 0 & 0 & 0 & 0 & 0 & 1 \end{bmatrix} \quad (\text{A.102})$$

The source jacobian matrix, $\partial \mathbf{H}/\partial \mathbf{Q}$, is

$$\begin{aligned}
\frac{\partial \mathbf{H}}{\partial \mathbf{Q}} = \sigma & \begin{pmatrix} 0 & 0 & 0 & 0 & 0 \\ 0 & -B_y^2 - B_z^2 & B_x B_y & B_x B_z & 0 \\ 0 & B_x B_y & -B_x^2 - B_z^2 & B_y B_z & 0 \\ 0 & B_x B_z & B_y B_z & -B_x^2 - B_y^2 & 0 \\ 0 & -B_z E_y + B_y E_z & B_z E_x - B_x E_z & -B_y E_x + B_x E_y & 0 \\ 0 & 0 & 0 & 0 & 0 \\ 0 & 0 & 0 & 0 & 0 \dots \\ 0 & 0 & 0 & 0 & 0 \\ 0 & -\varrho_e & -\frac{B_z}{\epsilon_0} & \frac{B_y}{\epsilon_0} & 0 \\ 0 & \frac{B_z}{\epsilon_0} & -\varrho_e & -\frac{B_x}{\epsilon_0} & 0 \\ 0 & -\frac{B_y}{\epsilon_0} & \frac{B_x}{\epsilon_0} & -\varrho_e & 0 \\ 0 & 0 & 0 & 0 & 0 \\ 0 & 0 & 0 & 0 & 0 \end{pmatrix} \\
& \begin{pmatrix} 0 & 0 & 0 \\ B_y v + B_z w & -E_z - B_y u - (B_y u - B_x v) & E_y - B_z u + (-B_z u + B_x w) \\ E_z - B_x v + (B_y u - B_x v) & B_x u + B_z w & -E_x - B_z v - (B_z v - B_y w) \\ -E_y - B_x w - (-B_z u + B_x w) & E_x - B_y w + (B_z v - B_y w) & B_x u + B_y v \\ -E_z v + E_y w & E_z u - E_x w & -E_y u + E_x v \\ 0 & 0 & 0 \\ 0 & 0 & 0 \\ 0 & \frac{w}{\epsilon_0} & -\frac{v}{\epsilon_0} \\ -\frac{w}{\epsilon_0} & 0 & \frac{u}{\epsilon_0} \\ \frac{v}{\epsilon_0} & -\frac{u}{\epsilon_0} & 0 \\ 0 & 0 & 0 \\ 0 & 0 & 0 \end{pmatrix} \dots \quad (\text{A.103}) \\
& \begin{pmatrix} 0 & 0 & 0 & 0 & 0 & 0 \\ \varrho_e & B_z & -B_y & 0 & 0 & 0 \\ -B_z & \varrho_e & B_x & 0 & 0 & 0 \\ B_y & -B_x & \varrho_e & 0 & 0 & 0 \\ 2E_x + (B_z v - B_y w) & 2E_y + (-B_z u + B_x w) & 2E_z + (B_y u - B_x v) & 0 & 0 & 0 \\ 0 & 0 & 0 & 0 & 0 & 0 \\ 0 & 0 & 0 & 0 & 0 & 0 \\ 0 & 0 & 0 & 0 & 0 & 0 \\ -\epsilon_0^{-1} & 0 & 0 & 0 & 0 & 0 \\ 0 & -\epsilon_0^{-1} & 0 & 0 & 0 & 0 \\ 0 & 0 & -\epsilon_0^{-1} & 0 & 0 & 0 \\ 0 & 0 & 0 & 0 & 0 & 0 \\ 0 & 0 & 0 & 0 & 0 & 0 \end{pmatrix}
\end{aligned}$$

where $V^2 = u^2 + v^2 + w^2$, $\hat{\gamma} = \gamma - 1$, $\bar{\mathbf{E}} = \mathbf{E}/(c_0^2 \mu_0)$ and $\bar{\mathbf{B}} = \mathbf{B}/(c_0^2 \mu_0)$.

A.5 Jacobians, Eigenvalues, and Eigenvectors of the Strong Conservative Navier-Stokes and Maxwell Equations

In this section, we present the form of the jacobians, eigenvalues, and eigenvectors for the strong conservative form. This formulation involves a new coupling matrix in the jacobian and eigenvectors, denoted by subscript c . The strong conservative equations are

$$\frac{\partial \mathbf{U}}{\partial t} + \nabla \cdot \mathbf{F} = \mathbf{H} \quad (\text{A.104})$$

where

$$\mathbf{U}_F = \begin{Bmatrix} \varrho \\ \varrho \mathbf{u} + \mathbf{S}^{EM}/c_0^2 \\ \mathcal{E} + \mathcal{E}^{EM} \\ \mathbf{B} \\ \mathbf{E} \\ \Psi_E \\ \Psi_B \end{Bmatrix}, \quad \mathbf{F}_F = \begin{Bmatrix} \varrho \mathbf{u} \\ \varrho \mathbf{u} \mathbf{u} + \hat{\mathbf{I}} p - \boldsymbol{\Sigma}^{EM} \\ [\mathcal{E} + p] \mathbf{u} + \mathbf{S}^{EM} \\ \hat{\mathbf{curl}}(\mathbf{E}) + \xi \nabla \Psi_B \\ -c_0^2 \hat{\mathbf{curl}}(\mathbf{B}) + \chi c_0^2 \Psi_E \\ \chi \mathbf{E} \\ \xi c_0^2 \mathbf{B} \end{Bmatrix}, \quad \mathbf{H}_F = \begin{Bmatrix} 0 \\ \mathbf{0} \\ 0 \\ \mathbf{0} \\ -\mathbf{j}_e/\epsilon_0 - \varrho_e \mathbf{u} \\ \varrho_e/\epsilon_0 \\ 0 \end{Bmatrix} \quad (\text{A.105})$$

A.5.1 Jacobian Matrix

If we recast equation A.104 into the quasilinear form discussed in Section 5.7, it can be expressed as

$$\frac{\partial \mathbf{U}}{\partial t} + \hat{\mathbf{A}}_x \frac{\partial \mathbf{U}}{\partial x} + \hat{\mathbf{A}}_y \frac{\partial \mathbf{U}}{\partial y} + \hat{\mathbf{A}}_z \frac{\partial \mathbf{U}}{\partial z} = \mathbf{H} \quad (\text{A.106})$$

or, in normal-projected form, as

$$\frac{\partial \mathbf{U}}{\partial t} + \hat{\mathbf{A}} \frac{\partial \mathbf{U}}{\partial x_k} = \mathbf{H} \quad (\text{A.107})$$

where $\hat{\mathbf{A}}$ is the jacobian matrix. The normal-projected form of the jacobian matrix for equations A.104 and A.105 is

$$\hat{\mathbf{A}} = \begin{pmatrix} \hat{\mathbf{A}}_f & \hat{\mathbf{A}}_c \\ \hat{\mathbf{0}} & \hat{\mathbf{A}}_m \end{pmatrix} \quad (\text{A.108})$$

where $\hat{\mathbf{A}}_f$ and $\hat{\mathbf{A}}_m$ are the fluid and Maxwell normal-projected jacobians, given by equations A.56 and A.79, respectively. The coupling jacobian, $\hat{\mathbf{A}}_c$, is the new term added in the strong conservative form to couple the Navier-Stokes and Maxwell equations; it is a zero matrix in the source-coupled formulation. There will be a matrix $\hat{\mathbf{A}}_c$ for each direction in the cartesian form (equation A.106) for equation A.107; these may be

written

$$\begin{aligned}
\hat{\mathbf{A}}_{c,x} = & \begin{pmatrix} 0 & D_z & & & \\ -\gamma H_x + \hat{\gamma}(D_z v - D_y w) & -H_y(\gamma - 2) - D_z(\gamma - 3)u + \hat{\gamma}D_x w & & & \\ -H_y - D_z u & -H_x + D_z v & & & \dots \\ -H_z + D_y u & -D_x u + D_z w & & & \\ u[-\gamma H_x + \hat{\gamma}(D_z v - D_y w)] & u(-\gamma H_y + \hat{\gamma}D_x w) - \frac{E_z}{\mu_0} + D_z(H - \hat{\gamma}u^2) & & & \\ & -D_y & 0 & & \\ & -H_z(\gamma - 2) + D_y(\gamma - 3)u - \hat{\gamma}D_x v & -\gamma D_x + \hat{\gamma}\epsilon_0(B_z v - B_y w) & & \\ \dots & D_x u - D_y v & -D_y + \epsilon_0 B_z u & & \dots \\ & -H_x - D_y w & -D_z + \epsilon_0 B_y u & & \\ & u(-\gamma H_z - \hat{\gamma}D_x v) + \frac{E_y}{\mu_0} - D_y(H - \hat{\gamma}u^2) & -u(D_x + \hat{\gamma}\epsilon_0(B_z v - B_y w)) & & \\ & -\epsilon_0 B_z & \epsilon_0 B_y & & \\ & -D_y(\gamma - 2) + \epsilon_0 B_z(\gamma - 3) - \epsilon_0 \hat{\gamma}B_x w & -D_z(\gamma - 2) - \epsilon_0 B_y(\gamma - 3)u + \epsilon_0 \hat{\gamma}B_x v & & \\ \dots & -D_x - \epsilon_0 B_z v & \epsilon_0(-B_x u + B_y v) & & \dots \\ & \epsilon_0(B_x u - B_z w) & -D_x + \epsilon_0 B_y w & & \\ & u(\gamma D_y - \hat{\gamma}\epsilon_0 B_x w) + \frac{B_z}{\mu_0} - \epsilon_0 B_z(H - \hat{\gamma}u^2) & u(\gamma D_z + \hat{\gamma}\epsilon_0 B_x v) - \frac{B_y}{\mu_0} + \epsilon_0 B_y(H - \hat{\gamma}u^2) & & \\ & 0 & 0 & & \\ & 0 & 0 & & \\ & \dots & 0 & 0 & \\ & 0 & 0 & & \\ & 0 & 0 & & \end{pmatrix} \quad (\text{A.109})
\end{aligned}$$

$$\begin{aligned}
\hat{\mathbf{A}}_{c,y} = & \begin{pmatrix} & -D_z & & 0 & \\ & -H_y - D_z u & & -H_x + D_z v & \\ & -H_x(\gamma - 2) + D_z(\gamma - 3)v - D_y \hat{\gamma}w & & -\gamma H_y + \hat{\gamma}(D_z u - D_x w) & \dots \\ & D_y v - D_z w & & -D_x v & \\ v(-\gamma H_x - D_y \hat{\gamma}w) + \frac{E_z}{\mu_0} - D_x(H - \hat{\gamma}v^2) & & & v(-\hat{\gamma}H_y - \hat{\gamma}(D_z u - D_x w)) & \\ & D_x & & \epsilon_0 B_z & \\ & D_x u - D_y v & & -D_y + \epsilon_0 B_z u & \\ \dots & -H_z(\gamma - 2) + \hat{\gamma}D_y u - D_x(\gamma - 3)v & & D_x(\gamma - 2) - \epsilon_0 B_z(\gamma - 3)v + \epsilon_0 \hat{\gamma}B_y w & \dots \\ & D_x w & & \epsilon_0(-B_y v + B_z w) & \\ v(-\gamma H_z + D_y \hat{\gamma}u) - \frac{E_x}{\mu_0} + D_x(H - \hat{\gamma}u^2) & & & v(-\gamma D_x + \epsilon_0 \hat{\gamma}B_y w) - H_z + \epsilon_0 B_z(H - \hat{\gamma}u^2) & \\ & 0 & & -\epsilon_0 B_x & \\ & -D_x - \epsilon_0 B_z v & & \epsilon_0(-B_x u + B_y v) & \\ \dots & -\gamma D_y + \epsilon_0 \hat{\gamma}(B_z u - B_x w) & & -D_x(\gamma - 2) - \epsilon_0 \hat{\gamma}B_y u - \epsilon_0 B_x(\gamma - 3)v & \dots \\ & \epsilon_0 B_x v & & -\epsilon_0 B_x w & \\ v(-\gamma D_y - \epsilon_0 \hat{\gamma}(B_z u - B_x w)) & & & v(-\gamma D_z - \epsilon_0 B_y \hat{\gamma}u) + H - x - \epsilon_0 B_x(H - \hat{\gamma}u^2) & \\ & 0 & 0 & & \\ & 0 & 0 & & \\ & \dots & 0 & 0 & \\ & 0 & 0 & & \\ & 0 & 0 & & \end{pmatrix} \quad (\text{A.110})
\end{aligned}$$

$$\hat{\mathbf{A}}_{c,z} = \begin{pmatrix}
D_y & -D_x & & & \\
-H_z + D_y u & -D_x u + D_z w & & & \\
D_y v - D_z w & -H_z - D_x v & & & \dots \\
-H_x(\gamma - 2) + D_z \hat{\gamma} v - D_y(\gamma - 3)w & -H_y(\gamma - 2) - D_z \hat{\gamma} u + D_x(\gamma - 3)w & & & \\
w(-\gamma H_x + D_x \hat{\gamma} v) - \frac{E_y}{\mu_0} + D_y(H - \hat{\gamma} u^2) & w(-\gamma H_y - D_z \hat{\gamma} u w) + \frac{E_x}{\mu_0} - D_x(H - \hat{\gamma} u^2) & & & \\
0 & -\epsilon_0 B_y & & & \\
-H_x - D_y w & -D_z - \epsilon_0 B_y u & & & \\
\dots & -H_y + D_x w & \epsilon_0(-B_y v + B_z w) & & \dots \\
-H_z \gamma + \hat{\gamma}(D_y u - D_x v) & -D_x(\gamma - 2) - \epsilon_0 \hat{\gamma} B_x v + \epsilon_0 B_y(\gamma - 3)w & & & \\
-(\gamma H_z + \hat{\gamma}(D_y u - D_x v))w & w(-\gamma D_x - \epsilon_0 \hat{\gamma} B_z v) + \frac{B_y}{\mu_0} - \epsilon_0 B_y(H - \hat{\gamma} u^2) & & & \\
\epsilon_0 B_x & 0 & & & \\
\epsilon_0(B - xu - B_z w) & -D_x + \epsilon_0 B_y w & & & \\
\dots & -D_z + \epsilon_0 B_x v & -D_y + \epsilon_0 B_x w & & \dots \\
-D_y(\gamma - 2) + \epsilon_0 \hat{\gamma} B_z u - \epsilon_0 B_x(\gamma - 3)w & -\gamma D_z - \epsilon_0 \hat{\gamma}(B_y u - B_x v) & & & \\
w(-\gamma D_y + \epsilon_0 \hat{\gamma} u) - \frac{B_x}{\mu_0} + \epsilon_0 B_x(H - \hat{\gamma} u^2) & -(\gamma D_z + \epsilon_0 \hat{\gamma}(B_y u - B_x v))w & & & \\
0 & 0 & & & \\
0 & 0 & & & \\
\dots & 0 & 0 & & \\
0 & 0 & & & \\
0 & 0 & & &
\end{pmatrix} \quad (\text{A.111})$$

A.5.2 Eigenvalues

The eigenvalues for the strong conservative form are identical to those for the source-coupled form. They are given in block matrix form as

$$\hat{\mathbf{\Lambda}} = \begin{pmatrix} \hat{\mathbf{\Lambda}}_f & \hat{\mathbf{0}} \\ \hat{\mathbf{0}} & \hat{\mathbf{\Lambda}}_m \end{pmatrix} \quad (\text{A.112})$$

where $\hat{\mathbf{\Lambda}}_f$ and $\hat{\mathbf{\Lambda}}_m$ are the diagonal matrices of eigenvalues for the fluid and Maxwell systems, given in equations A.57 and A.80, respectively.

A.5.3 Eigenvectors

The eigenvectors for the strong conservative form may be written in block matrix form as

$$\hat{\mathbf{K}} = \begin{pmatrix} \hat{\mathbf{K}}_f & \hat{\mathbf{K}}_c \\ \hat{\mathbf{0}} & \hat{\mathbf{K}}_m \end{pmatrix} \quad (\text{A.113})$$

where $\hat{\mathbf{K}}_f$ and $\hat{\mathbf{K}}_m$ are the fluid and Maxwell normal-projected eigenvectors, given in equations A.61 and A.85, respectively. The coupling eigenmatrix, $\hat{\mathbf{K}}_c$, has a complicated form for the strong conservative system; it is

zero for the source-coupled system.

$$\mathbf{K}_{c,x}^{(1)} = \begin{pmatrix} 0 \\ -\epsilon_0 (B_y + E_z/c_0) \\ \epsilon_0 B_x \\ \epsilon_0 E_x/c_0 \\ \epsilon_0 (B_y c_0 + E_z) \end{pmatrix} \quad (\text{A.114})$$

$$\mathbf{K}_{c,x}^{(2)} = \begin{pmatrix} 0 \\ \epsilon_0 (B_z - E_y/c_0) \\ \epsilon_0 E_x/c_0 \\ -\epsilon_0 B_x \\ \epsilon_0 (-B_x c_0 + E_y) \end{pmatrix} \quad (\text{A.115})$$

$$\mathbf{K}_{c,x}^{(3)} = \begin{pmatrix} 0 \\ \epsilon_0 (B_y + E_z/c_0) \\ \epsilon_0 B_x \\ -\epsilon_0 E_x/c_0 \\ \epsilon_0 (B_y + E_z/c_0) \end{pmatrix} \quad (\text{A.116})$$

$$\mathbf{K}_{c,x}^{(4)} = \begin{pmatrix} 0 \\ \epsilon_0 (B_z + E_y/c_0) \\ -\epsilon_0 E_x/c_0 \\ -\epsilon_0 B_x \\ \epsilon_0 (B_z c_0 + E_y) \end{pmatrix} \quad (\text{A.117})$$

$$\mathbf{K}_{c,x}^{(5)} = \begin{pmatrix} \frac{\varrho(E_x \gamma u + \hat{\gamma}(E_y v + E_z w) + c\chi(E_x \gamma + \hat{\gamma}(B_z v - B_y w)))}{c\mu_0(c\chi + u)(-\gamma p + \varrho(c\chi + u)^2)} \\ -\frac{\chi\varrho(E_x \gamma u + \hat{\gamma}(E_y v + E_z w) + c\chi(E_x \gamma + \hat{\gamma}(B_z v - B_y w)))}{\mu_0(c\chi + u)(-\gamma p + \varrho(c\chi + u)^2)} \\ \frac{B_z u(-\gamma p + \varrho(c\chi + u)^2) + B_z c\chi\hat{\gamma}\varrho v^2 + E_y(-\varrho(c\chi + u)^2 - \varrho v^2 + \gamma(p + \varrho v^2)) + \varrho v(E_x \gamma(c\chi + u) - (B_y c\chi - E_z)\hat{\gamma}w)}{c\mu_0(c\chi + u)(-\gamma p + \varrho(c\chi + u)^2)} \\ -\frac{(E_z + B_y u)(-\gamma p + \varrho(c\chi + u)^2) + \varrho(E_x \gamma(c\chi + u) + (B_z c\chi + E_y)\hat{\gamma}v)w + (-B_y c\chi + E_z)\hat{\gamma}\varrho w^2}{c\mu_0(c\chi + u)(-\gamma p + \varrho(c\chi + u)^2)} \\ -\frac{(E_x \gamma u + \hat{\gamma}(E_y v + E_z w) + c\chi(E_x \gamma + \hat{\gamma}(B_z v - B_y w))) (\varrho(-u(2c\chi + u) + v^2 + w^2) - \gamma(2p + \varrho(-u(2c\chi + u) + v^2 + w^2)))}{2c\hat{\gamma}\mu_0(c\chi + u)(-\gamma p + \varrho(c\chi + u)^2)} \end{pmatrix} \quad (\text{A.118})$$

$$\mathbf{K}_{c,x}^{(6)} = \left(\begin{array}{c} \frac{\varrho(E_x \gamma u + \hat{\gamma}(E_y v + E_z w) - c\chi(E_x \gamma + \hat{\gamma}(B_z v - B_y w)))}{c\mu_0(c\chi - u)(-\gamma p + \varrho(-c\chi + u)^2)} \\ \frac{\chi \varrho(E_x \gamma u + \hat{\gamma}(E_y v + E_z w) - c\chi(E_x \gamma + \hat{\gamma}(B_z v - B_y w)))}{\mu_0(c\chi - u)(-\gamma p + \varrho(-c\chi + u)^2)} \\ \frac{B_z u(-\gamma p + \varrho(-c\chi + u)^2) - B_z c\chi \hat{\gamma} \varrho v^2 + E_y(-\varrho(-c\chi + u)^2 - \varrho v^2 + \gamma(p + \varrho v^2)) + \varrho v(E_x \gamma(-c\chi + u) + (B_y c\chi + E_z) \hat{\gamma} w)}{c\mu_0(c\chi - u)(-\gamma p + \varrho(-c\chi + u)^2)} \\ \frac{(E_z + B_y u)(\gamma p - \varrho(-c\chi + u)^2) + \varrho(E_x \gamma(-c\chi + u) + (-B_z c\chi + E_y) \hat{\gamma} v) w + (B_y c\chi + E_z) \hat{\gamma} \varrho w^2}{c\mu_0(c\chi - u)(-\gamma p + \varrho(-c\chi + u)^2)} \\ - \frac{(-E_x \gamma u - \hat{\gamma}(E_y v + E_z w) + c\chi(E_x \gamma + \hat{\gamma}(B_z v - B_y w)))(-\varrho(2c\chi u - u^2 + v^2 + w^2) + \gamma(2p + \varrho(2c\chi u - u^2 + v^2 + w^2)))}{2c\hat{\gamma}\mu_0(c\chi - u)(-\gamma p + \varrho(-c\chi + u)^2)} \end{array} \right) \quad (\text{A.119})$$

$$\mathbf{K}_{c,x}^{(7)} = \left(\begin{array}{c} \frac{\varrho(B_x c\gamma(c\xi + u) + \hat{\gamma}(B_y cv - \xi E_z v + B_z cw + \xi E_y w))}{c^2\mu_0(c\xi + u)(-\gamma p + \varrho(c\xi + u)^2)} \\ - \frac{\xi \varrho(B_x c\gamma(c\xi + u) + \hat{\gamma}(B_y cv - \xi E_z v + B_z cw + \xi E_y w))}{c\mu_0(c\xi + u)(-\gamma p + \varrho(c\xi + u)^2)} \\ - \frac{E_z u(-\gamma p + \varrho(c\xi + u)^2) + c\xi E_z \hat{\gamma} \varrho v^2 + B_y c^2(\varrho((c\xi + u)^2 + v^2) - \gamma(p + \varrho v^2)) - c\varrho v(B_x c\gamma(c\xi + u) + (B_z c + \xi E_y) \hat{\gamma} w)}{c^3\mu_0(c\xi + u)(-\gamma p + \varrho(c\xi + u)^2)} \\ - \frac{(B_z c^2 - E_y u)(-\gamma p + \varrho(c\xi + u)^2) + c\varrho(B_x c\gamma(c\xi + u) + (B_y c - \xi E_z) \hat{\gamma} v) w + c(B_z c + \xi E_y) \hat{\gamma} \varrho w^2}{c^3\mu_0(c\xi + u)(-\gamma p + \varrho(c\xi + u)^2)} \\ - \frac{(B_x c\gamma(c\xi + u) + \hat{\gamma}(B_y cv - \xi E_z v + B_z cw + \xi E_y w))(\varrho(-u(2c\xi + u) + v^2 + w^2) - \gamma(2p + \varrho(-u(2c\xi + u) + v^2 + w^2)))}{2c^2\hat{\gamma}\mu_0(c\xi + u)(-\gamma p + \varrho(c\xi + u)^2)} \end{array} \right) \quad (\text{A.120})$$

$$\mathbf{K}_{c,x}^{(8)} = \left(\begin{array}{c} \frac{\varrho(B_x c\gamma(-c\xi + u) + \hat{\gamma}(B_y cv + \xi E_z v + B_z cw - \xi E_y w))}{c^2\mu_0(c\xi - u)(-\gamma p + \varrho(-c\xi + u)^2)} \\ \frac{\xi \varrho(B_x c\gamma(-c\xi + u) + \hat{\gamma}(B_y cv + \xi E_z v + B_z cw - \xi E_y w))}{c\mu_0(c\xi - u)(-\gamma p + \varrho(-c\xi + u)^2)} \\ \frac{E_z u(\gamma p - \varrho(-c\xi + u)^2) + c\xi E_z \hat{\gamma} \varrho v^2 + B_y c^2(-\varrho(-c\xi + u)^2 - \varrho v^2 + \gamma(p + \varrho v^2)) + c\varrho v(B_x c\gamma(-c\xi + u) + (B_z c - \xi E_y) \hat{\gamma} w)}{c^3\mu_0(c\xi - u)(-\gamma p + \varrho(-c\xi + u)^2)} \\ - \frac{(B_z c^2 - E_y u)(-\gamma p + \varrho(-c\xi + u)^2) + c\varrho(B_x c\gamma(-c\xi + u) + (B_y c + \xi E_z) \hat{\gamma} v) w + c(B_z c - \xi E_y) \hat{\gamma} \varrho w^2}{c^3\mu_0(c\xi - u)(-\gamma p + \varrho(-c\xi + u)^2)} \\ - \frac{(B_x c\gamma(c\xi - u) - \hat{\gamma}(B_y cv + \xi E_z v + B_z cw - \xi E_y w))(\varrho(2c\xi u - u^2 + v^2 + w^2) + \gamma(2p + \varrho(2c\xi u - u^2 + v^2 + w^2)))}{2c^2\hat{\gamma}\mu_0(c\xi - u)(-\gamma p + \varrho(-c\xi + u)^2)} \end{array} \right) \quad (\text{A.121})$$

$$\mathbf{K}_{c,y}^{(1)} = \left(\begin{array}{c} \frac{E_y \hat{\gamma} \varrho w}{c^2\mu_0(c+v)(-\gamma p + \varrho(c+v)^2)} \\ - B_y + \frac{E_y \hat{\gamma} \varrho u w}{(c+v)(-\gamma p + \varrho(c+v)^2)} \\ \frac{c^2\mu_0}{-E_z + c \left(B_x - \frac{cE_y \hat{\gamma} \varrho w}{(c+v)(-\gamma p + \varrho(c+v)^2)} \right)} \\ \frac{E_y v(-\gamma p + \varrho(c+v)^2) + cE_y \hat{\gamma} \varrho w^2}{c^3\mu_0(c+v)(-\gamma p + \varrho(c+v)^2)} \\ - \frac{2(B_x c - E_z)(c+v)(-\gamma p + \varrho(c+v)^2) + E_y(-\varrho u^2 + \varrho v(2c+v) + \gamma(2p + \varrho(u^2 - v(2c+v)))) w + E_y \hat{\gamma} \varrho w^3}{2c^2\mu_0(c+v)(-\gamma p + \varrho(c+v)^2)} \end{array} \right) \quad (\text{A.122})$$

$$\mathbf{K}_{c,y}^{(2)} = \left(\begin{array}{c} \frac{B_y \hat{\gamma} \varrho w}{c\mu_0(c+v)(-\gamma p + \varrho(c+v)^2)} \\ E_y + \frac{B_y c^2 \hat{\gamma} \varrho u w}{(c+v)(-\gamma p + \varrho(c+v)^2)} \\ \frac{c^3\mu_0}{- \frac{B_z c + E_x}{c^3} + \frac{B_y \hat{\gamma} \varrho w}{(c+v)(-\gamma p + \varrho(c+v)^2)}} \\ - \frac{B_y v(-\gamma p + \varrho(c+v)^2) + B_y c \hat{\gamma} \varrho w^2}{c^2\mu_0(c+v)(-\gamma p + \varrho(c+v)^2)} \\ \frac{2(B_z c + E_x)(c+v)(-\gamma p + \varrho(c+v)^2) + B_y c(-\varrho u^2 + \varrho v(2c+v) + \gamma(2p + \varrho(u^2 - v(2c+v)))) w + B_y c \hat{\gamma} \varrho w^3}{2c^2\mu_0(c+v)(-\gamma p + \varrho(c+v)^2)} \end{array} \right) \quad (\text{A.123})$$

$$\mathbf{K}_{c,y}^{(3)} = \begin{pmatrix} -\frac{E_y \hat{\gamma} \varrho w}{c^2 \mu_0 (-\gamma p + \varrho(c-v)^2)(c-v)} \\ B_y + \frac{E_y \hat{\gamma} \varrho u w}{(-\gamma p + \varrho(c-v)^2)(c-v)} \\ E_z + c \left(B_x - \frac{c E_y \hat{\gamma} \varrho w}{(-\gamma p + \varrho(c-v)^2)(c-v)} \right) \\ \frac{E_y (-\gamma p + \varrho(c-v)^2) v - c E_y \hat{\gamma} \varrho w^2}{c^3 \mu_0 (-\gamma p + \varrho(c-v)^2)(c-v)} \\ \frac{2(B_x c + E_z)(-\gamma p + \varrho(c-v)^2)(c-v) + E_y (-2\gamma p + \varrho u^2 - \gamma \varrho u^2 - 2c \hat{\gamma} \varrho v + \hat{\gamma} \varrho v^2) w - E_y \hat{\gamma} \varrho w^3}{2c^2 \mu_0 (-\gamma p + \varrho(c-v)^2)(c-v)} \end{pmatrix} \quad (\text{A.124})$$

$$\mathbf{K}_{c,y}^{(4)} = \begin{pmatrix} \frac{B_y \hat{\gamma} \varrho w}{c \mu_0 (-\gamma p + \varrho(c-v)^2)(c-v)} \\ -E_y + \frac{B_y c^2 \hat{\gamma} \varrho u w}{(-\gamma p + \varrho(c-v)^2)(c-v)} \\ \frac{c^3 \mu_0}{-B_z c + E_x} + \frac{B_y \hat{\gamma} \varrho w}{(-\gamma p + \varrho(c-v)^2)(c-v)} \\ \frac{B_y (\gamma p - \varrho(c-v)^2) v + B_y c \hat{\gamma} \varrho w^2}{c^2 \mu_0 (-\gamma p + \varrho(c-v)^2)(c-v)} \\ \frac{-2(B_z c - E_x)(-\gamma p + \varrho(c-v)^2)(c-v) + B_y c (2\gamma p - \varrho u^2 + \gamma \varrho u^2 + 2c \hat{\gamma} \varrho v - \hat{\gamma} \varrho v^2) w + B_y c \hat{\gamma} \varrho w^3}{2c^2 \mu_0 (-\gamma p + \varrho(c-v)^2)(c-v)} \end{pmatrix} \quad (\text{A.125})$$

$$\mathbf{K}_{c,y}^{(5)} = \begin{pmatrix} \frac{\varrho(E_x \hat{\gamma} u + E_y \gamma v + c \chi(E_y \gamma - \hat{\gamma}(B_z u - B_x w)))}{c \mu_0 (c \chi + v)(-\gamma p + \varrho(c \chi + v)^2)} \\ -B_z c^2 \chi^2 \varrho v + v(B_z \gamma p + E_y \gamma \varrho u - B_z \varrho v^2) + E_x (\gamma(p + \varrho u^2) - \varrho(u^2 + (c \chi + v)^2)) + c \chi \varrho(E_y \gamma u + B_z(u^2 - \gamma u^2 - 2v^2) + B_x \hat{\gamma} u w) \\ -\frac{c \mu_0 (c \chi + v)(-\gamma p + \varrho(c \chi + v)^2)}{\chi \varrho(E_x \hat{\gamma} u + E_y \gamma v + c \chi(E_y \gamma - \hat{\gamma}(B_z u - B_x w)))} \\ \frac{\mu_0 (c \chi + v)(-\gamma p + \varrho(c \chi + v)^2)}{B_x v(-\gamma p + \varrho(c \chi + v)^2) + \varrho(E_x \hat{\gamma} u + c \chi(E_y \gamma + B_z u - B_z \gamma u) + E_y \gamma v) w + B_x c \chi \hat{\gamma} \varrho w^2} \\ -\frac{c \mu_0 (c \chi + v)(-\gamma p + \varrho(c \chi + v)^2)}{(E_x \hat{\gamma} u + E_y \gamma v + c \chi(E_y \gamma - \hat{\gamma}(B_z u - B_x w))) (\varrho(u^2 - v(2c \chi + v) + w^2) - \gamma(2p + \varrho(u^2 - v(2c \chi + v) + w^2)))} \\ \frac{2c \hat{\gamma} \mu_0 (c \chi + v)(-\gamma p + \varrho(c \chi + v)^2)}{2c \hat{\gamma} \mu_0 (c \chi + v)(-\gamma p + \varrho(c \chi + v)^2)} \end{pmatrix} \quad (\text{A.126})$$

$$\mathbf{K}_{c,y}^{(6)} = \begin{pmatrix} \frac{\varrho(E_x \hat{\gamma} u + E_y \gamma v - c \chi(E_y \gamma - \hat{\gamma}(B_z u - B_x w)))}{c \mu_0 (c \chi - v)(-\gamma p + \varrho(-c \chi + v)^2)} \\ -B_z c^2 \chi^2 \varrho v + v(B_z \gamma p + E_y \gamma \varrho u - B_z \varrho v^2) + E_x (\gamma(p + \varrho u^2) - \varrho(u^2 + (-c \chi + v)^2)) + c \chi \varrho(-E_y \gamma u + B_z \hat{\gamma} u^2 + 2B_z v^2 - B_x \hat{\gamma} u w) \\ \frac{c \mu_0 (c \chi - v)(-\gamma p + \varrho(-c \chi + v)^2)}{\chi \varrho(E_x \hat{\gamma} u + E_y \gamma v - c \chi(E_y \gamma - \hat{\gamma}(B_z u - B_x w)))} \\ \frac{\mu_0 (c \chi - v)(-\gamma p + \varrho(-c \chi + v)^2)}{B_x v(-\gamma p + \varrho(-c \chi + v)^2) + \varrho(E_x \hat{\gamma} u + c \chi(-E_y \gamma + B_z \hat{\gamma} u) + E_y \gamma v) w - B_x c \chi \hat{\gamma} \varrho w^2} \\ \frac{c \mu_0 (c \chi - v)(-\gamma p + \varrho(-c \chi + v)^2)}{(E_x \hat{\gamma} u + E_y \gamma v - c \chi(E_y \gamma - \hat{\gamma}(B_z u - B_x w))) (\varrho(u^2 + 2c \chi v - v^2 + w^2) + \gamma(2p + \varrho(u^2 + 2c \chi v - v^2 + w^2)))} \\ \frac{2c \hat{\gamma} \mu_0 (c \chi - v)(-\gamma p + \varrho(-c \chi + v)^2)}{2c \hat{\gamma} \mu_0 (c \chi - v)(-\gamma p + \varrho(-c \chi + v)^2)} \end{pmatrix} \quad (\text{A.127})$$

$$\mathbf{K}_{c,y}^{(7)} = \begin{pmatrix} \frac{\varrho(B_y c \gamma(c \xi + v) + \hat{\gamma}(B_x c u + \xi E_z u - \xi E_x w))}{c^2 \mu_0 (c \xi + v)(-\gamma p + \varrho(c \xi + v)^2)} \\ B_y c^2 \gamma \varrho u(c \xi + v) + E_z (-\gamma p v + c^2 \xi^2 \varrho v + \varrho v^3 + c \xi \varrho(\hat{\gamma} u^2 + 2v^2)) - B_x c^2 (-\gamma(p + \varrho u^2) + \varrho(u^2 + (c \xi + v)^2)) - c \xi E_x \hat{\gamma} \varrho u w \\ \frac{c^3 \mu_0 (c \xi + v)(-\gamma p + \varrho(c \xi + v)^2)}{-\xi \varrho(B_y c \gamma(c \xi + v) + \hat{\gamma}(B_x c u + \xi E_z u - \xi E_x w))} \\ \frac{c \mu_0 (c \xi + v)(-\gamma p + \varrho(c \xi + v)^2)}{-E_x v(-\gamma p + \varrho(c \xi + v)^2) + c \varrho((B_x c + \xi E_z) \hat{\gamma} u + B_y c \gamma(c \xi + v)) w - c \xi E_x \hat{\gamma} \varrho w^2} \\ \frac{c^3 \mu_0 (c \xi + v)(-\gamma p + \varrho(c \xi + v)^2)}{(B_y c \gamma(c \xi + v) + \hat{\gamma}(B_x c u + \xi E_z u - \xi E_x w)) (\varrho(u^2 - v(2c \xi + v) + w^2) - \gamma(2p + \varrho(u^2 - v(2c \xi + v) + w^2)))} \\ \frac{2c^2 \hat{\gamma} \mu_0 (c \xi + v)(-\gamma p + \varrho(c \xi + v)^2)}{2c^2 \hat{\gamma} \mu_0 (c \xi + v)(-\gamma p + \varrho(c \xi + v)^2)} \end{pmatrix} \quad (\text{A.128})$$

$$\mathbf{K}_{c,y}^{(8)} = \left(\begin{array}{c} \frac{\varrho(B_y c \gamma(-c\xi+v) + \hat{\gamma}(B_x c u - \xi E_z u + \xi E_x w))}{c^2 \mu_0 (c\xi-v)(-\gamma p + \varrho(-c\xi+v)^2)} \\ \frac{B_y c^2 \gamma \varrho u(-c\xi+v) + E_z(-\gamma p v + c^2 \xi^2 \varrho v + \varrho v^3 + c \xi \varrho(u^2 - \gamma u^2 - 2v^2)) + B_x c^2(\gamma(p + \varrho u^2) - \varrho(u^2 + (-c\xi+v)^2)) + c \xi E_x \hat{\gamma} \varrho u w}{c^3 \mu_0 (c\xi-v)(-\gamma p + \varrho(-c\xi+v)^2)} \\ \frac{\xi \varrho(B_y c \gamma(-c\xi+v) + \hat{\gamma}(B_x c u - \xi E_z u + \xi E_x w))}{c \mu_0 (c\xi-v)(-\gamma p + \varrho(-c\xi+v)^2)} \\ \frac{E_x v(\gamma p - \varrho(-c\xi+v)^2) + c \varrho((B_x c - \xi E_z) \hat{\gamma} u + B_y c \gamma(-c\xi+v)) w + c \xi E_x \hat{\gamma} \varrho w^2}{c^3 \mu_0 (c\xi-v)(-\gamma p + \varrho(-c\xi+v)^2)} \\ - \frac{(B_y c \gamma(c\xi-v) - \hat{\gamma}(B_x c u - \xi E_z u + \xi E_x w))(-\varrho(u^2 + 2c\xi v - v^2 + w^2) + \gamma(2p + \varrho(u^2 + 2c\xi v - v^2 + w^2)))}{2c^2 \hat{\gamma} \mu_0 (c\xi-v)(-\gamma p + \varrho(-c\xi+v)^2)} \end{array} \right) \quad (\text{A.129})$$

$$\mathbf{K}_{c,z}^{(1)} = \left(\begin{array}{c} 0 \\ \frac{B_z}{c^2 \mu_0} \\ \frac{E_z}{c^3 \mu_0} \\ -\frac{B_x c + E_y}{c^3 \mu_0} \\ \frac{B_x c + E_y}{c^2 \mu_0} \end{array} \right) \quad (\text{A.130})$$

$$\mathbf{K}_{c,z}^{(2)} = \left(\begin{array}{c} 0 \\ \frac{E_z}{c^3 \mu_0} \\ -\frac{B_z}{c^2 \mu_0} \\ \frac{B_y c - E_x}{c^3 \mu_0} \\ -\frac{B_y c + E_x}{c^2 \mu_0} \end{array} \right) \quad (\text{A.131})$$

$$\mathbf{K}_{c,z}^{(3)} = \left(\begin{array}{c} 0 \\ \frac{B_z}{c^2 \mu_0} \\ -\frac{E_z}{c^3 \mu_0} \\ \frac{-B_x c + E_y}{c^3 \mu_0} \\ \frac{-B_x c + E_y}{c^2 \mu_0} \end{array} \right) \quad (\text{A.132})$$

$$\mathbf{K}_{c,z}^{(4)} = \left(\begin{array}{c} 0 \\ -\frac{E_z}{c^3 \mu_0} \\ -\frac{B_z}{c^2 \mu_0} \\ \frac{B_y c + E_x}{c^3 \mu_0} \\ \frac{B_y c + E_x}{c^2 \mu_0} \end{array} \right) \quad (\text{A.133})$$

$$\mathbf{K}_{c,z}^{(5)} = \left(\begin{array}{c} \frac{\rho(\hat{\gamma}(E_x u + E_y v) + c\chi(E_z \gamma + \hat{\gamma}(B_y u - B_x v)) + E_z \gamma w)}{c\mu_0(c\chi + w)(-\gamma p + \rho(c\chi + w)^2)} \\ \frac{\rho u(c\chi(E_z \gamma + B_y \hat{\gamma} u) + (-B_x c\chi + E_y)\hat{\gamma} v) + (-B_y \gamma p + B_y c^2 \chi^2 \rho + E_z \gamma \rho u) w + 2B_y c\chi \rho w^2 + B_y \rho w^3 + E_x(\gamma(p + \rho u^2) - \rho(u^2 + (c\chi + w)^2))}{c\mu_0(c\chi + w)(-\gamma p + \rho(c\chi + w)^2)} \\ \frac{\rho v(E_x \hat{\gamma} u + c\chi(E_z \gamma + \hat{\gamma}(B_y u - B_x v))) + (B_x \gamma p - B_x c^2 \chi^2 \rho + E_z \gamma \rho v) w - 2B_x c\chi \rho w^2 - B_x \rho w^3 + E_y(\gamma(p + \rho v^2) - \rho(v^2 + (c\chi + w)^2))}{c\mu_0(c\chi + w)(-\gamma p + \rho(c\chi + w)^2)} \\ - \frac{\chi \rho(\hat{\gamma}(E_x u + E_y v) + c\chi(E_z \gamma + \hat{\gamma}(B_y u - B_x v)) + E_z \gamma w)}{\mu_0(c\chi + w)(-\gamma p + \rho(c\chi + w)^2)} \\ - \frac{(\hat{\gamma}(E_x u + E_y v) + c\chi(E_z \gamma + \hat{\gamma}(B_y u - B_x v)) + E_z \gamma w)(\rho(u^2 + v^2 - w(2c\chi + w)) - \gamma(2p + \rho(u^2 + v^2 - w(2c\chi + w))))}{2c\hat{\gamma}\mu_0(c\chi + w)(-\gamma p + \rho(c\chi + w)^2)} \end{array} \right) \quad (\text{A.134})$$

$$\mathbf{K}_{c,z}^{(6)} = \left(\begin{array}{c} \frac{\rho(\hat{\gamma}(E_x u + E_y v) - c\chi(E_z \gamma + \hat{\gamma}(B_y u - B_x v)) + E_z \gamma w)}{c\mu_0(c\chi - w)(-\gamma p + \rho(-c\chi + w)^2)} \\ \frac{\rho u(-c\chi(E_z \gamma + B_y \hat{\gamma} u) + (B_x c\chi + E_y)\hat{\gamma} v) + (-B_y \gamma p + B_y c^2 \chi^2 \rho + E_z \gamma \rho u) w - 2B_y c\chi \rho w^2 + B_y \rho w^3 + E_x(\gamma(p + \rho u^2) - \rho(u^2 + (-c\chi + w)^2))}{c\mu_0(c\chi - w)(-\gamma p + \rho(-c\chi + w)^2)} \\ \frac{\rho v(E_x \hat{\gamma} u - c\chi(E_z \gamma + \hat{\gamma}(B_y u - B_x v))) + (B_x \gamma p - B_x c^2 \chi^2 \rho + E_z \gamma \rho v) w + 2B_x c\chi \rho w^2 - B_x \rho w^3 + E_y(\gamma(p + \rho v^2) - \rho(v^2 + (-c\chi + w)^2))}{c\mu_0(c\chi - w)(-\gamma p + \rho(-c\chi + w)^2)} \\ - \frac{\chi \rho(\hat{\gamma}(E_x u + E_y v) - c\chi(E_z \gamma + \hat{\gamma}(B_y u - B_x v)) + E_z \gamma w)}{\mu_0(c\chi - w)(-\gamma p + \rho(-c\chi + w)^2)} \\ - \frac{(-\hat{\gamma}(E_x u + E_y v) + c\chi(E_z \gamma + \hat{\gamma}(B_y u - B_x v)) - E_z \gamma w)(-\rho(u^2 + v^2 + 2c\chi w - w^2) + \gamma(2p + \rho(u^2 + v^2 + 2c\chi w - w^2)))}{2c\hat{\gamma}\mu_0(c\chi - w)(-\gamma p + \rho(-c\chi + w)^2)} \end{array} \right) \quad (\text{A.135})$$

$$\mathbf{K}_{c,z}^{(7)} = \left(\begin{array}{c} \frac{\rho(\hat{\gamma}(B_x c u - \xi E_y u + B_y c v + \xi E_x v) + B_z c \gamma(c\xi + w))}{c^2 \mu_0(c\xi + w)(-\gamma p + \rho(c\xi + w)^2)} \\ \frac{c\hat{\gamma} \rho u(-\xi E_y u + B_y c v + \xi E_x v) + E_y(\gamma p - c^2 \xi^2 \rho) w - 2c\xi E_y \rho w^2 - E_y \rho w^3 + B_z c^2 \gamma \rho u(c\xi + w) - B_x c^2(-\gamma(p + \rho u^2) + \rho(u^2 + (c\xi + w)^2))}{c^3 \mu_0(c\xi + w)(-\gamma p + \rho(c\xi + w)^2)} \\ \frac{c\hat{\gamma} \rho v(B_x c u - \xi E_y u + \xi E_x v) + E_x(-\gamma p + c^2 \xi^2 \rho) w + 2c\xi E_x \rho w^2 + E_x \rho w^3 + B_z c^2 \gamma \rho v(c\xi + w) - B_y c^2(-\gamma(p + \rho v^2) + \rho(v^2 + (c\xi + w)^2))}{c^3 \mu_0(c\xi + w)(-\gamma p + \rho(c\xi + w)^2)} \\ - \frac{\xi \rho(\hat{\gamma}(B_x c u - \xi E_y u + B_y c v + \xi E_x v) + B_z c \gamma(c\xi + w))}{c\mu_0(c\xi + w)(-\gamma p + \rho(c\xi + w)^2)} \\ - \frac{(\hat{\gamma}(B_x c u - \xi E_y u + B_y c v + \xi E_x v) + B_z c \gamma(c\xi + w))(\rho(u^2 + v^2 - w(2c\xi + w)) - \gamma(2p + \rho(u^2 + v^2 - w(2c\xi + w))))}{2c^2 \hat{\gamma} \mu_0(c\xi + w)(-\gamma p + \rho(c\xi + w)^2)} \end{array} \right) \quad (\text{A.136})$$

$$\mathbf{K}_{c,z}^{(8)} = \left(\begin{array}{c} \frac{\rho(\hat{\gamma}(B_x c u + \xi E_y u + B_y c v - \xi E_x v) + B_z c \gamma(-c\xi + w))}{c^2 \mu_0(c\xi - w)(-\gamma p + \rho(-c\xi + w)^2)} \\ \frac{c\hat{\gamma} \rho u(\xi E_y u + B_y c v - \xi E_x v) + E_y(\gamma p - c^2 \xi^2 \rho) w + 2c\xi E_y \rho w^2 - E_y \rho w^3 + B_z c^2 \gamma \rho u(-c\xi + w) + B_x c^2(\gamma(p + \rho u^2) - \rho(u^2 + (-c\xi + w)^2))}{c^3 \mu_0(c\xi - w)(-\gamma p + \rho(-c\xi + w)^2)} \\ \frac{c\hat{\gamma} \rho v(B_x c u + \xi E_y u - \xi E_x v) + E_x(-\gamma p + c^2 \xi^2 \rho) w - 2c\xi E_x \rho w^2 + E_x \rho w^3 + B_z c^2 \gamma \rho v(-c\xi + w) + B_y c^2(\gamma(p + \rho v^2) - \rho(v^2 + (-c\xi + w)^2))}{c^3 \mu_0(c\xi - w)(-\gamma p + \rho(-c\xi + w)^2)} \\ - \frac{\xi \rho(\hat{\gamma}(B_x c u + \xi E_y u + B_y c v - \xi E_x v) + B_z c \gamma(-c\xi + w))}{c\mu_0(c\xi - w)(-\gamma p + \rho(-c\xi + w)^2)} \\ - \frac{(-\hat{\gamma}(B_x c u + \xi E_y u + B_y c v - \xi E_x v) + B_z c \gamma(-c\xi + w))(\rho(u^2 + v^2 + 2c\xi w - w^2) + \gamma(2p + \rho(u^2 + v^2 + 2c\xi w - w^2)))}{2c^2 \hat{\gamma} \mu_0(c\xi - w)(-\gamma p + \rho(-c\xi + w)^2)} \end{array} \right) \quad (\text{A.137})$$

The matrices $\hat{\mathbf{K}}_x$, $\hat{\mathbf{K}}_y$ and $\hat{\mathbf{K}}_z$ comprised of the above column eigenvectors, along with its inverse matrix and the diagonal matrix given in equation A.112 (where q becomes u , v or w depending on the direction) can be shown to fully diagonalize the jacobian matrix presented in equation A.108.

A.5.4 Jacobian Matrices for Implicit Scheme

The implicit scheme described in Section 5.9 outlines a procedure for updating the plasmadynamic equations, but requires the calculation of the matrices $\hat{\mathbf{r}}$, $\partial \mathbf{U} / \partial \mathbf{Q}$ and $\partial \mathbf{R} / \partial \mathbf{Q}$. For simplicity of presentation, we assume that the flux vector, \mathbf{F} , is only updated explicitly every timestep, such that the residual Jacobian becomes $\partial \mathbf{R} / \partial \mathbf{Q} = \partial \mathbf{H} / \partial \mathbf{Q}$. Below, we present the forms of these matrices used in the investigations detailed in

Chapters 5 and 6.

$$\hat{\mathbf{r}} = \begin{bmatrix} 1 & 0 & 0 & 0 & 0 & 0 & 0 & 0 & 0 & 0 & 0 & 0 & 0 \\ u & \varrho & 0 & 0 & 0 & 0 & -\bar{E}_z & \bar{E}_y & 0 & \bar{B}_z & -\bar{B}_y & 0 & 0 \\ v & 0 & \varrho & 0 & 0 & \bar{E}_z & 0 & -\bar{E}_x & -\bar{B}_z & 0 & \bar{B}_x & 0 & 0 \\ w & 0 & 0 & \varrho & 0 & -\bar{E}_y & \bar{E}_x & 0 & \bar{B}_y & -\bar{B}_x & 0 & 0 & 0 \\ V^2/2 & \varrho u & \varrho v & \varrho w & 1/\hat{\gamma} & B_x/\mu_0 & B_y/\mu_0 & B_z/\mu_0 & \bar{E}_x & \bar{E}_y & \bar{E}_z & 0 & 0 \\ 0 & 0 & 0 & 0 & 0 & 1 & 0 & 0 & 0 & 0 & 0 & 0 & 0 \\ 0 & 0 & 0 & 0 & 0 & 0 & 1 & 0 & 0 & 0 & 0 & 0 & 0 \\ 0 & 0 & 0 & 0 & 0 & 0 & 0 & 1 & 0 & 0 & 0 & 0 & 0 \\ 0 & 0 & 0 & 0 & 0 & 0 & 0 & 0 & \beta^{-2} & 0 & 0 & 0 & 0 \\ 0 & 0 & 0 & 0 & 0 & 0 & 0 & 0 & 0 & \beta^{-2} & 0 & 0 & 0 \\ 0 & 0 & 0 & 0 & 0 & 0 & 0 & 0 & 0 & 0 & \beta^{-2} & 0 & 0 \\ 0 & 0 & 0 & 0 & 0 & 0 & 0 & 0 & 0 & 0 & 0 & 1 & 0 \\ 0 & 0 & 0 & 0 & 0 & 0 & 0 & 0 & 0 & 0 & 0 & 0 & 1 \end{bmatrix} \quad (\text{A.138})$$

where $V^2 = u^2 + v^2 + w^2$, $\hat{\gamma} = \gamma - 1$, $\bar{\mathbf{E}} = \mathbf{E}/(c_0^2\mu_0)$, $\bar{\mathbf{B}} = \mathbf{B}/(c_0^2\mu_0)$, and β is the preconditioning parameter.

The jacobian matrix $\partial\mathbf{U}/\partial\mathbf{Q}$ is

$$\frac{\partial\mathbf{U}}{\partial\mathbf{Q}} = \begin{bmatrix} 1 & 0 & 0 & 0 & 0 & 0 & 0 & 0 & 0 & 0 & 0 & 0 & 0 \\ u & \varrho & 0 & 0 & 0 & 0 & -\bar{E}_z & \bar{E}_y & 0 & \bar{B}_z & -\bar{B}_y & 0 & 0 \\ v & 0 & \varrho & 0 & 0 & \bar{E}_z & 0 & -\bar{E}_x & -\bar{B}_z & 0 & \bar{B}_x & 0 & 0 \\ w & 0 & 0 & \varrho & 0 & -\bar{E}_y & \bar{E}_x & 0 & \bar{B}_y & -\bar{B}_x & 0 & 0 & 0 \\ V^2/2 & \varrho u & \varrho v & \varrho w & 1/\hat{\gamma} & B_x/\mu_0 & B_y/\mu_0 & B_z/\mu_0 & \bar{E}_x & \bar{E}_y & \bar{E}_z & 0 & 0 \\ 0 & 0 & 0 & 0 & 0 & 1 & 0 & 0 & 0 & 0 & 0 & 0 & 0 \\ 0 & 0 & 0 & 0 & 0 & 0 & 1 & 0 & 0 & 0 & 0 & 0 & 0 \\ 0 & 0 & 0 & 0 & 0 & 0 & 0 & 1 & 0 & 0 & 0 & 0 & 0 \\ 0 & 0 & 0 & 0 & 0 & 0 & 0 & 0 & 1 & 0 & 0 & 0 & 0 \\ 0 & 0 & 0 & 0 & 0 & 0 & 0 & 0 & 0 & 1 & 0 & 0 & 0 \\ 0 & 0 & 0 & 0 & 0 & 0 & 0 & 0 & 0 & 0 & 1 & 0 & 0 \\ 0 & 0 & 0 & 0 & 0 & 0 & 0 & 0 & 0 & 0 & 0 & 1 & 0 \\ 0 & 0 & 0 & 0 & 0 & 0 & 0 & 0 & 0 & 0 & 0 & 0 & 1 \end{bmatrix} \quad (\text{A.139})$$

where $V^2 = u^2 + v^2 + w^2$, $\hat{\gamma} = \gamma - 1$, $\bar{\mathbf{E}} = \mathbf{E}/(c_0^2\mu_0)$ and $\bar{\mathbf{B}} = \mathbf{B}/(c_0^2\mu_0)$. The source jacobian matrix, $\partial\mathbf{H}/\partial\mathbf{Q}$,

is

$$\frac{\partial \mathbf{H}}{\partial \mathbf{Q}} = \frac{\sigma}{\epsilon_0} \begin{bmatrix} 0 & 0 & 0 & 0 & 0 & 0 & 0 & 0 & 0 & 0 & 0 & 0 & 0 \\ 0 & 0 & 0 & 0 & 0 & 0 & 0 & 0 & 0 & 0 & 0 & 0 & 0 \\ 0 & 0 & 0 & 0 & 0 & 0 & 0 & 0 & 0 & 0 & 0 & 0 & 0 \\ 0 & 0 & 0 & 0 & 0 & 0 & 0 & 0 & 0 & 0 & 0 & 0 & 0 \\ 0 & 0 & 0 & 0 & 0 & 0 & 0 & 0 & 0 & 0 & 0 & 0 & 0 \\ 0 & 0 & 0 & 0 & 0 & 0 & 0 & 0 & 0 & 0 & 0 & 0 & 0 \\ 0 & 0 & 0 & 0 & 0 & 0 & 0 & 0 & 0 & 0 & 0 & 0 & 0 \\ 0 & 0 & 0 & 0 & 0 & 0 & 0 & 0 & 0 & 0 & 0 & 0 & 0 \\ 0 & 0 & -B_z & B_y & 0 & 0 & w & -v & -1 & 0 & 0 & 0 & 0 \\ 0 & B_z & 0 & -B_x & 0 & -w & 0 & u & 0 & -1 & 0 & 0 & 0 \\ 0 & -B_y & B_x & 0 & 0 & v & -u & 0 & 0 & 0 & -1 & 0 & 0 \\ 0 & 0 & 0 & 0 & 0 & 0 & 0 & 0 & 0 & 0 & 0 & 0 & 0 \\ 0 & 0 & 0 & 0 & 0 & 0 & 0 & 0 & 0 & 0 & 0 & 0 & 0 \end{bmatrix} \quad (\text{A.140})$$

Vita

Mr. Thompson was born in North Carolina. He was awarded his degree in physics from Lipscomb University in 2007, and in 2009 was awarded his M.Sc degree in Mechanical Engineering from the University of Tennessee Space Institute. This dissertation represents the completion of his doctoral studies at the University of Tennessee Space Institute in 2013. He is happily married, with two children. His research interests center around theoretical and computational modeling of fluids and plasmas with applications to propulsion and energy. When he is not working, he enjoys spending time with his wife and children, presenting local art shows, writing code to generate fractal art, and writing simulations of the Zombie Apocalypse using Lanchestrian combat models.